THÈSE

En vue de l'obtention du

DOCTORAT DE L'UNIVERSITÉ DE TOULOUSE

Délivré par *l'Institut National Polytechnique de Toulouse*
Discipline ou spécialité : *Génie des Procédés et de l'Environnement*

Présentée et soutenue par *Norbert Völkel*
Le *04 décembre 2009*

Design and characterization of gas-liquid microreactors

JURY

Yves Gonthier	*Rapporteur*
Ryszard Pohorecki	*Rapporteur*
Claude de Bellefon	*Examinateur*
Stéphane Colin	*Examinateur*
Catherine Xuereb	*Directrice de Thèse*
Joelle Aubin	*Co-Encadrante*

Ecole doctorale : *Mécanique, Energétique, Génie Civil, Procédés (MEGEP)*
Unité de recherche : *Laboratoire de Génie Chimique (LGC), Toulouse*
Directrice de Thèse : *Catherine Xuereb*

Summary

The present project deals with the improvement of the design of gas-liquid microreactors. The term microreactor characterizes devices composed of channels that have dimensions in the several tens to several hundreds of microns. Due to their increased surface to volume ratios these devices are a promising way to control fast and highly exothermic reactions, often employed in the production of fine chemicals and pharmaceutical compounds. In the case of gas-liquid systems, these are for example direct fluorination, hydrogenation or oxidation reactions. Compared to conventional equipment microreactors offer the possibility to suppress hot spots and to operate hazardous reaction systems at increased reactant concentrations. Thereby selectivity may be increased and operating costs decreased. In this manner microreaction technology well fits in the challenges the chemical industry is continuously confronted to, which are amongst others the reduction of energy consumption and better feedstock utilization. The main topics which have to be considered with respect to the design of gas-liquid µ-reactors are heat and mass transfer. In two phase systems both are strongly influenced by the nature of the flow and thus hydrodynamics play a central role. Consequently we focused our work on the hydrodynamics of the two-phase flow in microchannels and the description of the inter-linkage to gas-liquid mass transfer. In this context we were initially concerned with the topic of gas-liquid flow regimes and the main parameters prescribing flow pattern transitions. From a comparison of flow patterns with respect to their mass transfer capacity, as well as the flexibility offered with respect to operating conditions, the Taylor flow pattern appears to be the most promising flow characteristic for performing fast, highly exothermic and mass transfer limited reactions. This flow pattern is characterized by elongated bubbles surrounded by a liquid film and separated from each other by liquid slugs. In addition to the fact that this flow regime is accessible within a large range of gas and liquid flow rates, and has a relatively high specific interfacial area, Taylor flow features a recirculation motion within the liquid slugs, which is generally assumed to increase molecular transport between the gas-liquid interface and the bulk of the liquid phase. From a closer look on the local hydrodynamics of Taylor flow, including the fundamentals of bubble transport and the description of the recirculation flow within the liquid phase, it turned out that two-phase pressure drop and gas-liquid mass transfer are governed by the bubble velocity, bubble lengths and slug lengths. In the following step we have dealt with the prediction of these key hydrodynamic parameters. In this connection the first part of our experimental study was concerned with the investigation of the formation of bubbles and slugs and the characterization of the liquid phase velocity field in microchannels of rectangular cross-section. In addition we also addressed the phenomenon of film dewetting, which plays an important role concerning pressure drop and mass-transfer in Taylor flow. In the second part we focused on the prediction of gas-liquid mass transfer in Taylor flow. Measurements of the volumetric liquid side mass transfer coefficient ($k_L a$-value) were conducted and the related two-phase flow was recorded. The measured bubble velocities, bubble lengths and slug lengths, as well as the findings previously obtained from the characterization of the velocity field were used to set-up a modified model for the prediction of $k_L a$-values in µ-channels of rectangular cross-section. Describing the interaction of channel design hydrodynamics and mass transfer our work thus provides an important contribution towards the control of the operation of fast, highly exothermic and mass transfer limited gas-liquid reactions in microchannels. In addition it enabled us to identify gaps of knowledge, whose investigation should be items of further research.

Résumé

Cette étude est dédiée à l'amélioration du design des microréacteurs gaz-liquide. Le terme de microréacteur correspond à des appareils composés de canaux dont les dimensions sont de l'ordre de quelques dizaines à quelques centaines de microns. Grâce à la valeur importante du ratio surface/volume, ces appareils constituent une issue prometteuse pour contrôler les réactions rapides fortement exothermiques, souvent rencontrées en chimie fine et pharmaceutique. Dans le cas des systèmes gaz-liquide, on peut citer par exemple les réactions de fluoration, d'hydrogénation ou d'oxydation. Comparés à des appareils conventionnels, les microréacteurs permettent de supprimer le risque d'apparition de points chauds, et d'envisager le fonctionnement dans des conditions plus critiques, par exemple avec des concentrations de réactifs plus élevées. En même temps, la sélectivité peut être augmentée et les coûts opératoires diminués. Ainsi, les technologies de microréacteurs s'inscrivent bien dans les nouveaux challenges auxquels l'industrie chimique est confrontée ; on peut citer en particulier la réduction de la consommation énergétique et la gestion des stocks de produits intermédiaires. Les principaux phénomènes qui doivent être étudiés lors de la conception d'un microréacteur sont le transfert de matière et le transfert thermique. Dans les systèmes diphasiques, ces transferts sont fortement influencés par la nature des écoulements, et l'hydrodynamique joue donc un rôle central. Par conséquent, nous avons focalisé notre travail sur l'hydrodynamique de l'écoulement diphasique dans les microcanaux et sur les couplages constatés avec le transfert de masse. Dans ce contexte, nous nous sommes dans un premier temps intéressés aux régimes d'écoulement et aux paramètres contrôlant la transition entre les différents régimes. Au vu des capacités de transfert de matière et à la flexibilité offerte en terme de conditions opératoires, le régime de Taylor semble le plus prometteur pour mettre en œuvre des réactions rapides fortement exothermiques et limitées par le transfert de matière. Ce régime d'écoulement est caractérisé par des bulles allongées entourées par un film liquide et séparées les unes des autres par une poche liquide. En plus du fait que ce régime est accessible à partir d'une large gamme de débits gazeux et liquide, l'aire interfaciale développée est assez élevée, et les mouvements de recirculation du liquide induits au sein de chaque poche sont supposés améliorer le transport des molécules entre la zone interfaciale et le liquide. A partir d'une étude de l'hydrodynamique locale d'un écoulement de Taylor, il s'est avéré que la perte de charge et le transfert de matière sont contrôlés par la vitesse des bulles, et la longueur des bulles et des poches. Dans l'étape suivante, nous avons étudié l'influence des paramètres de fonctionnement sur ces caractéristiques de l'écoulement. Une première phase de notre travail expérimental a porté sur la formation des bulles et des poches et la mesure des champs de vitesse de la phase liquide dans des microcanaux de section rectangulaire. Nous avons également pris en compte le phénomène de démouillage, qui joue un rôle important au niveau de la perte de charge et du transfert de matière. Des mesures du coefficient de transfert de matière ($k_L a$) ont été réalisées tandis que l'écoulement associé était enregistré. Les vitesses de bulles, longueurs de bulles et de poches, ainsi que les caractéristiques issues de l'exploitation des champs de vitesse précédemment obtenus, ont été utilisées afin de proposer un modèle modifié pour la prédiction du $k_L a$ dans des microcanaux de section rectangulaire. En mettant en évidence l'influence du design du microcanal sur l'hydrodynamique et le transfert de matière, notre travail apporte une contribution importante dans le contrôle en microréacteur des réactions rapides fortement exothermiques et limitées par le transfert de matière. De plus, ce travail a permis d'identifier certaines lacunes en termes de connaissance, ce qui devrait pouvoir constituer l'objet de futures recherches.

Acknowledgements/Rémerciements

Within this section I would like to express my appreciation to the people who contributed either directly or indirectly to this thesis. But before going to the specific enumeration of co-operating partners, contributors and people who inspired this work I like to thank the 6th Framework Programme of the European Commission for funding through the Integrated Project IMPULSE (project no. NMP2-CT-2005-011816, www.impulse-project.net [2005-2009]). The following acknowledgements are written in the languages I used to address myself to the respective individuals.

Je tiens en premier lieu à remercier ma directrice Catherine Xuereb et ma co-encadrante Joëlle Aubin pour m'avoir donné la possibilité de travailler sur ce sujet. Je les remercie également pour leur confiance dans le processus de développement du projet ainsi que pour leur soutien scientifique et organisationnel dans la réalisation de ce travail. Je remercie en outre Joëlle Aubin pour sa collaboration au sujet de la micro-PIV ainsi que pour les corrections du manuscrit.

Je remercie les rapporteurs, Ryszard Pohorecki et Yves Gonthier, pour l'évaluation détaillée du manuscrit. Je tiens également à remercier les autres examinateurs du jury, Claude de Bellefon et Stéphane Colin, pour l'intérêt porté à ce travail. Je suis également très reconnaissant envers l'ensemble des membres du jury pour leurs remarques critiques ainsi que pour les discussions abondantes et enrichissantes menées sur ce sujet en liaison avec des nouvelles idées à poursuivre.

I owe many thanks to Professor Ryszard Pohorecki, Dr. Pawel Sobieszuk, Karolina Kula, Pawel Cyganski and Filip Ilnicki from the Faculty of Chemical and Process Engineering, Warsaw University of Technology (WUT), for giving me the possibility to carry out a part of my experimental study at their laboratory, for sharing their insight and experience in the field of methods for characterizing gas-liquid mass transfer as well as for providing their equipment and support for conducting the corresponding measurements. Furthermore, I would like to thank Professor Ryszard Pohorecki for numerous inspiring discussions about hydrodynamics and mass transfer in microchannels.

Je tiens également à exprimer ma reconnaissance envers Josiane Tasselli du Laboratoire d'Analyse et d'Architecture des Systèmes (LAAS), Toulouse, pour la fabrication des micro-canaux. Dans ce contexte j'ai également beaucoup apprécié d'avoir eu la possibilité d'accéder à la salle blanche pour assister à plusieurs étapes de ce processus.

La partie principale de ce travail a été réalisée au sein du Laboratoire de Génie Chimique (LGC) de l'Institut National Polytechnique de Toulouse (INPT). À ce titre je remercie Joël Bertrand, directeur du LGC, de m'avoir accueilli dans son laboratoire.
Je suis très reconnaissant envers les membres du personnel technique : Christine Rey-Rouch, Alain Pontier, Lahcen Farhi, Alec Maunoury, Bernard Galy, Denis Plotton, Rafik Taiar, Alain Philip et Alain Muller pour leur disponibilité et leurs conseils au niveau de la mis en pratique du projet. Je remercie en particulier les techniciens avec qui j'ai travaillé : Alain Pontier et Lahcen Farhi pour leur engagement et leurs compétences apportées dans la réalisation de l'installation expérimentale.
Je tiens également à remercier les membres de l'équipe administrative : Claudine Lorenzon, Maria Escobar-Munoz, Danièle Bouscary et Georgette Pollini pour leur soutien organisationnel.

Je remercie Martine Poux, Laurent Prat et Olivier Masbernat pour l'intérêt porté à ce travail ainsi que pour les nombreuses discussions au sujet des écoulements diphasiques, des réacteurs intensifiés et du Génie des Procédés en général.
Je souhaiterais également remercier mes collègues doctorants de la salle « micro » : Nathalie Di-Miceli, Fahima Rachedi et Alain Marcati pour le partage des appareils de mesure et autres équipements ainsi que pour les discussions et les aperçus des applications multiples des composants micro-structurées.
Je remercie Aloisiyus Yuli Widianto pour les mesures hydrodynamiques effectuées pendant son stage de Master. Je remercie également Matthieu Roudet pour les nombreuses explications au sujet de la mécanique des fluides ainsi que pour les nombreuses discussions menées au niveau des phénomènes de transfert et des méthodes de caractérisation associées.
Finalement, je tiens à remercier très chaleureusement les doctorants de mon équipe d'Agitation et Mélange : Maria-Patricia Rodriguez-Rojas, Jean-Philippe Torré, Grégory Couerbe, Felicie Theron, Emeline Lobry, Tanya Matova et Ioana-Miruna Dorobantu pour leurs conseils, renseignements, l'aperçu intéressant de leurs projet de recherche ainsi que pour l'ambiance agréable dans notre bureau.

Table of Contents

1 General Introduction

The chemical industry is one of the most important industrial sectors. It provides a broad range of products covering for example plastics, cleaning agents, plant protection and pharmaceutical compounds. In this connection it is also an important supplier of materials and substances for many "downstream" sectors like healthcare, automobile or electronic industries. The chemical industry is thus indirectly a part of our daily life and increases the quality of our lifestyle (see figure 1.1a). On the other hand, the chemical industry is also the sector with the highest energy consumption. It uses almost 12 % of the total energy demand of the European Union and energy costs may amount up to 60 % of company operating costs. The most common energy sources are coal, oil and gas; the latter two serving also as feedstock for chemical processes (see figure 1.1b).

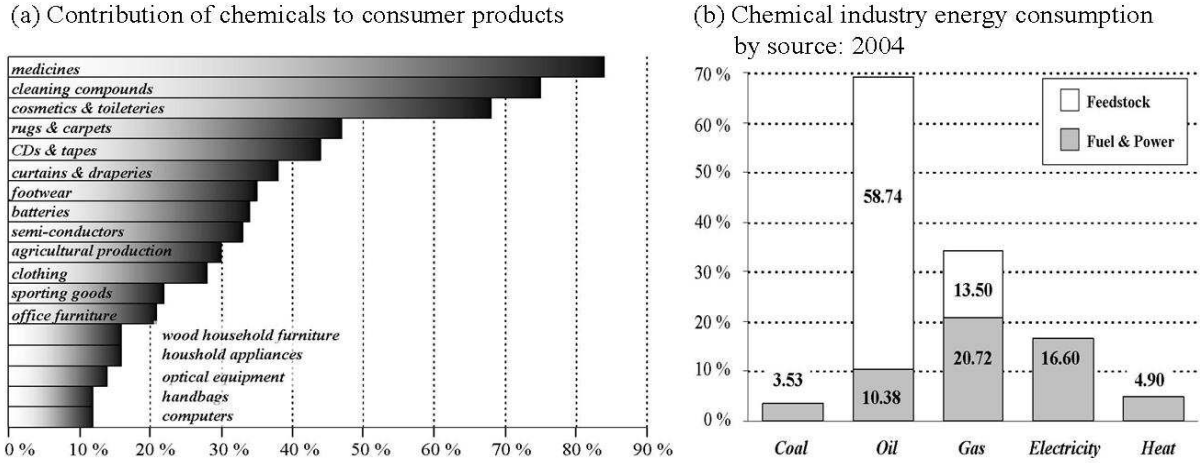

Figure 1.1: Facts and statistics about the impact of the chemical industry (source: The European Chemical Industry Council, see www.cefic.be).

The finite nature of fossil fuels, as well as the targets of the Kyoto protocol to reduce greenhouse gas emissions, have in part incited the chemical industry to continuously improve the efficiency of their production processes. In this context one of the main challenges are the reduction of energy consumption and better feedstock utilization.

Besides basic chemicals, polymers and consumer products an important sub-sector of the chemical industry are specialty and fine chemicals (see figure1.2), involving for example pharmaceutical and plant protection compounds. It represents 24 % of all chemical sales and up to 30 % of the total manufacturing activity.

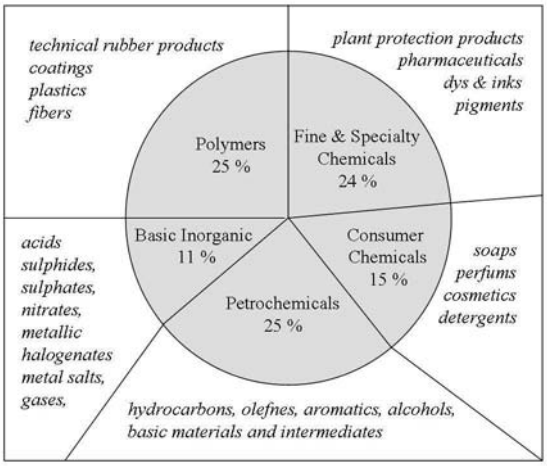

Figure 1.2: Important sub-sectors of the chemical industry and examples of products (source: The European Chemical Industry Council, see www.cefic.be).

The production processes of most fine chemicals and pharmaceuticals involve multiphase reaction systems (Mills and Chaudhari, 1997). A great number of these reaction systems are fast and highly exothermic, non-catalyzed or catalyzed, gas-liquid reactions. In this connection, the fast and highly exothermic character of these reaction systems may lead to the reactor run-away and explosion. The traditional equipment, which is commonly used are mid to large scale batch

stirred reactors or loop recycle reactors (Chaudhari and Mills, 2004). However, such reactors have relatively low heat transfer performance. In order to control the reaction systems mentioned above they are operated at high dilution of reactants, which requires the use of large amounts of solvents. Additionally, the dilution of reactants may not ensure prevention of local accumulation of reaction heat (hot spots), which favours the appearance of undesired side reactions lowering the selectivity and thus represents a loss of feedstock and product. As a result product recovery requires intensive separation, which increases processing time, energy consumption and operating costs. In some cases the direct reaction route is not safely realizable even at high dilution and therefore alternative synthesis routes requiring several reaction steps and additional equipment are used.

Microreaction technology provides the possibility to confront the challenges related to process improvement of the chemical industry. Microreaction technology refers to structured devices composed of small channels that have dimensions of the order of several tens to several hundreds of microns and are used to perform a variety of operations, like mixing, reaction, heat transfer and separation. The main idea behind this approach is based on the fact that heat transfer is directly proportional to the surface to volume ratio of the channel, which is inversely proportional to its diameter. As an example, for a 100 µm diameter microchannel the surface to volume ratio is 40000 m^2/m^3 whilst in a single 30 mm channel of a tubular reactor this ratio is 133 m^2/m^3. Referring to the conventional equipment mentioned above, loop recycle reactors and jacketed batch reactors offer surface to volume ratios of the order of 10^1 - 10^0 m^2/m^3 (Stoessel 2008). Consequently, microreactors are a promising approach for controlling fast and highly exothermic reactions and thus lowering the risks of reactor explosion. Their remarkable heat transfer efficiency additionally offers the possibility to suppress hot-spots, thereby increasing selectivity. Furthermore, the reactions considered here may be operated at higher reactant concentrations than in conventional equipment. These are key points for the reduction of operating costs. Summing up, compared to conventional equipment, microreactors represent an opportunity to safely run hazardous reactions with less energy consumption and better feedstock utilization.

Due to their high heat transfer capacity, research on the industrial application of micro-structured devices was initially focused on heat exchangers. Furthermore, since the reduction of the channel diameter also reduces diffusion lengths, a second area of early interest was concerned with single phase mixing processes. This resulted in the development of a large variety of micro-heat exchangers and micromixers (Ehrfeld et al. 2000), and the industrial feasibility has been largely proven. Only more recently have we been informed of the successful implementation of micromixers in industrial processes (Kirschneck and Tekautz, 2007). The proof of performance of these specific devices gave rise to a growing interest of microreaction technology to multiphase applications, such as gas-liquid reactions. The studies undertaken with respect to this topic indeed showed that fast and highly exothermic gas-liquid reactions may be operated in microchannels with less cooling than in conventional reactors or even at room temperature (de Mas et al., 2003; Jähnisch et al., 2004). In addition, an increase of selectivity has also been demonstrated. Following these successful demonstrations it is now of interest to fundamentally understand and better design gas-liquid microreactors. In this context the project IMPULSE (Integrated Multiscale Process Units with Locally Structured Elements), financed in the 6th European Framework Program, has brought academics and industrialists together to integrate innovative multiscale process equipment and create flexible production plants that satisfy economical requirements. Within this project one workpackage has dealt with generic methodologies for the design of innovative process equipment which, amongst other applications, involves the fundamental understanding of the phenomena that have to be considered for the development of multiphase microreactors. The points that must be accounted for in the design of microreactors for fast and highly exothermic gas-liquid reactions are shown in figure 1.3.

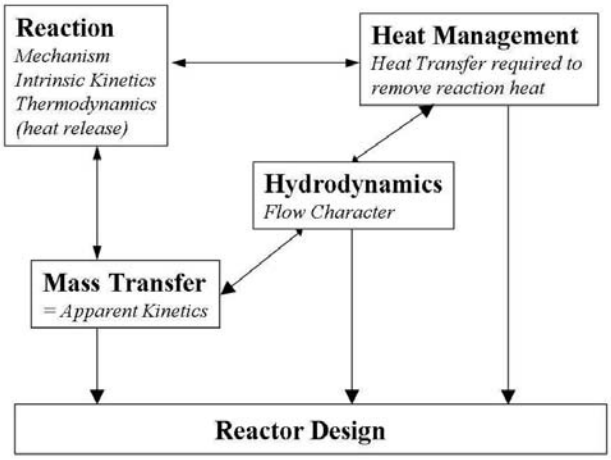

Figure 1.3: Points that must be considered for the design of microreactors in the case of fast, highly exothermic and mass-transfer limited gas-liquid reaction systems.

The starting point of the schematic diagram given in figure 1.3 is reaction. The heat released by the reaction determines the heat transfer that has to be achieved in order to remove it. The type of reactions considered here generally assumes that the reaction rate is significantly greater than that of mass transfer. Thus the progress of the reaction and its heat release is entirely dependent on the gas-liquid mass transfer. The gas-liquid mass transfer itself depends on the hydrodynamics, which characterizes the distribution of both phases along the channel. It can thus be seen that hydrodynamics play a central role regarding the microreactor design. For this reason we decided to concentrate our work on the hydrodynamics of two-phase flow and to establish the link with mass transfer.

The present study is divided into two parts: Part A, fundamentals and theory; and Part B, experimental aspects. Within part A we will start with a detailed literature review of gas-liquid two phase flows in microchannels. In this context we will discuss the factors influencing the hydrodynamics and the importance of their impact. Following this review we evaluate the most promising flow regime(s) that may be applied to the fast and highly exothermic gas-liquid reactions and carry out a detailed analysis of the hydrodynamic parameters and their link to gas-liquid mass transfer. Based on this analysis we will identify the gaps in knowledge which will then be used to define the experimental framework, which is presented in part B along with the corresponding results.

PART A

FUNDAMENTALS & THEORY

2 Adiabatic gas-liquid flow in small tubes and microchannels: an overview

2.1 Fundamental Considerations

In terms of a first approximation to the topic of gas-liquid two phase flow it may be useful to derive relevant parameters fundamentally prescribing the flow behaviour. This can be done by a dimensional analysis considering in general a fluid of density ρ and viscosity μ with a surface tension γ, flowing at a velocity U through a channel with a hydraulic diameter d_h in the presence of a gravitational field g. The system thus contains six influencing variables (ρ, μ, γ, d_h, U, g), which are based on three fundamental units: mass, length and time. Using Buckingham's π-theorem (Buckingham, 1914; Zlokarnik, 1983) results in the following characteristic dimensionless groups:

- the Weber number: $$We = \frac{\rho \cdot U^2 \cdot d_h}{\gamma} \qquad (2.1\text{-}1),$$
- the Bond number: $$Bo = \frac{\rho \cdot g \cdot d_h^2}{\gamma} \qquad (2.1\text{-}2),$$
- the ratio of the Capillary- and the Reynolds number: $$\frac{Ca}{Re} = \frac{\mu^2}{\rho \cdot \gamma \cdot d_h} \qquad (2.1\text{-}3).$$

Details of the derivation of these parameters can be seen in appendix A1. The Weber number and the Bond number represent the magnitude of inertia and gravitational acceleration relative to surface tension force, respectively. The third group is independent of the velocity and is a measure of the influence of fluid properties on the flow. As shown above, it corresponds to the ratio of two dimensionless numbers, given as:

- the Capillary number: $$Ca = \frac{\mu \cdot U}{\gamma} \qquad (2.1\text{-}4),$$
- the Reynolds number: $$\mathrm{Re} = \frac{\rho \cdot U \cdot d_h}{\mu} \qquad (2.1\text{-}5).$$

The Capillary number constitutes the ratio of viscous force to surface tension force, whilst the Reynolds number characterizes the relative importance of inertial to viscous forces and indicates whether the flow is laminar or turbulent. As the interior dimensions of microchannels are typically in a range between several micrometers and 1000 μm (Ehrfeld et al, 2000), the flow behaviour in such channels can be generally expected as laminar with Reynolds-numbers usually smaller than 2000. In addition to this classification usually employed if only one fluid is considered, the interaction of surface tension, gravitational, inertial and viscous forces in two-phase flow leads to the formation of a variety of flow patterns, which describe the way how both phases are distributed along the channel. The manner in which the competition between the abovementioned forces influences the phase distributions will be discussed in the following section.

2.2 Phase distributions and flow pattern transitions

From the dimensionless numbers, it can be seen that as the channel diameter decreases, the influence surface tension becomes more important. As a first example, one may consider the competition between gravitational acceleration and the surface tension force, which is expressed by the Bond number. Taking into account the fluid properties of both phases it may be written as:

$$Bo = \frac{(\rho_L - \rho_G) \cdot g \cdot d_h^2}{\gamma} \qquad (2.2\text{-}1).$$

Here the subscripts L and G denote the liquid and gas phases, respectively. Expression (2.2-1) suggests that there is a certain threshold diameter at which gravity and interfacial force are comparable

(*Bo* =1). However, the diameter appears here only because it was chosen as a characteristic length within the derivation of dimensionless parameters. That means that, the length value which would be obtained for *Bo* = 1, may also be a channel radius, or the channel width etc. Another characteristic length, which is widely used in this context, is the Capillary length or the Laplace-length constant, given as:

$$\lambda_C = \sqrt{\frac{\gamma}{(\rho_L - \rho_G)\cdot g}} \qquad (2.2\text{-}2).$$

For example, in the case of an air-ethanol fluid combination at 20 °C one obtains λ_C ~ 1.7 mm, and for air-water λ_C ~ 2.7 mm. At length scales smaller than the Capillary length, surface tension dominates over gravitational acceleration. In principle, λ_C gives a measure of the maximum size of raindrops or pendant drops but in the literature it is often used in terms of a threshold diameter for gravity independent flow. The channel is than referred to as a capillary or microchannel. In order to verify if this criterion holds, some exemplifying studies of gas-liquid flow in small tubes with diameters ranging from one to several millimetres will be firstly presented and the corresponding flow patterns will be compared with those occurring in large diameter pipes. In this context the competition between inertial and surface tension forces, which is represented by the Weber-number, will also be treated. Furthermore, the fundamentals acquired through section 2.2.1 will serve as a guide for the discussion of gas-liquid flow features in microchannels presented in section 2.2.2.

2.2.1 Adiabatic gas-liquid flow patterns in small tubes

The previously reported investigations that are presented in this section are summarized in table 2.1, which indicates the corresponding operating conditions (working-fluids and superficial velocities), as well as information on the tube geometry (cross-sectional shape and hydraulic diameters). The superficial velocities (U_{GS}, U_{LS}) are obtained by dividing the respective flow rates by the cross-sectional area of the channel. In order to evaluate the influence of gravitational acceleration and surface tension, tube inclinations and contact angles θ are also included.

A first set of gas-liquid flow patterns in small tubes has been presented by Yang and Shieh (2001) and Barajas and Panton (1993). In these studies, air and water were employed as fluids (λ_C ~ 2.7 mm, θ = 34°) and the channels diameters were 2 mm (*Bo* ~ 0.54) and 1.6 mm (*Bo* ~ 0.35), respectively. Figure 2.1 shows the six flow patterns reported by both investigations, which are described as:

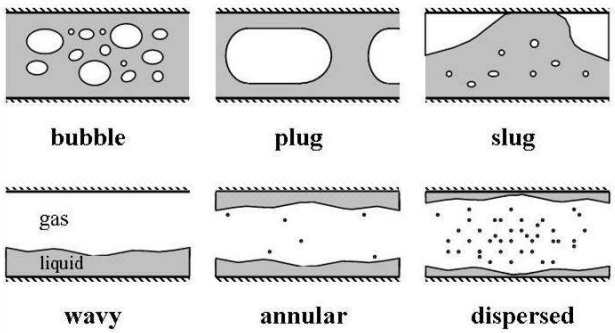

Figure 2.1: Illustration of gas-liquid flow patterns reported for horizontal flow in circular channels of 2 mm and 1.6 mm in diameter, by Barajas and Panton (1993) and Yang and Shieh (2001), respectively.

- **Bubble flow** consists of discrete and irregular distributed bubbles that are smaller than the channel diameter.
- **Plug flow** is characterized by cylindrical bubbles with lengths larger than the channel diameter. The bubbles are surrounded by a liquid film and are separated from each other by sections of liquid phase.
- **Slug flow** may be seen as a stratified flow where liquid slugs are formed by waves touching the upper channel wall.

- **Wavy flow** is a stratified flow pattern with a wavy interface.
- **Annular flow** exhibits a core flow of the gas phase in the centre of the channel and the liquid flows as a film along the channel wall.
- **Dispersed flow** shows a similar morphology than the annular flow pattern, except that most of the liquid is entrained as droplets into the gas phase.

Even though the diameters of the channels employed by Yang and Shieh (2001) and Barajas and Panton (1993) were smaller than the capillary length, the flow patterns found are similar to those found in large diameter tubes (Coulsen et al., 1990). The characteristics of the slug flow regime, as well as the existence of wavy flow show that gravity still strongly influences the flow behaviour in these small channels where Bo < 1. In addition Barajas and Panton (1993) examined the effect of the contact angle on the flow patterns and found that for $\theta > 34°$, wavy flow was completely replaced by **rivulet** or **multi-rivulet flow**. In this flow pattern, the liquid phase on the channel wall does not flow as a closed liquid film but in solitary streams, which are twisting like rivers. The existence of this flow pattern was ascribed to the increasing contact angle and therefore decreasing wettability, which prevents the liquid from spreading on the tube wall. Their results were summarized in a flow pattern map, which is a plot of log (U_{LS}) versus log (U_{GS}) indicating the velocity dependence of the occurrence of a certain flow pattern (see figure 2.2).

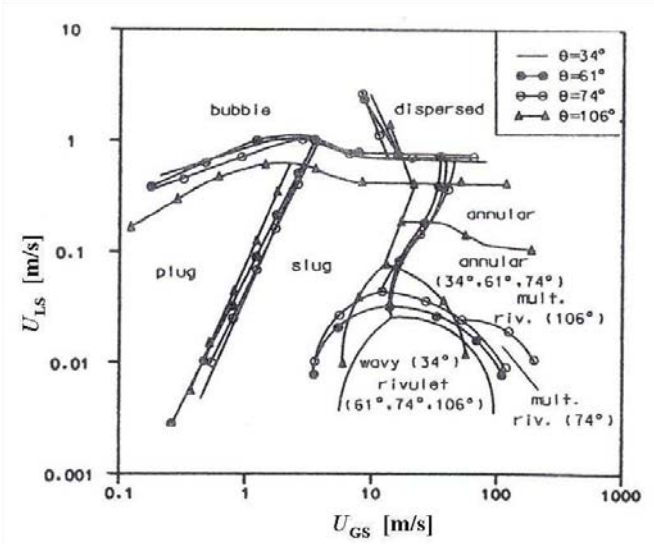

Figure 2.2: Flow-pattern map obtained by Barajas and Panton (1993) for horizontal air-water flow in circular tubes with diameters of 1.6 mm and contact angles ranging form 34° to 106° (U_{LS} = superficial liquid phase velocity; U_{GS} = superficial gas phase velocity)

Figure 2.2 shows that the flow pattern transition lines are almost the same for contact angles smaller than 90°, except in region where wavy or rivulet flow appeared. The biggest shift in flow transitions is observed for the partially non-wetting tube material (θ = 106°), where additionally a great part of the annular flow area was occupied by multi-rivulet flow.

Another set of gas-liquid flow patterns in small diameter tubes has been reported by Triplett et al. (1999a). In this investigation, air and water were contacted in tubes with circular and smoothed corner triangular cross-sectional areas, with diameters ranging from 1.088 mm to 1.493 mm (Bo ~ 0.16-0.3; see table 2.1). The different flow regimes identified were similar within all test sections and were termed as bubbly, slug, churn, slug-annular and annular flow. A representative flow pattern map with corresponding example images of the flow patterns is shown in figure 2.3 for a circular channel with a diameter of 1.097 mm.

source	design parameters		operating parameters				
	cross-sectional shape & channel inclination	**hydraulic diameter** d_h **[mm]**	**working-fluids**	**material**	**contact angle**	**superficial phase velocities** U_{LS} **[m/s]**	U_{GS} **[m/s]**
Barajas and Panton (1993)	circular (horizontal)	1.6	air/water	pyrex-glass polyethylene polyurethane FEP-fluoropolymer	34° 61° 74° 106°	0.003-2	0.1-100
Yang and Shieh (2001)	circular (horizontal)	2	air/water	pyrex-glass	34°	0.006- 2.1	0.15- 86
Triplett et al. (1999a)	circular semi-triangular (horizontal)	1.097, 1.45 1.088 1.493	air/water	pyrex-glass acryl polycarbonate	34° 72° 78°	0.02-8	0.02- 80
Chen et al. (2002)	circular (horizontal)	1, 1.5	nitrogen/water	glass	0-30°	0.399 – 3.53	0.502 - 11
Simmons et al. (2003)	circular (vertical downward)	2	air/water	glass	0-30°	0.0001- 1	0.001 - 10
Liu and Wang (2008)	circular (vertical upward)	1.47, 2.37, 3.04	air/water	quartz-glass	0-20°	≈ 0.002- ≈ 3*	≈ 0.001- ≈ 11*

Table 2.1: Compilation of investigations and corresponding parameters of adiabatic gas-liquid flow in small tubes (all investigations performed under ambient conditions, T = 298.15 K, p = 1.013 bar; * value estimated from flow pattern map, not explicitly stated by the corresponding study).

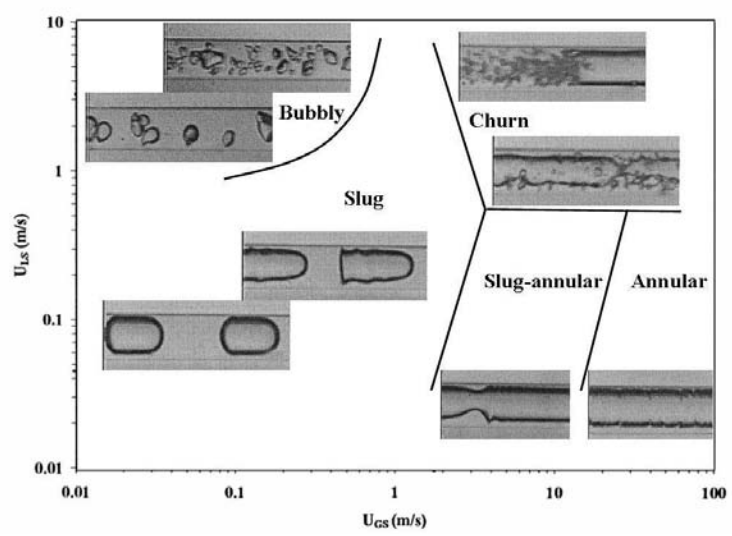

Figure 2.3: Flow-pattern map and corresponding example images obtained by Triplett et al. (1999a) for horizontal air-water flow in a circular channel with a diameter of 1.097 mm (U_{LS} superficial liquid phase velocity; U_{GS} superficial gas phase velocity).

The flow regimes pictured in figure 2.3 are described as follows:

- **Bubbly flow** appears at high liquid and low gas velocities. It generally corresponds to bubble flow reported for large diameter tubes.
- **Slug flow** occurs within a large range of low and intermediate superficial gas and liquid phase velocities. Its morphology is very similar to the plug flow regime as previously reported by Barajas and Panton (1993) and Yang and Shieh (2001). The name slug flow was chosen here because the sections of liquid phase separating the bubbles were called slugs.
- **Slug-annular flow** and **annular flow** are almost equal in their characteristics, with the gas phase in the centre of the channel and the liquid at the side walls. They were distinguished here because, over a wide range of superficial gas velocities, the liquid film shows single waves, which however do not grow sufficiently to fill the entire channel cross-section.
- **Churn flow** is formed at high superficial gas and liquid phase velocities. It may develop by two different ways. Considering slug flow at high liquid velocities, an increase in gas velocity causes the bubbles to become unstable at their rear ends, leading to their disruption into tiny bubbles, which are then dispersed into the liquid slug. The other possibility for the occurrence of churn flow is given by an increase of the liquid velocity from slug-annular or annular flow. The flow pattern is then characterized by a highly irregular interface with the detachment of droplets into the gas-stream and entrainment of bubbles into the liquid phase.

The absence of stratified flow patterns in the work of Triplett et al. (1999) clearly indicates the predominance of the surface tension force over gravitational acceleration. Therefore, the flow patterns described above may be considered characteristic for gas-liquid flow through capillaries. In order to evaluate the effect of channel diameter, cross-section and contact angle, the flow transitions of the circular test sections (d = 1.097 mm and 1.45mm; θ = 34°), the semi-triangular test section (d_h = 1.088 mm; θ = 72°) are plotted in figure 2.4. It can be seen that a change in the channel diameter affects the slug to churn transition only in a significant manner. With respect to a change of cross-sectional area and contact angle, there is little influence of these parameters on the flow transition lines. It is just worth noting that the transitions from slug-annular and annular to churn flow were shifted to lower liquid velocities.

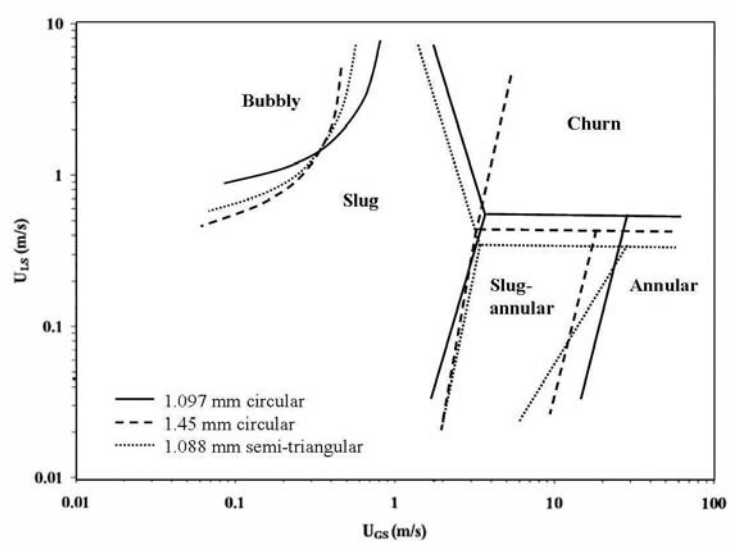

Figure 2.4: A comparison of gas-liquid flow transition lines obtained by Triplett et al. (1999a) for horizontal air-water two-phase flow in circular (d = 1.097 mm, 1.45 mm, contact angle = 34°) and semi-triangular (d_h = 1.088 mm, contact angle = 72°) channels (U_{LS} 1 superficial liquid phase velocity; U_{GS} 1 superficial gas phase velocity).

A third group of gas-liquid flow patterns was denominated by Chen et al. (2002), who studied gas-liquid flow in horizontal circular glass-capillaries with diameters of 1 mm and 1.5 mm using nitrogen and water as fluids (see table 2.1). Five flow patterns were observed and termed as bubbly, slug, bubble-train slug, churn and annular flow. The latter strongly resembled slug-annular flow as defined by Triplett et al. (1999a), whilst the bubble-train slug flow (see figure 2.5) was identified as a new flow pattern and is described as:

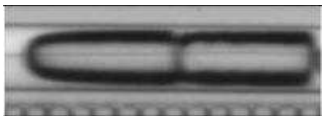

Figure 2.5: Example image of bubble-train slug flow found by Chen et al. (2002) for horizontal gas-liquid two-phase flow through a circular channel of 1 mm in diameter.

- **Bubble-train slug flow** is a transitional flow pattern that appears between slug flow and churn flow. It is characterized by elongated bubbles, which are in contact but are separated from each other by a clear interface. The number of bubbles that are connected in this way varies in a random manner. These so-called bubble-trains are separated from each other by liquid slugs.

Under the operating conditions of bubble-train slug flow as given by Chen et al. (2002), the bubble Weber number We_{GB}, based on the density of the gas-phase and the bubble velocity U_B (see expression 2.2-3), is of the order of unity ($We_{GB} \sim 1$). This means that inertial force is not strong yet enough to overcome surface tension force and to break the interface between the two bubbles that are in contact.

$$We_{GB} = \frac{\rho_G \cdot U_B^2 \cdot d_h}{\gamma} \qquad (2.2\text{-}3).$$

Aware of the differences between the various gas-liquid flow regimes and flow regime maps reported in the literature, Akbar et al. (2003) have tried to unify the data on a universal flow map. They gathered the experimental results of various investigators, which were mainly concerned with air-water flow in horizontal circular and near circular channels with hydraulic diameters of approximately 1 mm. Based on these data, a universal flow pattern map was developed by plotting the superficial gas phase Weber number (We_{GS}) versus the superficial liquid-phase Weber number (We_{LS}). The dimensionless numbers are given as:

- superficial liquid phase Weber-number We_{LS}: $$We_{LS} = \frac{\rho_L \cdot U_{LS}^2 \cdot d_h}{\gamma} \qquad (2.2\text{-}4)$$
- superficial gas phase Weber-number We_{GS}: $$We_{GS} = \frac{\rho_G \cdot U_{GS}^2 \cdot d_h}{\gamma} \qquad (2.2\text{-}5).$$

Within this Weber number based flow map, four regions were identified: a surface tension dominated zone; an inertia dominated zone 1; an inertia dominated zone 2; and a transition zone between the inertia dominated zone 1 and the surface tension dominated area. Using the flow regime terms provided by Triplett et al. (1999a), the surface tension dominated zone consists of bubbly flow and slug flow. The inertia dominated zone 1 includes annular flow and the transitional zone covers slug-annular flow. The churn flow regime can be ascribed to the inertia dominated zone 2. Figure 2.6 shows the flow regime transition criteria derived by Akbar et al. (2003), which are superimposed on a conventional flow pattern map of Triplett et al. (1999a).

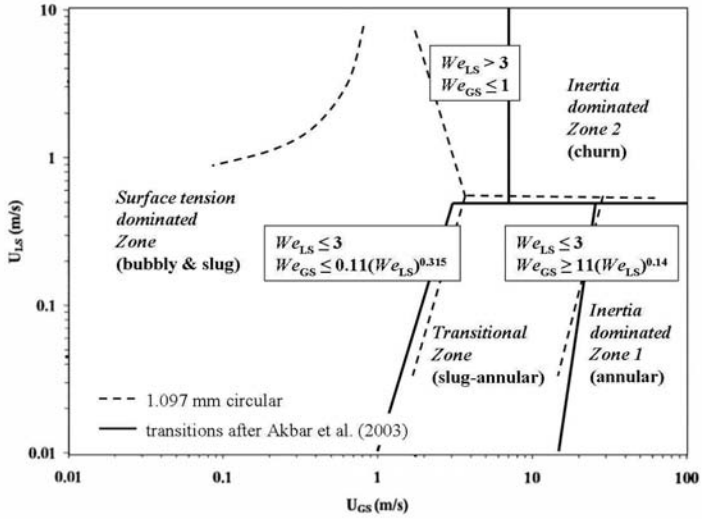

Figure 2.6: Flow pattern map with flow transitions and corresponding criteria proposed by Akbar et al. (2003, solid line) and comparison with flow transitions obtained by Triplett et al. (1999a) for horizontal air-water flow in circular tube (d = 1.097 mm, broken line), (U_{LS} superficial liquid phase velocity; U_{GS} superficial gas phase velocity).

The advantage of the universal map approach given by Akbar et al. (2003) is that it takes into account fluid properties and the tube diameter, which are not considered in a typical flow pattern map using superficial velocities. By use of the Weber numbers, the influence of the competition between the surface tension force and the inertial force on the formation of a certain flow pattern is clearly illustrated. The flow pattern map is divided into two areas: one from low to intermediate superficial gas-velocities, where surface tension dominates and the other from intermediate to high superficial gas velocities, where inertia dominates. The main parameter characterizing this transition is thus the superficial gas phase Weber-number We_{GS}. It is also interesting to determine if, and under which conditions, viscous forces influence the formation of flow patterns. The dimensionless parameters which are important then are the Reynolds and the Capillary numbers. Let's firstly consider these numbers based on the superficial velocity of the liquid phase and when the viscous forces dominate, i.e. for $Re_{LS} < 1$ and $Ca_{LS} > 1$. Table 2.2 shows example values for air-water flow in a 1 mm hydraulic diameter channel. In the first case, the superficial liquid velocity is determined from the Reynolds number and used to calculate the corresponding Capillary number. A similar procedure is used starting from a fixed value of the Capillary-number (see table 2.2).

Re_{LS}	U_{LS} [m/s]	Ca_{LS}	**importance of forces involved**
< 1	$< 1 \cdot 10^{-3}$	$< 1.4 \cdot 10^{-5}$	inertial force < viscous force < surface tension force
> 72000	> 72	> 1	surface tension force < viscous force < inertial force

Table 2.2: Results of an example calculation showing the importance of the viscous force in air-water flow in a 1 mm hydraulic diameter channel. (Re_{LS} superficial liquid phase Reynolds number; U_{LS} superficial liquid phase velocity; Ca_{LS} superficial liquid phase Capillary number; superficial velocities are determined directly from $Re_{LS} < 1$ and $Ca_{LS} > 1$ and used to calculate the respective remaining dimensionless number. The fluid properties are: $\mu_L = 1 \cdot 10^{-3}$ Pa·s, $\rho_L = 1000$ kg/m^3 and $\gamma = 0.072$ N/m).

From the example calculations given in table 2.2, it can be seen that viscous forces are always dominated either by surface tension or inertial forces. This suggests that the liquid viscosity has little

influence on the formation of flow patterns and their transitions. A similar trend is expected via the analysis of the dimensionless numbers based on gas-phase.
In addition to the channel diameter, the orientation of the tube and the direction of flow can modify the gas-liquid flow patterns in small tubes. Figure 2.7 shows the air-water (λ_C ~ 2.7 mm) flow pattern maps obtained for upward and downward flow in vertically oriented circular capillaries with diameters of 2.37 mm and 2 mm, respectively (Liu and Wang, 2008; Simmons et al., 2003).

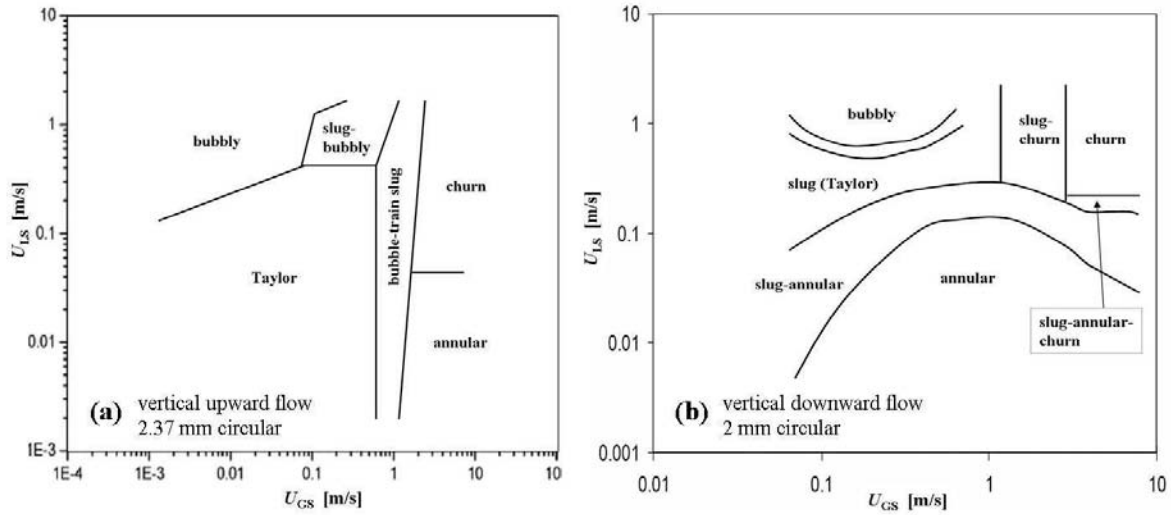

Figure 2.7: Flow-pattern maps with flow transitions for vertical air-water flow through vertically oriented small tubes (a: data obtained by Lui and Wang (2008); b: data obtained by Simmons et al. (2003); U_{LS} superficial liquid phase velocity; U_{GS} superficial gas phase velocity).

In figure 2.7, the main flow regimes observed in both test sections correspond for the most part to those found by Triplett et al. (1999a), excepting that Liu and Wang (2008) did not distinguish between annular and slug-annular flow. It should also be pointed out that the term Taylor is used as an alternative expression for slug flow. In addition, several transitional flow patterns have been identified. **Slug-bubbly flow** contains elongated bubbles with a length larger than the channel diameter, as well as bubbles with diameters smaller than that of the tube. **Slug-churn flow** resembles the bubble train flow as identified by Chen et al. (2002) (see figure 2.5) but the interface at the rear end of the bubble trains is disrupted into tiny bubbles (similar to the churn flow shown in figure 2.3). **Slug-annular-churn flow** may be regarded as an annular flow with sections where the gas-liquid interface is irregular in shape and bubbles are entrained into the liquid phase. Furthermore, figure 2.7(a) shows that bubble-train slug flow divides the flow pattern map, separating Taylor/slug flow from churn and annular flow, and occurs for low to high superficial liquid velocities. The existence of these transitional flow patterns suggests that the flow transitions should be represented by areas rather than sharp lines. Additional flow pattern maps determined by Liu and Wang (2008) for upward flow in tubes with diameters between 3.04 and 1.47 mm are similar to that of Triplett et al. (1999a). The flow map is divided into a surface tension dominated zone, which includes bubbly and slug flow and an inertia dominated zone, which is characterized by annular and churn flow. This similarity suggests that for vertical flow through channels with diameters in the order of the capillary length, the flow behaviour is generally less influenced by gravitational acceleration. However, for flow patterns of downward flow shown in figure 2.7(b) the annular and slug-annular flow occupy an area at low superficial velocities, which according to the flow map given by Triplett et la. (1999) would usually be covered by slug flow. This occupation of the surface tension dominated zone by annular and slug annular flow may be explained by the dominance of gravitational acceleration, which facilitates the liquid to flow as a falling film rather than in form of slug and thus, enabling the gas phase to flow in the centre of the channel. Unfortunately, no data are available for vertical downward flow in tubes

with $d < 2$ mm, which would enable to identify at which conditions (d, Bo) this behaviour would vanish.

The insight gained into gas-liquid flow in small tubes, as presented above, clearly indicates that for tubes with diameters of the order of the Laplace-length constant the flow patterns still depend on gravitational acceleration. The existence of stratified flow patterns, as well as the differences in flow patterns for downward and upward flow at low superficial phase velocities demonstrate that gravitational effects still play a significant role in the formation of two-phase flow characteristics. Consequently, the Laplace-length constant λ_C is not an adequate criterion to predict the threshold diameter where the surface tension force dominates gravity. From examination of the data in the literature, this boundary seems to be between a diameter of 1.5 mm (Triplett et al., 1999a; Chen et al., 2002) and 1.6 mm (Barajas and Panton, 1993) for horizontal flow of air-water systems and is better approximated by $\lambda_c/2$, which corresponds to $Bo \approx 0.3$. If gravitational effects can well be excluded, the competition between surface tension force and inertia force divides the flow pattern map into two regions. In this case, one region includes bubbly flow and slug low, while the other comprises annular and churn flow patterns. Furthermore, the behaviour of flow transitions was either not observed, due to strong changes in flow rates, or ascribed to one of the main flow regimes. However, nearly all investigations presented in the literature have been carried out using air and water. The influence of surface tension on the existence of flow transitions, demonstrated by employing materials of different contact angels, was shown to be less pronounced for channels with diameters down to approximately 1 mm. The impact of viscosity seems to be of minor influence for the flow behaviour. However, experimental data which confirm this hypothesis do not yet exist.

2.2.2 Adiabatic gas-liquid flow patterns in microchannels

The following section is concerned with gas-liquid flows in channels with hydraulic diameters smaller than 1000 µm. The studies that are referred to in this literature survey are summarized in table 2.3. Similar to table 2.1, the information in table 2.3 is divided into design parameters and operating parameters. Additional information on the design of the gas-liquid contacting sections is presented together with the hydrodynamic results of each respective study. This is important information that must be taken into account and included in the decision-making process regarding the microreactor design. Presentation of the literature investigations will be sorted with respect to the shape of the channel cross-sectional area, since the influence of this parameter can not be neglected in the studies undertaken in small tubes. In all of the following assessments and discussions, the terminology used to describe two-phase flow patterns will be refer to that used by Triplett et al. (1999a).

source	design parameters		operating parameters				
	channel geometry	**hydraulic diameter** d_h **[µm]**	**working-fluids**	**material**	**contact angle**	**superficial phase velocities** U_{LS} **[m/s]**	U_{GS} **[m/s]**
Serizawa et al. (2002)	circular	25, 100	nitrogen/water	quartz	0-20°	0.0032-17.5	0.0022-295.3
Kawahara et al. (2002)	circular	100	nitrogen/water	quartz	0-20°	0.02-4	0.1-60
Chung & Kawaji (2004)	circular	50, 100, 250, 530	nitrogen/water	quartz	0-20°	0.01-5.77	0.02- 72.98
Cubaud and Ho (2004)	square	200, 525	air/water	silicon (pyrex)	9° (≈ 34°)	$O(10^{-3})$ - ≤ 0.2*	$O(10^{-3})$ - < 20*
de Mas et al. (2003)	triangular	224 (w = 435 µm h = 305 µm)	nitrogen /acetonitrile	silicon (pyrex)	15° (≈ 15°)	$O(10^{-4})$ - ≤ 2*	$O(10^{-2})$ - < 20*
Yue et al. (2007)	rectangular	677 (w = 1000 µm h = 500 µm)	CO_2/water	PMMA	≈ 72°	0.09-1	0.7-13
Haverkamp (2002)	rectangular	150 (w = 300 µm h = 100 µm)	nitrogen/water	stainless steel (pyrex)	70-90° (≈ 34°)	0.009-0.074	0.056-22
			nitrogen/isopropanol		n. a. (n. a.)	0.009-0.074	0.039-22
Waelchli and von Rohr (2006)	rectangular	187.5 (w = 250 µm h = 150 µm)	nitrogen/water	silicon (glass)	9° (n. a.)	≈ 0.0014 - ≈ 1.4*	≈ 0.028 - ≈ 6*
		218 (w = 400 µm h = 150 µm)	nitrogen/ethanol nitrogen/glycerol		n. a. (n. a.) n. a. (n. a.)		

Table 2.3: Compilation of investigations and corresponding parameters of adiabatic gas-liquid two-phase flow in microchannels (w = channel width, h = cannel height; * values taken from flow pattern map, not stated by the corresponding study; for contact angles indicated as n. a., $\theta < 90°$ can be assumed; in studies with channel materials like silicon or stainless steel, visual access was provided by covering one side of the test section with a glass wafer; all investigations carried out at ambient conditions, T = 293 K, p = 1.013 bar).

2.2.2.1 Microchannels with a circular cross sectional area

Serizawa et al. (2002) fed air and water into circular channels with diameters of 25 µm and 100 µm. Before entering the test section both phases were contacted in a mixing zone, as shown in figure 2.8, where air was introduced coaxially into a peripheral stream of water. The mixing chamber was then gradually reduced to the diameter of the test section.

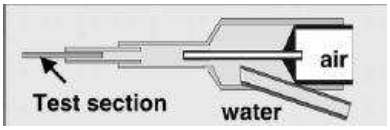

Figure 2.8: Example image of the gas-liquid contacting section with its inlet to the test-section used by Serizawa et al. (2002) for the investigation of nitrogen-water flow in circular microchannels.

In a very large range of liquid and gas superficial velocities (see table 2.3), four flow patterns were observed for both test sections and referred to as bubbly, slug, liquid-ring and liquid-lump flow. Example images of these flow characteristics are illustrated in figure 2.9a.

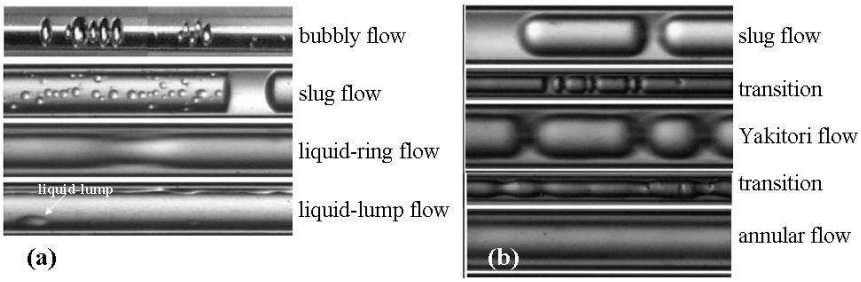

Figure 2.9: Example images of nitrogen-water flow patterns as observed by Serizawa et al. (2002) inside of a circular microchannel with an inner diameter of 100 µm (a: after cleaning of the test-section with ethanol; b: additional flow patterns after cleaning of the test-section with hydrochlorid acid and ethanol).

Figure 2.9a shows droplets sticking at the channel wall in slug flow, which indicates that the liquid film around the bubble is almost dried out. The flow characteristics termed as **liquid-ring** may be considered as an annular flow with a relatively thick liquid layer at the tube wall. **Liquid-lump flow** may be classified in the same manner, except that here pockets of liquid are sliding on the liquid film at the channel wall. However, the authors did point out that the liquid-lump flow behaviour was generally unstable and changing over time. This characteristic may be taken out of the flow pattern map, where different flow regimes appeared at the same set of gas-and liquid velocities. The authors attributed this behaviour to the geometry of the contacting section, whose volume was much larger than that of the test section.

The above mentioned flow patterns were observed after pre-treatment of the test sections with ethanol. By repeating the experiments after cleaning the channel (d = 100 µm) with hydrochloric acid and ethanol, several additional flow characteristics were detected. In addition to bubbly, slug and liquid-ring flow, two transitional patterns appeared, as well as some new flow regimes denoted as **stable annular**, **frothy annular**, **rivulet** and **Yakitori flow** (see example images in figure 2.9b). The **rivulet flow** pattern is similar in morphology to that previously reported for larger channels (Barajas and Panton, 1993). The name **frothy annular flow** is used if tiny bubbles are captured within the liquid film at the channel wall. **Yakitori flow** may be regarded as slug flow, whereby the bubbles are connected by gas stems in the centre of the channel. In addition to this, the bubbles in slug flow are always lubricated by a continuous liquid film.

Even though almost all of the flow conditions presented by Serizawa et al. (2002) were hydrodynamically unstable, this study delivers a first insight into the effect of the contact angle in microchannel two-phase flows.

Kawahara et al. (2002) also performed experiments with a 100 μm circular tube using water and nitrogen as fluids (see table 2.3). The geometry used for gas and liquid contacting is shown in figure 2.10. Two gas-substreams are injected peripherally into a coaxial mainstream of water followed by a stepwise reduction of the mixing chamber down to the diameter of the test section.

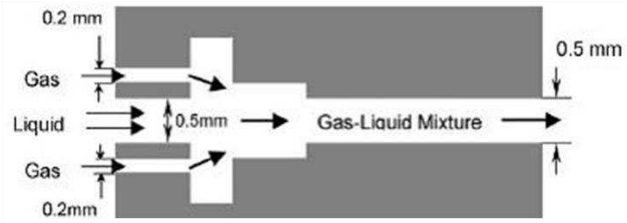

Figure 2.10: Illustration of the gas-liquid contacting section used by Kawahara et al. (2002) [15] during the investigation of nitrogen-water flow in a circular microchannel.

In contrast to Serizawa et al. (2002), only **slug flow** was observed by Kawahara et al. (2002). Depending on the flow rate, the bubbles attained lengths larger than that of the test section with various shapes of the gas-liquid interface, as shown in figure 2.11. It was noted that the flow behaviour was generally unstable, but in the present context this meant that, the two-phase flow was interrupted by long sections of single phase liquid flow.

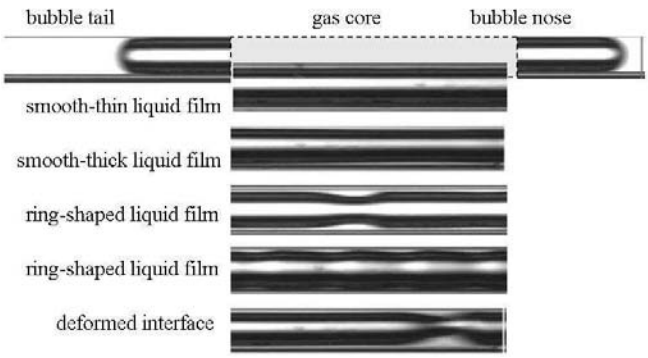

Figure 2.11: Example images of nitrogen-water flow with possible shapes of the gas-liquid interface between the nose and the tail of a bubble as reported by Kawahara et al. (2002) for a circular microchannel with a diameter of 100 μm.

For a same flow, condition more than one of the shapes of the gas-liquid interface as shown in figure 2.11 was observed. In order to illustrate the flow behaviour by a conventional flow pattern map, a probability analysis of the appearance of each type of interface was carried out. This resulted in the definition of four sub-classes of slug-flow, denoted as slug-ring, ring-slug, semi-annular and multiple flows. For instance, in the case of slug-ring flow the probability for the existence of a smooth-thin liquid film is higher than that of a ring-shaped liquid film. However, once more, the general character of the flow seems to be governed by the volume of the contacting section and the volume added by the intersection, which reduces the diameter down to that of the test section. From figure 2.10 it can be seen that the diameter of the contacting chamber is five times larger than that of the test section. Even though the length of the contacting chamber was not specified, it is likely that a bubble generated in this section may exceed the volume of the test section. Consequently large packages of gas and liquid are fed into the test section leading to the general flow characteristics reported here.

Chung and Kawaji (2004) performed a systematic investigation with channels of 50, 100, 250 and 530 μm in diameter, using a similar contacting section to that shown in figure 2.10. The flow characteristics found in the test sections with $d \leq 100$ μm were in agreement with that reported by Kawahara et al. (2002). The flow patterns observed in the 250 μm and 530 μm in diameter test sections showed the morphological characteristics of those obtained by Triplett et al. (1999a) and were referred to as **bubbly**, **slug**, **churn**, **slug-annular** and **annular flow**. The flow pattern maps plotted on the basis of that classification are shown in figure 2.12a together with the flow transitions predicted by the criteria developed by Akbar et al. (2003). However, the term churn flow used here includes all of the flow characteristics obtained at high liquid and gas velocities. Different to the churn flow reported

for channels with d_h ~1 mm (Triplett et al. 1999a), Chung and Kawaji (2004) found that this velocity range was characterized by the formation of more than one flow pattern for a given flow condition. Figure 2.12b shows example images of this unstable flow behaviour. It can be seen that the gas phase shows mostly a core-stream with the liquid distributed in various shapes at the channel wall, separated by periods of liquid phase flowing alone. This is similar to the observations made within the test sections with $d \leq 100$ µm.

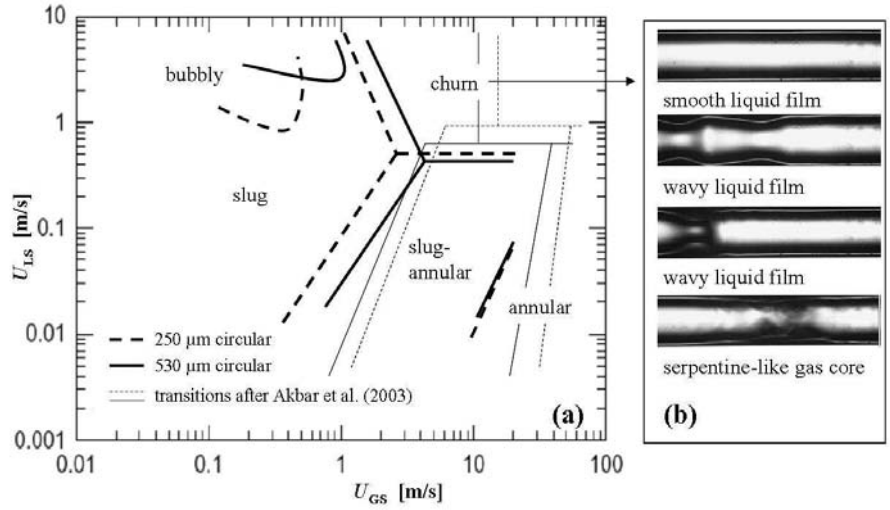

Figure 2.12: Results of nitrogen-water flow reported by Chung and Kawaji (2004) for microcahnnels of circular-cross section (a: flow-pattern map with flow transitions for channels of 250 µm and 530 µm in diameter and corresponding criteria proposed by Akbar et al. (2003); U_{LS} superficial liquid phase velocity; U_{GS} superficial gas phase velocity; b: example images of the flow characteristics summarized under the term churn flow for the same flow conditions within the test section of 250 µm in diameter (an image of single phase liquid flow is not shown).

In figure 2.12a it can initially be seen that with decreasing channel diameters the flow transitions are shifted to lower superficial gas phase velocities. Furthermore, for the 530 µm channel at intermediate superficial liquid velocities the slug to slug-annular flow transition agrees well with that predicted by the criterion of Akbar et al. (2003). However, the other flow transitions are generally over-predicted by the criterion of Akbar et al. (2003), which may be due to the fact that they were developed with data obtained in channels of larger diameter. Following the discussion concerning the competition of surface tension force and inertia, a decrease in the channel diameter should increase the influence of surface tension and with that it should increase the area of the occurrence of surface tension dominated flow patterns to higher gas velocities, as shown by the shift of the transitions predicted by the criteria of Akbar et al. (2003). However, examination of the results of Chung and Kawaji (2004) shows the opposite trend.

2.2.2.2 Microchannels with a square cross sectional area

Cubaud and Ho (2004) studied air-water flow in square channels with hydraulic diameters of 200 µm and 525 µm. Visual access was achieved by a transversal etching of silicon-wafers, and enclosing them between pyrex wafers. The contacting section consists of a straight cross with three inlets and one outlet as shown in figure 2.13a. All channels within the contacting zone have a square cross sectional area with a hydraulic diameter of 100 µm. The gas phase is injected via the centre channel, while water was supplied through the surrounding channels. The flow rates, as well as the pressure drops were identical for both liquid inlet channels. In figure 2.13a the flow behaviour at the gas-liquid contacting region is illustrated for increasing gas flow rates. At low gas velocities it can be seen that

air is periodically squeezed by the liquid phase, forming a stable two phase flow with round or elongated bubbles, which are almost uniformly spaced. At high gas velocities an annular flow pattern with a thick wavy film is created. The existence of these stable flow patterns contradicts the findings previously reported for circular channels of these dimensions (Serizawa et al., 2002; Kawahara et al., 2002; Chung and Kawaji, 2004), as it demonstrates that it is possible to generate a stable gas liquid flow in a microchannel with 100 µm in diameter and it confirms that unstable flow behaviour is linked to the design of the contacting section. From the contacting section the two phase flow is directly introduced into the test section consisting of a meandering channel with sharp corner bends, inside of which bubbly, wedging, slug, annular and dry flow regimes are observed as shown in figure 2.13b).

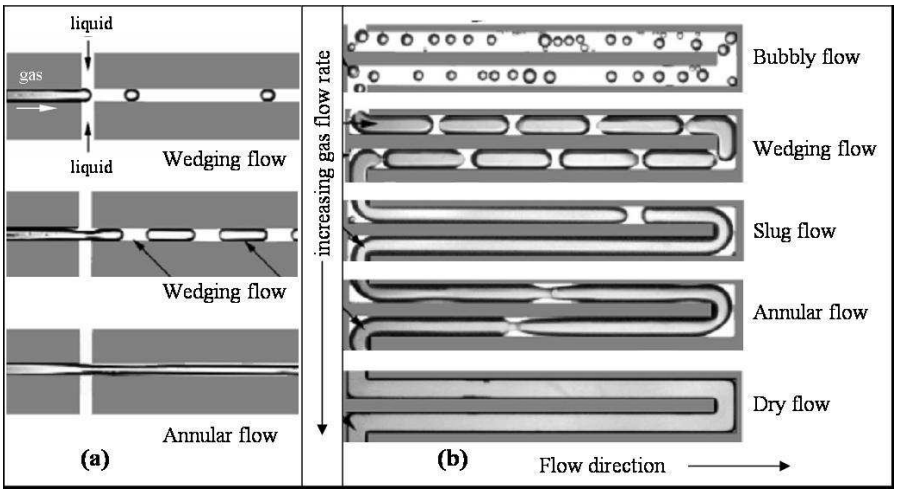

Figure 2.13: Example images of air-water flow recorded by Cubaud and Ho (2004) in microchannels of square cross-section (a: contacting section with channels of 100 µm in hydraulic diameter; b: section of the corresponding main channel with a hydraulic diameter of 525 µm, arranged in a meandering shape with sharp corner bends).

From figure 2.13 it appears that **wedging flow** principally corresponds to slug flow. The reason why it was classified separately is due to the partial drying-out of the liquid film between the bubbles and the channel wall, involving the formation of liquid/gas/solid contact lines. It was observed that the extent to which these contact lines exist depends on the ratio of the bubble velocity and the dewetting velocity. The latter specifies how fast a dry patch grows and depends on the contact angle, as well as the surface tension and the viscosity of the liquid (Redon et al., 1991; de Gennes et al., 2002). For example, if the bubble velocity is smaller than the dewetting velocity, a dry area propagates across the whole length of the bubble. On the other hand, bubbles at velocities greater than the dewetting velocity show dry patches only at their rear ends or are completely surrounded by a liquid film. The term wedging flow originates from the circumstance that the film dried out in the centre of the channel wall. Thus, the cross sectional area occupied by the liquid in the corners of the square channel was assumed to resemble the shape of a wedge. **Dry flow** is generated as the liquid film in annular flow starts to dry out, whereby the liquid merely flows in the corners of the channel cross section.
In figure 2.13a it can be seen that the bubbles generated at low gas flow rates are always larger in length than the channel diameter of the contacting section. Hence, in Cubaud and Ho's experiments, the formation of bubbly flow was achieved as a result of the difference in diameter between the contacting section and the main channel.

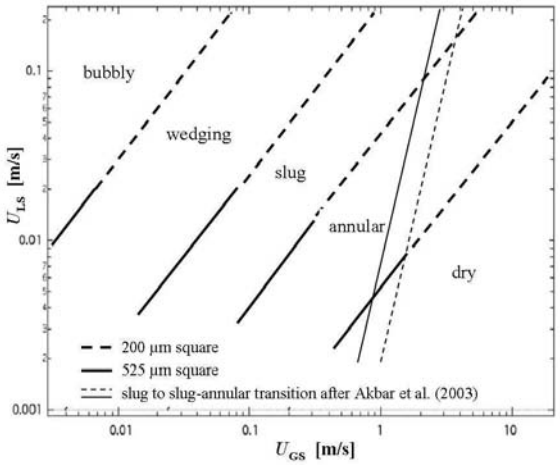

Figure 2.14: Flow-pattern map with flow transitions reported by Cubaud and Ho et al. (2004) for air-water two-phase flow in square microchannles with hydraulic diameters of 200 µm and 530 µm (the thin lines indicate the corresponding transitions from slug to slug-annular proposed by Akbar et al. (2003); U_{LS} superficial liquid phase velocity; U_{GS} superficial gas phase velocity).

Figure 2.14 summarizes the flow pattern transition lines found for both main channels. Compared with the preceding studies in circular channels, the operating window of this investigation was restricted to relatively low superficial velocities. As a result the flow transition criteria proposed by Akbar et al. (2003) can only be applied to the boundary between the surface tension dominated zone (slug and bubbly flows) and the transitional zone (slug-annular). Similar to what was shown in the case of circular channels, Akbar et al. (2003) transition lines generally over-predict the experimental results. A comparison with respect to the effect of the channel diameter is complicated since the flow inside of both test sections was studied within the same range of flow rates, but not at comparable superficial liquid phase velocities. Furthermore the significance of a comparison of the flow pattern transitions obtained for the 525 µm square channel with those in a 530 µm circular channel (Chung and Kawaji, 2004; see figure 2.12a) is questionable since the ranges of superficial liquid phase velocities are not comparable (highest liquid velocity studied by Cubaud and Ho (2004) is $U_{LS} \leq 0.02$ m/s, which corresponds approximately to the lowest liquid velocities examined by Chung and Kawaji, 2004).

2.2.2.3 Microchannels with a triangular cross sectional area

In the framework of the direct fluorination of aromatics in microreactors, de Mas et al. (2003) examined nitrogen-acetonitrile two-phase flow in a triangular channel with a width of 435 µm and a height of 305 µm (d_h = 224 µm). The channel was etched in silicon and covered with a pyrex wafer providing visual access to the flow. The gas and liquid phases were directly contacted within the test section, at which the gas-phase was injected by an opening of approximately 60 µm at the bottom of the main channel. Pulsed laser fluorescence microscopy was used to observe the flow behaviour. The different flow patterns identified were denoted as bubbly, slug, annular, wavy annular, churn, wavy annular dry and annular dry flow. The **bubbly flow** features bubbles slightly smaller in width than the channel. **Wavy annular flow** is characterized by a wavy liquid film. The **annular dry flows** are marked by a partial drying of the pyrex wall. **Churn flow** shows a highly irregular gas-liquid interface, but the entrainment of bubbles into the liquid phase was not observed. Figure 2.15a shows the corresponding flow pattern map. It reveals that for the present fluid combination (ρ_L = 780 kg/m^3, γ = 0.029 N/m) and channel diameter, the transition from slug to annular flows is well predicted by the criteria of Akbar et al. (2003). Figure 2.15b compares these data with the studies carried out in circular, as well as square channels of comparable diameter. It can be seen that the formation of annular dry flows or dry flows falls in the velocity range of slug-annular flow. A second run, where the gas phase was saturated with acetonitrile revealed the same result, which excludes solvent evaporation as a possible cause of this characteristic. This suggests that the occurrence of dry flows is

typical for channels of non-circular cross-sections and it may be attributed to the accumulation of the liquid phase in the corners of the channel leading to a thinner liquid layer at the channel walls. Furthermore, with respect to the churn flow region, periods of single phase liquid flow were not reported by de Mas et al. (2003). This also suggests that the unstable character of the flow at high gas and liquid velocities found by Chung and Kawaji (2004) within the 250 and 530 µm test sections may be attributed to the design of the contacting section.

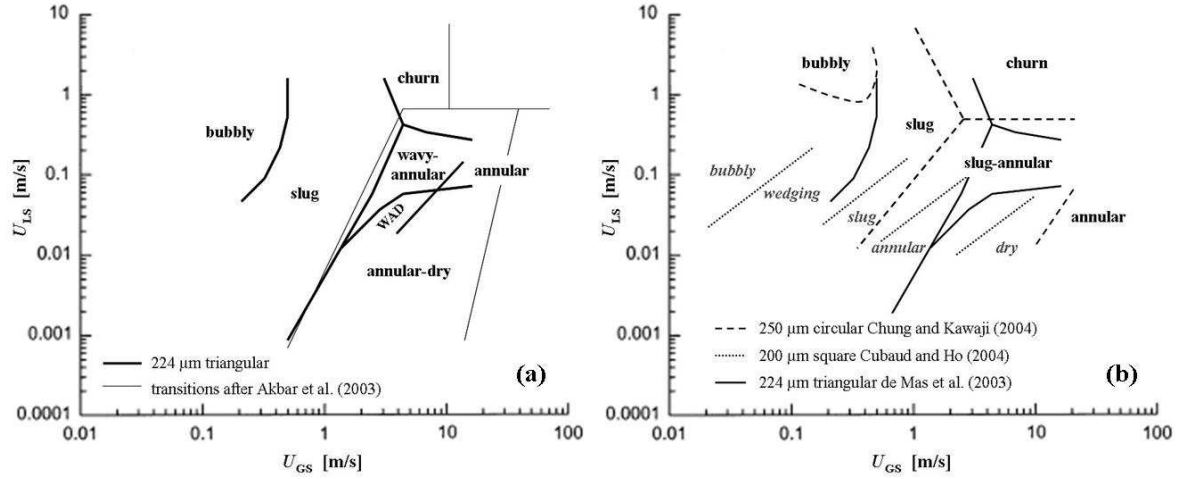

Figure 2.15: Flow pattern maps of nitrogen-acetonitrile flow reported by de Mas et al. (2003) for a triangular microchannel with a hydraulic diameter of 224 µm (a: flow transitions and corresponding criteria proposed by Akbar et al. (2003), WAD wavy annular dry; b: comparison of flow transition with studies carried out in circular and square microchannels of comparable diameters; U_{LS} superficial liquid phase velocity, U_{GS} superficial gas phase velocity).

2.2.2.4 Microchannels with a rectangular cross sectional area

Yue et al. (2007) studied CO_2-water flow in a rectangular channel made of PMMA with a width of 1000 µm and a height of 500 µm (d_h = 667 µm). Both fluids were directly injected into the main channel at Y-shaped junction as schematically illustrated in figure 2.16a. At this the inlet channels were of the same dimensions as the test section. The flow patterns observed inside of the test section were classified as slug, churn and slug-annular. Representative example images together with the corresponding flow pattern map are shown in figure 2.16b. As previously described for triangular microchannels by de Mas et al. (2003), a stable churn flow characterized by an irregular gas-liquid interface was also found by Yue et al. (2007). Additionally, it can be seen that the transitions from slug to slug-annular and from slug-annular to churn flow are well predicted by the criteria of Akbar et al. (2003).

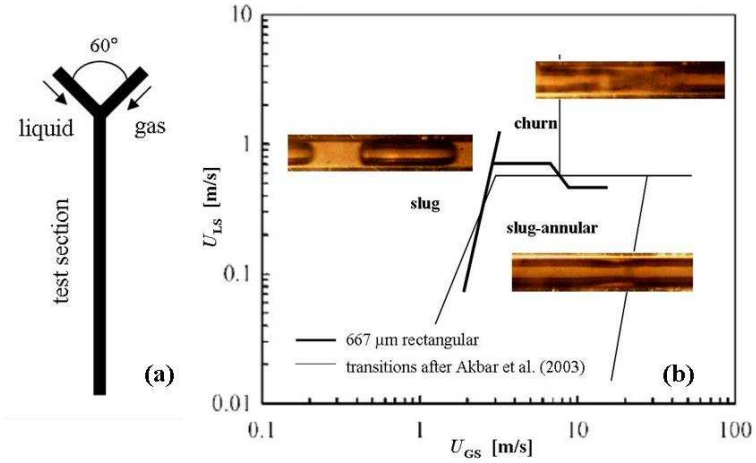

Figure 2.16: Illustration of the microfluidic component and hydrodynamic results presented by Yue et al. (2007) for CO_2-water two-phase flow in a rectangular microchannel of 667 µm in hydraulic diameter (a: principle sketch of the contacting mode, all channels are of equal dimensions with a width of 1000 µm and a height of 500 µm; b: flow pattern map with flow transitions, example images of flow patterns and corresponding criteria proposed by Akbar et al. (2003), U_{LS} superficial liquid phase velocity, U_{GS} superficial gas phase velocity).

Haverkamp (2002) examined the flow characteristics of nitrogen-water and nitrogen-isopropanol systems in a channel of 300 µm in width and 100 µm in height (d_h = 150 µm). The channel was etched in a nickel-iron alloy and covered with a glass wafer. The gas and the liquid phase were directly supplied to the test section by two parallel channels as shown in figure 2.17. The inlet channels were arranged perpendicular to the entrance of the main channel and were opened to its cross section within the whole overlapping region. The width of the gas inlet was in a range between 3 µm and 10 µm, whilst the liquid inlet was approximately 20 µm in width. The height of both feeding channels was fixed to 20 µm.

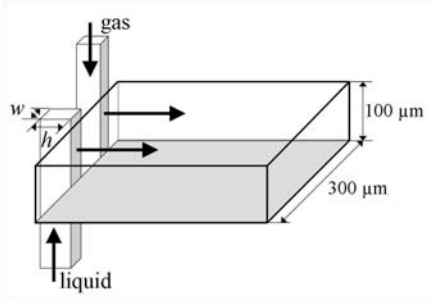

Figure 2.17: Principle sketch of the gas and liquid feeding with its entrance to the main channel as used by Haverkamp (2002) for the investigation of gas-liquid flow in a rectangular microchannel with a width of 300 µm and a height of 100 µm (w width of an inlet channel, h height of an inlet channel; gas inlet: w = 3 µm – 10 µm, h = 20 µm; liquid inlet: $w \approx 20$ µm, h = 20 µm).

The investigation of the two-phase flow behaviour yielded slug, slug-annular and annular flow patterns for both fluid combinations. In the case of nitrogen-isopropanol, bubbly flow was additionally detected. However, this is due to the fact that the same velocity range was not used for the nitrogen-water system. The bubbly flow regime was characterized by uniformly distributed bubbles, which were slightly smaller or slightly larger than the channel width. Churn flow was not observed due to the range of superficial liquid phase velocities being limited to $U_{LS} < 0.1$ m/s. Furthermore, for the annular flow range of the nitrogen-water system, the slug-annular and annular flow patterns seemed to appear randomly with increasing superficial liquid phase velocities at fixed gas velocities. Since their principal morphological characteristics are almost equal, this suggests that it might not be useful to distinguish both flow patterns. From the corresponding flow regime map as shown in figure 2.18, it can initially be seen that for nitrogen-water the slug to annular transition shows a good agreement with the criteria developed by Akbar et al. (2003).

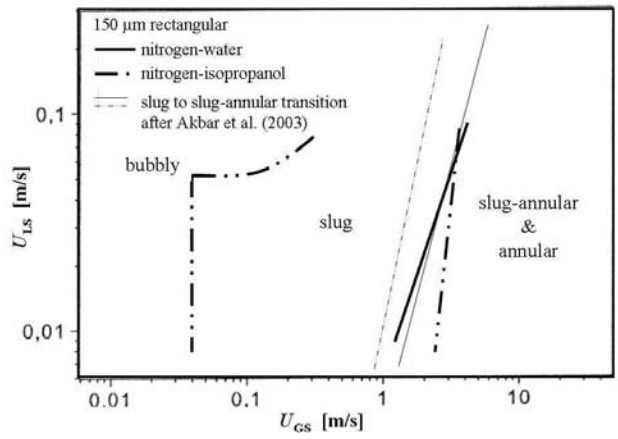

Figure 2.18: Flow-pattern map with flow transitions reported by Haverkamp (2002) for nitrogen-water and nitrogen-isopropanol two-phase flow in a rectangular microchannel with a hydraulic diameter of 150 µm (the thin lines indicate the corresponding transitions from slug to slug-annular proposed by Akbar et al. (2003); U_{LS} superficial liquid phase velocity; U_{GS} superficial gas phase velocity).

A comparison of the nitrogen-water flow patterns with those of the nitrogen-isopropanol system should give an indication on the influence of fluid properties. For the liquids used here the surface tension ratio may be approximated as $\gamma_{water}/\ \gamma_{isoprop} \approx 3$ (at 20 °C). With respect to the competition between surface tension and inertia, a reduction of the surface tension should lead to a decrease of the surface tension dominated zone. That means transition between slug and annular flow patterns should be shifted to smaller superficial gas velocities. This tendency is indicated by the corresponding transition predicted on the base of Akbar et al. (2003). However, looking at the experimental results shows an opposite trend, especially for low superficial liquid velocities. A possible explanation of this behaviour may be linked to the viscosity differences of the liquids. The viscosity ratio of both liquids is $\mu_{isoprop}/\ \mu_{water} \approx 2$, which suggests that, even though the surface tension of isopropanol is three times smaller than that of water, a possible effect of viscosity can not be excluded here. This assumption however, would be in contradiction to the estimations made in table 2.2. Furthermore, since the contact angle is directly linked to the surface tension this study demonstrates that a change in wettability does not lead to the generation of new flow characteristics. This is in contradiction to the findings of Serizawa et al. (2002) in 100 µm circular channels.

Waelchli and von Rohr (2006) carried out a systematic investigation on the influence of liquid-phase properties, as well as channel diameter on gas-liquid flow in rectangular microchannels. The test sections used within this study were of 250 and 400 µm in width, whilst their height was fixed at 150 µm, resulting in hydraulic diameters of about 187 µm and 218 µm, respectively. The channels were etched in silicon and covered by a pyrex wafer. The influence of surface tension was studied by employing water and ethanol as liquids ($\gamma_{water}/\ \gamma_{ethanol} = 3.26$, $\mu_{water}/\ \mu_{ethanol} = 0.85$, at 20 °C). In order to evaluate the effect of viscosity, an aqueous solution of glycerol (20 %wt) was employed ($\gamma_{water}/\ \gamma_{glycerol} = 0.99$, $\mu_{glycerol}/\ \mu_{water} = 1.54$, at 20 °C). Nitrogen served as the gas-phase and was contacted with the liquid in a T-shaped inlet structure, which included a chamber with embedded barriers, as shown in figure 2.19. The width of the contacting zone was then reduced down to that of the microchannel.

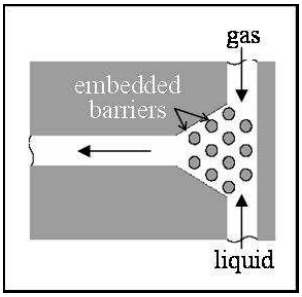

Figure 2.19: Schematic illustration of the gas-liquid contacting section with its inlet to the test-section as used by Waelchli and von Rohr (2006) for the investigation of gas-liquid flow in rectangular microchannels with hydraulic diameters of about 187 µm and 218 µm (the barriers inside of the mixing chamber are 50 µm in diameter).

The flow regimes observed by Waelchli and von Rohr (2006) were identical for all gas-liquid combinations in both test sections and were denominated as bubbly, intermittent and annular flow. Here the term intermittent flow corresponds to the slug flow pattern observed in previous studies. The bubbles with a length slightly larger than the channel width were included in the bubbly flow pattern. The annular flow regime featured a smooth liquid film. The transition between the flow regimes was characterized by oscillations between the three "clear-cut" flow patterns. For a given flow condition within these transition zones, the flow behaviour was labelled according to the dominating flow pattern. This underlines once more, that flow transitions are rather areas, whose positioning is represented by transition lines. In order to asses the effect of surface tension, the flow transition lines obtained in the 187 µm channel for nitrogen-water and nitrogen-ethanol combinations are compared in figure 2.20a. The effect of channel diameter is illustrated in figure 2.20b by a comparison of the flow pattern transition lines found for nitrogen-water in the 187 µm and 218 µm test sections.
As already mentioned above, a decrease of surface tension would result in a decrease of the surface tension dominated zone (bubbly and slug flows) and would shift the slug-to-annular flow transition line to lower superficial gas velocities. Examination of the experimental transition lines in figure 2.20a indeed confirms this assumption. Furthermore, it can be seen that for nitrogen-water flow at intermediate and high liquid velocities, the transition from slug to annular flow shows a good agreement with that estimated by the criteria of Akbar et al. (2003). However, with respect to nitrogen-ethanol these criteria generally over predict the results.

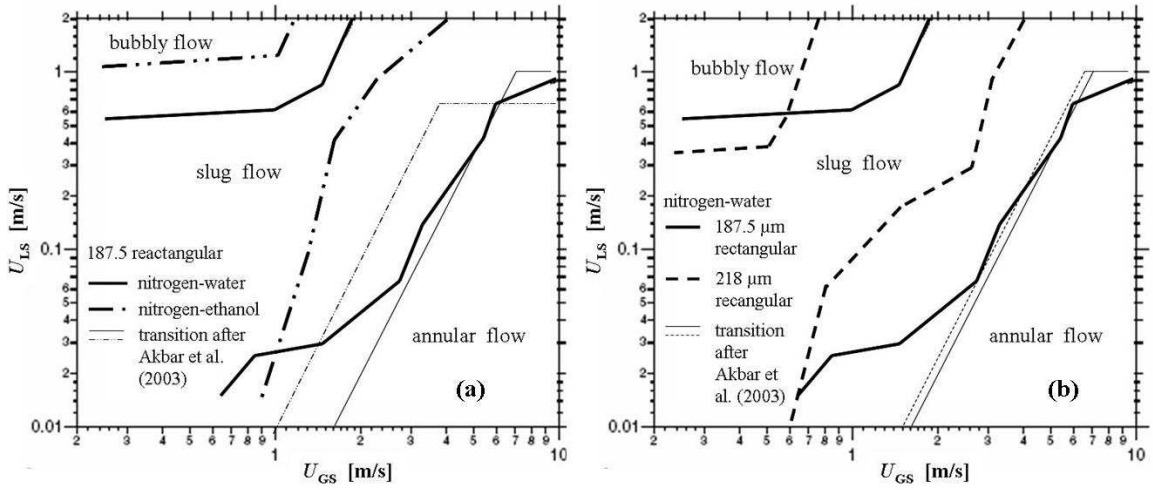

Figure 2.20: Flow pattern maps obtained by Wealchli and von Rohr (2006) and the corresponding transition lines proposed by Akbar et al. (2003) for gas-liquid flow in rectangular microchannels with a height of 150 µm and widths of 250 µm and 400 µm. (a: comparison of flow transitions with respect to the effect of surface tension; b: comparison with respect to the effect of the hydraulic diameter; U_{LS} superficial liquid phase velocity, U_{GS} superficial gas phase velocity).

Following the discussion concerning the competition of the surface tension force and inertia, the impact of an increase in the channel diameter is expected to be similar to when there is a decrease in surface tension; a shift of the slug to annular transition to lower superficial gas velocities is expected. The results presented by Waechli and von Rohr (2006), as shown in figure 2.20b are in agreement with this, but the shift is remarkably greater than that predicted by the criteria of Akbar et al. (2003). In the first instance, this behaviour may possibly be due to the fact that on the one hand the channel width was increased by about 150 µm (from 250 µm to 400 µm), whilst on the other hand the hydraulic diameter, which is used to predict the flow transitions, only changed by about 30 µm. This suggests that in rectangular channels the aspect ratio comes into play as an important factor

influencing the flow transitions. The aspect ratios (h/w) of the test sections used here are 0.6 (d_h = 187 µm) and 0.38 (d_h = 218 µm). Assessment of this work and the study of Yue et al. (2007; h/w = 0.5; see figure 2.16) may lead to the assumption that the criteria of Akbar et al. (2003) is still applicable for rectangular channels with aspect ratios $h/w \geq 0.5$, however this does not hold for the work of Haverkamp (2002; h/w = 0.33; see figure 2.18).

Another parameter which is not included in the Weber-number based approach of Akbar et al. (2003) is the viscosity. The impact of viscosity on the flow transition lines is shown in figure 2.21, which compares the flow pattern maps obtained in the 187 µm channel using water and an aqueous glycerol solution as the liquid phase. It can be seen that an increase of viscosity appears to influence the slug to annular transition in two different ways. Firstly, from intermediate to high liquid phase velocities, the surface tension dominated zone is reduced and the transition is shifted to low gas velocities. Secondly, from intermediate to low superficial liquid phase velocities, the surface tension dominated zone is expanded to higher gas velocities. The latter trend is almost equal to that found for flow maps presented by Haverkamp (2002; see figure 2.20) and confirms that liquid viscosity is an important parameter to account for with respect to flow pattern transitions.

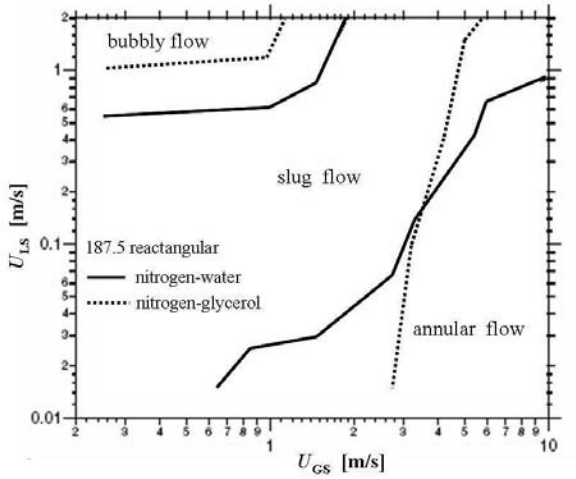

Figure 2.21: Flow-pattern map with flow transitions obtained by Waechli and von Rohr (2006) for nitrogen-water and nitrogen-glycerol two-phase flow in a rectangular microchannel with a hydraulic diameter of 187 µm (h = 150 µm, w = 250 µm; U_{LS} superficial liquid phase velocity; U_{GS} superficial gas phase velocity).

2.3 Gas-liquid flow versus chemical reactions

After the presentation of the characteristics of gas-liquid flow in microchannels, the aim of the following section is to discuss which of these flow patterns may constitute interesting operating conditions for gas-liquid reaction systems. The reactions that are typically considered for operation in microreactors are fast and highly exothermic reactions. In this context, a first category comprises non-catalyzed gas-liquid reactions like direct fluorinations or sulfonations (de Mas et al., 2003; Chambers et al, 2005; Jähnisch et al., 2004; Hessel et al., 2005). Since these reactions are very fast, they take place close to the gas-liquid interface and are therefore susceptible to a limitation of the reaction rate by the gas-liquid mass transfer. For the case of the direct fluorination, this effect is even more pronounced due to the low solubility of fluorine. Two further categories of reaction systems are homogeneous (Mills and Chaudhari, 1997; Mills and Chaudhari, 1999; Leclerc et al., 2008) and heterogeneous catalyzed gas-liquid reactions (Kreutzer et al., 2005a, Hessel et al., 2005), for example oxidations and hydrogenations. In these cases, the poor solubility of oxygen and hydrogen in the liquid phase results in the same mass transfer limitation as mentioned above. For strong limitation of the reaction rate by the gas-liquid mass transfer, the effective volumetric reaction rate may be given as follows (Klemm et al., 2007):

$$r_{eff} = k_L a \cdot H_i p_i \qquad (2.4\text{-}1),$$

where p_i is the partial pressure of the gaseous reactant and H_i the corresponding Henry's law constant. The term indicated as $k_L a$ is the volumetric liquid side mass transfer coefficient, composed of the mass transfer coefficient k_L and the specific interfacial area a. In the case of the sulfonation reaction, the $k_L a$ is replaced by $k_G a$ since sulphur trioxide shows good solubility in the liquid phase and the resistance to mass transfer is located on the gas side.

Expression 2.4-1 thus shows the reaction related parameters which must be considered in conjunction with the physical characteristics of the two-phase flow for performing gas-liquid reactions in microreactor systems. One way to diminish the mass transfer limitation and to increase the reaction rate is to increase the pressure of the gas phase. This is generally done for performing homogeneous and heterogeneous catalyzed gas-liquid reactions in conventional reactors and can also be implemented in the case of microreactors. In this context, it is important to know how the increase in pressure influences the flow patterns and the conditions at which they occur. A contribution to this question was provided by Fries et al. (2006). They studied gas-liquid flow under pressures between 30 bar and 120 bar in a square microchannel with a hydraulic diameter of 200 µm. The corresponding flow pattern map is shown in figure 2.22.

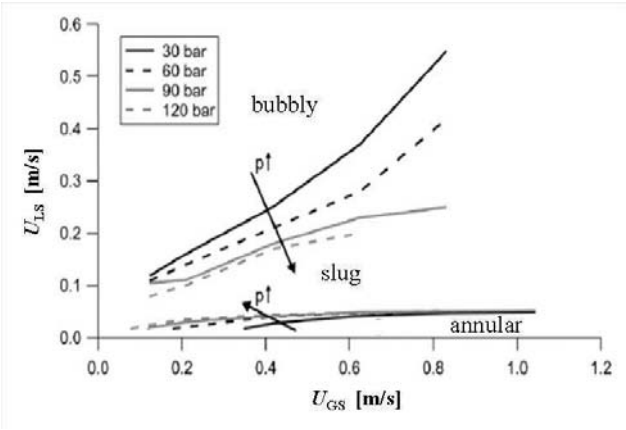

Figure 2.22: Flow-pattern map with flow transitions obtained by Fries et al. (2006) for gas-liquid two-phase flow at various system pressures in square microchannel with d_h = 200 µm (U_{LS} superficial liquid phase velocity; U_{GS} superficial gas phase velocity).

From figure 2.22 it can be seen that with increasing pressure the area of occurrence of bubbly flow increases, whilst that for slug flow decreases. On the other hand, the transition from slug to annular flow remains almost constant. Furthermore, compared with the areas of bubbly and slug flow, the flow window of the annular pattern appears to be small. This favours the bubbly and the slug flow patterns as possible operating conditions.

According to equation 2.4-1, a second way to decrease a strong gas-liquid mass transfer limitation is given by the increase of the specific interfacial area. A study concerned with this parameter was carried out by Hessel et al. (2000). Here, the specific interfacial areas were determined as a function of the gas-liquid flow regime. The microchannel was of rectangular cross section with a width of 300 µm and a height of 100 µm. Example values of the specific interfacial area obtained by measurement of CO_2 absorption into a sodium hydroxide solution are specified in table 2.4.

Flow regime	a [m^2/m^3]
bubbly	5100
slug	18700
annular	25300

Table 2.4: Values of specific interfacial areas as a function of the flow regime measured by Hessel et al. (2000) through absorption of CO_2 in a solution of sodium hydroxide in a rectangular microchannel with w = 300 µm and h = 100 µm.

From table 2.4 it can be seen that the specific interfacial area increases with increasing bubble size. The maximum value is reached in the annular flow regime, since under these conditions the specific

interfacial area approaches the surface to volume ratio of the microchannel, which is about 26667 m^2/m^3 for the device used by Hessel et al. (2000). From the comparison made above, one may rank the annular flow regime as the most preferable operating condition, whilst the bubbly flow pattern may be excluded. At this point in the discussion, we thus identify slug flow and annular flow as the most interesting conditions for performing gas-liquid reactions in microchannels.
In order to follow up this discussion, one should supplement the considerations made above by a particular characteristic of the slug flow pattern, firstly mentioned by Taylor (1961) who proposed that within this region a recirculation motion is created (see figure 2.23). This behaviour, confirmed later by numerous studies using particle image velocimetry (PIV; Thulasidas et al, 1997; Günther et al, 2004; Günther et al., 2005; Waelchli and von Rohr, 2006), is believed to increase the molecular transport between the gas-liquid interface and the bulk of the liquid slug, thus increasing k_L and enhancing mass transfer between both phases.

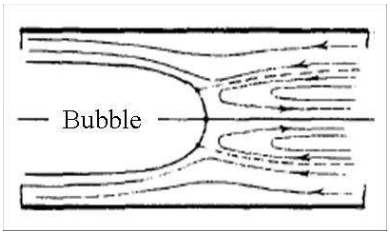

Figure 2.23: Streamline patterns of the recirculation motion within a liquid slug in front of the bubble, proposed by Taylor (1961).

Consequently, we may state that although annular flow offers the greatest specific interfacial area for mass transfer, slug flow or Taylor flow offers a larger operating window at normal, as well as elevated system pressure. The latter point is especially of interest with respect to homogeneous and heterogeneous catalyzed gas-liquid reactions. Additionally, slug flow has a recirculation motion within the liquid phase, which is a promising feature for increasing gas-liquid mass transfer. As a result, we consider slug flow as the most adapted flow regime to carry out the different reaction categories mentioned above in microreactors.

2.4 Conclusions

This chapter has presented a detailed review on the state of the art of gas-liquid flow regimes in small channels and microchannels. It attempts to clarify the effects of geometry (diameter, cross section, and gas-liquid contacting section), as well as fluid properties on the flow regimes generated and also the potential of these characteristics of gas-liquid flow in microchannel reactors for performing chemical reactions. The concluding points from this analysis can be summarised as followed.

- If a stable two-phase flow is generated, the gas-liquid flow patterns generated in microchannels are similar to those found in capillaries with inner diameters of approximately 1 mm. As a result, the same terminologies for classifying the flow regimes in small channels can be adopted for the two phase flow in microchannels. However, one difference observed in in non-circular microchannels is the appearance of so-called dry flows at low liquid velocities in the annular flow regime.
- The stability of gas-liquid flow patterns in microchannels is strongly dependent on the way the fluids are contacted and therefore the geometry of the contacting section of the microchannel. Direct and indirect contacting modes have been identified; the latter designating the case where both fluids are contacted in a separate zone, before entering the main channel. It was shown that the design of the contacting section determines if a stable or an unstable two-phase flow is generated. At this, an unstable flow is marked by interruptions of the two-phase flow

by sections of single phase liquid flow and/or the occurrence of different flow patterns at a fixed set of superficial velocities. Analysis of the literature suggests that a direct supply of the gas phase to the main channel by employing simple Y- or pseudo-T-junctions always resulted in the formation of a stable two-phase flow.

- A change in channel diameter has been shown to affect the position of the flow transitions on the flow regime map, but does not lead to the appearance of new flow patterns. This is also the case for a variation in the contact angle (providing that it concerns partially wetting conditions (θ < 90°)) since it is directly linked to the surface tension. The way in which the flow transitions are shifted can be explained by the competition between surface tension and inertia forces. According to this the flow pattern map is divided into two areas: a surface tension dominated zone with bubbly and slug flow and an inertia dominated zone, containing annular and churn flow regimes. Especially in the case of direct contacting using low viscous liquids ($\mu_l \leq 1$ mPa·s), the transition correlations originally developed for circular capillaries correctly predict the transition from slug to annular flow in microchannels. However, since these correlations are based on superficial Weber numbers the effect of viscosity is not included. As a result, the prediction of flow transitions in microchannels fails when higher viscous liquids are used. For microchannels of rectangular cross-section the effect of the aspect ratio on flow transitions seems to be more pronounced than expected when considering the corresponding hydraulic diameters. Consequently, the characterization of flow transitions with respect to the effect of the liquid viscosity, as well as the channel aspect ratio still requires further systematic investigations.
- Little importance has been attributed to the fact that the transition between divers flow patterns is a process that is gradually developed. Flow transitions however have been exclusively presented as sharp lines within the flow pattern maps and almost no explanations have been given concerning the manner in which they are positioned. Displaying the flow transitions as areas within a flow pattern map may simplify the comparison with existing transition criteria, as well as their development.
- With respect to the operation of chemical reactions it appears that Taylor flow offers the largest operating window and has unique flow characteristics that maybe particularly interesting for gas-liquid mass transfer and mass transfer limited multiphase reaction systems.

3 Hydrodynamics and Mass-Transfer in Taylor flow through microchannels

The particularity of the liquid phase velocity field as well as the flexibility offered by a large range of superficial velocities turns the Taylor flow regime into an interesting operating condition for gas-liquid systems involving chemical reactions. The questions, which need to be considered now, are with parameters the velocity field depends on and how the two-phase pressure drop as well as the gas-liquid mass transfer may be estimated. The response to these points initially requires a closer look into the fundamentals of bubble transport through microchannnels and the parameters involved in this process. The insight gained by this section is then used to discuss the modeling of the two-phase pressure drop. Afterwards the evolution and some additional features of the liquid phase velocity field will be treated in detail, followed by a demonstration concerning the modeling of gas-liquid mass transfer. Based on these sections the fundamental hydrodynamic parameters to be controlled will be identified and their prediction in dependency of design features like shape of the channel cross section and the gas-liquid contacting mode will be discussed. In this context, additional phenomena related to these parameters will also be presented.
The following sections constitute a theoretical analysis based on a detailed review of the literature.

3.1 Fundamentals of bubble transport

A bubble in a liquid is in equilibrium if the tendency of the surface tension to minimize its interfacial area is compensated by an excess pressure. This pressure is called the Laplace or capillary pressure. Thus the pressure inside of a bubble p_{in} is always larger than that of the liquid around it p_{out}. For a spherical bubble of radius r (as illustrated in figure 2.1a), the Laplace pressure writes as:

$$\Delta p = p_{in} - p_{out} = \frac{2\gamma}{r} \qquad (3.1\text{-}1).$$

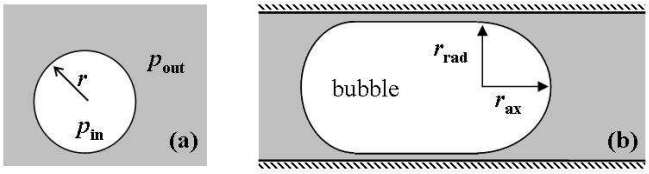

Figure 3.1: Schematic illustration of parameters related to the Laplace pressure of bubbles submerged in liquid phase.

An elongated bubble in a capillary or microchannel has two caps, one at its front and one at its rear end (see figure 3.1b). The Laplace pressure across a bubble cap is determined by its radial and axial curvature.

$$\Delta p_{cap} = \gamma\left(\frac{1}{r_{ax}} + \frac{1}{r_{rad}}\right) \qquad (3.1\text{-}2).$$

The force enabling a fluid to move horizontally is a pressure gradient and according to that the bubble flows from a zone of high pressure to a zone of low pressure. If one considers a bubble of length l_B, the pressure gradient generated between the bubble caps may be written as (de Gennes et al, 2002):

$$-\frac{\partial p}{\partial x} = \frac{\Delta p_{cap,rear} - \Delta p_{cap,front}}{l_B} \qquad (3.1\text{-}3).$$

The minus sign in equation 3.1-3 indicates that the pressure decreases in the downstream direction. As a result the Laplace pressure across the front cap of the bubble must be greater than that at the rear end. Thus the curvature of the front cap of a moving bubble is always smaller than that at its back cap. Once, the bubble is in motion it would now be interesting to have a look on the characteristic parameters of the Taylor flow pattern and their dependency on the initial flow rates. In this context it may be useful to derive a mass-continuity relationship for both phases. This will be done by means of

the model illustrated in figure 3.2. Here a control volume is drawn around an area containing the main morphological characteristics of the flow.

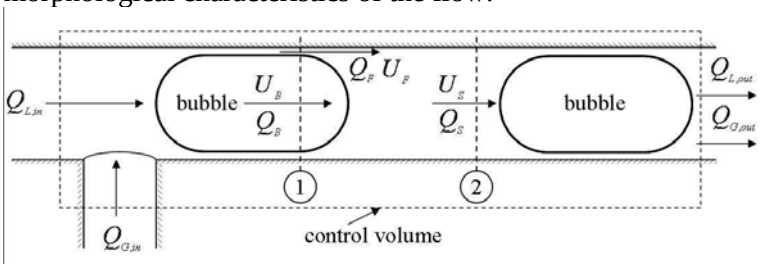

Figure 3.2: Schematic illustration of the model used to derive the mass-continuity relationship for Taylor flow (Q volumetric flow rate, U velocity; subscripts: l liquid phase, g gas phase, *in* inflow, *out* outflow, B bubble, F liquid film, S liquid slug).

The mass - continuity relationships for both phases may basically be written as:

$$Q_{G,in}\rho_G - Q_{G,out}\rho_G = \rho_G \frac{dV_G}{dt} + V_G \frac{d\rho_G}{dt} \qquad (3.1\text{-}4a)$$

and

$$Q_{L,in}\rho_L - Q_{L,out}\rho_L = \rho_L \frac{dV_L}{dt} + V_L \frac{d\rho_L}{dt} \qquad (3.1\text{-}5a).$$

Assuming that both fluids are incompressible, the second term on the right hand side may be neglected. As next the density can be eliminated in both equations and the following expressions are yielded:

$$Q_{G,in} - Q_{G,out} = \frac{dV_G}{dt} \qquad (3.1\text{-}4b) \qquad\qquad Q_{L,in} - Q_{L,out} = \frac{dV_L}{dt} \qquad (3.1\text{-}5b).$$

If one further considers that the control volume remains constant one may suppose that the volume of the liquid leaving the control volume is equal to that of the gas flowing in.

$$\frac{dV_G}{dt} = -\frac{dV_L}{dt} \qquad (3.1\text{-}6a).$$

Insertion of equation 3.1-4b and 3.1-5b into 3.1-6a yields:

$$Q_{L,in} + Q_{G,in} = Q_{L,out} + Q_{G,out} \qquad (3.1\text{-}6b).$$

That means that the total volume flow at any point of the channel is equal to the sum of the inlet flow rates. The inlet flow rates itself can be expressed by means of the respective superficial phase velocities in the main channel multiplied by its cross-sectional area.

$$A_{Ch}\left(U_{LS} + U_{GS}\right) = Q_{L,out} + Q_{G,out} \qquad (3.1\text{-}6c).$$

In the following the control volume is reduced to the space between the positions labeled as 1 and 2 in figure 3.2, so that the entry is located across a bubble and the exit across a liquid slug. With respect to plane 1 the liquid flow in the film can be stated as:

$$Q_F = Q_{L,in} \qquad A_F U_F = A_{Ch} U_{LS} \qquad U_{LS} = \varepsilon_F U_F \qquad (3.1\text{-}7a\text{-}c).$$

At this U_F represents the liquid velocity within the film and ε_F the fraction of the cross-sectional area of the channel which is occupied by the liquid film. In a similar way the expression for the flow of the gas phase can be found.

$$Q_B = Q_{G,in} \qquad A_B U_B = A_{Ch} U_{GS} \qquad U_{GS} = \left(1 - \varepsilon_F\right) U_B \qquad (3.1\text{-}8a\text{-}c).$$

Since plane 2 is located across a liquid slug the flow of the gas-phase equals zero ($Q_G = 0$). Thus the volume flow of the slug is equal to the sum of inlet flow rates and the average velocity of the liquid phase within a slug U_S is equal to superficial two-phase velocity U_{TP}.

$$Q_S = Q_{L,in} + Q_{G,in} \qquad A_{Ch} U_S = A_{Ch}\left(U_{LS} + U_{GS}\right) \qquad U_S = U_{TP} \qquad (3.1\text{-}9a\text{-}c).$$

Combination of equations 3.1-7, 3.1-8 and 3.1-9 yields the following expression:

$$U_{TP} = \varepsilon_F U_F + (1-\varepsilon_F) U_B \qquad (3.1\text{-}10a).$$

In the literature measured bubble velocities U_B are mostly represented as a function of the superficial two phase velocity U_{TP}. Rearranging equation 3.1-10a, this may basically be written as:

$$U_B = \frac{1}{(1-\varepsilon_F)} U_{TP} - \frac{\varepsilon_F}{(1-\varepsilon_F)} U_F \qquad (3.1\text{-}10b).$$

That means that a plot of U_B versus U_{TP} should, in principle, furnish a linear correlation whose slope and y-intercept contain information about the area of the liquid film region. The following discussion, however, will be resumed by means of the dimensionless form of equations 3.1-10a-b:

$$\psi = \frac{U_B}{U_{TP}} = 1 - \frac{\varepsilon_F}{U_{TP}} (U_F - U_B) \qquad (3.1\text{-}10c).$$

At this ψ denotes the dimensionless bubble velocity. In Taylor flow through vertical oriented small tubes the action of gravitational acceleration induces a film flow (Kolb and Cerro, 1991, 1993; Thulasidas et al., 1995, 1997) which is of counter-current nature in the case of upward flow and in co-current direction for downward Taylor flow. This circumstance has a significant influence on the residence time behavior of the liquid. While the downward configuration may be considered to show a plug-flow behavior, the counter-current film flow within the upward configuration causes a remarkable degree of back-mixing (Kolb and Cerro, 1993). The extent of the film flow was shown to be strongly pronounced in channels of non-circular cross-section. The data of Kolb and Cerro (1991) show that it diminishes with increasing Capillary number and vanishes at a ratio of about $Bo/Ca < 0.8$ (Bond number based on d_h). In the case of horizontal Taylor flow in small tubes the influence of gravity can generally be neglected. Than the pressure gradient needed to induce a flow around the bubble would essentially depend on the Laplace pressure across the bubble body (region between the bubble caps). According to equation 3.1-1 the Laplace pressure at any point in this region may be written as:

$$\Delta p = p_B - p_F = \frac{\gamma}{r_{BB}} \qquad (3.1\text{-}11).$$

Here, p_B and p_F are the pressure within the bubble and the liquid film, respectively and r_{BB} is the radius of the bubble body. Since, the viscosity of the gas phase is of negligible value compared to that of the liquid, the pressure within the bubble can be assumed as uniform. Furthermore, if the surface tension is considered as constant, the only changes in the Laplace pressure may be brought by a change of the radius of the bubble body in the axial direction. However, the flat annular film around the bubble indicates that the bubble radius nearly remains constant. Hence, under these conditions no axial pressure gradient is present within the liquid film. The film is laid down at the front cap and does not move anymore until the bubble passed by. Setting $U_F = 0$, equation 3.1-10c transforms into:

$$\frac{U_B}{U_{TP}} = \frac{1}{(1-\varepsilon_F)} \qquad (3.1\text{-}12).$$

The only flow occurs within the region near the bubble cap, where the film is no longer of constant thickness. The deposition of the film in this region was firstly analyzed by Bretherton (1961). According to that the area near the bubble cap is divided into three sub-regions, a hemispherical bubble cap, the flat liquid film and a transitional region (see figure 3.3). Within the latter one a so-called dynamic meniscus connects the bubble cap (static meniscus) to the flat film.

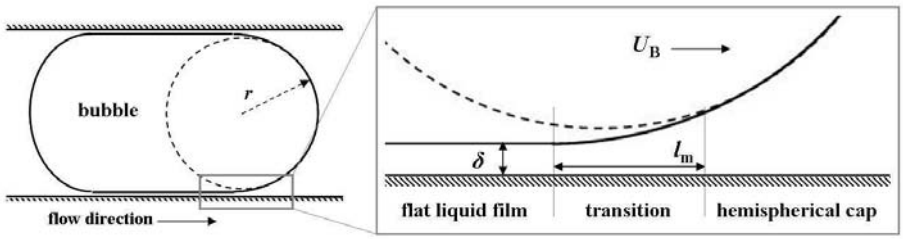

Figure 3.3: Schematic sketch of the model used by Bretherton (1961) to analyze the deposition of the liquid film at the front cap of an elongated bubble in Taylor flow (r radius of the hemispherical bubble cap, the axial and radial curvature equal each other; δ liquid film thickness; l_m length of the dynamic meniscus within the transition region; U_B bubble velocity).

The approach of Bretherton (1961) is based on the Navier-Stokes equations. Neglecting the influence of gravity or any other body forces the Navier-Stokes equations for incompressible flow are principally written as:

$$\rho\frac{\partial U}{\partial t}+\rho(U\cdot\nabla)U=-\nabla p+\mu\nabla^2 U \qquad (3.1\text{-}13).$$

At this, the term ∇ is denoted as del-operator and labels the first derivation after the space coordinates. The term ∇^2 is the Laplace-operator displaying the second derivation after the space coordinates. The left hand side of 3.1-13 represents inertial forces, while the right hand side contains the pressure force and viscous stresses. If one considers that the flow is steady, the time derivative on the left hand side can be eliminated. Furthermore, from figure 3.3 it can be seen that the thickness of the liquid film δ is small compared to the radius of the bubble cap ($\delta << r$). This radius does not exceed an order of 10^{-4} m in a microchannel. Bearing in mind the competition between inertia and viscous forces, expressed by the Reynolds number, this suggests that in the length scale of the transition region the influence of inertia may be neglected. Regarding these assumptions the Navier-Stokes equations reduce to:

$$\nabla p=\mu\nabla^2 U \qquad (3.1\text{-}14).$$

That means that the deposition of the liquid film within the transition region is characterized by the balance between the pressure gradient along the dynamic meniscus (see figure 3.3) and viscous stresses. Assuming that the flow is unidirectional and that $\delta << r$, expression 3.1-14 may be rewritten in terms of order of magnitudes. This was firstly demonstrated by Aussilous and Quéré (2000). Taking into account the model illustrated in figure 3.3 they principally stated that:

$$\frac{\Delta p}{l_m}=\frac{\mu_L U_B}{\delta^2} \qquad (3.1\text{-}15).$$

Here, l_m is the length of the transition region. At this, the pressure gradient drives the liquid into the film, which is deposited at the velocity of the bubble. Assuming that the radius of the bubble cap and the curvature of the bubble body are of same order of magnitude, the difference in Laplace pressures between these regions may be approximated as γ/r (Aussilous and Quéré, 2000). Thus, equation 3.1-15 may be rewritten as:

$$\frac{\delta}{l_m}\cdot\frac{\delta}{r}=\frac{\mu_L U_B}{\gamma} \qquad (3.1\text{-}16).$$

From equation 3.1-16, it can be seen that the bubble curvature, the liquid film thickness and the length of the transition region are a function of the Capillary number, representing the competition between shear stresses and surface tension forces.

$$Ca=\frac{\mu_L U_B}{\gamma} \qquad (3.1\text{-}17).$$

From the analysis undertaken by Bretherton (1961) it turned out that the film thickness and length of the dynamic meniscus scale with $Ca^{2/3}$ and $Ca^{1/3}$, respectively. It also demonstrates that the film

thickness and the Laplace pressure and with that the pressure within the bubble are directly linked to each other. Consequently the bubble pressure is also a function of *Ca*. Since the film is laid down at the front cap, the pressure within the bubble is mainly determined in this region and is thus independent of the bubble length. Within a range of Ca < $3 \cdot 10^{-3}$ the bubble pressure drop at the font cap was derived by Bretherton (1961) as:

$$\Delta p_B = 7.45 \cdot (Ca)^{\frac{2}{3}} \left(\frac{\gamma}{r} \right) \qquad (3.1\text{-}18).$$

For the pressure drop across the whole bubble Bretherton (1961) found a factor of about 9.4. As already mentioned, the descriptions made above are representative for the case where the surface tension can be considered as constant. Going back to equation 3.1-11 it can be seen that a pressure gradient within the film may also be generated by changes in the surface tension. This may be the case if the liquid phase contains surface active substances contaminating the gas-liquid interface. During the flow these surfactants are swept form the front cap of the bubble to its rear end, where it accumulates, leading to the generation of a surface tension gradient. This situation is sometimes referred to as Marangoni-effect. Under these circumstances the stress-condition (Ajaev and Homsy, 2006) supposes that the surface-tension gradient is balanced by tangential stress at the gas-liquid interface. This no-slip condition at the interface induces a linear Couette-flow field within the liquid around the bubble body. According to that the average velocity within the film may be approximated as $U_F = 0.5U_B$. Insertion into equation 3.1-10c results in:

$$\frac{U_B}{U_{TP}} = \frac{1}{(1 - 0.5\varepsilon_F)} \qquad (3.1\text{-}19).$$

In contrast to the statement given by equation 3.1-10b a plot of U_B versus U_{TP} does not contain a y-intercept, because here the velocity of the film is a function of the bubble velocity. Furthermore, since the liquid around the bubble is moving, its fraction is lower as in the static case. The effect of surfactants will be more pronounced for short bubbles at low Capillary numbers ($Ca \leq O(10^{-3})$). Compared to the expression obtained for a static film (see equation 3.1-12) it turns out that in both cases the slop obtained from a plot of U_B versus U_{TP} should generally be greater than unity. Returning to the scaling found by Bretherton (1961) in the case of a static film one obtains a dimensionless film thickness δ/r in the order of 0.01. That means that under these conditions ($Ca \leq O(10^{-3})$) the liquid film only occupies a small percentage of the channel cross-section. As a result the bubble velocity would be approximately equal to the superficial two-phase velocity ($U_B \approx U_{TP}$) and the two cases discussed above would not be distinguishable by a plot of U_B versus U_{TP}. Furthermore, since the film is the only way for axial mass transfer between successive slugs of liquid, backmixing is significantly reduced (Salman et al., 2004) and the liquid phase residence time behavior in horizontal Taylor flow may also be approximated by a plug flow.

3.2 Gas-liquid two phase pressure drop

The total pressure drop in two-phase flow is composed of three contributions: the pressure drop due to friction, acceleration and the static pressure drop (see equation 3.2-1). The latter one can be neglected for horizontal flow, while the acceleration pressure drop needs to be taken into account if a phase change occurs and in the case of high frictional pressure drops.

$$\Delta p_{tot} = \Delta p_f + \Delta p_a + \Delta p_s \qquad (3.2\text{-}1).$$

A common way to estimate gas-liquid two phase frictional pressure drops is to employ either the homogenous or the separated flow model (Wallis, 1969; Liu and Wang, 2008). In the homogeneous model the two-phase flow is considered as a homogeneous fluid with average properties obeying the

equations of single component flow. In order to calculate the friction factor it is necessary to estimate the two-phase mixture viscosity. For this purpose several correlations are given in the literature (a summarizing table can be found in Kawahara et al. (2002)). In this context however, the problem is to know which of these models can be applied. Thus, experimental data are usually compared to the pressure drop predicted on the basis of these mixture viscosity models, resulting in a variation of propositions concerning the model which fits the best (Kawahara et al., 2002; Chung and Kawaji, 2004; Yue et al., 2004; Triplett et al., 1999b; Liu and Wang, 2008). For example, Chung and Kawaji (2004) showed that their data for nitrogen-water flow in circular microchannels with 50 µm and 100 µm in diameter can be estimated using the Dukler viscosity model, while in the test-sections with diameters of 250 µm and 530 µm the Beattic&Whalley model better approached the measured values. On the other hand, a better agreement with the McAdams viscosity model was reported in the case of nitrogen-water flow through rectangular channels with hydraulic diameters of 528 µm (575 µm×488 µm) and 333 µm (333 µm×332 µm; Yue et al., 2004). This finally weakens the reliability of the homogeneous flow model in predicting gas-liquid two-phase pressure drops in microchannels.

Concerning the separated flow model the two-phase frictional pressure drop can be calculated using the Lockhart-Martinelli correlation (Lockhart and Martinelli, 1949). Through this the two-phase pressure drop gradient is related to the single-phase liquid pressure drop gradient by a two-phase frictional multiplier. This multiplier is determined by two parameters, the Lockhart-Martinelli parameter and the Chisholm parameter (also called the C-value; Chisholm, 1967). The former one contains the ratio of single phase liquid to single phase gas pressure drop gradient, while the latter one is a constant depending on whether the flow of the respective phase is laminar or turbulent. Mishima and Hibiki (1996, 1993) as well as Lee and Lee (2001) applied the Lockhart-Martinelli approach to circular and rectangular channels with diameters between 0.78 mm and 6.67 mm. It turned out that the frictional pressure drop predicted on the basis of the classical Chisholm-parameter was not able to represent the experimental results. Hence, modified C-values accounting for the hydraulic diameter of the channel (Mishima and Hibiki, 1996) as well as fluid properties (Lee and Lee, 2001) were proposed. These correlations were indeed shown to predict the two-phase frictional multiplier for nitrogen-water flow in circular microchannels with diameters ranging form 50 µm to 530 µm (Kawahara et al., 2002; Chung and Kawaji, 2004). However, no comparison was undertaken to measurements conducted in rectangular microchannels with hydraulic diameters of 528 µm and 333 µm using the same fluid combination (Yue et al., 2004), as well as to CO_2-water flow in a 667 µm channel (Yue et al., 2007). In the case of the latter investigations another type of correlation was proposed for the Chisholm parameter.

A possible explanation for this number of correlations can be deduced from a study of Cubaud and Ho (2004). At this the pressure drop, measured for air-water two-phase flow in a square channel with d_h = 200 µm, was plotted versus the superficial gas flow rate and the capillary number. To this plot, Cubaud and Ho (2004) added the transitions between flow regimes and demonstrated that the trend or the gradient of the two-phase pressure drop is particular for each flow pattern. For example, in the case of Taylor flow, it was observed that the pressure drop decreases with increasing gas flow rate (decrease of liquid hold-up). Consequently, since the homogeneous and the separated flow models are flow pattern independent, it was concluded that an approach, which takes the hydrodynamic characteristics of the flow pattern into account would be more appropriate. Ratulowski and Chang (1989) proposed that the pressure drop in horizontal Taylor flow could be modeled as the sum of the frictional pressure drop Δp_{fs} of the liquid slugs and the pressure across the bubbles.

$$\Delta p_{tot} = n_S \Delta p_{fS} + n_B \Delta p_B \qquad (3.2\text{-}2).$$

At this n_S and n_B are the number of slugs and bubbles within the channel. The frictional pressure drop of the liquid slug may be estimated by means of the Hagen-Poiseuille equation, using the length l_S and the average velocity U_{TP} of the liquid slug (see equation 3.2-3).

$$\Delta p_{fS} = k\left(\frac{\mu_L U_{TP}}{d}\right)\left(\frac{l_S}{d}\right) \qquad (3.2\text{-}3).$$

At this d is the diameter of the largest inscribed sphere within the channel cross-section. For example, in the case of a rectangular channel this corresponds to the channel height. The value of the coefficient k is 32 for a circular channel and about 28.45 in the case of a square channel cross section. For a rectangular channel the coefficient k is a function of the aspect ratio w/h and may be approximated as follows (Fuerstman et al., 2007):

$$k = 12\left[1 - \frac{192}{\pi^5}\frac{h}{w}\tanh\left(\frac{\pi}{2}\frac{w}{h}\right)\right]^{-1} \text{ with } \quad \tanh(x) = 1 - \frac{2}{e^{2x}+1} \qquad (3.2\text{-}4).$$

Equation 3.2-4 is valid for w/h > 1 and $Re \leq 1000$. In connection with Taylor flow the Reynolds number for the liquid phase would be based on the superficial two-phase velocity and is given as:

$$\mathrm{Re}_{L,TP} = \frac{\rho_L U_{TP} d}{\mu_L} \qquad (3.2\text{-}5).$$

As mentioned above the pressure across a Taylor bubble was firstly derived by Bretherton (1961) from an analysis of the bubble motion in circular capillaries at low Capillary numbers. This topic was seized again later by Wong et al. (1995b) in the framework of a numerically study and was extended to channels of non-circular cross section. According to both studies the pressure drop across an elongated bubble for $Ca < 3 \cdot 10^{-3}$ may be represented by the following general correlation:

$$\Delta p_B = a \cdot Ca^{\frac{2}{3}}\left(\frac{\gamma}{r}\right) \qquad (3.2\text{-}6).$$

At this r is the radius of the largest inscribed sphere in the channel cross-section. The corresponding factors a are listed in table 3.1 for different cross-sectional shapes. Here the values taken from the study of Wong et al. (1995b) are valid for bubbles, whose lengths are smaller than 1000 times the radius r.

cross-section	***a***	***reference***
circular	≈ 9.4	Bretherton (1961)
	≈ 10	
square	≈ 3.4	Wong et al.
rectangular	≈ 3.2 ± 0.1	(1995b)
	(w/h = 1.2 - 2)	for $l_B/r << Ca^{-1}$

Table 3.1: Values of the factor a in equation 3.2-6 found by Bretherton (1961) and Wong et al. (1995b) for the pressure across an entire elongated bubble in Taylor flow through capillaries of varies cross-sectional shapes at $Ca < 3 \cdot 10^{-3}$ (w/h aspect ratio, l_B bubble length, r radius of the largest inscribed sphere within the channel cross-section).

In table 3.1 it can be seen that the values of the coefficient a found by Bretherton (1961) and Wong et al. (1995b) for the circular channel cross-section are close to each other. However, in the case of the non-circular channels the coefficient a is approximately three times smaller than that shows in a circular capillary, which means that the pressure drop across the bubble in square and rectangular channels is about three times smaller than in a circular channel (Wong et al., 1995b). For higher Capillary numbers ($Ca > 3 \cdot 10^{-3}$) Ratulowski and Chang (1989) correlated the bubble pressure in the following way:

$$\Delta p_B = \left(a_1 \cdot Ca^{n_1} - a_2 \cdot Ca^{n_2}\right)\left(\frac{\gamma}{r}\right) \qquad (3.2\text{-}7).$$

Values of the factors and the exponents are given in table 3.2 for circular and square channels.

cross-section	a_1	n_1	a_2	n_2	*range of validity*
circular	9.4	2/3	12.6	0.95	$10^{-2} \leq Ca < 0.1$
square	12.2	0.55	-	-	$Ca < 0.04$
	3.14	0.16	-	-	$Ca > 0.04$

Table 3.2: Values of the factors (a_1, a_2) and the exponents (n_1, n_2) in equation 3.2-7 found by Ratulowski and Chang (1989) for the pressure across an entire elongated bubble in Taylor flow through capillaries of varies cross-sectional shapes at $Ca > 3 \cdot 10^{-3}$.

Assuming a Capillary number of 0.04 it turns out that the bubble pressure in a channel of square cross-section is 4 times that in a circular channel. This is the contrary tendency to what was reported for $Ca < 3 \cdot 10^{-3}$ (see table 3.1).

In general it can be stated that with increasing bubble length at constant slug length the number of bubbles within the channel diminishes leading to a decrease of the two-phase pressure drop.

Kreutzer et al. (2005a, 2005b) studied the pressure drop of Taylor flow in a circular capillary by means of numerical simulations as well as experimental measurements. They argued that for infinitely long slugs, the pressure drop would be equal to the frictional pressure drop computed by the Hagen-Poiseuille equation for single phase liquid flow. Based on this assumption it was proposed that the contribution of the bubbles may be modeled as a part of the total frictional pressure drop Δp_f across the channel. Assuming an equal number of slugs and bubbles along the channel, equation 3.2-2 may be rewritten as:

$$\Delta p_{tot} = \Delta p_f = n_S \Delta p_{fS} \left(1 + \frac{\Delta p_B}{\Delta p_{fS}} \right) \qquad (3.2\text{-}8).$$

The frictional pressure drop across the slugs may alternatively be expressed as:

$$n_S \Delta p_{fS} = \frac{16}{\mathrm{Re}_{L,TP}} \left(\frac{1}{2} \rho_L U_{TP}^2 \right) \left(\frac{4}{d} \right) n_S l_S \qquad (3.2\text{-}9).$$

Combination of 3.2-8 and 3.2-9 yields:

$$\Delta p_f = n_S \frac{16}{\mathrm{Re}_{L,TP}} \left(1 + \frac{\Delta p_B}{\Delta p_{fS}} \right) \cdot \left(\frac{1}{2} \rho_L U_{TP}^2 \right) \left(\frac{4}{d} l_S \right) = n_S f \cdot \left(\frac{1}{2} \rho_L U_{TP}^2 \right) \left(\frac{4}{d} l_S \right) \qquad (3.2\text{-}10).$$

Thus the relative contribution of the bubble pressure is incorporated within the friction factor *f*. Using the dynamic liquid hold-up ε_L, which represents the fraction of the channel length occupied by the liquid slugs, the final expression proposed by Kreutzer et al. (2005a, 2005b) is obtained.

$$\Delta p_f = \varepsilon_L f \left(\frac{1}{2} \rho_L U_{TP}^2 \right) \left(\frac{4}{d} l_{Ch} \right) \quad (3.2\text{-}11), \text{ whereas } \varepsilon_L \text{ is approximated as: } \varepsilon_L \approx \frac{l_s}{(l_B + l_s)} \quad (3.2\text{-}12).$$

For the case of negligible inertia ($CaRe = We << 1$, $Re_{L,TP} < 10$), assuming $U_B \approx U_{TP}$, the friction factor was given as:

$$f = \frac{16}{\mathrm{Re}_{L,TP}} \left[1 + \frac{14.9 (Ca_{TP})^{\frac{2}{3}} \left(y/d \right)}{32 \left(\mu_L U_{TP}/d \right) \left(l_S/d \right)} \right] = \frac{16}{\mathrm{Re}_{L,TP}} \left[1 + \frac{0.465}{Ca_{TP}^{1/3} \left(l_S/d \right)} \right] \qquad (3.2\text{-}13).$$

At this the ratio of pressures was expressed by means of equations 3.2-3 and 3.1-18 (pressure across the bubble cap after Bretherton (1961)). Furthermore it can be seen that the friction factor becomes a function of the two-phase capillary number Ca_{TP}:

$$Ca_{TP} = \frac{\mu_L U_{TP}}{\gamma} \qquad (3.2\text{-}14).$$

Kreutzer et al. (2005a, 2005b) performed experimental measurements in a range of $0.002 \leq Ca_{TP} \leq 0.04$ and $150 \leq Re_{L,TP} \leq 1370$, using water and two different organic solvents as liquids. From a plot of $fRe_{L,TP}$ versus l_S/d the friction factor appeared to be rather dependent on liquid phase properties (γ, μ_L) than on velocity. In gas-liquid flow, this behavior can be accounted for by the ratio Ca/Re (see chapter 2, section 2.1). Hence the friction factor was correlated as follows:

$$f = \frac{16}{\mathrm{Re}_{L,TP}}\left[1 + a \cdot \left(\frac{Ca_{TP}}{\mathrm{Re}_{L,TP}}\right)^{n}\right] \qquad (3.2\text{-}15).$$

For $Ca_{TP} = O(10^{-1})$ and $Re_{L,TP} = O(10^{2})$ the fitting parameters a and n were found to be 0.17 and 0.33, respectively.

Another interesting investigation in this area was carried out by Fuerstman et al. (2007) in a rectangular microchannel with 35 µm in height and 100 µm in width. Similar to the approaches presented above the pressure drop was modeled in dependency of the hydrodynamic characteristics of the flow. In addition to pure water, aqueous surfactant solutions were also employed as liquids. Since, the presence of surfactants may induce a flow of the liquid around the bubble (see section 3.1), the frictional pressure drop along the bubble body was accounted for. The total two-phase pressure drop was modeled as follows:

$$\Delta p_{tot} = \frac{\mu_L \psi^{-1} U_B}{h^2}\left[k\left(l_{Ch} - n_B l_B\right) + a n_B Ca_{TP}^{-1/3} h + b n_B l_{BB}\right] \text{ with } l_{Ch} - n_B l_B = n_S l_S \text{ and } \psi^{-1} U_B = U_{TP} \quad (3.2\text{-}16).$$

Here, ψ labels a coefficient obtained from the slope of the plot of U_B versus U_{TP} and thus represents the dimensionless bubble velocity (U_B/U_{TP}). The parameter l_{BB} is the length of the bubble body. The first and the second terms within the brackets are referred to the frictional pressure drop over the liquid slugs and the pressure across the bubble caps according to equations 3.2-3 and 3.2-6, respectively. The value of the coefficient k can be estimated by means of equation 3.2-4 and was about 15 for the geometry used here. The third term is due to the frictional pressure drop of the liquid around the bubble body, which arises if the liquid is flowing through the channel corners of the rectangular cross-section. The factors a and b are fitting parameters, whereas b includes the friction factor as well as the ratio of the characteristic length of the channel corners to the height of the channel. The reason for the way how the superficial two-phase velocity and the total slug length were expressed in equation 3.2-16 is due to the method employed to measure the pressure drop (see figure 3.4). At this the main channel was split into two branches. Since they were of identical dimensions the pressure drop across both branches must also be the same. Hence, the method initially consisted in measuring U_B, n_B, l_B, l_{BB} in each branch and their insertion into equation 3.2-16. In the following the fitting parameters a and b were derived by setting $\Delta p_{tot,1} = \Delta p_{tot,2}$.

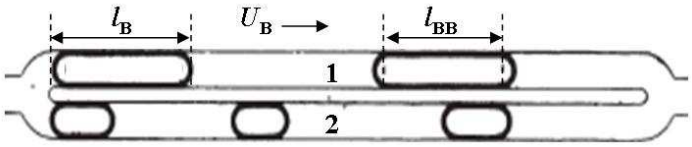

Figure 3.4: Schematic illustration of the device and the method employed by Fuerstman et al. (2007) to measure the two-phase pressure drop in Taylor flow through a rectangular microchannel of 35 µm in height and 100 µm in width using the model given in equation 3.2-16 (l_B bubble length; U_B bubble velocity; l_{BB} length of the bubble body; the pressure drops across both branches are considered to be equal, $\Delta p_{tot,1} = \Delta p_{tot,2}$).

A selection of the results obtained by Fuerstman et al. (2007) in a range of $Ca = O(10^{-3})$ is shown in table 3.3.

liquid-phase	$U_B/U_{TP} = \psi$	***k*** *(liquid slugs)*	***a*** *(bubble caps)*	***b*** *(bubble body)*
pure water	≈ 1	15	12	1.3
aqueous surfactant solutions:				
0.01 ≤ CMC < 100	not reported	15	< 10	> 1.3
100 CMC	≈ 0.48	15	0	96
1000 CMC	≈ 0.8	15	35	48

Table 3.3: Values of the dimensionless bubble velocity ψ and the fitting parameters *a* and *b* found by Fuerstman et al. (2007) from measurements of the two-phase pressure drop in Taylor flow through a rectangular microchannel of 35 µm in height and 100 µm in width in a range of Ca = $O(10^{-3})$ using the model given in equation 3.2-16 (U_B bubble velocity; U_{TP} superficial two-phase velocity; the coefficient *k* is obtained from equation 3.2-4; Tween-20 was used as surfactant; CMC critical micelle concentration).

In table 3.3 it can be seen that for pure water as liquid phase the contribution of the bubble body is of negligible value compared to the friction of the liquid slugs and the pressure across the bubble caps. This result is in good agreement to the considerations made above (see also section 3.1) since the liquid around the bubble should be static in this case and thus the pressure drop independent of the bubble length. With increasing surfactant concentration Fuerstman et al. (2007) showed that the contribution of the bubble caps decreases and that of the bubble body increases. This behavior confirms the assumption that the presence of surfactants may cause the liquid around the bubble to flow (see section 3.1). For surfactant concentrations around 1 CMC (critical micelle concentration) it was observed that the liquid film dewets, causing the bubbles to slow down or even to stop completely. This situation corresponds to wedging flow previously reported by Cubaud and Ho (2004). The decrease of the bubble velocity is caused by the adhesion of the bubble at the gas-liquid-solid contact line which induces a higher resistance to flow (Blackmore et al., 2001) and favors the liquid to bypass the bubble through the corners of the rectangular channel cross-section. The average velocity of the liquid U_{TP} would then be greater than U_B, leading to dimensionless bubble velocities ψ smaller than 1. For larger surfactant concentrations (100 times CMC) Fuerstman et al. (2007) reported that this dewetting phenomenon disappeared and that the bubbles were fully lubricated again. However, a look at the values of ψ in table 3.3 suggests that partial dewetting still existed. The value assigned to the contribution of the bubble body (*b*) given at 100 CMC thus demonstrates that the dewetting causes a remarkable increase of the pressure drop (by a factor of about 8) compared to that of fully lubricated bubbles. This confirms the findings of Cubaud and Ho (2004), who observed a strong decline of the pressure drop at the transition from wedging flow to slug flow (Taylor flow with fully lubricated bubbles). Furthermore, the considerations mentioned above are underlined by the results obtained for 1000 CMC. Here the dimensionless bubble velocity ψ is closer to unity, hence the extent of corner flow and with that of dewetting is less pronounced and consequently the contribution of the bubble body to the total pressure drop is smaller than for 100 CMC.
Finally the investigation conducted by Fuerstman et al. (2007) well illustrates the dependency of the two-phase pressure drop on the behavior of the liquid film region and gives an indication of the phenomena playing an important role in this context.

3.3 Characteristics of the liquid phase velocity field

A particular feature of Taylor flow is the recirculation motion created within the liquid slugs. Its formation is due to the fact that the bubble velocity U_B is greater than the average liquid velocity U_{TP} but smaller than the maximum liquid velocity at the centre axis. This results in a stagnation of the liquid phase in front of and behind the bubble causing a reverse flow and the creation of a recirculation motion over the whole length of the liquid slug. This behaviour, firstly predicted by Taylor (1961),

was confirmed later by numerous studies, using particle tracking techniques as well as particle image velocimetry (PIV; Thulasidas et al, 1997; Günther et al, 2004; Günther et al., 2005; Waelchli and von Rohr, 2006). However, most of these investigations published instantaneous images of the velocity field obtained for a certain Capillary number. A closer insight into the evolution of the liquid phase velocity is given by a numerical study of Taha and Cui (2004; see figure 3.5). From the latter it can be seen that with increasing bubble velocity (and therefore increasing *Ca*) the ring shaped vortex moves towards the centre axis of the channel leading to a reduction of the propagation of the recirculation motion within the slug and more liquid to flow into the film. This process takes place until the bubble velocity equals the maximum liquid velocity at the channel centre axis, which is $U_B = 2U_{TP}$ in a channel of circular cross section. At this point the vortices disappear and all of the liquid flows towards the bubble. The liquid velocity field is then referred to as complete bypass flow.

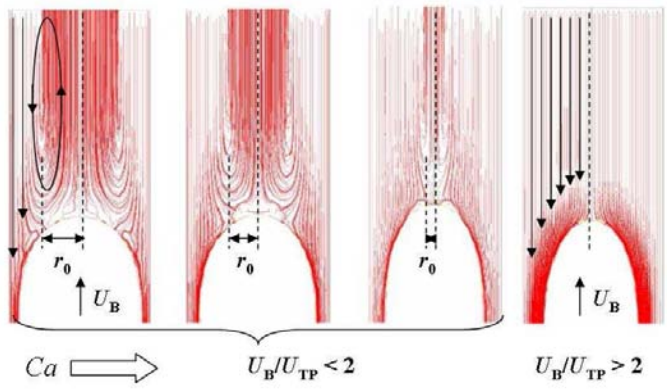

Figure 3.5: Example images of Taylor flow from a numerical study of Taha and Cui (2004) showing the evolution of the liquid phase velocity field inside of a liquid slug with increasing Capillary number (r_0 radial position of the centre of the recirculation vortex relative to the channel centre axis; U_B bubble velocity; U_{TP} superficial two-phase velocity/average liquid velocity).

The streamline patterns shown in figure 3.5 were experimentally validated by Kolb and Cerro (1991) and Thulasidas et al. (1997). From figure 3.5 it can be seen, that the shift of the centre of the vortex towards the channel centre-line remarkably reduces the volume of recirculation flow. Since the particular feature of the recirculation motion is one of the main arguments for operating chemical reactions in Taylor flow, it is of interest to depict its evolution in a quantitative manner. In this context we will also provide an explanation for the transition criterion between recirculation and bypass flow. An attempt in this direction was made by Thulasidas et al. (1997). Here it was initially supposed that the liquid slug is sufficiently long to develop a parabolic Poiseuille profile. For a channel of circular cross-section with the radius *R* this may basically be written as a function of the radial position *r*:

$$U(r) = U_{max}\left[1-\left(\frac{r}{R}\right)^2\right] \qquad (3.3\text{-}1).$$

In Taylor flow through a circular channel the maximum velocity U_{max} within the slug corresponds to two times the average velocity U_{TP}. Additionally, in order to obtain the relative velocity profile, reflecting the recirculation motion, it is necessary to subtract the bubble velocity from the parabolic profile. As a result equation 3.3-1 transforms in:

$$U_{rc}(r) = 2U_{TP}\left[1-\left(\frac{r}{R}\right)^2\right] - U_B \qquad (3.3\text{-}2).$$

At this U_{rc} denotes the recirculation velocity. A schematic sketch of the recirculation velocity profile $U_{rc}(r)$ is given in figure 3.6 together with further parameters related to the recirculation flow within the liquid slug.

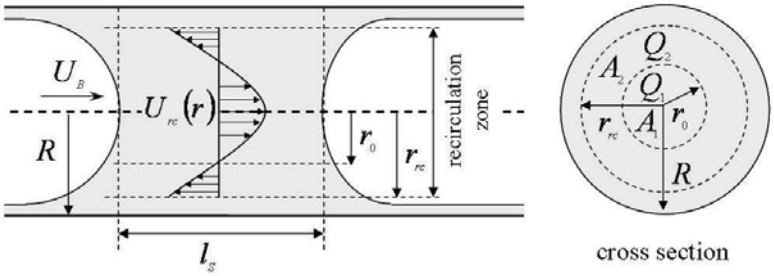

Figure 3.6: Schematic sketch of the recirculation velocity profile $U_{rc}(r)$ and further parameters related to the recirculation flow within a liquid slug in Taylor flow through a channel of circular cross section (R channel radius; r_0 radial position of the centre of the recirculation vortex relative to the channel centre axis; r_{rc} radius of the entire recirculation zone, U_B bubble velocity; l_S liquid slug length; A_1 and Q_1 cross sectional area and volumetric liquid flow rate of the inner recirculation region; A_2 and Q_2 cross sectional area and volumetric liquid flow rate of the outer recirculation region).

In figure 3.6 it can initially be seen that the recirculation zone within the liquid slug is divided into two regions, an inner recirculation region confined by the radial position of the centre of the vortex r_0 and an outer region (reverse flow) confined by the radius of the entire recirculation zone r_{rc} and r_0. So that the recirculation zone can exist it is required that the pressure between both regions is equilibrated. With respect to the illustration made in figure 3.6 this means that the volumetric flow rate through the inner region Q_1 equals the flow rate through the outer region Q_2 and corresponds to the average volumetric flow rate of recirculation Q_{rc}. Considering that the average velocity in both regions is the same, it follows that the respective cross sectional areas A_1 and A_2 (see figure 3.6) equal each other. We thus may express the dimensionless radius of the entire recirculation zone as follows:

$$\frac{r_{rc}}{R} = \sqrt{2}\,\frac{r_0}{R} \qquad (3.3\text{-}3).$$

The radial position of the centre of the vortex r_0 can be determined from equation 3.3-2, assuming that at this point the recirculation velocity equals zero (Thulasidas et al., 1997).

$$\frac{r_0}{R} = \sqrt{\left(1-\frac{1}{2}\psi\right)} \qquad \text{with } \psi = \frac{U_B}{U_{TP}} \qquad (3.3\text{-}4).$$

In order to quantitatively represent the descriptions undertaken in connection with figure 3.5 the dimensionless position of the vortex centre as well as the dimensionless radius of the recirculation zone are plotted as a function of the dimensionless bubble velocity ψ (see figure 3.7).

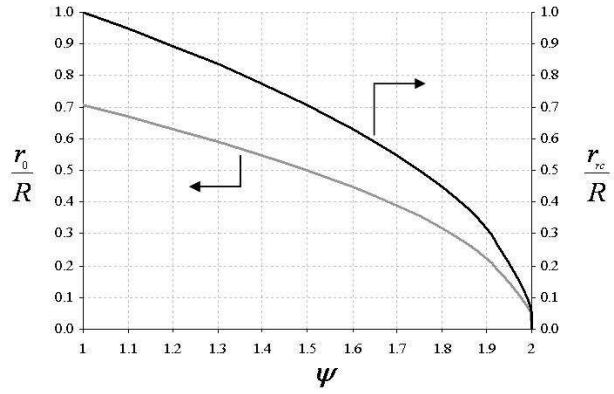

Figure 3.7: Plot of the dimensionless position of the vortex centre r_0/R and the dimensionless radius of the recirculation zone r_{rc}/R as a function of the dimensionless bubble velocity ψ according to equations 3.3-3 and 3.3-4 for a range of $1 \leq \psi \leq 2$.

From figure 3.7 it can be seen that at $\psi = 1$ the radial position of the vortex centre is at about $0.7R$, while the radius of the entire recirculation zone corresponds to the radius of the channel. This means that under these conditions the recirculation zone propagates across the whole channel cross section.

With increasing ψ both values shift towards the channel centre line and tend towards zero (coincide with the channel centre line) for $\psi \rightarrow 2$. In connection with the parameters plotted in figure 3.7 it would be interesting to depict the evolution of the corresponding fraction of liquid phase carried within the recirculation flow. We term this as the recirculation fraction ε_{rc} and it may be specified by dividing the volume of the recirculation zone V_{rc} by the volume of the liquid slug V_S (see expression 3.3-5a).

$$\varepsilon_{rc} = \frac{V_{rc}}{V_S} \qquad \text{with} \qquad V_{rc} = l_S \pi r_{rc}^2 \qquad \text{and} \qquad V_S = l_S \pi R^2 \tag{3.3-5a},$$

Taking into account equations 3.3-3 and 3.3-4, this may be rewritten as a function of the dimensionless bubble velocity (see expression 3.3-5b).

$$\varepsilon_{rc} = 2\left(\frac{r_0}{R}\right)^2 = 2 - \psi \tag{3.3-5b}$$

A second parameter of interest in this context is the average recirculation velocity. It may be obtained by integrating equation 3.3-2 over the cross-sectional area of the inner recirculation region. In dimensionless form this can be written as:

$$\frac{U_{rc}}{U_{TP}} = \frac{1}{r_0^2} \int_0^{r_0} \left[2 - 2\left(\frac{r}{R}\right)^2 - \psi \right] \cdot 2r \cdot dr \tag{3.3-6}.$$

The integration of 3.3-6 yields:

$$\frac{U_{rc}}{U_{TP}} = 2 - \left(\frac{r_0}{R}\right)^2 - \psi \tag{3.3-7}.$$

Insertion of 3.3-4 into 3.3-7 results in:

$$\frac{U_{rc}}{U_{TP}} = 1 - \frac{1}{2}\psi \tag{3.3-8}.$$

For illustrative purposes the evolution of the recirculation fraction and the dimensionless recirculation velocity are plotted versus the dimensionless bubble velocity in figure 3.8.

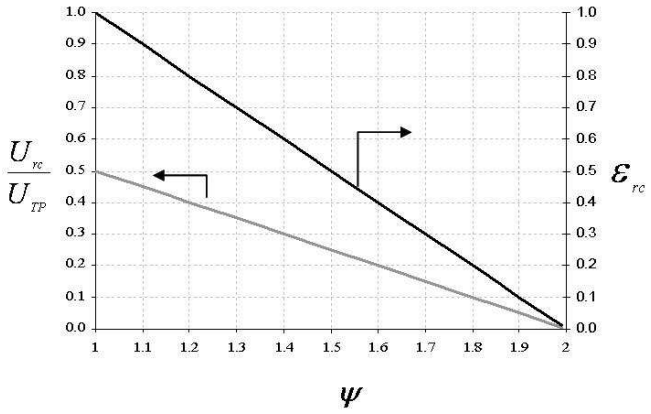

Figure 3.8: Plot of the dimensionless recirculation velocity U_{rc}/U_{TP} and the recirculation fraction ε_{rc} as a function of the dimensionless bubble velocity ψ according to equations 3.3-8 and 3.3-5 for a range of $1 \leq \psi \leq 2$.

In figure 3.8 it can be seen that the recirculation fraction and the average dimensionless recirculation velocity tends towards zero for $\psi \rightarrow 2$. It generally shows that with increasing dimensionless bubble velocity and with that with increasing Capillary number not only the volume but also the velocity of recirculation within the liquid slug decreases. As an example, at $\psi = 1.5$ only half of the liquid volume within the slug is recirculated ($\varepsilon_{rc} = 0.5$) at half of the velocity, compared to the conditions at $\psi = 1$. This suggests a reduction of the axial mass transfer within the liquid slugs, which lowers the possibility to exploit the recirculation flow as a beneficial feature for operating gas-liquid or gas-liquid-solid reaction systems in Taylor flow. Another important parameter characteristic for the

mixing and mass transfer within the liquid slug is the recirculation time t_{rc}. A first study to deal with this term was carried out by Thulasidas et al. (1997). At this the recirculation time was defined as the time the liquid travels in the axial direction from one end of the liquid slug to the other end and it was suggested that it may be approximated by dividing the liquid slug length by the average recirculation velocity. As an example concerning the impact of the recirculation time Thulasidas et al. (1997) discussed the results of several studies where an increase of radial heat and mass transfer with decreasing slug length was observed. Considering two slugs of different lengths at the same ψ, Thulasidas et al. (1997) explained these findings by the fact that the recirculation time in the shorter slug is smaller and the liquid phase thus comes more frequently in contact with the channel walls.
However, the definition of the recirculation time given by Thulasidas et al., 1997 does not consider the time the liquid travels though the outer region of the recirculation loop. We thus propose to define the recirculation time as the time required by the liquid to complete an entire recirculation loop in the slug. In this context the recirculation time may basically be written as the volume of the entire recirculation zone V_{rc} divided by the average volumetric flow rate of recirculation Q_{rc} as shown in equation 3.3-9.

$$t_{rc} = \frac{V_{rc}}{Q_{rc}} \qquad \text{with} \qquad V_{rc} = l_S \pi r_{rc}^{\,2} = 2 l_S \pi r_0^2 \tag{3.3-9}$$

Similar to the deduction of the average recirculation velocity, the average recirculation flow rate may be obtained by integrating the relative axial velocity profile (see equation 3.3-2) over the cross-sectional area of the inner recirculation region:

$$Q_{rc} = \int_0^{r_0} U_{rc}(r) \cdot 2\pi r \cdot dr \tag{3.3-10}$$

The integration of 3.3-10 yields:

$$Q_{rc} = \pi r_0^2 U_{TP} \left(1 - \frac{1}{2}\psi\right) \tag{3.3-11}$$

Insertion of 3.3-11 into 3.3-9 results in:

$$t_{rc} = \frac{2 l_S}{U_{TP}\left(1 - \frac{1}{2}\psi\right)} \tag{3.3-12}$$

In order to display its evolution as a function of ψ one need to define the dimensionless recirculation time. According to Thulasidas et al., 1997 the dimensionless recirculation time τ_{rc} corresponds to the reciprocal value of the dimensionless recirculation velocity. However, with respect to equation 3.3-12 and the example mentioned above, we decided that it would be rather appropriate to include a dimensionless slug length as well. We propose that the dimensionless recirculation time may be written as:

$$\tau_{rc} = \frac{2\left(\frac{l_S}{l_S + l_B}\right)}{\left(1 - \frac{1}{2}\psi\right)} \tag{3.3-13}$$

Physically, this means that the dimensionless recirculation time is the ratio of the recirculation time to the residence time of a liquid slug in a unit cell, which is composed of one bubble and one slug. Assuming equal bubble an slug lengths, a dimensionless slug length of $l_S/(l_S+l_B) = 0.5$, the tendency of the dimensionless recirculation time is now plotted in figure 3.9. Since after equation 3.3-13 τ_{rc} is inversely proportional to the dimensionless recirculation velocity it increases with increasing ψ and tends towards infinity close to the transition from recirculation to bypass flow ($\psi = 2$). From figure 3.9 it can be seen that this dependency appears as a curve and not in a linear manner as shown in figure 3.8 for U_{rc}/U_{TP} and ε_{rc}. Starting at a minimum of $\tau_{rc} = 2$ at $\psi = 1$, the value of the dimensionless

recirculation time doubles at ψ = 1.5 (τ_{rc} = 4). Afterwards the curve starts to rise more steeply attaining, for example, τ_{rc} = 20 at ψ = 1.9, which is 5 times the value at ψ = 1.5. Thus, the graph sketched in figure 3.9 well emphasizes the drastic reduction of the liquid recirculation with increasing bubble velocity.

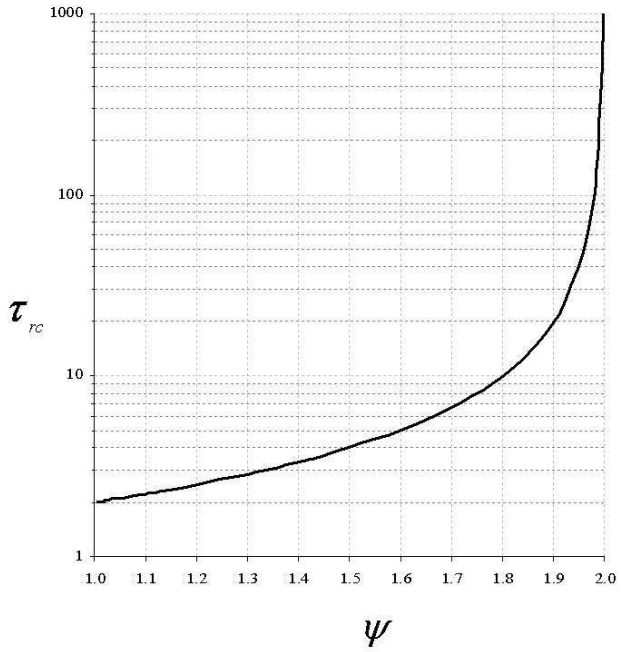

Figure 3.9: Plot of the dimensionless recirculation time τ_{rc} as a function of the dimensionless bubble velocity ψ according to equation 3.3-13 assuming a dimensionless slug length of 0.5.

At this point it has to be noted that the considerations mentioned above are valid if the velocity field is axial-symmetrical with respect to the channel centre axis. That this is not always the case was firstly demonstrated by Günther et al. (2004, 2005). Their studies were aimed on the exploitation of the recirculation within the liquid slugs for the micromixing of miscible liquids regarding mixing sensitive applications like the synthesis of nanoparticles. In order to provide sufficient residence time for such systems bearing in mind that the device remains its compactness, the reaction channel was arranged in a meandering manner with smoothed U-return bends (turning angle 180°). From microPIV measurements undertaken in the channel bends it turned out that the velocity field within the slug is noticeably distorted. This is shown in figure 3.10 in comparison to the streamline patterns obtained in a straight segment of the same channel.

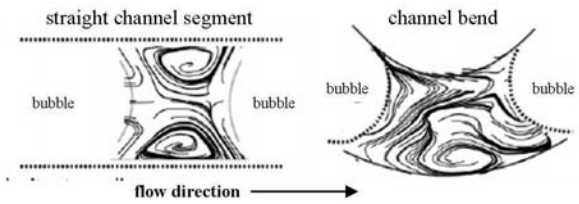

Figure 3.10: Streamline patterns of the velocity field within the liquid slug in Taylor flow through rectangular microchannels (d_h = 220 µm and 340 µm) with smoothed U-return bends (turning angle 180 °) measured by Günther et al. (2004, 2005) using microparticle image velocimetry (microPIV).

In figure 3.10 it can be seen that by passing the channel bend the velocity field within the liquid slug looses its symmetry with respect the channel centre line. It needs to be pointed out here, that the symmetry of the velocity field constitutes itself a limitation to mass transfer. The recirculation motion increases the axial mass transfer (along the streamlines) within the liquid slug but radial mass transfer can only take place by diffusion between the streamlines. In this context the distortion of the velocity field is considered to bring a convective contribution in radial transport and thus to increase the mixing within the liquid slug. This feature was closer regarded later by Fries et al. (2007). In this investigation it was shown that the mixing within the liquid slug may further be enhanced by small radii of

curvature, high turning angles (≥ 180°) and increased phase velocities. An improved mixing with decreasing curvature radius of the channel bend agrees with the observations made for increasing Dean numbers in single phase flows (Jiang et al., 2004).
In general this section demonstrates how hydrodynamic parameters and channel design influence the mixing and thus the axial and radial mass transfer inside of the liquid slug. It would now be interesting to go one step further and to have a look on the gas-liquid mass transfer.

3.4 Gas-liquid mass transfer in Taylor flow

One argument for choosing Taylor flow as operating condition is that the recirculation motion within the liquid slug is assumed to enhance the mass transfer between the gas and the liquid phase. As shown in section 3.3 the mixing process within the liquid slug is governed by the dimensionless bubble velocity and the slug length. It may thus be considered that the gas-liquid mass transfer also depends on these parameters. A first indication in this direction was given by Bercic and Pintar (1997), who studied the absorption of methane in water for Taylor flow through small tubes. The correlation deduced from their experimental results showed that the liquid-side volumetric mass transfer coefficient ($k_L a$-value) was inversely proportional to the liquid slug length. The idea of correlating the $k_L a$-value to the hydrodynamic characteristics of the flow was later readopted in the model developed by van Baten and Krishna (2004) and Vandu et al. (2005). Their approach distinguishes two contributions to the mass-transfer from Taylor bubbles: (i) from the bubble caps to the liquid slugs, and (ii) form the bubble body to the surrounding liquid film (see figure 3.11). Accordingly, the volumetric mass transfer coefficient was stated as:

$$k_L a = k_{L,cap} a_{cap} + k_{L,film} a_{film} \qquad (3.4\text{-}1).$$

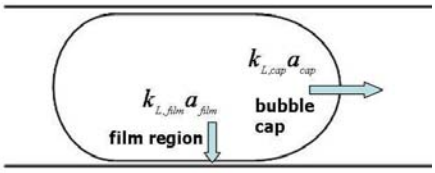

Figure 3.11: Principle illustration of contributions to gas-liquid mass transfer in Taylor flow after the model of van Baten and Krishna (2004) and Vandu et al. (2005).

Assuming that the caps are of hemispherical shape and that the bubble diameter equals approximately those of the channel, a_{cap}, given through the surface of the bubble caps divided by the volume of the unit-cell, was estimated as:

$$a_{cap} = \frac{4}{(l_s + l_B)} \qquad (3.4\text{-}2).$$

The specific interfacial area in the film region a_{film}, was modeled as the lateral shell of the cylindrical bubble body divided by the unit-cell volume. Supposing that the length of the bubble body is approximately equal to the bubble length it was obtained that:

$$a_{film} = \frac{4\varepsilon_G}{d} \qquad (3.4\text{-}3),$$

where ε_G is the gas-hold up, approximated as:

$$\varepsilon_G \approx \frac{l_B}{(l_B + l_S)} \qquad (3.4\text{-}4).$$

The liquid-side mass-transfer coefficient is formulated according to the Higbie penetration theory (Higbie, 1935).

$$k_L = 2\sqrt{\frac{D}{\pi t}} \qquad (3.4\text{-}5).$$

Here, D is the diffusivity of the gas in the liquid and t describes the surface renewal time. As an approach, the latter one can be considered as the contact time between gas and liquid phase. For the liquid which passes by the perimeter of the bubble caps it was suggested that:

$$t_{cap} = \frac{\pi d}{2U_B} \tag{3.4-6}.$$

The contact time within the film region can be estimated by dividing the bubble length by the bubble velocity. Involving the gas hold-up according to equation 3.4-4, it was presented as:

$$t_{film} = \varepsilon_G \frac{\left(l_s + l_B\right)}{U_B} \tag{3.4-7}.$$

Combining the above equations gives the volumetric liquid-side mass transfer coefficient as follows:

$$k_L a = 8\sqrt{DU_B}\left[\sqrt{\frac{2}{\pi^2 d\left(l_S + l_B\right)^2}} + \sqrt{\frac{\varepsilon_G}{\pi d^2\left(l_s + l_B\right)}}\right] \tag{3.4-8},$$

where the first and second terms within the brackets are the contributions to the mass transfer coefficient by the bubble caps and the liquid film, respectively.

From equation 3.4-8 it can generally be seen that the gas-liquid mass transfer is inversely proportional to the diameter of the channel. Furthermore, it turns out that the $k_L a$-value increases with increasing bubble velocity, since it is directly linked to a decrease of the gas-liquid contact time. It should be noted that considering the way the contact times were modeled, the volumetric mass transfer coefficient given above refers to the unit-cell (a section which contains one bubble and one slug) only. Furthermore, instead of using the bubble velocity for scaling the cap contact time, the average recirculation velocity of the liquid within the slugs may be applied. According to section 3.3 it can be obtained by integration of the relative liquid velocity profile in the slugs, with respect to the radial position of the vortex centre (see expressions 3.3-6 to 3.3-8). The cap contact time would then show the inverted tendency, since the average recirculation velocity decreases with increasing bubble velocity.

Van Baten and Krishna (2004) found that the major contribution to the mass transfer process comes from the liquid film region, which was shown later to well agree with experimental results gained from mass transfer measurements using the absorption of oxygen into water at film contact times smaller than 0.1 s (Vandu et al., 2005; $1 \cdot 10^{-3} < Ca < 9 \cdot 10^{-3}$). As it is indicated, the condition for the dominance of the mass transfer within the film region may only be assumed for a certain range of film contact times. Considering the case of the physical absorption of a gas into the film a gas-liquid mass transfer occurs as long as the contact time remains small enough to prevent the absorbed gaseous component to diffuse across the entire thickness of the liquid layer. A further increase of the film contact time will lead to the saturation of the liquid film whereby the whole film region and with it the interfacial area along the bubble body become ineffective in the mass transfer process. The effectiveness of interfacial area was examined closely by Pohorecki (2007). Based on a theoretical analysis of gas absorption with and without chemical reaction Pohorecki (2007) proposed the following criterion for the preservation of the surface area activity:

$$\frac{l_B}{U_B} << \frac{\delta^2}{D} \tag{3.4-9}.$$

For the case of gas absorption with instantaneous reaction D is the diffusivity of the liquid reactant within the liquid film and the right hand side of expression 3.4-9 corresponds to the minimum time necessary for its total consumption, denoted by Pohorecki (2007) as exhaustion time. For the physical absorption case D represents the diffusivity of the gaseous component within the liquid phase, whereby the term on the right hand side of 3.4-9 may be considered as the saturation time. Thus 3.4-9 suggests that in order to exploit the interfacial area within the film region for the gas-liquid mass

transfer the film contact time should be much smaller than the saturation time or the exhaustion time. On the other hand for a gas-liquid-solid reaction Pohorecki (2007) stated that the saturation of the liquid film would be privileged and the reverse case of the criterion mentioned above should be applied. For estimating the order of magnitude of this contact time one may initially assume that the diffusion coefficient D is in the order of 10^{-9} m^2/s ($D \sim O(10^{-9})$ m^2/s). According to the explanations given in section 3.1 the dimensionless liquid film thickness δ/r depends on the value of the bubble velocity since it is directly proportional to $Ca^{2/3}$. This correlation was proven by Bretherton (1961) for capillary numbers in a range of $Ca \leq O(10^{-3})$. Hence, considering $Ca \sim O(10^{-3})$ and a channel radius of $r \sim O(10^{-4})$ m, a film thickness of $\delta \sim O(10^{-6})$ m is obtained. Insertion in the right hand side of expression 3.4-9 then yields a film contact time in the order of 10^{-3} s. For Capillary numbers of higher order of magnitude one may generally assume that the film thickness increases and therefore the corresponding film contact time limit shifts to higher values.

In consideration of the literature analysis given above, it appears that with the knowledge of the hydrodynamic parameters that characterize the Taylor flow pattern (e.g. bubble velocities, film thickness, bubble lengths and slug lengths), the prediction of the two-phase pressure drop and mass transfer should be possible. In this context, especially, the dimensionless bubble velocity was shown to be a key parameter serving as an indication of the behavior of the liquid phase velocity field. Consequently, one needs to have an idea about the prediction of these hydrodynamic properties. This will be the aim within the following sections.

3.5 Prediction/Estimation of hydrodynamic parameters

3.5.1 Bubble velocities and related phenomena

The procedure applied in the literature for the development of correlations predicting the velocity of bubbles is generally as follows. For a given set of flow rates the bubble velocity is measured and is then plotted versus the superficial two phase velocity U_{TP} (schematically illustrated in figure 3.11). This plot usually shows a linear correlation whose slope serves as a correlation factor. This coefficient represents the dimensionless bubble velocity which was derived in section 3.1 as:

$$\psi = \frac{U_B}{U_{TP}} = 1 - \frac{\varepsilon_F}{U_{TP}}\left(U_F - U_B\right) \qquad \text{(3.1-10c).}$$

According to section 3.1, the dimensionless velocity of a fully lubricated bubble is approximately equal or greater than one ($U_F = 0$ or $U_F < U_B$). Within this region it was demonstrated in section 3.3 that with increasing dimensionless bubble velocity the recirculation motion diminishes until the vortex completely disappear. This transition from recirculation to bypass flow was shown to occur in a circular channel at $U_B/U_{TP} = 2$. In sections 2.2.2 (see chapter 2) and 3.2 it was shown that in the case of a non-circular channel cross-section the liquid film can dewet. Based on the discussion carried out in section 3.2 it may be assumed that in this case the liquid phase bypasses the bubble through the channel corners. As an approximation we may assume the velocity of the liquid around the bubble as $U_F > U_B$. With equation 3.1.-10c it can be seen that in this case the dimensionless bubble velocity should be smaller than one. We can thus distinguish three sub-flow characteristics of the Taylor flow pattern, which may be denoted as corner-flow, recirculation flow and bypass-flow (see figure 3.12).

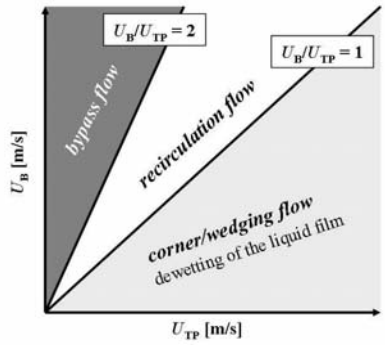

Figure 3.12: Schematic illustration of a plot of bubble velocities U_B versus superficial two-phase velocities U_{TP} with indications explaining the meaning of the value of the dimensionless bubble velocity U_B/U_{TP} with respect to a certain sub-flow characteristic of Taylor flow.

With respect to the operation of chemical reactions in Taylor flow, the region of interest is the recirculation flow area. In the surfactant free case (see section 3.1) the liquid film may be considered as static ($U_F = 0$) and equation 3.1-10c may be rewritten as:

$$\frac{U_B}{U_{TP}} = \frac{1}{(1-\varepsilon_F)} \qquad (3.5\text{-}1).$$

Thus the dimensionless bubble velocity is determined by the fraction of the liquid surrounding the bubble. Its value depends on the thickness of the liquid film which is, however, a function of the Capillary number and with that of the bubble velocity itself (see section 3.1). In order to deal with the prediction of bubble velocities in this manner it would be necessary to have an idea about the range of superficial phase velocities. This may be obtained from the Weber number based flow transition criteria developed by Akbar et al. (2003; see chapter 2, section 2.2.1, figure 2.6) for the range of the Taylor flow pattern. Since the range of interest is bounded by $1 \leq U_B/U_{TP} < 2$, the superficial phase velocities may be used to calculate two phase Capillary numbers, which themselves can serve to represent the order of magnitude of the *Ca* and this finally allows to trace the trend of the dimensionless bubble velocity between the respective orders of magnitudes of Capillary numbers. Thus it is not possible to predict the bubble velocity alone, but to associate the dimensionless bubble velocity and the Capillary number.

Before starting with this topic it may be useful to complement this section by specifying the gas hold-up ε_G and the liquid hold-up ε_L, since these parameters are linked to pressure drop and mass transfer (see sections 3.2 and 3.4). After Wallis (1969) they are given as:

$$\varepsilon_G = \frac{U_{GS}}{U_B} \qquad (3.5\text{-}2) \text{ and} \qquad \varepsilon_L = (1-\varepsilon_G) \qquad (3.5\text{-}3).$$

Combining equations 3.5.1 and 3.5-2 results in: $$\varepsilon_G = (1-\varepsilon_F)\frac{U_{GS}}{U_{TP}} \qquad (3.5\text{-}4).$$

In the flowing it will be shown how the film hold-up ε_F can be estimated for a certain shape of the channel cross-section and a given flow condition, and which result is entrained concerning the dimensionless bubble velocity. Afterwards the phenomena of bubble velocity fluctuations and the dewetting of the liquid film will be treated. Especially, the depiction and the prediction of the drying out of the liquid film is of great importance since it leads to a strong increase of pressure drop and the area of the liquid film is lost for gas-liquid mass transfer.

3.5.1.1 Circular channel cross-section

A bubble moving through a microchannel or a small channel of circular cross-section is of axisymmetrical shape and is surrounded by a liquid film of constant thickness δ, which is related to the film fraction in the following manner:

$$\varepsilon_F = \frac{4\delta}{d}\left(1-\frac{\delta}{d}\right) \qquad (3.5\text{-}5).$$

At this the ratio of δ/d is the dimensionless film thickness. A first study reported in this area was undertaken by Fairbrother and Stubbs (1935) in a range of $7.5\cdot10^{-5} < Ca < 0.014$. They found that the liquid film fraction is a function of the Capillary number. Experiments conducted by Taylor (1961) within a large range of Capillary numbers ($2\cdot10^{-3} < Ca < 2$) confirmed this behavior and showed that the liquid film fraction increases with increasing Ca until it tends towards an asymptotic limit of 0.56 within $1 < Ca \leq 2$. Bretherton (1961) performed a detailed theoretical analysis of the film deposition and proposed that the dimensionless film thickness is directly proportional to $Ca^{2/3}$ (see section 3.1). Aussilous and Quéré (2000) readopted Bretherton's approach and modified it with respect to higher Capillary numbers, where the thickness of the film may be considered as no longer negligible in comparison with the bubble radius. In this way a general scaling law was derived, which writes as follows:

$$\frac{\delta}{r} \approx \frac{Ca^{2/3}}{1+Ca^{2/3}} \qquad (3.5\text{-}6a).$$

For large Capillary numbers expression 3.5-6a suggests a convergence of the film thickness, which is in general conformity with the tendency observed by Taylor (1961). On the basis of this general scaling and the results of their experimental measurements conducted in a range of $10^{-4} < Ca < 1.3$, Aussilous and Quéré (2000) developed an empirical correlation, which revealed an excellent agreement with the data of the three studies mentioned above. This correlation was presented as follows:

$$\frac{\delta}{d} = \frac{2Ca^{2/3}}{3+10Ca^{2/3}} \qquad (3.5\text{-}6b).$$

However, Aussilous and Quéré (2000) found that in the case of low viscosity liquids ($\mu_L \leq 1$ mPa·s) at $Ca > 10^{-2}$, the measured film thickness is noticeably greater than it is predicted by expression 3.5-6b and that with increasing channel diameter this behavior is shifted to lower Capillary numbers. Note, that liquids with such viscosities include most organic solvents. Aussilous and Quéré (2000) explained this behavior as an effect of inertia and indeed regarding their experiments undertaken with ethanol, one may deduce a divergence of the film thickness from 3.5-6b to occur at bubble Weber numbers (We_{LB}; computed by means of ρ_L, d_h and U_B) in the order of 10^0. Nevertheless, equations 3.5-5, 3.5-6b and 3.5-1 are used in the following in order to compute the evolution of the dimensionless film thickness, the liquid film fraction and finally the dimensionless bubble velocity for Capillary numbers with orders of magnitude between 10^{-4} and 10^0. These results are summarized in table 3.4, and figure 3.13.

Ca	10^{-4}	10^{-3}	10^{-2}	10^{-1}	10^0
δ/d	$1.4\cdot10^{-3}$	$6.4\cdot10^{-3}$	$2.7\cdot10^{-2}$	$8.3\cdot10^{-2}$	$1.5\cdot10^{-1}$
ε_F	0,006	0.025	0.103	0.304	0.517
U_B/U_{TP}	1.01	1.03	1.12	1.44	2.07

Table 3.4: Comparison of the dimensionless film thickness δ/d, the liquid film fraction ε_F and the dimensionless bubble velocity U_B/U_{TP} in microchannels of circular cross-section, computed for Capillary numbers of several orders of magnitude from equations 3.5-5, 3.5-6b and 3.5-1, respectively.

Figure 3.13a shows the trend of the dimensionless film thickness and the film hold-up ε_F as a function of the Capillary number. The reason why the curve progression of the film hold-up appears to be different from that of the film thickness is due to the fact that ε_F is not applied on a logarithmic scale. Table 3.4 and figure 3.13 reveal that for $Ca < 10^{-2}$, the film is of negligible thickness compared with

the channel diameter (film covers less than 10% of the channel cross-section) and hence the bubble velocity may be considered as to be approximately equal to superficial two-phase velocity. Concerning the explanations undertaken in section 3.3, one may thus conclude that in this range of Capillary numbers almost the entire liquid volume within the slug is recirculated ($\varepsilon_{rc} \approx$ 90 % - 100 %, see figure 3.8, section 3.3). Afterwards, the film hold-up and the dimensionless bubble velocity strongly increase. For example in the range of $10^{-2} \leq Ca \leq 10^{-1}$ the liquid film hold-up increases from about 10 % to 30 %. In figure 3.13b it is shown that a dimensionless bubble velocity of 1.5 is reached at a Capillary number between 0.1 and 0.2. This is the point where only half of the liquid volume within the slug is transported by the recirculation motion ($\varepsilon_{rc} \approx$ 50 %) at twice the recirculation time t_{rc} (see figure 3.9, section 3.3) compared to the range of $Ca < 10^{-2}$. Furthermore, it can be seen that the transition from recirculation to bypass flow (U_B/U_{TP} = 2, ε_F = 0.5) occurs at a Capillary number between 0.7 and 0.8. Since this transition constitutes the disappearance of a beneficial feature of Taylor we generally limit our considerations to low and intermediate Capillary numbers (Ca ≤ 1).

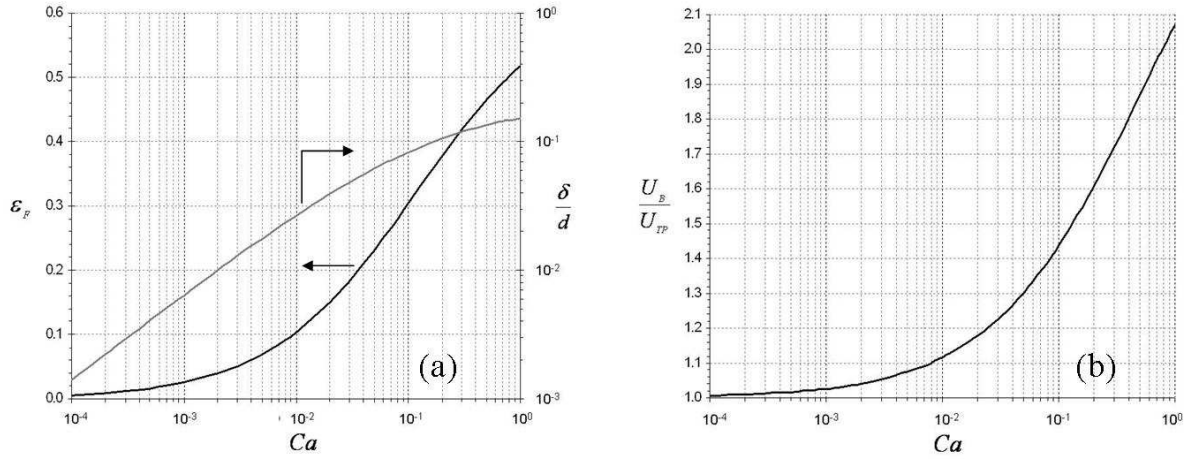

Figure 3.13: Evolution of the dimensionless film thickness δ/d, the liquid film hold-up ε_F (a) and the dimensionless bubble velocity U_B/U_{TP} (b) as a function of the Capillary number *Ca* in microchannels of circular cross-section.

3.5.1.2 Square channel cross-section

In contrast to circular channels, the profile of a bubble moving through a microchannel or a small tube of square cross-section can either take an axisymmetrical or a non-axisymmetrical shape (see figure 3.14). Wong et al. (1995a, 1995b) theoretically studied the motion of long bubbles in polygonal capillaries and showed that at $Ca < 10^{-3}$ the liquid phase is mainly accumulated in the corner regions of the channel cross-section. At this, the shape of gas-liquid interface is characterized by a curvature of constant radius, which intersects the channel walls trapping a liquid film of non-uniform thickness at sides (see figure 3.14b). The liquid film at the side walls scales with $Ca^{2/3}$ and the interfacial curvature in the channel corners differs from that of a static bubble (see figure 3.14a) by $O(Ca^{2/3})$. Since in the limit of $Ca < 10^{-3}$ this difference in curvature, as well as the thickness of the film at the sides, can be assumed as negligible (compare values in table 3.4), it was proposed by Wong et al. (1995a, 1995b) that the bubble profile may be represented by its static shape (see figure 3.14a). Kolb and Cerro (1991) performed experiments for upward, downward and horizontal Taylor flow in a square capillary ($Bo \sim 1.8$). They measured the diameters of bubbles in the side plane as well as in the diagonal plane (see figure 3.14c) for a range of $O(10^{-3}) \leq Ca < 10$. At low capillary numbers the bubble was found to be non-axisymmetrical in shape. The profile derived from their measurements exhibited a flat liquid film of constant thickness in the side plane and a constant interfacial curvature in the corners of the

channel cross-section. With increasing *Ca* the dimensionless bubble diameter in the side plane (d_{sp}/d_h) remained constant at about 0.95, while the gas-liquid interface in the diagonal plane moved towards the centre axis of the channel. At *Ca* ~ 0.1 the diameter in both planes match each other, indicating the transition to an axisymmetrical bubble profile (see figure 3.14d). However, in an earlier numerical study carried out by Ratulowski and Chang (1989) for *Bo* ~ $2 \cdot 10^{-3}$, it was proposed that the transition from a non-axisymmetrical to an axisymmetrical bubble profile takes place at Ca ~ 0.04. This value was confirmed experimentally (*Bo* ~ 1.7) by Thulasidas et al. (1995).

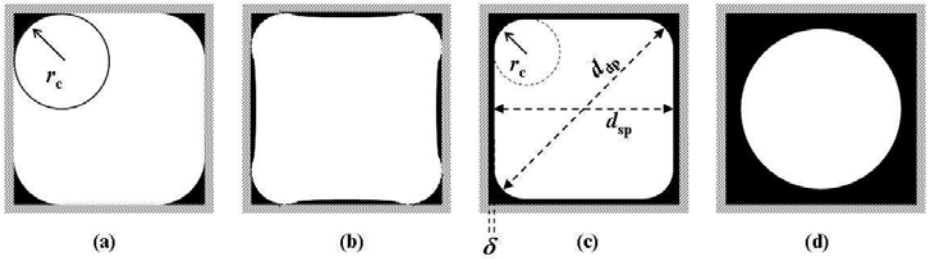

Figure 3.14: Principal illustration of the evolution of the bubble profile in microchannels and small tubes of square cross-section with increasing Capillary number: (a) *Ca* = 0, static bubble, r_c is the radius of the interface curvature in the corners of the channel cross-section; (b) *Ca* < 10^{-3}; (c) $10^{-3} \leq Ca < 0.04$, d_{sp} and d_{dp} are the bubble diameters in the side and diagonal planes, respectively; δ is the liquid film thickness; (d) *Ca* > 0.04.

Hazel and Heil (2002) numerically investigated the influence of gravitational acceleration on the bubble profile using the conditions of Kolb and Cerro (1991). They examined vertical upward and downward flow configurations and compared them to a situation of zero gravity (*Bo* = 0). In vertically oriented capillaries, the gravitational force induces a flow of the liquid phase in the corners of the channel cross-section. In the upward configuration this corner flow is in counter-current direction and leads to a thickening of the film. For the downward flow configuration, however, the liquid in the corners flows in the same direction as the bubbles and thus produces a thinner film in comparison with *Bo* = 0 and upward flow conditions. As a result, the transition from a non-axisymmetrical to an axisymmetrical bubble profile was found to occur at lower Capillary numbers ($0.03 < Ca < 0.04$) for upward flow than in the case of negligible gravitational acceleration (transition at *Ca* ~ 0.05) and downward flow ($0.05 < Ca < 0.06$). With a further increase in the Capillary number, the bubble diameter decreases until it reaches an asymptotic value.
The explanation made above will be used in the following to estimate the film-hold in dependency of different bubble shapes and the corresponding flow conditions.

<u>*Ca* < 10^{-3} (non-axisymmetrical bubble, see figures 3.14a and 3.14b):</u>
In this case the bubble profile may be estimated by means of the shape of a static bubble as shown in figure 3.14a. The film hold-up then writes as:

$$\varepsilon_F = (4-\pi)\left(\frac{r_C}{d_h}\right)^2 \qquad \text{(3.5-7), with} \qquad \frac{r_c}{d_h} = \frac{1}{2\alpha_c} \qquad \text{(3.5-8).}$$

The ratio r_c/d_h is the dimensionless mean radius of the interfacial curvature in the corners of the channel and α_c its inverse value scaled by the radius of the largest inscribed sphere, given by Wong et al. (1992) as:

$$\alpha_C = \frac{\left\{\left(\frac{w}{h}+1\right)\cos\theta + \left[\left(\frac{w}{h}-1\right)^2\cos^2\theta + 4\frac{w}{h}\left(\frac{\pi}{4}-\theta+\sin\theta\cos\theta\right)\right]^{1/2}\right\}}{2\frac{w}{h}} \qquad (3.5\text{-}9),$$

where w/h is the aspect ratio (for square cross-sectional channels $w/h = 1$) and θ the contact angle. Equation 3.5-9 is valid for contact angles in a range of $0 \le \theta \le \pi/4$ (45°). As an example, table 3.5 lists values of α_c and corresponding dimensionless curvatures r_c/d_h, as well as the resulting film fraction ε_F and the dimensionless bubble velocity U_B/U_{TP} for different values of contact angles.

θ	0	π/12 (15°)	π/6 (30°)	π/4 (45°)
α_c	1.8862	1.8455	1.6996	1.4142 (√2)
r_c/d_h	0.265	0.271	0.294	0.354
ε_F	0.060	0.063	0.074	0.107
U_B/U_{TP}	1.06	1.07	1.08	1.12

Table 3.5: Comparison of α_c, the dimensionless mean curvature of the gas-liquid interface in the channel corners r_c/d_h , the liquid film fraction ε_F and the dimensionless bubble velocity U_B/U_{TP} in microchannels of square cross-section at Ca < 10^{-3}, estimated for different values of contact angles θ using equations 3.5-7 - 3.5-9 and 3.5-1, respectively.

From table 3.5, it can be seen that for contact angles of $\theta < \pi/4$ (45°), the film hold-up only slightly varies between 6 % and 10 % and the bubble velocity may be considered as to be approximately equal to the superficial two-phase velocity.

$10^{-3} \le Ca < 0.04$ (non-axisymmetrical bubble, as sketched in figure 3.14c):

In addition to the liquid in the corners, it is necessary here to account for the liquid film between the gas-liquid interface and the wall in the side plane of the channel cross-section. Correspondingly, the liquid fraction around the bubble body may be calculated as follows:

$$\varepsilon_F = (4-\pi)\left(\frac{r_C}{d_h}\right)^2 + \frac{4\delta}{d_h}\left(1-\frac{\delta}{d_h}\right) \qquad (3.5\text{-}10), \text{ with } \quad \frac{\delta}{d_h} = \frac{1}{2}\left(1-\frac{d_{sp}}{d_h}\right) \qquad (3.5\text{-}11).$$

Here equation 3.5-11 relates the dimensionless thickness of the film δ/d_h to the dimensionless diameter in the side plane d_{sp}/d_h which, as mentioned above, remains constant. From the measurements of Kolb and Cerro (1991) it was found to be about 0.95, while the numerical study of Hazel and Heil (2002) proposes a value of 0.99. The dimensionless radius of the curvature in the corners can be obtained from:

$$\frac{r_c}{d_h} = \frac{1}{2}(1+\tan\omega)\left(\frac{d_{sp}}{d_h} - \frac{1}{\sqrt{2}}\frac{d_{dp}}{d_h}\right) \text{ with } \omega = 67.5° \qquad (3.5\text{-}12).$$

Based on the data of Kolb and Cerro (1991), Thulasidas et al (1995) and Hazel and Heil (2002), Kreutzer et al. (2005a) developed a correlation for the estimation of the dimensionless diameter in the diagonal plane d_{dp}/d_h (see equation 3.5-13).

$$\frac{d_{dp}}{d_h} = 0.7 + 0.5\exp\left(-2.25Ca^{0.445}\right) \qquad (3.5\text{-}13).$$

For $Ca = 0.04$ equation 3.5-13 yields a dimensionless diameter of about 0.99. This corresponds to an axisymmetrical bubble profile, which will be considered in the following paragraph. From equation 3.5-13, it can be seen furthermore that at large Capillary numbers the dimensionless bubble diameter tends towards an asymptotic value of 0.7.

$Ca \geq 0.04$ (axisymmetrical bubble, as sketched in figure 3.14d):

In connection with equation 3.5-13, the film-hold up in the case of an axisymmetric bubble is written as:

$$\varepsilon_F = 1 - \frac{\pi}{4}\left(\frac{d_{dp}}{d_h}\right)^2 \qquad (3.5\text{-}14).$$

Equations 3.5-9 - 3.5-14 are now used in order to estimate the evolution of the liquid film fraction and the dimensionless bubble velocity for Capillary numbers in orders of magnitude between 10^{-3} and 10^{0} (see table 3.6). In order to illustrate the influence of the channel corners, the corresponding results are compared in figure 3.15 with those obtained for the case of a circular cross-section. Following correlation 3.5-13 and the study of Hazel and Heil (2002), the dimensionless diameter in the side plane was assumed here as 0.99, which results in a dimensionless film thickness of $\delta/d_h = 0.005$.

	non-axisymmetrical		axissymmetrical		
Ca	10^{-3}	10^{-2}	0.04	10^{-1}	10^{0}
d_{dp}/d_h	1.151	1.074	0.992	0.923	0.753
r_c/d_h	0.301	0.393	(0.492)	-	-
ε_F	0,098	0.153	0.227	0.331	0.555
U_B/U_{TP}	1.11	1.18	1.29	1.49	2.25

Table 3.6: Comparison of the dimensionless bubble radius in the diagonal plane d_{dp}/d_h, the dimensionless mean curvature of the gas-liquid interface in the channel corners r_c/d_h , the liquid film fraction ε_F and the dimensionless bubble velocity U_B/U_{TP} in a microchannel of square cross-section, estimated for Capillary numbers of several orders of magnitude. For Ca < 0.04 (non-axisymmetrical bubble profile), equations 3.5-10 – 3.5-13 and 3.5-1 are used and a dimensionless bubble diameter in the side plane d_{sp}/d_h of 0.99 was assumed. For Ca ≥ 0.04 (axisymmetrical bubble profile), equations 3.5-13, 3.5-14 and 3.5-1 are employed.

.

From figure 3.15 it can be seen that the evolution of the liquid film fraction and the dimensionless bubble velocity for a square and circular channel follow similar tendencies. Due to the liquid in the corners of the channel cross-section and the assumption that the film thickness in the side planes remains constant, the film hold-up and with it the dimensionless bubble velocities are generally larger in a square channel than in a circular channel.

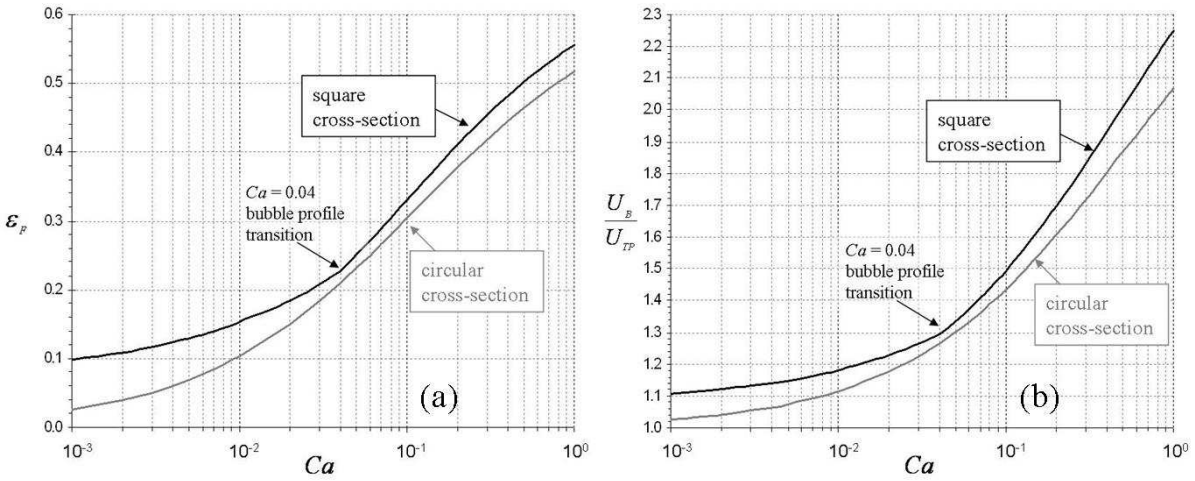

Figure 3.15: Comparison of the evolution of the liquid film hold-up ε_F (a) and the dimensionless bubble velocity U_B/U_{TP} (b) as a function of the Capillary number *Ca* in microchannels of square and circular cross-section.

3.5.1.3 Rectangular channel cross-section (aspect ratio ≠ 1)

Only a few investigations have focused on bubble shapes in rectangular channels. Similar to channels of square cross-section, the bubble profile at $Ca < 10^{-3}$ may be depicted with the shape of a static bubble (see figure 3.16a). For greater Capillary numbers and aspect ratios $w/h \geq 1.5$, Hazel and Heil (2002) showed that the bubble profile is essentially non-axisymmetrical in shape, with a liquid film which is much thicker in the horizontal plane than in the vertical plane (see figure 3.16b). This fact is attributed to surface tension forces. Caused by the latter, a bubble aims to achieve the lowest surface energy by minimizing its perimeter. Confined in a channel of rectangular cross section, this results in a thinner film at the bottom and the top as in the side planes of the channel. As already demonstrated for circular and square channels, we will be concerned in the following with the possibilities to estimate film fractions and dimensionless bubble velocities for different ranges of Capillary numbers.

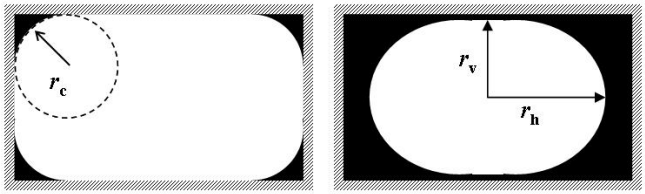

Figure 3.16: Principle sketch of bubble profiles in channels of rectangular cross-section under different flow conditions. (a) interface shape at $Ca < 10^{-3}$, after Wong et al. (1992, 1995), r_c is the mean radius of the interface in the channel corners; (b) bubble shape at $Ca \geq 10^{-3}$ in channels with aspect ratios w/h ≥ 1.5, after Hazel and Heil (2002), r_v and r_h, are the bubble radii in the vertical and horizontal planes, respectively.

<u>$Ca < 10^{-3}$ (static profile, see figure 3.16a):</u>

The film hold-up for a static bubble profile in rectangular channel can be written as follows:

$$\varepsilon_F = (4-\pi)\frac{h}{w}\left(\frac{r_c}{h}\right)^2 \qquad \text{(3.5-15), with} \qquad \frac{r_c}{h} = \frac{1}{2\alpha_C} \qquad \text{(3.5-16),}$$

where α_c is determined according to Wong et al. (1992) using equation (3.5-9). In the following the influence of the contact angle on the film hold-up ε_F and the dimensionless bubble velocity U_B/U_{TP} will be displayed in table 3.7 for the case where the aspect ratio $w/h = 2$.

θ	0	π/12 (15°)	π/6 (30°)	π/4 (45°)
α_c	1.4247	1.3939	1.2865	1.0811
r_c/h	0.351	0.359	0.389	0.463
ε_F	0.053	0.055	0.065	0.092
U_B/U_{TP}	1.06	1.06	1.07	1.10

Table 3.7: Comparison of α_c, the dimensionless mean curvature of the gas-liquid interface in the channel corners r_c/h , the liquid film hold-up ε_F and the dimensionless bubble velocity U_B/U_{TP} in a microchannel of rectangular cross-section with an aspect ratio of $w/h = 2$ at $Ca < 10^{-3}$, estimated for different values of contact angles θ using equations 3.5-11, 3.5-15 – 3.5-16 and 3.5-1, respectively.

As in the case of a square channel cross section (see table 3.5) the influence of the contact angle till a value of $\theta = \pi/4$ appears to be negligible. Assuming a constant contact angle, for example $\theta = \pi/6$ (30°), the influence of the aspect ratio can be checked. The results are listed in table 3.8.

w/h	2	3	4
α_c	1.2865	1.1564	1.0935
r_c/h	0.389	0.432	0.457
ε_F	0.065	0.053	0.045
U_B/U_{TP}	1.07	1.06	1.05

Table 3.8: Comparison of α_c, the dimensionless mean curvature of the gas-liquid interface in the channel corners r_c/h , the liquid film hold-up ε_F and the dimensionless bubble velocity U_B/U_{TP} in a microchannel of rectangular cross-section at Ca < 10^{-3}, assuming a contact angle of $\theta = 30°$, estimated for different values of aspect ratios w/h using equations 3.5-11, 3.5-15-16 and 3.5-1, respectively.

From table 3.8 it turns out that with an increase of the aspect ratio up to $w/h = 4$, the film fraction remains almost constant. Thus, tables 3.7 and 3.8 confirm that for rectangular channels at $Ca < 10^{-3}$ the bubble velocity may also be considered as to be approximately equal to the superficial two-phase velocity. In comparison to table 3.5, one may generally state that at $Ca < 10^{-3}$ the film fraction in a rectangular and square are approximately the same.

<u>$Ca \geq 10^{-3}$ and $w/h \geq 1.5$ (bubble profile sketched in figure 3.16b):</u>

The only study dealing with the behavior of the film hold-up in microchannels of rectangular cross-section at $Ca \geq 10^{-3}$ was undertaken by Warnier et al. (2008). Through this, a range of Capillary numbers of $3.3 \cdot 10^{-3} < Ca < 0.098$ was covered using a N_2/water system in a 50 µm×100 µm cross-section ($Bo \sim 6 \cdot 10^{-4}$). Based on measurements of bubble frequencies, bubble lengths and slug lengths it was proposed that the gas hold-up can be represented by the Armand-correlation.

$$\varepsilon_G = 0.833 \frac{U_{GS}}{U_{TP}} \qquad (3.5\text{-}17).$$

Taking equation 3.5-4 into consideration, the corresponding film hold-up is about 17 % and using expression 3.5-1 one may attribute an average dimensionless bubble velocity of $U_B/U_{TP} \sim 1.2$. In consideration of this result, Warnier et al. (2008) concluded that the liquid film occupies a fixed fraction of the channel cross-section over a wide range of Capillary numbers. Since their experimental runs were conducted in a range of bubble Weber numbers of $0.05 \leq We_{LB} \leq 47$, Warnier et al. (2008) attributed this characteristic to the influence of inertia. They argued that, according to the findings of Aussilous and Quéré (2000), in Taylor flows with significant inertial effects, the liquid film fraction converges to a fixed value. However, regarding the analysis of Aussilous and Quéré (2000), as discussed above for circular channels, this convergence is a result of the general scaling law (see equations 3.5-6a and 3.5-6b), which was derived on the basis of the presumption that inertia is negligible (compare also section 3.1 and expression 3.1-14). Aussilous and Quéré (2000) stated explicitly that inertia favors the thickening of the film, but it is not responsible for the circumstance that it tends towards an asymptotic limit. Thus, in connection with the outline given above for circular and square channels one may generally assume that, in a range from small to intermediate Capillary numbers (Ca ≤ 1), the liquid film thickness and hence the film fraction continuously increase. Comparing channels of different shapes but of the same value of the cross-sectional area, one may expect that the value of the film hold-up in a rectangular channel is more likely to lie in between those of a circular and a square channel (see figure 3.15a).

3.5.1.4 Fluctuations of the bubble velocity

Within the outline given above it was basically assumed that the bubble propagates with a constant velocity along the entire length of the channel. That this assumption is not always fulfilled was firstly demonstrated by van Steijn et al. (2008). Their investigation was based on the observation that at low Capillary numbers ($Ca \sim 10^{-3}$) bubbles may show a jerky movement. That means that the bubble velocity may vary with time. Van Steijn et al. (2007) identified three possible sources contributing to this phenomenon: (i) the bubble break-up at the inlet section, (ii) fluctuations of the liquid flow due to the performance of the feeding equipment (syringe pump), (iii) the rupture of the gas-liquid interface at the exit of the channel. From measurements at different positions along the channel it was shown that the fluctuations of the bubble velocity increase with increasing traveling distance. Consequently it was concluded that the main contribution is due to the Laplace pressure jump caused by the interface rupture at the channel exit. This pressure jump induces a relative fluctuation of the total pressure drop which in turn generates a relative fluctuation of the bubble velocity. In a quantitative manner this process may initially be written as:

$$\frac{\Delta U_B}{U_B} = \frac{\Delta(\Delta p)}{\Delta p_{tot}} \qquad (3.5\text{-}18).$$

Since the total pressure drop itself is a function of the bubble velocity (see section 3.2) it has to be taken into account the way it changes if the bubble velocity changes. This may be expressed by the partial derivative of the total pressure drop after the bubble velocity. Hence, equation (3.5-18) is correctly represented as:

$$\frac{\Delta U_B}{U_B} = \frac{1}{U_B}\left(\frac{\partial \Delta p_{tot}}{\partial U_B}\right)^{-1} \Delta(\Delta p) \qquad (3.5\text{-}19).$$

An exact calculation of the relative bubble velocity fluctuations is difficult to implement since the shape of the bubble and the Laplace pressure in the moment of the interface rupture are unknown. However, equations 3.5-18 and 3.5-19 are sufficient to depict several features of this topic. It can be seen that fluctuations of the bubble velocity may be reduced or avoided if the total pressure drop is increased. According to section 3.2, this can be obtained by an extension of the channel length, and by an increase of the bubble velocity and the number of bubbles present along the channel. Thus, an operation with short bubbles would be advantageous. To avoid bubble velocity fluctuations van Steijn et al. (2008) proposed to enlarge the section at the channel exit. This would increase the curvature of the bubble interface and thus decreases the Laplace pressure of the bubble before the interface rupture. Consequently, if an operation with long bubbles is necessary the size of the exit section may be adjusted to the bubble size. These design features would generally offer the possibility to better control hydrodynamic conditions. However, it is not clear yet, if bubble velocity fluctuations and the corresponding impact on film contact times as well as recirculation times, represent a disadvantage with respect to gas-liquid mass transfer and mixing.

3.5.1.5 Dewetting of the liquid film

From the studies of Cubaud and Ho (2004; see chapter 2) and Fuerstman et al. (2007; see section 3.2) it was shown that in Taylor flow through microchannels of non-circular cross-section the liquid film between the bubble and the channel wall may dry-out. Cubaud and Ho observed this characteristic for an air-water fluid system in a square microchannel with d_h = 200 µm in range of $2.4 \cdot 10^{-3} \leq Ca_{TP} \leq 6 \cdot 10^{-3}$ and denoted it as wedging flow. Bearing in mind the considerations above, this flow range is representative for a non-axisymmetrical bubble profile. The film thus dries out at the flat regions in the side planes of the channel cross-section and the liquid phase remains exclusively accumulated in the corner regions.

According to de Gennes et al. (2002) a liquid film spreading on a surface may dewet by two mechanisms. In this context one distinguishes between spontaneous dewetting and dewetting induced by nucleation and growth of dry patches. A Spontaneous dewetting occurs in the case where the film thickness is smaller than 10 nm. Wong et al. (1995a, 199b) stated that for $Ca \leq O(10^{-3})$ the liquid film at the side walls of square or rectangular cross-section scales with $Ca^{2/3}$ and thus its dimensionless thickness may roughly be estimated by:

$$\frac{\delta}{r} \approx Ca^{\frac{2}{3}} \qquad \text{(3.5-20)},$$

where r is the radius of the largest inscribed sphere in the channel cross-section, corresponding to $h/2$ for a rectangular channel. Assuming that $Ca \approx Ca_{TP}$ and r = 100 µm one may estimate the film thickness in the case of the study of Cubaud and Ho as 1.8 µm $\leq \delta \leq$ 3.3 µm. These values are two orders of magnitudes greater than the thickness which would induce a spontaneous dewetting of the liquid film according to de Gennes et al. (2002). Consequently, the dewetting phenomenon reported here is rather due to the second mechanism, the dewetting induced by nucleation and growth of a dry patch. For this, two conditions need to be fulfilled (de Gennes et al., 2002). First of all, the film thickness has to be below a certain critical value. The film is then characterized as metastable and a dry patch may occure by nucleation induced, for example, by surface heterogeneities. Secondly, a dry area starts to grow at a constant velocity if its initial radius is larger than a certain critical radius. This latter can be assumed to be in the order of magnitude of the film thickness, which corresponds to some micrometers, regarding the estimation shown above. Hence, this condition may generally be considered as to be fulfilled. According to de Gennes et al. (2002), the critical film thickness may be computed as:

$$\delta_{crit} = 2\lambda_C \sin\frac{\theta}{2} \qquad \text{(3.5-21), with} \quad \lambda_C = \sqrt{\frac{\gamma}{(\rho_L - \rho_G)\cdot g}} \qquad \text{(2.2-2)}.$$

At this θ is the equilibrium contact angle and λ_C is the Capillary or Laplace length constant. Considering an air-water system as it was employed in the study of Cubaud and Ho (2004), one obtains $\lambda_C \sim 2.7 \cdot 10^{-3}$ m. In the case of this investigation, the drying-out of the liquid film was observed between bubbles and a pyrex-glass layer covering the microchannel. Assuming a corresponding contact angle between 20° ($\pi/9$) and 30° ($\pi/6$), 3.5-21 yields a critical film thickness between 16 µm and 25 µm. Compared with a film thickness of $\delta \leq$ 3.3 µm estimated for the operating range above, it turns out that the critical film thickness is one order of magnitude larger than this value. Thus, the estimation of the critical film thickness is not a sufficient criterion to indicate the appearance of the drying-out of the liquid film. Cubaud and Ho (2004) examined the dewetting process in detail and measured the velocity of growth of a dry patch during the passage of a bubble. This so-called dewetting velocity U_{dew} was found to be about 7 mm/s. In this context the following observations were reported:

- for $U_B < U_{dew}$ the liquid film is dried-out across the entire length of the bubble
- for $U_{dew} < U_B < U_{B,crit}$ the film region shows a partial dewetting
- for $U_B > U_{B,crit}$ the bubble is fully lubricated.

Here $U_{B,crit}$ is the critical bubble velocity indicating the limit of the film to be dried out at the rear end of the bubble. It was approximated by Cubaud and Ho (2004) as:

$$U_{B,crit} \approx U_{dew}\frac{l_B}{w} \qquad \text{(3.5-22a)}.$$

To give a physical explanation of this expression it may by useful to rearrange it in the following manner.

$$\frac{l_B}{U_{B,crit}} \approx \frac{w}{U_{dew}} \qquad \text{(3.5-22b).}$$

We thus have a critical contact time on the left hand side and a dewetting time on the right hand side of expression 3.5-22b. The dewetting time is considered as the time a dry patch opens at the channel centre line and grows across the flat film region. The length of this region is usually given by the channel width minus the length of the corner regions. Consequently, the use of w in 3.5-22b constitutes a rough estimate and the dewetting time can be assumed to be slightly smaller as stated above. In general, expression 3.5-22b suggests that, besides the bubble velocity and the film thickness linked to it, the appearance of the drying-out of the liquid film in Taylor flow is also a function of the bubble length and the design of the channel cross-section. Based on this discussion we may propose a criterion for the prevention of the dewetting of the liquid film (corresponding to the preservation of a fully lubricated bubble) as follows:

$$\frac{l_B}{U_B} << \frac{w}{U_{dew}} \qquad \text{(3.5-23).}$$

In order to estimate the dewetting time one needs to have an idea about the velocity of growth of a dry patch. According to de Gennes et al. (2002) the dewetting velocity may be computed as:

$$U_{dew} = \varsigma \frac{\gamma}{\mu_L} \theta^3 \qquad \text{(3.5-24),}$$

where ς is a prefactor depending on the properties of the liquid phase, its molecular size, the contact angle and the liquid film thickness (Redon et al., 1991; de Gennes et al., 2002). Experimental measurements of dewetting velocities were mainly made for polymer films or other high molecular size liquids. Only a few data are available for the case of organic solvents. One example in this context is the study undertaken by Redon et al. (1991). Here, different alkanes with surface tensions between 22.9 mN/m and 27.6 mN/m, as well as viscosities ranging from 0.7 mPa·s to 3.3 mPa·s were used to create uniform films ($\delta << \delta_{crit}$; $\delta \approx O(10^1)$ µm) on the surface of a fluorinated silicon wafer. This resulted in contact angles between 15.3° and 36°. By suction of the liquid, a hole was generated in the centre of the film and its growth was followed in order to determine U_{dew}. Based on their measurements Redon et al. (1991) proposed the prefactor as:

$$\varsigma = \frac{1}{12\iota\sqrt{2}} \qquad \text{with } \iota \approx 6 \qquad \text{and thus } \varsigma \approx 0.01 \qquad \text{(3.5-25).}$$

However, this estimate may only be applied in the case where a comparable combination of parameters (δ, γ, θ, μ_L) is possible. Consequently, an universal expression of the prefactor and with that the computation of the dewetting velocity is still a controversial issue. The corresponding dewetting velocities measured by Redon et al. (1991) were in a range between 6 mm/s and 20 mm/s. Compared with the dewetting velocity measured by Cubaud and Ho (2004), it turns out that these values are in a similar velocity range. We may thus consider that the dewetting velocity is generally $U_{dew} \leq O(10^{-2})$ m/s. This allows estimation of the order of magnitude of the dewetting time, serving as threshold of contact time according to expression 3.5-23. Assuming that $w \sim O(10^{-4})$ m one may conclude that dry patches are likely to appear for contact times in the order of or greater than 10^{-2} s. Since the contact time depends on the bubble length one may obtain comparable values at Capillary numbers where film thickness may be larger than the critical film thickness. The above mentioned criterion should thus be supplemented by the estimation of a critical Capillary number. According to the observation carried out by Cubaud and Ho (2004) one may state that this value should be located in a range of $Ca_{crit} \sim O(10^{-3})$.

3.5.2 Bubble and slug formation – scaling laws and mechanisms

In order to investigate the behavior of bubble and slug lengths in dependency of operating parameters, usually single microchannel devices are employed. The simplest and more widely used inlet geometries of these components are shown in figure 3.17.

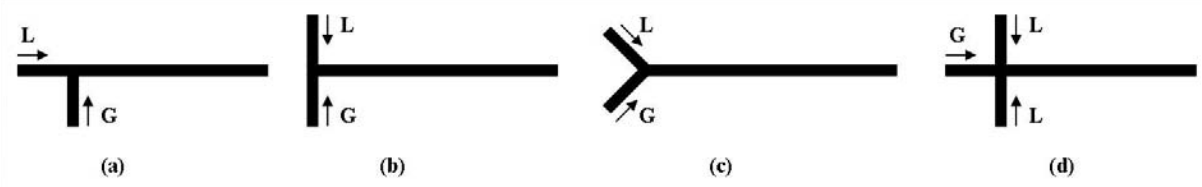

Figure 3.17: Principal illustration of commonly used inlet geometries for single microchannel components. L and G stand for liquid phase and gas phase inlet, respectively. (a) pseudo-T-shaped junction; (b) T-shaped junction; (c) Y-shaped junction; (d) X-shaped junction.

Before treating the studies concerned with this topic it may be useful to state some fundamental relationships. In the first instance the volume of the bubble may be obtained through multiplying the volume of the unit-cell by the gas hold-up. If the liquid around the bubble caps is neglected it can be written that:

$$A_B l_B = \varepsilon_G A_{Ch}\left(l_B + l_s\right) \qquad (3.5\text{-}26) \qquad \text{with} \qquad A_B = A_{Ch}\left(1-\varepsilon_F\right) \qquad (3.5\text{-}27).$$

Insertion of 3.5-27 into 3.5-26 yields:

$$\varepsilon_G = \left(1-\varepsilon_F\right)\frac{l_B}{\left(l_B + l_S\right)} \qquad (3.5\text{-}28).$$

In comparison with equation (3.5-4) it follows that:

$$\frac{l_B}{\left(l_B + l_S\right)} = \frac{U_{GS}}{U_{TP}} \qquad (3.5\text{-}29) \qquad \text{and} \qquad \frac{l_s}{\left(l_B + l_S\right)} = \frac{U_{LS}}{U_{TP}} \qquad (3.5\text{-}30).$$

Dividing (3.5-29) by (3.5-30) results in:

$$\frac{l_B}{l_S} \approx \frac{U_{GS}}{U_{LS}} \qquad (3.5\text{-}31).$$

This simple expression may be applied if bubble and slug length can be considered to be independent of fluid properties and the shape of the inlet section. In this case, for a given set of flow rates either the bubble length or the slug length needs to be predicted.

Qian and Lawal (2006) performed 2-dimensional simulations of the formation of Taylor flow at a T-junction (see figure 3.17b) as well as at a pseudo-T-junction (see figure 3.17a). From a systematic examination it turned out that at $Bo < 0.1$ the bubble and slug lengths are influenced by superficial velocities, surface tension, contact angle and the dimensions of the inlet channel. For example, in the case of the T-junction it was shown that an increase of the width of the inlet channels (w_{in}) from 250 µm to 1000 µm leads to an increase of the bubble and slug lengths by a factor of about three. On the other hand less difference between l_B and l_S was found when comparing a T-junction and the pseudo-T-junction at the same flow rates. Additionally, for the pseudo-T-junction the influence of the contacting configuration, that is the inversion of the inlet flows, was checked. It revealed that at the same flow rates, the inverted pseudo-T-configuration (the liquid enters by the side channel) produces bubbles and slugs which are two times longer than these in the normal pseudo-T-configuration (sketched in figure 3.17a). From a dimensional analysis of the flow it was suggested that the bubble and slug lengths are correlated to three main parameters: the two phase Reynolds-number $Re_{L,TP}$, the two-phase Capillary number Ca_{TP} and the gas hold-up. Since the film hold-up was assumed here as $\varepsilon_F \rightarrow 0$, the gas hold-up corresponds to $\varepsilon_G \sim U_{GS}/U_{TP}$ and $U_B/U_{TP} \sim 1$. From the results gained by simulations, undertaken in a range of $15 < Re_{L,TP} < 1500$, $2.78 \cdot 10^{-4} < Ca_{TP} < 0.01$ and $0.09 < \varepsilon_G < 0.098$, using a T-junction with $w_{in} = w = 1$ mm, the following correlations were proposed:

$$\frac{l_B}{w} = 1.637 \varepsilon_G^{0.107} \left(1-\varepsilon_G\right)^{-1.05} \mathrm{Re}_{L,TP}^{-0.075} Ca_{TP}^{-0.0687} \qquad (3.5\text{-}32),$$

$$\frac{l_S}{w} = 1.637 \varepsilon_G^{-0.893} \left(1-\varepsilon_G\right)^{-0.05} \mathrm{Re}_{L,TP}^{-0.075} Ca_{TP}^{-0.0687} \qquad (3.5\text{-}33),$$

$$\frac{\left(l_B + l_S\right)}{w} = 1.637 \varepsilon_G^{-0.893} \left(1-\varepsilon_G\right)^{-1.05} \mathrm{Re}_{L,TP}^{-0.075} Ca_{TP}^{-0.0687} \qquad (3.5\text{-}34).$$

In equations 3.5-32 to 3.5-34, all lengths values are expressed in dimensionless form by dividing them by the channel width *w*. Usually *w* is a characteristic parameter for channels of rectangular cross-section, but for the purpose of simplification it will be used in the following for all correlations including studies carried out with channels of various shapes. That means that in the case of channels with circular cross-section *w* corresponds to the channel diameter and in the case of square channels it equals the hydraulic diameter. From the exponents in equations 3.5-32 and 3.5-33, it can be seen that the dimensionless bubble length mainly depends on the liquid hold-up ε_L and the dimensionless slug length on the gas hold-up ε_G. Furthermore, the exponents of the Reynolds number and the Capillary number indicate that the bubble and slug lengths are less influenced by liquid phase properties, which involves the contact angle as well, since it is associated to the surface tension.

Sobieszuk et al. (2007) and Pohorecki and Kula (2008) performed experiments using ethanol and nitrogen in microchannels of circular cross section (d = 400 µm) and square cross section (d_h = 150 µm) made of glass and PDMS (polydimethyloxosilane), respectively ($Bo \leq 0.056$). The fluids were contacted at a Y-shaped junction (illustrated in figure 3.17c) with inlet channels of identical dimensions as the main channel ($w_{in} = w$), located from each other at an angle of 120°. The bubble lengths measured in a range of $4.4 \leq Re_{L,TP} < 466$ and $2.4 \cdot 10^{-3} < Ca_{TP} < 0.095$ were shown to follow the correlation of Qian and Lawal (2006) in its general form (see 3.5-35).

$$\frac{l_B}{w} = A \varepsilon_G^B \left(1-\varepsilon_G\right)^C \mathrm{Re}_{L,TP}^D Ca_{TP}^E \qquad (3.5\text{-}35).$$

The values of the coefficient *A* and the exponents *B-E*, which gave the best fit of the experimental data are summarized in table 3.9, together with these originally obtained by Quian and Lawal (2006).

	A	*B*	*C*	*D*	*E*
Qian and Lawal (2006) ***w* = 1 mm**:	1.637	0.107	-1.05	-0.075	-0.0687
Sobiezuk et al. (2007); Pohorecki and Kula (2008):					
PDMS ($w=d_h$ = 150 µm)	1.300	0.106	-1.00	-0.009	-0.0130
Glass ($w=d$ = 400 µm)	1.310	0.028	-1.07	-0.143	-0.1850

Table 3.9: Comparison of the coefficient *A* and the exponents *B-E* obtained from the studies of Quian and Lawal (2006) using a T-junction, Sobiezuk et al. (2007) and Pohorecki and Kula (2008) using a Y-junction for correlating the dimensionless bubble length according to equation 3.5-35. (PDMS (polydimethyloxosilane) and glass are the channel materials, *w* stands for the channel width used for the scaling of the dimensionless bubble length, the inlet channels were of same dimensions as the main channel).

In table 3.9, a comparison of the exponents *C-E*, found experimentally by Sobieszuk et al. (2007) and Pohorecki and Kula (2008), shows that the dependency of the dimensionless bubble length on the liquid hold-up is more pronounced than that on the contact angle. This confirms the findings of the simulations carried out by Quian and Lawal (2006) and underlines a scaling of $l_B/w \sim \varepsilon_L^{-1}$. This tendency is even more distinctive if one regards the results of an earlier study undertaken by Cubaud et al. (2005). Here an X-shaped junction (see figure 3.17d) with square channels of d_h = 100 µm was employed. Air and water as well as an aqueous surfactant solution ($\gamma \sim 38$ mN/m) served as fluids

($Bo \leq 2.6 \cdot 10^{-3}$). Within a range of $2 \cdot 10^{-3} \leq Ca \leq 0.034$, $15 \leq Re_{L,TP} \leq 130$ and $0 < \varepsilon_G < 0.9$ the dimensionless bubble length was found as:

$$\frac{l_B}{w} = \varepsilon_L^{-1} \qquad \text{with} \qquad \varepsilon_L = \frac{U_{LS}}{U_{TP}} \qquad (3.5\text{-}36).$$

For $l_B/w > 4$ the dimensionless unit-cell lengths was approximated as follows:

$$\frac{(l_B + l_S)}{w} = \frac{\left(l_B/w\right)^2}{\left(l_B/w - 1\right)} \qquad (3.5\text{-}37).$$

According to the results of this investigation the bubble and slug length are completely independent of fluid properties. Cubaud et al. (2005) explained their results by comparison of the pressure gradients of a cylindrical gas-core in a channel of square cross-section with those of single-phase liquid flow. It was argued that due to the large viscosity ratio between gas and liquid, the resistance offered by the gas for the liquid to flow across the channel cross-section may be considered as negligible and thus the process of bubble formation as independent of liquid phase properties. However, it has to be noted here, that correlation 3.5-36 was established on the basis of a double logarithmic plot.

The studies shown above employed different inlet geometries but have two points in common. Firstly, the inlet channels and the main channel were always of equal dimensions. Secondly the correlations found to have the following characteristic scaling:

$$\frac{l_B}{w} \approx \varepsilon_L^{-1} \qquad (3.5\text{-}38), \qquad \frac{l_S}{w} \approx \varepsilon_G^{-1} \qquad (3.5\text{-}39), \qquad \frac{(l_B + l_S)}{w} \approx \varepsilon_L^{-1}\varepsilon_G^{-1} \qquad (3.5\text{-}40).$$

Dividing 3.5-38 by 3.5-39 one returns to equation 3.5-31 and thus either the bubble length or the slug length need to be known to gain access to the other lengths values. Pohorecki and Kula (2008) modeled this scaling by assuming the bubble and slug formation as a so-called switching mechanism. Considering a Y-shaped junction as an example one may imagine this mechanism as an alternate occupation of the volume at the conjunction of the inlet channels by the gas and liquid phase. In this context, the estimate of the bubble length is based on the assumption that the time for the bubble to break-up (pinch-off time) is equal to the time the liquid phase needs to fill the entire channel cross-section at the confluence of both phases. Cubaud et al. (2005) observed that the bubble length is proportional to the bubble velocity. Thus, as an approximation, one may consider that the volume of the bubble is proportional to its volume flow rate times the pinch-off time (see 3.5-41).

$$A_B l_B \approx U_B A_B \cdot \tau_{pinch-off} \qquad (3.5\text{-}41).$$

If one further assumes that $\varepsilon_F \rightarrow 0$, 3.5-41 may be rewritten as:

$$l_B \approx U_{TP} \cdot \tau_{pinch-off} \qquad (3.5\text{-}42).$$

For a liquid inlet and a main channel of same dimensions, the pinch-off time may be approximated by dividing the volume of the confluence by the flow rate of the liquid phase.

$$\tau_{pinch-off} \approx \frac{w}{U_{LS}} \qquad (3.5\text{-}43).$$

Insertion of 3.5-43 into 3.5-42 and setting $\varepsilon_L \approx U_{LS}/U_{TP}$, then yields 3.5-38. In a similar manner one may approximate the volume of the liquid slug to be proportional to its volume flow rate times the time the gas-phase need to block the channel cross-section.

$$l_S \approx U_{TP} \cdot \tau_{blockage} \qquad (3.5\text{-}44).$$

If one considers that the gas-phase unhampered penetrates into the channel, the blockage time may be written as:

$$\tau_{blockage} \approx \frac{w}{U_{GS}} \qquad (3.5\text{-}45).$$

Combination of both expressions, setting $\varepsilon_G \approx U_{GS}/U_{TP}$, finally results in the general scaling law given in 3.5-39. Another study, dealing with this topic was carried out by Garstecki et al. (2006). Here, the bubble break-up at a pseudo-T-junction (see figures 3.17a and 3.18) in rectangular microchannels was investigated. The mechanism of bubble formation (here referred to as squeezing mechanism), observed during this study, may be divided into three steps. At first the gas phase penetrates into the main channel and the bubble grows until it approximately fills the channel cross-section. In this initial step illustrated in figure 3.18 the length of the bubble is at least approximately equal to or slightly larger than the channel width. Then the bubble grows in the downstream direction. At the same time the liquid phase starts to constrict the bubble-neck, connecting the bubble tip to the gas inlet, until it is pinched-off from the inlet section.

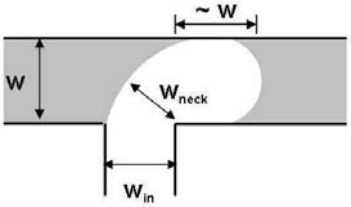

Figure 3.18: Principle illustration of the initial step of bubble formation at a pseudo-T-junction according to Garstecki et al. (2006); (w and w_{in} are the width of the main channel and the gas inlet channel, respectively; w_{neck} is the width of the bubble neck which connects the bubble tip to the inlet channel).

In this context Garstecki et al. (2006) discussed the forces involved in the break-up mechanism. In order that the bubble can be formed the surface tension force stabilizing the gas-liquid interface at the gas inlet needs to be overcome. It was suggested that, the principal contribution to the bubble detachment comes from the frictional pressure drop generated through the flow of the liquid phase around the bubble tip. The corresponding pressure force exerted by the liquid phase on the gas-liquid interface causes the bubble neck to thin and is finally responsible for the pinch-off of the bubble. In order to compare the orders of magnitude of both forces Garstecki et al. (2006) attempted to quantitatively describe this process. They estimated the surface tension force on the basis of the shape the bubble takes in the initial step of its formation. Assuming that the axial and radial expansion of the bubble is bounded by the dimensions of the channel the Laplace pressure across the bubble nose was approximated as:

$$\Delta p_{nose} \approx -\gamma\left(\frac{2}{h}+\frac{2}{w}\right) \qquad (3.5\text{-}46),$$

where the minus sign indicates that it is oriented in upstream direction. In a similar manner the Laplace pressure across the bubble neck can be estimated, considering that the radius of its axial curvature approximately equals the channel width.

$$\Delta p_{neck} \approx \gamma\left(\frac{2}{h}+\frac{1}{w}\right) \qquad (3.5\text{-}47).$$

Accordingly the surface tension force in the initial stage of bubble formation was stated as:

$$F_\gamma \approx \left(\Delta p_{nose} + \Delta p_{neck}\right) hw = -\gamma h \qquad (3.5\text{-}48).$$

Equation 3.5-48 shows that the surface tension force is oriented upstream and therefore stabilizes the forming bubble. For estimating the pressure force Garstecki et al. (2006) supposed that in the initial step the bubble does not touch the channel wall opposing the gas-inlet, leaving a gap for the liquid to flow along the bubble tip with an initial length of approximately w. Accordingly, it was assumed that the pressure force is mainly determined by the pressure drop generated by the liquid flow through this area. However, a bubble in a non-circular channel does not completely fill the corner regions of the channel cross-section. As a result one may consider that in the initial stage of bubble formation the liquid around the bubble tip would rather flow through the corners of the channel cross-section. For this case we may roughly estimate the pressure force exerted on the bubble neck as follows:

$$F_P \approx \Delta p_{f,corners} hw \qquad \text{with} \qquad \Delta p_{f,corners} \approx \frac{\mu_L Q_L w}{A_{corners}^2} \qquad (3.5\text{-}49).$$

Since the corner region represents a certain percentage of the entire channel cross-section one may suppose that its value is one order of magnitude smaller than that of the latter. With respect to the study of Garstecki et al. (2006) one may indicate the orders of magnitudes of the respective parameters by $\gamma \sim O(10^{-2})$ N/m, $\mu_L \sim O(10^{-3})$ Pa·s, $Q_L \sim O(10^{-10})$ m^3/s, $h \sim O(10^{-5})$ m, $w \sim O(10^{-4})$ m and with it $A_{corners} \sim O(10^{-10})$ m^2. From 3.5-48 and 3.5-49 it follows that $F_\gamma \sim O(10^{-7})$ N and $F_P \sim O(10^{-6})$ N. This means that in the initial stage of bubble formation the pressure force exerted at the bubble neck is at least one order of magnitude greater than the surface tension force. This principally agrees with the conclusions drawn by Garstecki et al. (2006). Under these circumstances, the bubble formation should be mainly governed by the pressure drop of the liquid generated through the blockage of the channel cross-section by the bubble tip and should be less dependent on fluid properties. It was thus concluded that the width of the bubble neck decreases at approximately the velocity of the liquid phase. This analysis and the observations made with respect to the break-up mechanism were used in the following to set-up a scaling law. Here, the bubble length was modeled as the sum of the initial bubble length and the length it achieved before being detached from the gas-inlet channel. This length is determined by the velocity at which the bubble grows in downstream direction and the time until the neck is pinched off. Hence the bubble length may be written as:

$$l_B \approx w + U_{growth} \cdot \tau_{pinch-off} \qquad (3.5\text{-}50).$$

Based on the conclusions made above and considering $w_{in} \sim w_{neck}$, the pinch-off time can be approximated as:

$$\tau_{pinch-off} \approx \frac{w_{in}}{U_{LS}} \qquad (3.5\text{-}51).$$

Insertion of 3.5-51 into 3.5-50 and assuming that the velocity of bubble growth is approximately equal to U_{GS}, yields:

$$\frac{l_B}{w} \approx 1 + \alpha \frac{U_{GS}}{U_{LS}} \qquad \text{with} \qquad \alpha \approx \frac{w_{in}}{w} \qquad (3.5\text{-}52).$$

Equation 3.5-52 constitutes the general scaling law proposed by Garstecki et al. (2006). It has the advantage that it accounts for the influence of the width of the inlet channel on bubble lengths, shown qualitatively in the study of Quian and Lawal (2006). In a similar manner we can derive an expression for the liquid slug length. At this we consider that the initial step of slug formation is the stage where the bubble detaches from the inlet channel. Thus the initial slug length corresponds to the width of the gas inlet channel. Afterwards the slug grows until the initial stage of bubble formation is reached, where the channel cross-section is blocked by the bubble tip. Hence one may write:

$$A_{Ch} l_S \approx A_{Ch} w_{in} + Q_L \cdot \tau_{blockage} \qquad (3.5\text{-}53).$$

For an unhindered penetration of the gas-phase into the main channel, the blockage time is given by the initial bubble volume ($\sim A_{Ch} \cdot w$) divided by the flow rate of the gas-phase, which results in the approximation given in 3.5-45. Insertion of 3.5-45 in 3.5-53 then yields:

$$\frac{l_S}{w} \approx \alpha + \frac{U_{LS}}{U_{GS}} \qquad \text{with} \qquad \alpha \approx \frac{w_{in}}{w} \qquad (3.5\text{-}54).$$

By setting $w_{in} = w$ in 3.5-52 and 3.5-54 one returns to the scaling given in 3.5-38 and 3.5-39, respectively.

Similar to the investigation of Cubaud et al. (2005), Garstecki et al. (2006) employed pure water as well as an aqueous surfactant solution ($\gamma \sim 35$ mN/m; $Bo \leq 9 \cdot 10^{-4}$). Within the range of $O(10^{-2}) \leq Ca \leq O(10^{-1})$, the bubble length measured for the surfactant solution agreed nearly perfectly

with 3.5-52. However, in the case of pure water the results started to strongly deviate at $U_{GS}/U_{LS} > 1$ ($\varepsilon_L < 0.5$). This result is in complete contradiction to the considerations discussed above as well as to the experimental findings of Cubaud al. (2005), since it suggests that surface tension plays an important role in the formation of bubbles.

In order to get more clarity concerning this problem it is necessary to have a look at a further study carried out by van Steijn et al. (2007). Here, the formation of Taylor bubbles at a pseudo-T-junction (see figures 3.17a) with $w = w_{in} = 800$ µm in a channel of square cross section was investigated in depth using microPIV and by measuring the evolution of the gas-liquid interface at the inlet section from high speed camera images. Air and ethanol were employed as working fluids. From the measurements of the liquid phase velocity field at $Ca_{TP} = 2.4 \cdot 10^{-3}$ and $Re_{L,TP} = 13.8$, it was shown that in the initial step of bubble formation (here referred to as the end of the filling stage) the liquid bypasses the bubble through the corners of the channel cross-section at velocities several times higher than the superficial liquid velocity. Thereafter, the bubble grows in the downstream direction, whilst its neck is constricted at the gas-inlet. This step was denoted here as squeezing stage. At this, the movement of the gas-liquid interface at the bubble neck was precisely recorded. From these images the difference in interfacial area between consecutive time steps was extracted and used in the following to estimate the value of the liquid flow rate pushing the interface. In the beginning of the squeezing stage this flow rate was approximated as to be about 50 % of the initial liquid flow rate. Hence, about 50 % of the total liquid flow rate bypasses the bubble through the channel corners. This leakage flow reaches a minimum of about 10 % of Q_L at 75 % of the total time of bubble formation process. This means that a remarkable amount of the liquid flow bypass the bubble tip leading to an increase of the pinch-off time since it does not contribute to the constriction of the bubble neck. The pressure gradient driving this leakage flow depends on the Laplace pressure at the bubble nose and the bubble neck. Neglecting the depth-wise curvature at the bubble neck it was stated here as:

$$\Delta p_{leakage} \approx \gamma \left(\frac{4}{w} - \frac{1}{r_{neck}} \right) \qquad (3.5\text{-}55).$$

Since the curvatures are limited by the dimensions of the channel, 3.5-55 suggests that the higher the surface tension, the greater the extent of leakage flow, the longer the pinch-off time and with it the higher the deviation of bubble and slug lengths from the scaling laws 3.5-52 and 3.5-54. For correlating the bubble length it was proposed to rewrite 3.5-52 as:

$$\frac{l_B}{w} \approx \alpha_1 + \alpha_2 \frac{U_{GS}}{U_{LS}} \qquad (3.5\text{-}56),$$

where according to Gastecki et al. (2006) α_1 is related to the initial length of the bubble tip and α_2 to the ratio of w_{in}/w. For ethanol in a range of $0.6 < Q_G/Q_L < 5$ van Steijn et al. (2007) found that $\alpha_1 = \alpha_2 = 1.5$. First of all, this shows that the initial bubble length is slightly larger than the channel width. Secondly, since $w = w_{in}$, one may understand the scaling of α_2 as that the leakage flow increases pinch-off time by a factor of about 1.5. In this context, the length of the liquid slug should follow a similar scaling with the same factor and we rewrite 3.5-54 as:

$$\frac{l_S}{w} \approx \alpha_2 + \alpha_1 \frac{U_{LS}}{U_{GS}} \qquad (3.5\text{-}57).$$

In general the study of van Steijn et al. (2007) gives an explanation of why Garstecki et al. (2006) found a strong increase of bubble lengths while employing water. On the other hand, for the aqueous surfactant solution, Grastecki et al. (2006) reported a good agreement with its scaling. This may be due to the fact that they used a rectangular channel, where the fraction of liquid and with it of leakage flow in the channel corners should be expected as smaller than for a square cross section. In general one may consider that, for organic solvents the correlation given by van Steijn et al. (2007) represents

the maximum influence of surface tension on bubble and slug lengths at low Capillary numbers ($Ca_{TP} \approx O(10^{-3})$). On the other hand, for microchannels of circular cross sections one may suppose that the influence of surface tension or liquid phase properties in general should be less pronounced, since the absence of channel corners should allow only a minimum of leakage flow within the process of bubble formation. In order to check these assumptions we compare the simple scaling law 3.5-38, as well as the correlation of van Steijn et al. (2007) with the bubble lengths computed from correlations which account for fluid properties by Ca_{TP} and $Re_{L,TP}$ (Qian and Lawal, 2006; Sobieszuk et al., 2007; Pohorecki and Kula, 2008, see 3.5-35 and table 3.9). This is shown in figure 3.19. In order to plot the length values, a channel with w = 500 µm and fluid properties characteristic for an organic solvent like ethanol (μ_L ~ 1 mPa·s, γ ~ 20 mN/m, ρ_L ~ 790 kg/m^3) are considered. Fixing a certain two-phase Capillary number then allows determination of U_{TP} and $Re_{L,TP}$. The Capillary numbers are chosen with respect to the ranges in which the correlations were developed. The dimensionless bubble lengths obtained in this way are displayed for a range of $0.1 \leq \varepsilon_L \leq 0.9$.

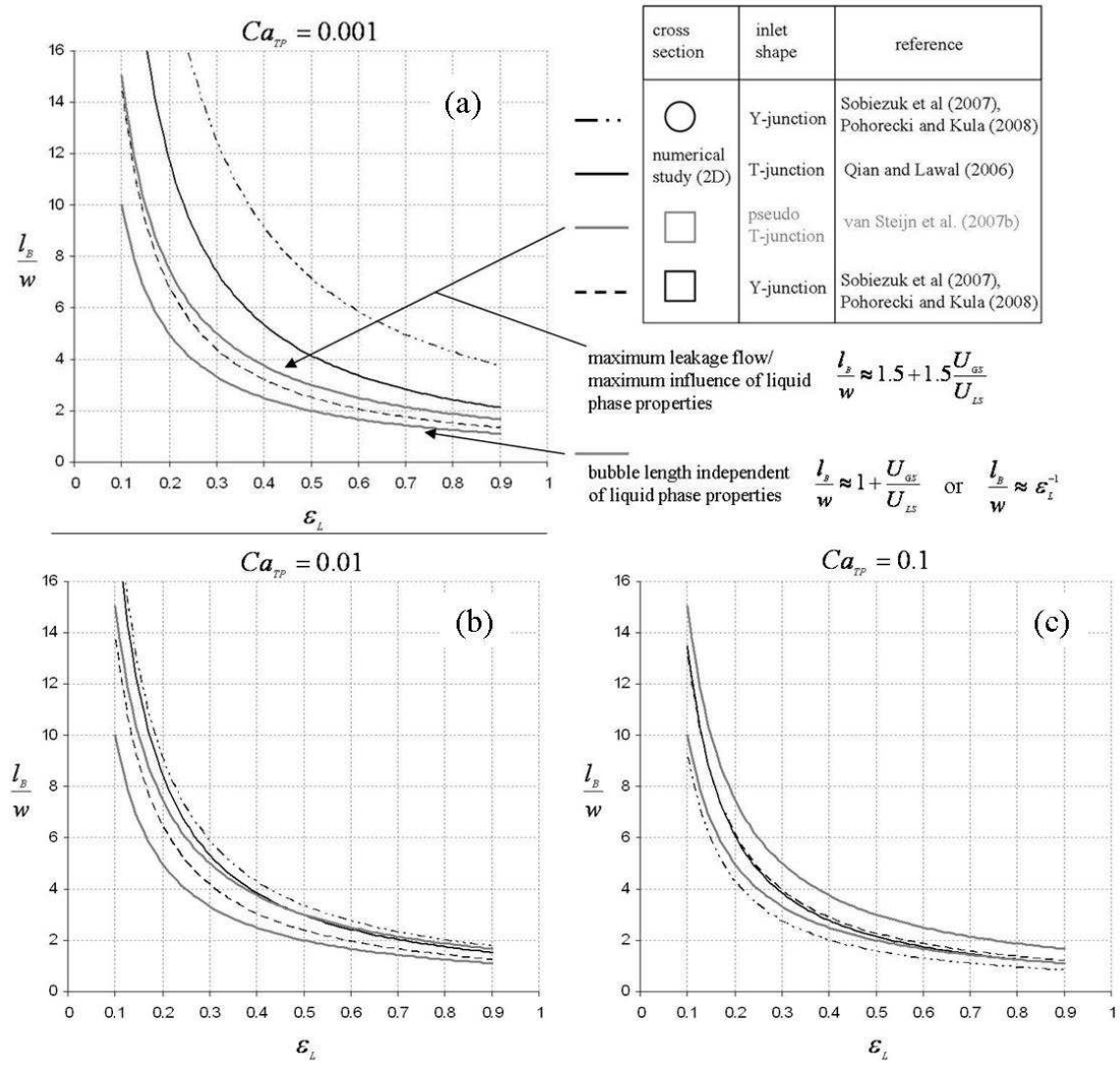

Figure 3.19: Plot of the dimensionless bubble length l_B/w versus the liquid hold-up ε_L obtained from correlations of various authors, for Capillary numbers Ca_{TP} of different orders of magnitude assuming μ_L ~ 1 mPa·s, γ ~ 20 mN/m, and ρ_L ~ 790 kg/m^3. Concerning the correlations of Quian and Lawal (2006), Sobieszuk et al. (2007) and Pohorecki and Kula (2008) the bubble length was computed by means of expression 3.5-35 and table 3.9.

With respect to the statements made above we can consider the dimensionless bubble length obtained from the correlation of van Steijn et al. (2007, see equation 3.5-56 and figure 3.19) as an upper limit, whilst the simple scaling law, completely independent of liquid phase properties, given in 3.5-38 can be assumed as the lower limit of the dimensionless bubble lengths. Since, the correlations of Qian and Lawal (2006), Sobieszuk et al. (2007) and Pohorecki and Kula (2008) indicate an additional dependency of the dimensionless bubble lengths on fluid properties, which is however less pronounced in comparison with that on the liquid hold-up ε_L (see expression 3.5-35 and table 3.9), one may expect that the values computed by means of these expressions lie at least in between the limits mentioned above. In figure 3.19a, dimensionless bubble lengths are displayed for the lowest Capillary number considered here. It can be seen that the curves obtained from the correlations of van Steijn et al. (2007, upper limit) and Sobieszuk et al. (2007) and Pohorecki and Kula (2008) for the square channel, give similar results and nearly coincide for $\varepsilon_L < 0.2$. This is in good agreement with the considerations made above. Both correlations are based on studies undertaken with the same fluid combination (air-ethanol) in channels of square cross-section and may thus be considered as different ways taking into account the influence of the leakage flow on bubble lengths. On the other hand, the bubble length computed by means of the correlation found by Sobieszuk et al. (2007) and Pohorecki and Kula (2008) for ethanol in a channel of circular cross section are significantly greater than those of the upper limit. However, the absence of channel corners should offer less space for the liquid phase to bypass the bubble tip and thus a lower extent of leakage flow. This should result in values of dimensionless bubble lengths substantially smaller than the upper limit and closer to the simple scaling law. The same trend should apply concerning the Qian and Lawal (2006) correlation, since it is based on a numerical study, where leakage flow was not accounted for. That means that the latter correlations may be considered as large overestimations if applied for $Ca_{TP} \approx O(10^{-3})$.

Comparing figure 3.19a with 3.19b, it can be seen that at $Ca = 0.01$ the curves of all correlations (except the fixed lower and upper limits) are shifted to lower dimensionless bubble lengths than in the case of $Ca = 0.001$. This tendency may be explained by taking into consideration the basic meaning of the Capillary number. An increase of the Capillary number is a synonym for an increase of the importance of viscous stresses relative to surface tension forces. The latter are amongst others responsible for the leakage flow. In connection with the formation of Taylor bubbles, viscous stresses may be expressed in terms of the pressure drop generated by the liquid flow around the bubble tip through the channel corners and the resulting pressure force (see 3.5-49) squeezing the bubble neck. That means that, with increasing Ca_{TP} the bubbles are more rapidly squeezed, leaving less time for leakage flow and thus bubble growths. The process of bubble formation may thus be understood as a competition between the pressure drop generated at the bubble neck (see 3.5-49) and the pressure gradient driving the leakage flow (see 3.5-55). In other words, concerning the influence of fluid properties one may state that viscosity and surface tension are playing opposed roles. As a result, increasing the Capillary number at a fixed liquid hold-up leads to a decrease of the dimensionless bubble lengths until a minimum value, represented by the simple scaling law, is reached. Following the progression of the curve obtained from the correlation found in a square channel by Sobieszuk et al. (2007) and Pohorecki and Kula (2008), it can be seen furthermore that for a given Ca_{TP} and increasing ε_L the dimensionless bubble lengths continuously approach the simple scaling law (lower limit). This trend may be explained once more by accounting for the pressure force squeezing the interface at the bubble neck, which is, according to expression 3.5-49, proportional to the liquid flow rate. Since, an increase of the liquid hold-up implies an increase of the liquid flow rate the pressure force at the bubble neck is increased and thus the pinch-off time reduced. Since the latter determines the time for the leakage flow to occur, an increase of the liquid hold-up at a fixed Capillary number has the same effect on bubble lengths as an increase of Ca_{TP} at fixed ε_L. An example for this can be

seen in figure 3.19c where the correlations of Qian and Lawal (2006) and that found in a square channel by Sobieszuk et al. (2007) and Pohorecki and Kula (2008) coincide with the lower limit for $\varepsilon_L \geq 0.5$. On the basis of the discussion undertaken above one may also give an additional explanation why Garstecki et al. (2006) found a good agreement with the simple scaling law, when employing a low surface tension liquid phase. Since their experiments were carried out in a range of $O(10^{-2}) \leq Ca \leq O(10^{-1})$, this behavior is possibly due to combined effects of less cross-section provided for leakage flow (rectangular channel) and an increased relative influence of viscous stresses.

From the three correlations evaluated by means of figure 3.19 (see also expression 3.5-35 and table 3.9), the expression found by Sobieszuk et al. (2007) and Pohorecki and Kula (2008) for a square microchannel appears to best match all theoretical considerations within a range of Capillary numbers of several orders of magnitude. The values, obtained form this correlation, are always located between the upper and lower limit and taking well into account the different influences of liquid phase properties. It may thus be considered as a good approximation for the prediction of bubble lengths in microchannels of square cross-section and may serve as an upper threshold concerning microchannels of circular or rectangular cross-sectional shape, provided that inlet channels and main channel are of the same dimensions. Concerning the latter point, the study of Garstecki et al. (2006) showed that the width of the gas inlet affects the width of the bubble neck and therewith the pinch-off time. One may thus expect that for a given Capillary number and a fixed liquid hold-up, the reduction of the gas inlet width results in a reduction of bubble lengths. In this case the scaling law given in 3.5-52 may be applied as lower limit.

With regards to the prediction of hydrodynamic parameters it has been shown that in the case of microchannels with circular or square cross-sections an estimation of dimensionless bubble velocities is generally possible for Capillary numbers of several orders of magnitude. On the other hand, less data are available for channels of rectangular cross-section. However, with respect to the theoretical considerations presented within this topic, e.g. evolution of film thickness and bubble profiles, one may expect that the values of dimensionless bubble velocities for a channel of rectangular cross-section lie between those of a square and circular channel of same cross-sectional area. Concerning the lengths of bubbles the prediction of a lower threshold and the estimation of an upper limit are generally possible if the dimensions of inlet channels and the main channel can be assumed as equal. According to the discussion and analysis of the literature, the upper limit may be expressed by a correlation, which takes into account the influence of fluid properties like surface tension and liquid viscosity for several orders of magnitude of two-phase Capillary numbers. Within these limits, the issue, how close the real values may be assumed to approach the upper limit depends on the fraction of the channel cross section offered for the liquid phase to flow around the bubble tip while it grows downstream. In this context, the lower limit is given by a simple scaling law, where bubble lengths are only dependent on the liquid hold-up or the ratio of superficial phase velocities. For this case, estimations are also possible as a function of the dimensions of the gas-inlet channel. On the other hand, only a few studies deal with the prediction of slug lengths. With respect to that, the estimation of a lower limit based on simple scaling laws should be possible. The role of the shape of the inlet section, as well as the contacting mode, were either not considered or only mentioned in qualitatively manner in the literature, so far.

3.6 Conclusions

In the literature, hydrodynamics and mass transfer in Taylor flow were intensively studied and characterized for channels of circular and square cross section. This is mainly due to the fact that these geometries are employed in the context with the concept of monolith reactors. However for operating gas-liquid and gas-liquid-solid reactions in microchannels it would be preferable to employ rectangular channel cross-sections with high aspect ratios since it offers an increase of the heat transfer area at the top and the bottom of the channel relative to its volume. Consequently, with respect to microchannels of rectangular cross section the following tasks should be items of further studies:

- Systematical investigation of the evolution of the bubble pressure for $Ca \geq O(10^{-3})$ in channels as a function of the aspect ratio.
- Characterization of the liquid phase velocity field within the slugs concerning the evolution of the recirculation velocity, as well as the recirculation time.
- Adoption of a correlation for the prediction of the volumetric mass transfer coefficient based on hydrodynamic parameters.

Especially the two latter cases would require supplementary information from:

- Characterization of the liquid film thickness at the top and the bottom of a rectangular microchannel for $Ca \geq O(10^{-3})$ in order to predict the saturation/exhaustion time
- Investigation of the evolution of the liquid film fraction and the dimensionless bubble velocity for $Ca \geq O(10^{-3})$ as a function of the aspect ratio.
- Determination of bubble and slug length as a function of Ca_{TP} and the channel aspect ratio.
- Systematical study of bubble and slug length as a function of the ratio w_{in}/w and the contacting mode.
- Examination of the influence of the design of the contacting section (T-, pseudo-T-, Y- or X-shaped) on bubble and slug length
- Investigation of the possible appearance of a drying-out of the liquid film as a function of *Ca*, the film contact time and the channel aspect ratio.

PART B

EXPERIMENTAL ASPECTS

Conceptual project design

After the presentation of the state of art and the identification of gaps in knowledge concerning the operation of gas-liquid systems in microchannels in Chapters 2 & 3, the aim of this section is to define the experimental framework of this project which will enable to fill some of the missing gaps with respect to the design of gas-liquid microreactors.

According to the conclusions drawn in the preceding chapter, it is obvious that knowledge is needed in the area of hydrodynamics and mass transfer in Taylor flow through rectangular microchannels and it is for this reason that we have selected this cross sectional channel shape for our study. Following this, this project is split into two parts.

The first part concerns the study of the gas-liquid hydrodynamics at low Capillary numbers ($Ca \approx O(10^{-3})$). From the literature review, it appears interesting to explore the following points:

- the influence of the leakage flow on bubble and slug lengths in microchannels of rectangular cross-section
- the occurrence of dry patches (dewetting phenomenon) according to the criterion proposed in section 3.5.1.5
- the dimensionless bubble velocity with respect to the cross-sectional bubble profile and its predictability compared with the equations presented in section 3.5.1.
- the liquid phase velocity field within the slugs, including visualization of the recirculation flow and determination of the recirculation velocity, which is an important parameter regards to mass transfer between bubble caps and liquid slugs.

The second part of the project couples the hydrodynamics and mass transfer in gas-liquid flow and focuses on the prediction of the volumetric liquid side mass transfer coefficient ($k_L a$-value) in microchannels of rectangular cross-section using a phenomenological model. This requires simultaneous measurements of the $k_L a$-value and hydrodynamic parameters like bubble velocities, bubble lengths and slug lengths. The microchannels to be used in the frame of this project will be depicted in the following.

Microchannel design

A primary point concerning the microchannel design for this project is the choice of dimensions of the channel cross-section. There are two criteria that need to be fulfilled for microchannel flow. Firstly the inner dimensions should be $\leq$ 1 mm and secondly, the surface tension forces should dominate gravitational acceleration g. According to chapter 2, in horizontal flow this may be assumed if:

$$d_h \leq \frac{\lambda_C}{2} \qquad \text{with} \qquad \lambda_C \approx \sqrt{\frac{\gamma}{\rho_L \cdot g}} \qquad (3.7\text{-}1).$$

In gas-liquid systems that are considered for operation in microchannels, the liquid phase usually consists of an organic compound, which is used as a liquid reactant or as a solvent (methanol, acetonitrile). The common property of these liquids is that they possess low surface tension (γ= 20 mN/m – 30 mN/m, at 20 °C). In this study, ethanol (γ ~ 22 mN/m, ρ_L ~ 790 kg/m^3, at 20 °C) has been used as a model solvent, as it is representative of these liquids with low surface tension. Using the criterion given above with ethanol, one obtains a threshold of d_h < 850 µm below which the surface tension forces dominate gravitational acceleration. The channel width has been chosen as 1000 µm, which is maximum dimension within the microscale. In order to find the appropriate channel height one needs to take into account the influence of the aspect ratio (w/h) on heat transfer and pressure drop. In this context, one may state that on the one hand an increasing ratio w/h increases heat transfer (Yarin et al., 2008), but on the other hand it also increases the frictional pressure drop (von Böckh, 2004). Since the evaluation of an optimum aspect ratio (Yarin et al., 2008) comprises a large

number of parameters, whose discussion would blast the frame of the present work, we decide to employ a channel of moderate aspect ratio $w/h = 2$. This results in a channel height of 500 µm and yields a hydraulic diameter of $d_h \approx 670$ µm, which is below the threshold value mentioned above. The next point to fix with respect to the channel design is the shape of the inlet section. In this context we consider that the simplest way of contacting both phases in a microreactor is to directly inject the gas-phase to the liquid already flowing through the main channel. We thus choose a pseudo-T-shaped junction (shown in figure 3.20) with a width of the gas inlet of 525 µm.

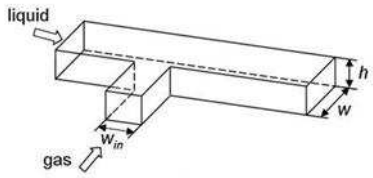

Figure 3.20: Microchannel contacting section used in this study, main channel with $w = 1000$ µm, $h = 500$ µm; gas-inlet channel with $w_{in} = 525$ µm, $h = 500$µm.

In order to provide sufficient residence time for a reactive system (especially in the case of homogeneous and heterogeneous catalyzed reactions), typically long microchannels are needed. Since one of the design requirements of miniaturized devices is that they are compact, an obvious solution is to employ meandering channel geometries. At this a high degree of compactness may be achieved by complete turnings of 180°. In this case however, the channel bends induce a noticeable distortion of the recirculation motion within the liquid slugs (see section 3.3). Since the perturbations of the liquid velocity field may constitute an interesting feature concerning the enhancement of gas-liquid mass-transfer, we decided to employ two configurations of meandering channels of comparable lengths, but different bend design - one with round bends and another one with sharp angled bends - and are compared with a straight channel configuration (see figure 3.21). In order to provide an excellent visual access, the microchannels were manufactured by etching a silicon wafer from the top to the bottom and enclosing it within two pyrex glass plates by anodic bonding (see figure 3.21d). The channel fabrication was carried out by the LAAS (Laboratoire d'Analyse et d'Architecture des Systèmes) in Toulouse. Further details concerning the microchannel design are specified in appendix A2.

Figure 3.21: Microchannel geometries used in this study with $w = 1000$ µm, $h = 500$ µm; gas-inlet channel with $w_{in} = 525$ µm, $h = 500$µm. (a) straight channel $l = 70$ mm, (b) meandering channel with curved bends, (c) meandering channel with sharp corner bends, (b) and (c) $l \approx 300$ mm, (d) cross-sectional sketch of the microchannel plate.

Example photographs of microchannels arranged on a silicon wafer are shown in figure 3.22.

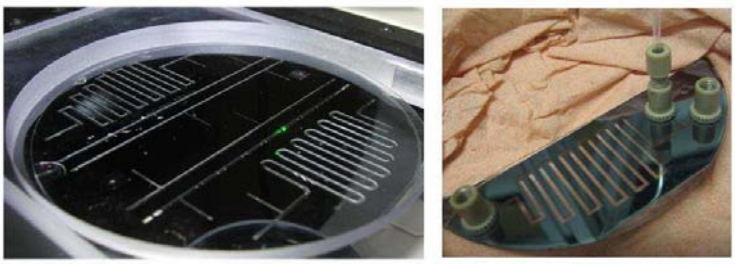

Figure 3.22: Example images of the microchannels fabricated for the experimental investigations of the present study (the image on the right hand side additionally shows the microfluidic connectors glued on the inlets and the outlet).

4 Characterization of hydrodynamics in Taylor flow through rectangular microchannels

This chapter is concerned with the experimental investigation of hydrodynamics. It is split into three parts. At first we will use an air-ethanol system to measure bubble velocities, bubble lengths and slug lengths in the three channel configurations indicated above. Afterwards, we will repeat similar measurements employing a N_2-water fluid combination. Even though, water is not an appropriate solvent for gas-liquid reaction systems coming into consideration for an operation in microreactors, it contains an interesting feature by its increased surface tension and offers wettability conditions quite different from that of ethanol. In addition to that it will serve as a solvent in the aqueous electrolyte solution employed for the characterization of gas-liquid mass transfer which will follow this chapter. In this context the study of hydrodynamics using water is an important item for finding appropriate operating conditions. According to the statements made with respect of the definition of our project the present chapter will be completed by the characterization of the liquid phase velocity field within the slugs using microparticle image velocimetry (microPIV). This task is carried out with the air-ethanol fluid combination. The equipment and the methods employed to undertake the task concerned with the present chapter are depicted in the following.

4.1 Experimental set-up and methods of measurement

A principle sketch of the experimental apparatus is shown in figure 4.1. With respect to this only general indications are given since the equipment varied in dependence of the fluid system or task. That means that measurements using the air-ethanol system were conducted at the Laboratory of Chemical Engineering Toulouse (LGC), while the investigation employing the N_2-water fluid combination was undertaken during a scientific stay at the Faculty of Chemical and Process Engineering at the Warsaw University of Technology (WUT).

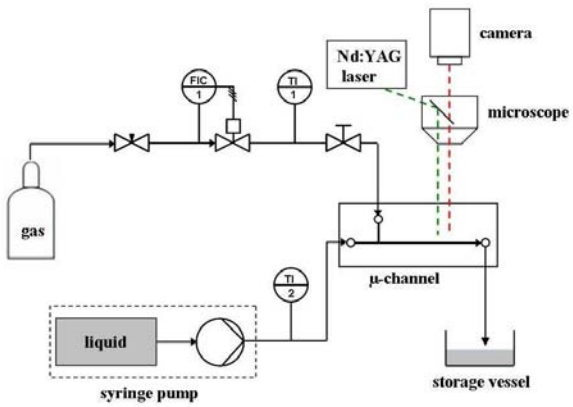

Figure 4.1: General illustration of the experimental set-up used in the present study for characterizing the hydrodynamics of Taylor flow (FIC flow indication and control; TI temperature indicator).

Concerning the air-ethanol fluid system it was necessary to select appropriate feeding equipment or more precisely to estimate the flow ranges required to achieve the intended operating conditions. This will be demonstrated in the following for the gas-phase. As mentioned within the project design section, we are initially interested to conduct experiments at Capillary numbers in the order of 10^{-3}. In order to have a rough idea we simply assume that:

$$Ca_{TP} = \frac{\mu_L U_{TP}}{\gamma} \approx 10^{-3} \quad \text{and} \quad \varepsilon_G \approx \frac{U_{GS}}{U_{TP}} \qquad (4.1\text{-}1).$$

Using the fluid properties of ethanol at 20 °C (γ ~ 22 mN/m, μ_L ~ $1.19 \cdot 10^{-3}$ Pa·s) and considering a gas hold-up between 0.1 and 0.9 one obtains a range of superficial gas phase velocities between 0.002 m/s and 0.0198 m/s. Multiplying by the cross sectional area of the channel (A_{Ch} = $5 \cdot 10^{-7}$ m^2) and the density of air (ρ_G ~ 1.2 kg/m^3) results in mass flow rates ranging from 0.004 g/h to 0.042 g/h. A commercial available mass flow controller corresponding to this flow range was found to be the Horiba SEC-7302, which offers a range of 0 – 0.078 g/h with a minimum regulation of 0.004 g/h. A similar estimation was carried in order to find the range of liquid phase flow rates.
As can be seen from figure 4.1 the two phase flow passing through the microchannel was recorded by means of a camera and the movies were treated in the following using an image processing software. The corresponding characteristics of the equipment employed are given in the following for each part of this study together with further explanations of the measurement method.

4.1.1 Measurements of hydrodynamic parameters

The apparatus employed within this task are summarized in table 4.1 according to the notations given in figure 4.1.

fluid system	FIC/MFC	syringe pump	microscope	camera	image processing software
air-ethanol	Horiba SEC-7302 (0-1 ml/min)	PHD-2000 (Havard Apparatus) syringe: 10 ml	SMZ-10 (Nikon) objective: 0.66x observation area: ≈ 4×4 mm^2	CCD HCC-1000 (VDS Vossmüller GmbH)	NV 1000 (New Vision Technologies)
N_2-water	Brooks 5850S/BC (0-10 ml/min)	AP14 & Sep11S (ascor) syringe: 100 ml	not required observation area: ≈ 24×24 mm^2	CMOS 1200hs (pco)	inhouse program (WUT)

Table 4.1: Equipment used in the present study for measuring bubble velocities, bubble lengths and slug lengths. (specifications are made according to the flow sheet in figure 4.1; FIC flow indication and control; MFC mass flow controller).

For both systems the measurements of bubble velocities were carried by tracking the interface of the bubble front cap at the entrance and the exit of the observation area. At this the image processing software furnished the corresponding time values and interface positions. The latter were transformed from pixel units into mircometers by using the channel width as a scale. Bubble and slug lengths were obtained by tracking the gas-liquid interface at the front and end caps of the bubbles. In the case of the air-ethanol set-up, only bubbles and slugs with lengths approximately equal or smaller than 4 mm were considered, because of the limited observation area. Furthermore, for this system all measurements were carried out at a fixed distance from the inlet of about 52 hydraulic diameters. The respective operating conditions for both fluid systems are given in table 4.2.

fluid system	Q_G [ml/min]	Q_L [ml/min]	U_{GS} [m/s]	U_{LS} [m/s]	U_{TP} [m/s]	$Ca_{TP}\cdot10^{-3}$
air-ethanol	0.36-1.19	0.2-1	0.012-0.04	0.007-0.033	0.022-0.06	1-3.2
N_2-water	1-6	0.22-4.05	0.033-0.202	0.007-0.135	0.040-0.337	0.6-.4.7

Table 4.2: Operating conditions of the fluid systems used in the present study for characterization of hydrodynamics (Q_G gas flow rate; Q_L liquid flow rate; U_{GS} superficial gas velocity; U_{LS} superficial liquid velocity; U_{TP} superficial two-phase velocity; Ca_{TP} two-phase Capillary number).

The values of the flow rates and the corresponding superficial phase velocities listed in table 4.2 are obtained from the calibration of the mass flow controllers and syringe pumps. Compared to the air-ethanol system, the ranges for the N_2-water are larger, since the study of this fluid combination should also serve to identify appropriate operating conditions with respect to mass transfer measurements (see chapter 5).

4.1.2 Characterization of the liquid phase velocity field

The velocity field measurements were carried out using air and ethanol as fluids and the feeding devices which correspond to those given in table 4.1. The characteristics of the microPIV equipment are summarized in table 4.3.

laser	**microscope**	**camera**	**image processing software**
double pulsed Nd:YAG (532 nm)	Axiovert 200M (Zeiss) objective: Zeiss Aplan 5x (NA: 0.12) observation area: ≈ 2×2 mm^2	CCD Imager Intense (LaVision), 12-bit double exposure, 10 Hz resolution : 1376×1040 pixels^2	Davis 7 (LaVision)

Table 4.3: Characteristics of the microparticle image velocimetry (microPIV) equipment used in the present study for measuring the velocity field within the liquid slugs during Taylor flow in a rectangular microchannel. (Nd:YAG Neodym:Yttrium-Aluminium-Garnet; NA numerical aperture).

The principle of this measurement method may shortly be depicted as follows. The liquid phase is seeded with polymer particles. Two laser pulses are emitted to the flow in a certain time interval δt. The laser light is absorbed by the particles, stipulating them to fluoresce. In this manner the particles are visualized within the flow field and two images are recorded by a CCD camera according to the δt of the laser. The velocity of the particles is then determined from the distance they travelled during the time interval. This task is undertaken by the image processing software. At this the flow filed is dissected in several domains called the interrogation areas (IA). The instantaneous velocity field is calculated from the detection of the most probable particle displacement between the two images by a cross-correlation algorithm in a multipass mode, using interrogation areas with decreasing sizes from 64×64 square pixels to 32×32 square pixels and an overlap of 50 %. An important parameter in this context is the depth of correlation also called depth of focus. It represents the extent of the region around the image plane in which the image appears to be sharp and depends on the numerical aperture and magnification of the objective (see table 4.3). For our set-up the depth of focus is approximately 200 µm. That means that the instantaneous velocity field is calculated for a liquid layer of 200 µm in thickness. The position h_z of the image plane depends in the position adjusted by the microscope $h_{z,m}$ and the refractive index of the liquid phase n (see equation 4.1-2).

$$h_z = h_{z,m} \cdot n \qquad \text{with } n = 1.36 \text{ (ethanol)} \qquad (4.1\text{-}2).$$

The average velocity field is obtained by averaging over the instantaneous velocity fields of a certain number of image pairs. In single phase liquid flow this can directly be carried out using the PIV processing software (Davis 7). However, this is not the case for measurements in two-phase flow, since the experimental set-up does not allow synchronisation of the measurements with the gas bubbles and liquid slugs along the channel. It is thus initially necessary to pre-select image pairs containing an entire liquid slug, to calculate the instantaneous velocity fields and to extract the corresponding data. This velocity data is then treated in Matlab (MathWorks) to obtain the average velocity field within the liquid slugs. In our study we used the velocity data of 40 image pairs. The flow conditions for our experiments were chosen with respect to two criteria. Due to the limited observation area, the lengths of the liquid slugs should not exceed a value of about 2 mm. Furthermore, considering the post-treatment of the data for obtaining the average velocity field, it would be advantageous to conduct the measurements under conditions presenting a high uniformity of the slug lengths and low fluctuations of the bubble velocity. A good combination of both was found in the meandering channel with sharp bends. The corresponding flow rates and the hydrodynamic parameters, as well as their standard deviations are indicated in table 4.4.

fluid system	Q_G [ml/min]	Q_L [ml/min]	U_B [m/s]	$\sigma(U_B)$ [m/s]	l_S [mm]	$\sigma(l_S)$ [mm]
air-ethanol	0.89	1	0.0584	0.0007 (≈ 1.2 %)	1.746	0.021 (≈ 1.2 %)

Table 4.4: Operating conditions of the fluid system used in the present study for characterization of the liquid phase velocity field by microparticle image velocimetry microPIV in Taylor flow through a meandering microchannel with sharp bends (Q_G gas flow rate; Q_L liquid flow rate; U_B bubble velocity; σ standard deviation; l_S liquid slug length).

For the performance of the microPIV measurements, two further parameters have to be taken into account. At first the particle concentration has to be adjusted and in the following the time interval δt between two images of an image pair has to be estimated according to the operating conditions listed in table 4.4. The seeding particles are doped with Rhodamine B (Microparticles GmbH) and have a diameter of 2.8 µm. Further characteristics related to the inertia and Brownian motion of the particles can be considered as negligible for the present operating conditions. With respect to its concentration one considers a seeding between 5 and 15 particles per interrogation area as appropriate. In our study we aimed on a seeding of about 10 particles for an interrogation area IA of 32×32 square pixels. In order to attain this value we carried out a drop-by-drop approach. This means that we firstly added one droplet of the particle suspension ($1.8 \cdot 10^{10}$ particles/ml) to 50 ml of ethanol. Afterwards the liquid was fed to the microchannel at a flow rate of 1 ml/min and exposed to the laser light. From the camera images the number of particles located in areas corresponding to IA (scale 1.25 µm/pixel) was counted. This way we obtained an initial working liquid employed for the first measurements which was prepared by adding 50 droplets of the particle suspension to 50 ml of ethanol. However since the particles stuck on the walls of the microchannel and the feeding tube, the particle concentration was checked and adjusted before each measurement. As already mentioned above, the second parameter to find is an adequate time interval δt between images in an image pair. In this context one has initially to consider a criterion fixing the limits of particle motion for performing microPIV measurements. It principally means that between two laser pulses the particles should not travel a distance Δx greater than one quarter of the interrogation area and is precisely written as:

$$0.1 \text{ pixel} < \Delta x < ¼ \text{ IA} \qquad (4.1\text{-}3).$$

Applying a scale of 1.25 µm/pixel one obtains the travelling distance in µm and division by the flow velocity results in the threshold for δt. This is shown in table 4.5 for the values corresponding to the respective sizes of interrogation areas. Concerning the velocity value to carry out this estimation we employed the maximum liquid velocity at the centre axis of the channel. For our flow conditions this value can be assumed to be roughly two times the value of the bubble velocity (see table 4.4), which is 0.117 m/s.

IA [pixels^2]	¼ IA [pixels^2]	¼ IA [µm^2]	δt [µs]
64×64	16×16	≈ 20×20	< 171
32×32	8×8	≈ 10×10	< 86

Table 4.5: Estimation of the threshold value for the time interval δt to be used for the characterization of the liquid phase velocity field by microparticle image velocimetry microPIV (IA interrogation area; scale: 1.25 µm/pixel; calculation undertaken using $(0.25\text{IA})^{0.5}$ and assuming a maximum velocity of 0.117 m/s).

According to table 4.5 we decided to use δt = 80 µs for the microPIV measurements. The validation of an appropriate level of particle seeding, as well as an adequate approximation of the time interval can usually be undertaken by plotting the velocity profile extracted from the average velocity field in comparison to the profile based on theoretical correlations. However, since under two-phase flow conditions the average velocity field can not be directly obtained using the image processing software of the PIV equipment due the periodic nature of the flow (see explanations above), we decided to validate the measurement technique by performing a preliminary run for single phase liquid flow. This was done for a flow rate of 1 ml/min (U_{LS} = 0.031 m/s) and δt = 150 µs. At this the time interval was estimated in the same manner as above assuming a maximum velocity value of 0.062 m/s.

4.2 Results

4.2.1 Characterization of hydrodynamic parameters

As already mentioned within the introduction of this chapter, this section starts with the results of the hydrodynamic parameters obtained for the air-ethanol fluid system at Capillary numbers in the order of 10^{-3}. Since the formation of the two phase flow starts at the inlet section, it would initially be interesting to have a look on the mechanism of bubble formation. This is shown for a series of images (Figure 4.2) taken at the inlet section of the meandering channel with sharp bends at the lowest flow rate combination employed in this study (U_{TP} = 0.022 m/s; $\varepsilon_L \approx 0.45$; $Ca_{TP} = 1 \cdot 10^{-3}$). At this t^* is the time value corresponding to each image normalized by the time of the entire image series, which was about 213 ms. The image given for $t^* = 0$ shows the situation just after the break-up of a bubble, indicated by a slight interface deformation at its rear end . It thus represents the end of the bubble formation and may be considered as the start of the formation of a new bubble. It can also be seen that the bubble interface appears as a kind of a thick dark bond. This indicates the depth-wise curvature of the bubble interface in the corners of the channel cross section, as well as at the bubble front and rear caps. The inner bright area of the bubble shows the region where the liquid film and the bubble interface are flattened out against the channel wall.

$t^* = 0$	$t^* = 0.33$	$t^* = 0.56$	$t^* = 0.67$	$t^* = 0.89$	$t^* = 1$
start of the formation of a new bubble	filling stage	end of filling stage	squeezing stage	end of squeezing stage	end of bubble formation

Figure 4.2: Representation of the mechanism of Taylor bubble formation for a series of images recorded at the inlet of a meandering microchannel using air and ethanol as working fluids at flow rates of 0.36 ml/min and 0.3 ml/min, respectively (superficial two phase velocity U_{TP} = 0.022 m/s; liquid hold-up $\varepsilon_L \approx 0.45$; two phase Capillary number $Ca_{TP} \approx 1 \cdot 10^{-3}$, t^* represents the time value of each image within the sequence, normalized by the total time of the sequence, here 213 ms).

As already mentioned in chapter 3 (section 3.5.2) the process of bubble formation is divided into different steps or stages. The first stage is the filling stage, shown in figure 4.2 at $t^* = 0.33$. Here, the gas phase penetrates into the main channel and fills the channel cross section until it touches the channel wall opposite to the gas inlet channel ($t^* = 0.56$ in figure 4.2). In chapter 3 (section 3.5.2), we also called this stage the initial step of bubble formation. From this moment the bubble tip starts to grow in the downstream direction, whilst the interface at the gas-inlet (bubble neck) is squeezed. This is indicated by the thinning of the bright area at the bubble neck comparing the images taken at $t^* = 0.56$ and $t^* = 0.67$ in figure 4.2. The end of this squeezing stage is attained at $t^* = 0.89$. At this the bubble neck is constricted and completely curved which can be seen by the disappearance of the bright area at the bubble neck. Finally the gas-liquid interface at the bubble neck is disrupted resulting in the formation of a Taylor bubble as shown at $t^* = 1$. These descriptions principally agree with the observations of Garstecki et al. (2006) and van Steijn et al. (2007), discussed in chapter 3 (section 3.5.2). According to this it was shown that for a pseudo-T inlet section the dimensionless bubble length may be correlated as follows:

$$\frac{l_B}{w} \approx \alpha_1 + \alpha_2 \frac{U_{GS}}{U_{LS}} \qquad (4.2\text{-}1),$$

where α_1 and α_2 are correlation constants. According to the section 3.5.2, α_1 corresponds to the dimensionless length of the bubble tip at the end of the filling stage. We will label this in the following as the dimensionless initial bubble length $l_{B,ini}/w$. The constant α_2 is related to the width of the gas inlet channel w_{in} and the extent of the leakage flow around the bubble tip during the squeezing stage (see chapter 3, section 3.5.2). In the following we intend to use equation 4.2-1 and the theoretical considerations in order to check the applicability of scaling law 4.2-1 in predicting the bubble lengths measured in this study. This firstly requires a closer look at the length of the bubble tip at the end of the filling stage (see figure 4.3). Concerning the measurement of this value, it turned out that capturing the moment where the bubble tip touches the channel wall opposite to the gas-inlet is the main difficulty. This is depicted by means of the two example images given in figure 4.3. At this the image on the left hand side where $l_{B,ini} \approx w$, shows a situation just before the interface reaches the channel wall. However, in the image on the right hand side of figure 4.3 ($l_{B,ini} \approx 1.1w$), it can be seen that the bubble neck is slightly thinned with what this situation may already be attributed to the squeezing stage. Nevertheless, it shows that the length of the bubble tip is only slightly different from the value of the channel width and thus $\alpha_1 = l_{B,ini}/w \approx 1$ may be considered as a good approximation.

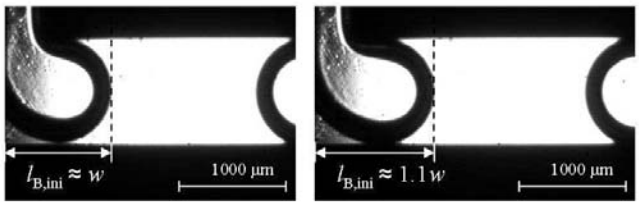

Figure 4.3: Example images showing the situation in the end of the filling stage during the formation of a Taylor bubble at the inlet of a meandering microchannel using air and ethanol as working fluids at flow rates of 0.36 ml/min and 0.3 ml/min, respectively ($l_{B,ini}$ initial bubble length, w channel width, superficial two phase velocity U_{TP} = 0.0218 m/s; liquid hold-up $\varepsilon_L \approx 0.45$; two phase Capillary number $Ca_{TP} \approx 1 \cdot 10^{-3}$).

As a next step we need to outline the possible values of the correlation constant α_2. According to the model of Garstecki et al. (2006), α_2 corresponds to the ratio w_{in}/w (see chapter 3, section 3.5.2). However, this approach does not account for the leakage flow around the bubble, which was visualized in the study of van Steijn et al. (2007). In their study, the extent of the leakage flow was taken into account by attributing $\alpha_2 = 1.5 w_{in}/w$ using a microchannel of square cross-section an inlet section with $w_{in}/w = 1$ at $Ca_{TP} = 2.4 \cdot 10^{-3}$. Since the operating conditions of our study ($1 \cdot 10^{-3} \leq Ca_{TP} \leq 3.2 \cdot 10^{-3}$) are similar to those of van Steijn et al. (2007), one may assume that the extent of the leakage flow should be approximately the same or slightly smaller. In order to check this we will compare our data to two different situations one without leakage flow by directly applying the model of Gastecki et al. (2006), and another one with leakage flow where α_2 is based on a combination of the Gastecki-model and the findings of van Steijn et al. (2007). The corresponding expressions for the respective correlation constants may thus be written as follows:

- no leakage flow (lower limit): $\alpha_1 = \frac{l_{B,ini}}{w} \approx 1$ and $\alpha_2 \approx \frac{w_{in}}{w} = 0.525$ (4.2-2).
- with leakage flow: $\alpha_1 = \frac{l_{B,ini}}{w} \approx 1$ and $\alpha_2 \approx 1.5 \frac{w_{in}}{w} \approx 0.788$ (4.2-3).

In figure 4.4 the experimental values of the dimensionless bubble length obtained with the straight and the meandering channel configurations are shown and compared to the predictions based on expressions 4.2-1 – 4.2-3. At this the error bars represent confidence intervals with a confidence level of 95 %, considering a series of 10 values. The largest deviations from the average values were detected for the straight channel configuration. This is even more distinctive if one only considers standard deviations. Those are between 1 and 10% in the case of the straight channel and in a range between 0.4 and 3% for both meandering channels. This result may be attributed to the difference in the channel length which is 70 mm for the straight channel and about 300 mm for the meandering channels. Accordingly, the disruption of the gas-liquid interface at the outlet induces a greater relative pressure fluctuation within the straight channel and it can thus be seen that these fluctuations have an influence on the bubble formation process.

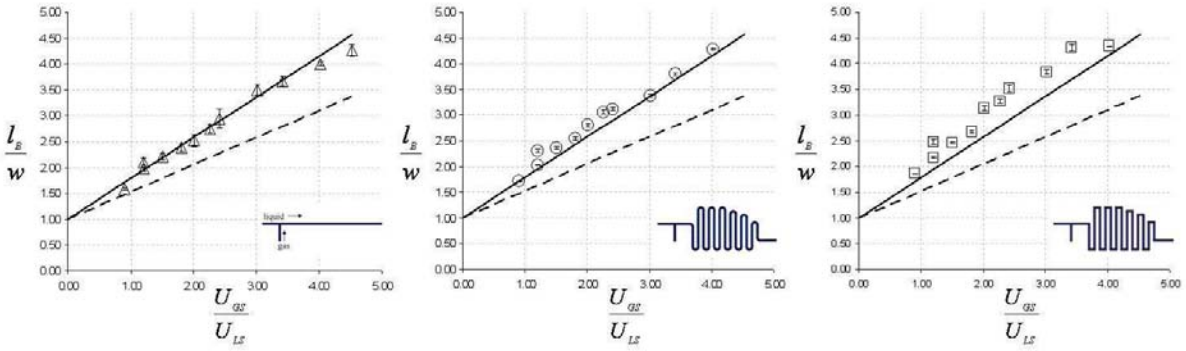

Figure 4.4: Graphs of measured and predicted dimensionless bubble lengths versus the ratio of superficial phase velocities for the three microchannel configurations employed in this study using air and ethanol as working fluids (l_B bubble length; w channel width, here 1mm; U_{GS} superficial gas phase velocity; U_{LS} superficial liquid phase velocity; continuous line: prediction according to 4.2-1 and 4.2-3; broken line: prediction according to 4.2-1 and 4.2-2; range of Capillary numbers: $1 \cdot 10^{-3} \leq Ca_{TP} \leq 3.2 \cdot 10^{-3}$; range of liquid hold-ups $0.18 \leq \varepsilon_L \leq 0.45$).

In figure 4.4 it can be seen that the data obtained for the straight channel and the meandering channel with smoothed bends appear to be well predicted by the expressions taking into account the influence of the leakage flow. On the other hand, the results obtained with the meandering channel with sharp corner bends are slightly greater than the predicted value. In general, the results shown in figure 4.4 suggest that for the present conditions, the bubble lengths are best fitted by applying the correlation constants in 4.2-3, which takes into account leakage flow. In order to perform a comparative evaluation, the entire experimental data are plotted in a single graph with the values predicted by relation 4.2-3. This is shown in figure 4.5. Referring to chapter 3 (section 3.5.2) the measured and predicted dimensionless bubble lengths are additionally plotted versus the liquid hold-up. This is done by assuming that $\varepsilon_L \approx U_{LS}/U_{TP}$ and that $\varepsilon_G \approx U_{GS}/U_{TP}$, which enables equation 4.2-1 to be rewritten as:

$$\frac{l_B}{w} \approx \alpha_1 + \alpha_2 \frac{\varepsilon_G}{\varepsilon_L} \qquad (4.2\text{-}4),$$

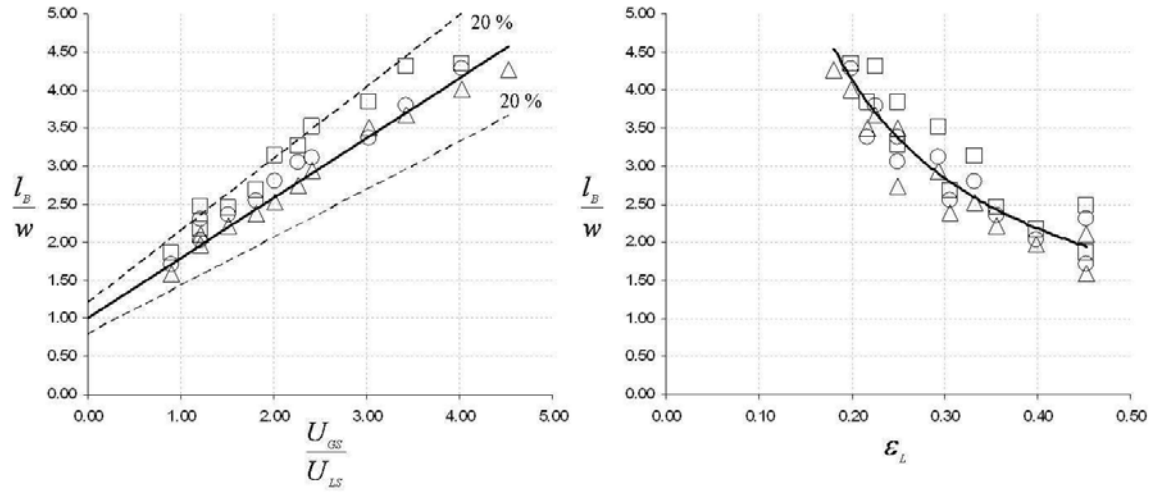

Figure 4.5: Graphs of measured and predicted dimensionless bubble lengths versus the ratio of superficial phase velocities and the liquid hold-up for the three microchannel configurations employed in this study using air and ethanol as working fluids (l_B bubble length; w channel width, here 1 mm; U_{GS} superficial gas phase velocity; U_{LS} superficial liquid phase velocity; ε_L liquid hold-up; continuous lines: predictions according to equations 4.2-1 and 4.2-4, using the constants given in 4.2-3; broken lines indicate 20 % deviation from the value predicted on the basis of expressions 4.2-1 and 4.2-.3; triangles: straight channel; circles: meandering channel with smoothed bends; squares: meandering channel with sharp bends; range of Capillary numbers: $1 \cdot 10^{-3} \leq Ca_{TP} \leq 3.2 \cdot 10^{-3}$).

Figure 4.5 verifies the reliability of the prediction of bubble lengths based on equation 4.2-1 and the correlation constants specified by expression 4.2-3 . It shows that 97 % of the measured bubble lengths may be predicted with an error of less than 20 %. This result strengthens the assumption that the application of a factor of 1.5 in α_2 (see expressions in 4.2-3) well approximates the influence of the leakage flow on the bubble formation at low Capillary numbers and low liquid hold-ups. In the following we will deal with the results of the corresponding dimensionless slug lengths in a similar manner. For this purpose we derived the following scaling, which is analogous to the bubble length correlation given in equation 4.2-4.

$$\frac{l_S}{w} \approx \alpha_2 + \alpha_1 \frac{U_{LS}}{U_{GS}} \qquad (4.2\text{-}5),$$

where the correlation constants α_1 and α_2 are defined by expressions 4.2-2 and 4.2-3. The values of the dimensionless slug length measured in the straight and the meandering channel configurations are shown in figure 4.6 together with the predictions based on expressions 4.2-5, 4.2-2 and 4.2-3. At this the error bars represent confidence intervals with a confidence level of 95 %, considering a series of 10 values. Once more, the largest deviations from the average values were detected for the straight channel configuration. In terms of standard deviations values differing by up to 25 % from the average were found here, while the standard deviations for the meandering channels were generally between 1% and 4%.

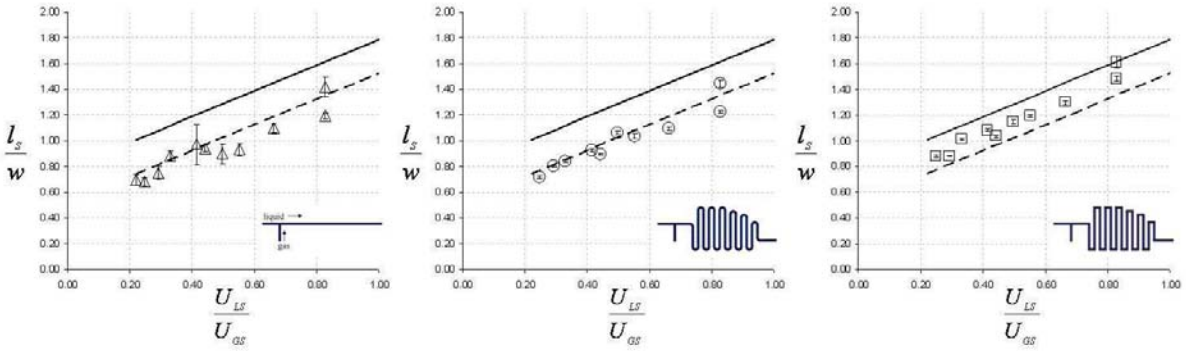

Figure 4.6: Graphs of measured and predicted dimensionless slug lengths versus the ratio of superficial phase velocities for the three microchannel configurations employed in this study using air and ethanol as working fluids (l_S slug length; w channel width, here 1 mm; U_{LS} superficial liquid phase velocity; U_{GS} superficial gas phase velocity; continuous line: prediction according to 4.2-5 and 4.2-3; broken line: prediction according to equations 4.2-5 and 4.2-2; range of Capillary numbers: $1 \cdot 10^{-3} \leq Ca_{TP} \leq 3.2 \cdot 10^{-3}$; range of gas hold-ups $0.55 \leq \varepsilon_G \leq 0.82$).

From figure 4.6 it can be seen that the dimensionless slug lengths obtained with the straight channel and the smoothed meandering seems to be independent of leakage flow, while the data for the sharp meandering channel rather tend to the prediction where leakage flow is accounted for. However, it has to be pointed out that here the difference between the two predictions is very small (about 200 µm). In order to emphasized a general tendency the data of all channel configurations are re-plotted in a single graph. This is shown in figure 4.7. Assuming that $\varepsilon_L \approx U_{LS}/U_{TP}$ and that $\varepsilon_G \approx U_{GS}/U_{TP}$ the measured and predicted dimensionless slug lengths are additionally plotted versus the gas hold-up by means of equation 4.2-6.

$$\frac{l_S}{w} \approx \alpha_2 + \alpha_1 \frac{\varepsilon_L}{\varepsilon_G} \qquad (4.2\text{-}6)$$

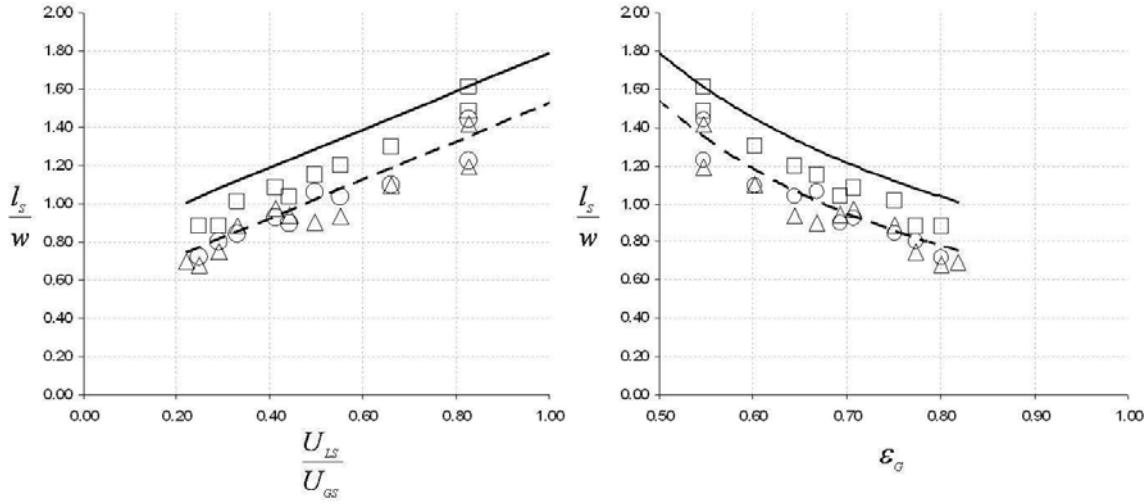

Figure 4.7: Graphs of measured and predicted dimensionless slug lengths versus the ratio of superficial phase velocities and the gas hold-up for the three microchannel configurations employed in this study using air and ethanol as working fluids (l_S bubble length; w channel width, here 1 mm; U_{LS} superficial liquid phase velocity; U_{GS} superficial gas phase velocity; ε_G gas hold-up; continuous line: prediction according to equations 4.2-5 and 4.2-6, using the constants given in 4.2-3; broken line: prediction according to equations 4.2-5 and 4.2-6, using the constants given in 4.2-2; triangles: straight channel; circles: meandering channel with smoothed bends; squares: meandering channel with sharp bends; range of Capillary numbers: $1 \cdot 10^{-3} \leq Ca_{TP} \leq 3.2 \cdot 10^{-3}$).

From figure 4.7 it may be concluded that compared to the dimensionless bubble lengths (see figure 4.4), the influence of leakage flow seems to be less pronounced for the range of slug lengths measured in this study. Due to the small difference between the lower and upper limits, all of the experimental slug lengths may be predicted by the lower limit with an error of less than 20 %. This shows that even at low Capillary numbers, where leakage flow is usually an important feature, the lower limit may still provide a good approximation for the prediction of slug lengths.

Next we are concerned with the results of the bubble velocities. According to the analysis undertaken in chapter 3 (see figure 3.12, section 3.5.1), the velocity of a fully lubricated bubble is generally greater than the superficial two phase velocity. Furthermore, it was suggested that for $Ca \geq O(10^{-3})$, the values of dimensionless bubble velocities in the case of a channel of rectangular cross-section should lie between those of a square and circular channel (compare figure 3.15, section 3.5.1). Hence, for the range studied here ($1 \cdot 10^{-3} \leq Ca_{TP} \leq 3.2 \cdot 10^{-3}$) we may expect a liquid film fraction of about 10 % and a corresponding dimensionless bubble velocity of about $U_B/U_{TP} \approx 1.1$. In order to check this, the bubble velocities measured in each channel configuration are plotted versus the superficial two phase velocity. This is shown in figure 4.8 together with the lines indicating the expected dimensionless bubble velocities. Here the fluctuations of the bubble velocities caused by the relative pressure fluctuations in the channel are illustrated by means of the standard deviations form the average values. The corresponding error bars are only indicated for the straight channel, where deviations up to 12 % were detected. In comparison, the bubble velocity fluctuations in the meandering channels were found to be of negligible value, with maximum standard deviations of about 3%.

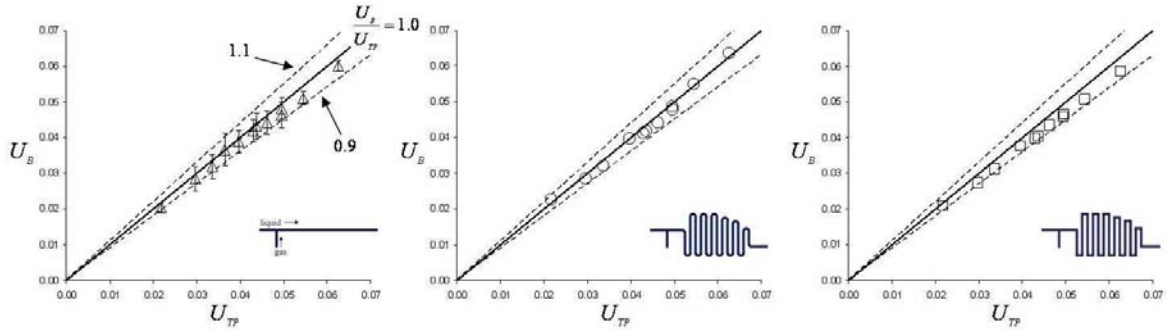

Figure 4.8: Graphs of measured bubble velocities U_B versus superficial two phase velocities U_{TP} for the three microchannel configurations employed in this study using air and ethanol as working fluids (range of Capillary numbers: $1 \cdot 10^{-3} \leq Ca \leq 3.5 \cdot 10^{-3}$).

In figure it can be seen that the experimental dimensionless bubble velocities are generally slightly lower than unity (U_B/U_{TP} = 1). According to chapter 3 (see figure 3.12, section 3.5.1), this would usually suggest a partial drying out of the liquid film. However, such a phenomenon was not observed here. A possible reason for this behavior may be attributed to the dimensions of the channel cross section. Up to now we assumed a channel width of 1000 µm and a height of 500 µm to compute the superficial phase velocities from the respective flow rates. As already mentioned in the section concerned with the microchannel design (see chapter 3, section 3.7) the present channels were fabricated by etching a silicon wafer from the top to the bottom. During this manufacturing process the etching plasma also attacks the side walls of the channel cross-section. In our case this finally led to a width of 1000 µm at the top and of about 1100 µm at the bottom of the microchannel. We thus obtain a cross-sectional area of about $5.25 \cdot 10^{-7}$ m^2 instead of $5.0 \cdot 10^{-7}$ m^2. In consideration of this we modify the superficial two phase velocities and re-plot our results. This is shown for the data of all channel configurations in figure 4.9.

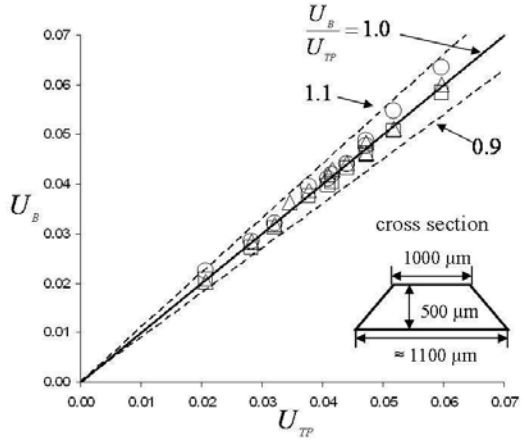

Figure 4.9: Graph of measured bubble velocities U_B versus superficial two phase velocities U_{TP} for the three microchannel configurations employed in this study using air and ethanol as working fluids after recalculation of U_{TP} using the dimensions of the channel cross section illustrated above (range of Capillary numbers: $1 \cdot 10^{-3} \leq Ca \leq 3.5 \cdot 10^{-3}$).

As can be seen in figure 4.9, the correction of the channel cross-section in the computation of superficial two phase velocities shifted the dimensionless bubble velocities to higher values, which are, however, still slightly lower than $U_B/U_{TP} \approx 1.1$ This means that the film faction occupies less than 10 % of the channel cross-section and that for Capillary numbers slightly larger than 10^{-3} the bubble profile in a rectangular microchannel may still be represented by that of a static bubble as proposed by Wong et al. (1992, 1995; see chapter 3, section 3.5.2, table 3.7).

In the following we intend to perform a similar investigation using nitrogen and water as working fluids. Here, the principle aim is to identify interesting operating conditions for the characterization of gas-liquid mass transfer as a function of hydrodynamic parameters, which will be treated in the next

chapter. For this reason, apparatus with a larger range of flow rates (see table 4.2) were employed. In a first step we performed an experimental run with the meandering channel with sharp corner bends at the lowest gas and liquid flow rates offered by the equipment (Q_G = 1 ml/min; Q_L = 0.22 ml/min). The same run was then repeated using ethanol as liquid phase, in order to check the influence of surface tension on bubble lengths, as previously discussed in chapter 3 (section 3.5.2). According to that, surface tension is an important parameter regarding the flow of liquid by-passing a growing bubble. The pressure gradient responsible for this leakage flow may be approximated, in the case of a pseudo-T junction and a rectangular cross-section, as follows:

$$\Delta p_{leakage} \approx \gamma\left(\frac{1}{w}\right) \qquad (4.2\text{-}7).$$

Since the surface tension of water is significantly greater than that of ethanol, the pressure gradient and therefore the extent of leakage flow should be more pronounced. This means, that with the present conditions, one may expect the bubble lengths obtained using water to be significantly greater than those for ethanol as liquid phase. The example images (see figure 4.10) taken from the test section for both fluid systems confirm these theoretical considerations.

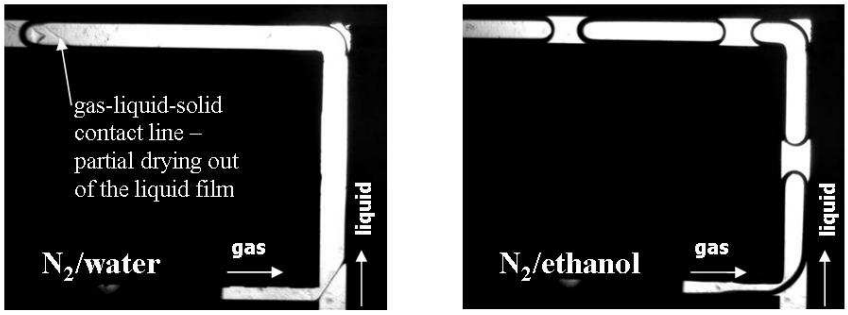

Figure 4.10: Example images of gas-liquid two-phase flow obtained in a meandering microchannel with sharp corner bends for different fluid systems at a fixed liquid hold-up of ε_L = 0.18 and a superficial two phase velocity of U_{TP} = 0.0405 m/s.

Following the discussion made above and taking into consideration the scaling law 4.2-1, one may state furthermore that due to the fact that the surface tension of water is approximately three-times the value of the surface tension of ethanol, the bubbles generated with the N_2-water system should be approximately three-times longer than those obtained with N_2-ethanol. In order to verify this assumption we measured the bubbles lengths for both fluid systems. In the case of N_2-ethanol we obtained an average value of $l_B \approx 6.2$ mm. For the N_2-water system the length of the growing bubble exceeded the area of observation. In order to make an estimation we measured the velocity of bubble growths, which was approximately equal to U_{TP} and determined the total time between the penetration of the gas phase into the main channel and the break-up of the bubble at the inlet section (here about 0.88 s). Based on that, we computed a bubble length of $l_B \approx 35.2$ mm, which is about six-times the value obtained for ethanol. A possible explanation of this behaviour can be found by taking into account the corresponding two-phase Capillary numbers, which are $Ca_{TP} = 1.8 \cdot 10^{-3}$ in the case of N_2-ethanol and $Ca_{TP} = 6 \cdot 10^{-4}$ for N_2-water. Referring to the considerations made in chapter 3 (section 3.5.2), a decrease in Ca_{TP} at fixed liquid hold-up ε_L physically represents an increase in the influence of surface tension forces relative to viscous stresses. The latter were identified as responsible for the squeezing of the interface at the bubble neck and finally the break-up of the bubble. With respect to the example shown in figure 4.10, this means that not only the surface tension of water is three-times greater, but also the relative influence of surface tension forces is increased and thus, in comparison with N_2-ethanol, the ratio of bubble lengths is greater than three. Consequently, this first experimental runs give also a good illustration about the influence of the Capillary number on bubble lengths, which

is in good agreement with the theoretical considerations undertaken in chapter 3 (section 3.5.2). However, regarding the slug lengths, which were measured here as $l_S \approx 0.95$ mm for N_2-ethanol and $l_S \approx 2.2$ mm for N_2-water, this tendency appears to be less pronounced.

A further look at the example images in figure 4.10 reveals another important feature. For the N_2-water system, it can be seen here that the liquid film at the front of the bubble tip dries out. The occurrence of this phenomenon allows checking in principle the corresponding criteria, derived in chapter 3 (see section 3.5.1.5). According to that, it was stated that a drying-out of the liquid film might be prevented if the film contact time is much smaller than the dewetting time (see 4.2-8).

$$\frac{l_B}{U_B} << \frac{w}{U_{dew}} \qquad \text{with Ca} \geq O(10^{-3}) \qquad (4.2\text{-}8).$$

The dewetting velocity U_{dew} of water on pyrex glass is about 7 mm/s with what one obtains a dewetting time of about 0.14 s for our channel geometry. Since, in the present example (see figure 4.10) a dry patch already occurred one should expect the opposite relation of 4.2-8, that means that the film contact time should be approximately equal or greater than the dewetting time. And indeed using the bubble length mentioned above and setting $U_B \approx U_{TP}$, a film contact time of 0.87 s is yielded, which corresponds to about six-times the value of the dewetting time. Finally, it has to be noted here that the long bubbles generated with N_2-water induced significant fluctuations of the two-phase flow.

In order to avoid the formation of bubbles with excessive lengths and with that the appearance of dewetting and strong flow fluctuation phenomena, the flow rates of nitrogen and water were strongly increased to ranges of $4.5 \leq Q_G \leq 6$ ml/min and $0.7 \leq Q_L \leq 4$ ml/min. At this, we considered ranges of superficial two-phase velocities 0.175 m/s $\leq U_{TP} \leq$ 0.337 m/s and liquid hold-ups of $0.13 \leq \varepsilon_L \leq 0.47$. Example images of the flow obtained at lower superficial velocities (U_{TP} = 0.22 m/s) of this range are shown in figure 4.11. These images were taken from a sequence and show situations just before and after the break-up of a bubble. Here, it can initially be seen that the formation of bubbles is not taking place at the inlet section, anymore. Gas and liquid phases co-flow until the end of the first channel branch, corresponding to the entry of the first U-return bend. At this position the bubble tip grows into the bend until the interface is ruptured at the entry of the bend, leading to the formation of a bubble. This process as well as the position of the interface rupture remained constant which resulted in the formation of a stable and regular Taylor flow (uniformly spaced bubbles and slugs).

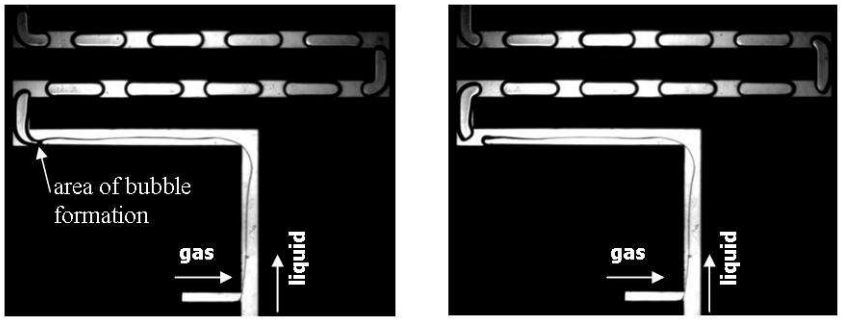

Figure 4.11: Example images of nitrogen-water flow obtained in a meandering microchannel with sharp corner bends at a superficial two phase velocity of U_{TP} = 0.22 m/s and a liquid hold-up of ε_L = 0.31 (two-phase Capillary number $Ca_{TP} = 3 \cdot 10^{-3}$).

Compared with figure 4.10, it can be seen furthermore that the bubbles shown in figure 4.11 are fully lubricated. The average bubble lengths measured here was about 3.7 mm. Assuming $U_B \approx U_{TP}$, one obtains a film contact time of 0.017 s. This is one order of magnitude smaller than the dewetting time (0.14 s) and thus well fulfills the criterion for the absence of the occurrence of dry-patches, as given in 4.2-8. The flow behavior shown in 4.11 is representative for three different flow rate combinations detected in a range of $U_{TP} \leq 0.291$ m/s and $\varepsilon_L \leq 0.31$. On the other hand, a further increase of the liquid

hold-up ($\varepsilon_L \geq 0.31$) in a range of two phase velocities of 0.241 m/s $\leq U_{TP} \leq$ 0.337 m/s resulted in the formation of a generally irregular Taylor flow, which means, that bubble and slug lengths remarkably varied for a fixed set of flow rates. In order to illustrate the origin of this characteristic a sequence of representative example images is shown in figure 4.12. At this each image is labeled with its corresponding time value t^*, normalized by the total time of the sequence, which was about 0.186 s. The situation at $t^* = 0$, showing the formation of a bubble in the end of the first branch, is similar to that depicted in connection with figure 4.11 and the resulting bubble can be seen at $t^* = 0.02$. However, for $t^* = 0.02$ it can also be seen that, instead of a bubble tip growing downstream, the gas-liquid interface is disrupted at the edge, located at the entry of the first branch. The resulting bubble shows a highly deformed interface and travels downstream until reaching the entry of the first U-return bend ($t^* = 0.08$). At this position its interface is constricted and ruptured to form two bubbles ($t^* = 0.09$). In the following the bubbles are initially formed for a certain period at the edge, located at the entry of the first branch ($t^* = 0.12$). Afterwards, the bubble tip grows more and more downstream, and the position of interface rupture continuously approaches the entry of the first U-return bend. Even if the flow appears to be regular at $t^* = 1$, the bubble and slug lengths are significantly larger compared to the beginning of the sequence ($t^* = 0$).

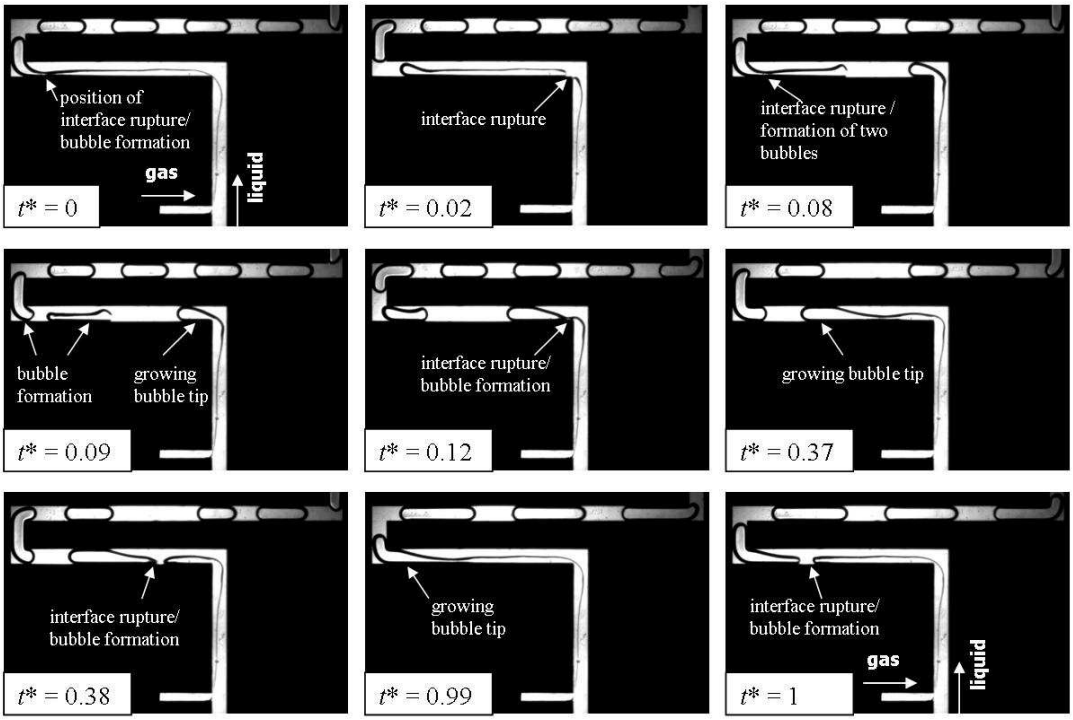

Figure 4.12: Sequence of example images of nitrogen-water flow obtained in a meandering microchannel with sharp corner bends at a superficial two phase velocity of U_{TP} = 0.241 m/s and a liquid hold-up of ε_L = 0.36 (two-phase Capillary number $Ca_{TP} = 3.3 \cdot 10^{-3}$; t^* represents the time value of each image within the sequence, normalized by the total time of the sequence, here 0.186 s).

Consequently, the formation of an irregular Taylor is due to multiple interface ruptures, as well as the fact that the position of the bubble break-up and with that the conditions of bubble formation continuously change.

In the following we decided to check the flow, which can be obtained for an inverted contacting mode. That means that the liquid phase now entered the main channel by the side-channel of the pseudo-T-junction. For the four conditions studied here, in a range of 0.175 m/s $\leq U_{TP} \leq$ 0.291 and 0.13 $\leq \varepsilon_L \leq$ 0.36, a stable and regular Taylor flow was always obtained. Example images and the

corresponding operating conditions are shown in detail in figure 4.13. Here, similar to the case of the normal contacting mode at lower flow rates (see figure 4.11), the gas and the liquid phases co-flow until the entry of the first U-return bend. At this area, indicated in figure 4.13a, the gas phase then invades approximately the entire channel corner, or at least a large portion of it. Afterwards, within this area the liquid phase pushes the interface towards the channel edge, which is located at the inner side of the entry of the first U-return bend. The example images in figure 4.13 thus show the state of maximum constriction of this bubble neck and with that the situation directly before the break-up and formation of a new bubble. In contrast to the normal contacting mode (compare figure 4.11 and 4.12), the rupture of the gas-liquid interface in the case of the inverted contacting mode (see figure 4.13) occurred always at the same position, the inner channel edge. This is the origin of the formation of a stable and regular Taylor flow for all the flow rate combinations studied here. A good illustration of this is given by a comparison of figure 4.13b with the sequence in figure 4.12, since for both, superficial two-phase velocities and liquid hold-ups are identical.

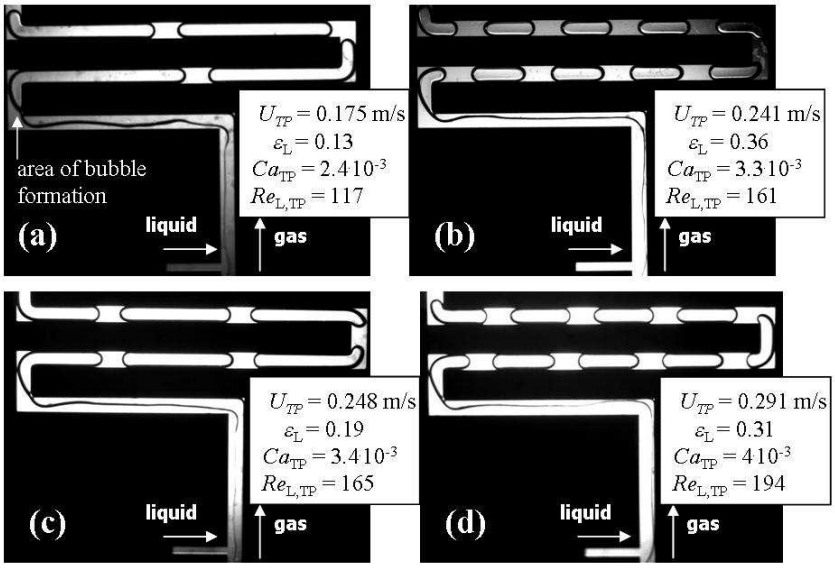

Figure 4.13: Example images of nitrogen-water flow, obtained in a meandering microchannel with sharp corner bends for an inverted contacting mode (U_{TP} superficial two-phase velocity; ε_L liquid hold-up; Ca_{TP} two-phase Capillary number; $Re_{L,TP}$ two-phase Reynolds number based on liquid phase properties and the hydraulic diameter of the channel).

According to the descriptions of the bubble formation process, made above, one may assume that the initial width of the bubble neck is approximately equal to channel width. With respect to the scaling of bubbles and slugs, we may thus consider the present case as comparable to a situation where gas and liquid inlets are of the same dimensions as the main channel. Hence, the lengths of bubbles and slugs measured from the recorded sequences of the flow may be compared to the corresponding scaling laws, discussed in chapter 3, section 3.5.2 (see explanations undertaken for figure 3.19). In this connection lower limits of dimensionless bubble and slug lengths can be expressed as follows:

$$\frac{l_B}{w} \approx \varepsilon_L^{-1} \qquad \text{(4.2-9), and} \qquad \frac{l_S}{w} \approx \varepsilon_G^{-1} \qquad \text{(4.2-10),}$$

Furthermore, it was shown that the influence of leakage flow on bubble lengths appeared to be well represented by a correlation of Sobieszuk et al. (2007) and Pohorecki and Kula (2008), which may thus serve as an upper limit (see 4.2-11).

$$\frac{l_B}{w} = 1.3\varepsilon_G^{0.106}\left(1-\varepsilon_G\right)^{-1} \mathrm{Re}_{L,TP}^{-0.009}\, Ca_{TP}^{-0.013} \qquad \text{(4.2-11).}$$

However, one has to bear in mind, that its consideration as an upper limit is based on an evaluation carried out for the case of liquids with low surface tension (see chapter 3, section 3.5.2). We thus decide to additionally include the correlations given by Qian and Lawal (2006). According to that, bubble and slug lengths are expressed as:

$$\frac{l_B}{w} = 1.637\varepsilon_G^{0.107}\left(1-\varepsilon_G\right)^{-1.05}\mathrm{Re}_{L,TP}^{-0.075}\,Ca_{TP}^{-0.0687} \qquad (4.2\text{-}12),$$

$$\frac{l_S}{w} = 1.637\varepsilon_G^{-0.893}\left(1-\varepsilon_G\right)^{-0.05}\mathrm{Re}_{L,TP}^{-0.075}\,Ca_{TP}^{-0.0687} \qquad (4.2\text{-}13).$$

The comparison of the data, obtained from image sequences of the operating conditions indicated in figure 4.13, with expressions 4.2-9 – 4.2-13 is shown in figure 4.14. Here, it can initially be seen that, the correlation given in 4.2-11 (continuous black colored curve in figure 4.14a) well fits the measured bubble lengths, with exception of the value obtained at the lowest liquid hold-up. However, since it was generally considered here as an upper limit one may suppose that, in the case of water as liquid phase, the influence of leakage flow and with that the influence of surface tension on bubble lengths seems to be more pronounced than it is predicted by this expression. On the other hand 4.2-12 (continuous grey colored curve in figure 4.14a), predicts values slightly larger than the experimental ones. Since, this expression was developed on the base of two-dimensional numerical simulations; one may assume it to be comparable to a channel of square cross-section when projected on three dimensions. Thus the correlation of Qian and Lawal (2006) may be considered as an upper limit for the case of water-like liquid phase properties.

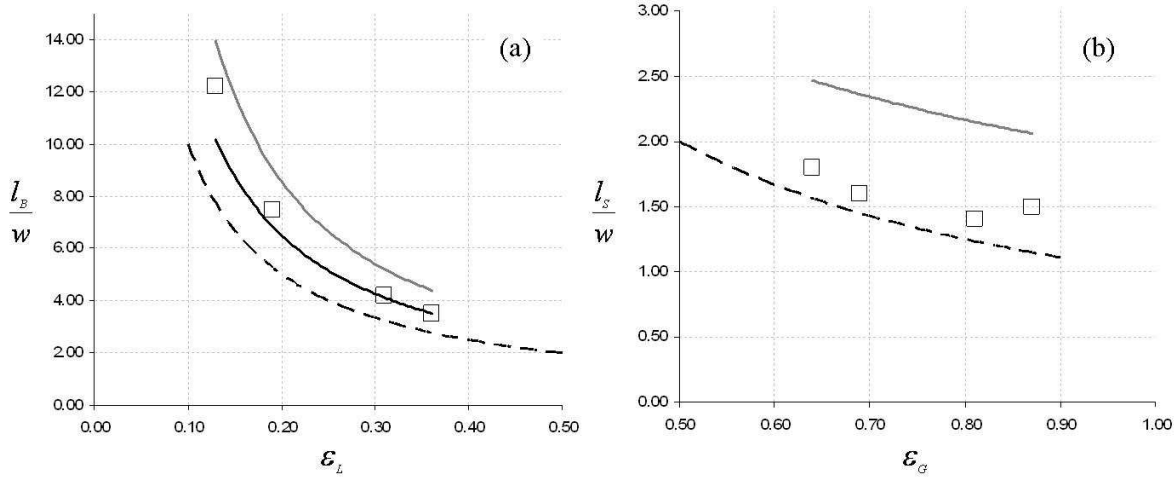

Figure 4.14: Graphs of dimensionless bubble and slug lengths as a function of liquid and gas hold-ups for a nitrogen and water fluid system (l_B bubble length; l_S slug length; w channel width, here 1 mm; ε_L liquid hold-up; ε_G gas hold-up; squares: experimental values obtained for an inverted contacting mode in a meandering microchannel with sharp corner bends in a range of two-phase Capillary numbers of $2.4\cdot10^{-3} \leq Ca_{TP} \leq 4\cdot10^{-3}$ and two-phase Reynolds numbers of $117 \leq Re_{L,TP} \leq 194$; broken curves: lower limits according to 4.2-9 and 4.2-10; continuous black colored curve: prediction of bubble lengths according to equation 4.2-11; continuous grey colored curves: predictions according to equation 4.2-12 and 4.2-13).

Furthermore, in figure 4.14a it can be seen that with increasing liquid hold-up the dimensionless bubble lengths tend to approach the simple scaling law 4.2-9, serving here as an lower limit (broken curve in figure 4.14a). This tendency is in good agreement with the theoretical analysis, carried out in chapter 3, section 3.5.2 (see explanations undertaken for figure 3.19). With respect to the slug lengths, shown in figure 4.14b, it can initially be seen that for the present range of operating conditions the estimations yielded from equations 4.2-10 (lower limit) and 4.2-13 (Qian and Lawal, 2006; continuous grey colored curve) differ from each other by less than 1 mm. The measured slug lengths generally tend to closely approach the lower limit, given by the scaling law 4.2-10. This result is similar to what was shown previously for the air-ethanol system (see figure 4.7). This means that for gas hold-ups in a range of $\varepsilon_G \geq 0.5$, the simple scaling laws, neglecting the influence of fluid properties, may generally serve as a good estimation for the prediction of slug lengths.

The bubble velocities measured for the present operating conditions are plotted versus the superficial two-phase velocities in figure 4.15. From this graph we obtain an average dimensionless bubble velocity of $U_B/U_{TP} \approx 1.6$. The corresponding range of Capillary numbers is $4 \cdot 10^{-3} \leq Ca \leq 6 \cdot 10^{-3}$.

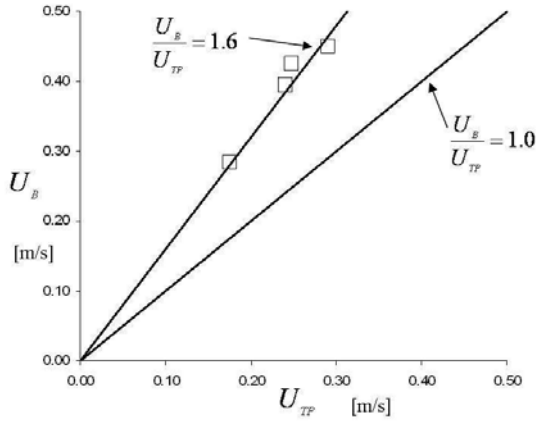

Figure 4.15: Graph of measured bubble velocities U_B versus superficial two phase velocities U_{TP} obtained for an inverted contacting mode of nitrogen and water in a meandering microchannel with sharp corner bends in a range of Capillary numbers of $4 \cdot 10^{-3} \leq Ca \leq 6 \cdot 10^{-3}$.

However, according to chapter 3, section 3.5.1 (see figure 3.15), the dimensionless bubble velocity expected for the range of Capillary numbers mentioned above should not exceed a value of $U_B/U_{TP} \approx 1.2$. For illustrative purpose it is useful to express this behavior in terms of the fraction of the channel cross-section occupied by the liquid film. According chapter 3, section 3.5.1 the correlation between the dimensionless velocity of a fully lubricated bubble and the film fraction ε_F is given as follows:

$$\frac{U_B}{U_{TP}} = \frac{1}{(1-\varepsilon_F)} \qquad (4.2\text{-}14).$$

Thus, in consideration of equation 4.2-14 the film fraction should generally not exceed a value of 17 %. The film fraction computed by means of the average dimensionless bubble velocity found here is about 38 %, which is more than twice the expected value. Referring to chapter 3, section 3.5.1 (see figure 3.15), such a value should not be achieved until $Ca \approx 10^{-1}$. On the other hand, however, the fact that the results of bubble and slug lengths agree well with the theoretical analysis, presented in chapter 3, is an aspect in favor for the reliability of our measurements. Concerning the literature review, presented in chapter 3, section 3.5.1.3 (see also figure 3.16), a film fraction greater than 10 % in a rectangular channel corresponds in general to the cross-sectional profile of a non-static bubble. This type of profile was proposed by Hazel and Heil (2002), and for the purpose of simplicity, it is sketched once more in figure 4.16.

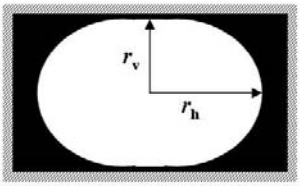

Figure 4.16: Principle sketch of the shape of a non-static bubble in a channel of rectangular cross-section according to Hazel and Heil (2002) (r_v and r_h, are the bubble radii in the vertical and horizontal plane, respectively).

Accounting for the bubble profile shown in figure 4.16, our experimental values suggest that the liquid film in the vertical plane of the channel cross-section should be of remarkable thickness. However, from our recordings of the flow (see figure 4.13), this characteristic is not evident since the bubbles appear to be extended across almost the entire channel width. This suggests that in the present case, the bubble profile may rather be approximated by an elliptical shape. The shape of the bubble profile is an important topic concerning the correlation of hydrodynamics and mass transfer, and will thus be reconsidered in chapter 5.

In a next step a similar study was undertaken using the meandering microchannel with smoothed bends, as well as the straight channel configuration. Example images, which summarize the general flow behaviour found for the channel with smoothed bends, are presented in figure 4.17. According to that, the flow was either irregular (see figure 4.17a) or was characterized by strong fluctuations induced by very long bubbles, where the liquid film dried-out along almost the entire bubble length (see figure 4.17b). We thus term this flow character as wedging or corner flow. The occurrence of the respective flow behaviour was dependent on the ranges of superficial two-phase velocities and liquid hold-ups, as well as on the contacting mode. An example for the latter case can be seen in figure 4.17, where the normal and inverted contacting mode are compared for U_{TP} = 0.241 and ε_L = 0.36. Note, that these operating conditions are the same as in figures 4.12 and 4.13b.

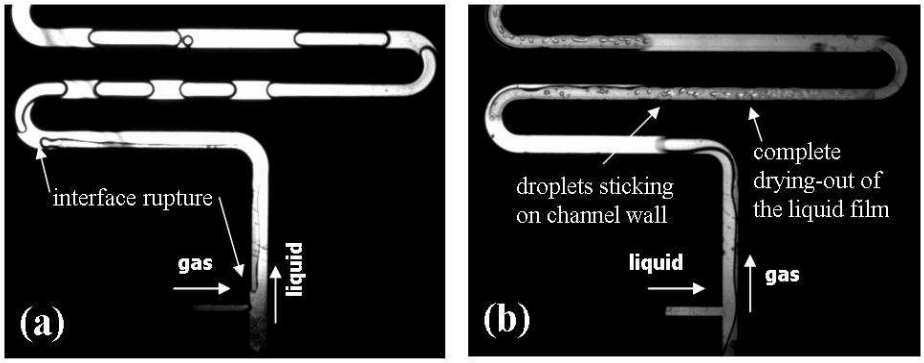

Figure 4.17: Example images of nitrogen-water flow obtained in a meandering microchannel with smoothed bends at a superficial two phase velocity of U_{TP} = 0.241 m/s and a liquid hold-up of ε_L = 0.36 (a: normal contacting mode; b: inverted contacting mode; two-phase Capillary number $Ca_{TP} = 3 \cdot 10^{-3}$).

With respect to the normal contacting mode, the flow shown in figure 4.17a was representative for a range of $U_{TP} \geq 0.241$ and $\varepsilon_L \geq 0.36$, while a decrease of the superficial two-phase velocity and the liquid hold-up resulted in the appearance of long bubbles and a complete dewetting of the liquid film. A similar behavior was detected for the inverted contacting mode. Here, the wedging flow shown in figure 4.17b was characteristic for a range of $U_{TP} \leq 0.241$ and $\varepsilon_L \leq 0.36$, while an increase of the superficial two-phase velocity and the liquid hold-up led to the formation of an irregular flow with fully lubricated bubbles. For the operating conditions studied here, figure 4.17b, thus represents an upper limit concerning the occurrence of a drying-out of the liquid film. According to the theoretical considerations of this phenomenon (see chapter 3, section 3.5.1.5), a dewetting of the liquid film is expected if the film contact time is equal to or greater than the dewetting time. From figure 4.17b we can estimate a bubble length of about 28 mm. Assuming $U_B \approx U_{TP}$, one obtains a film contact time of 0.12 s. This is almost the same value as the dewetting time (0.14 s) and confirms once more our considerations in connection with this topic.
Since the straight channel is significantly shorter than the meandering channel configurations, the flow behavior observed here was either characterized by a co-flow of gas and liquid along the entire lengths of the channel or by alternating sections of single phase flows.

4.2.2 Characterization of the liquid phase velocity field

The aim of this section is to explore the characteristics of the velocity field within the liquid slugs using the microPIV technique. Before measurements in two-phase flow, we initially conducted experiments in single-phase liquid flow in order to verify if operating parameters, like the seeding particle concentration and the time interval between the laser pulses, are properly adjusted. For this purpose we compare the velocity profile obtained from our experimental data with that computed by

means of a theoretical expression from the literature. According to Shah and London (1978), the velocity profile in a rectangular channel may be approximated by:

$$U(y,z) = U_{\max}\left[1-\left(\frac{2y}{h}\right)^{n}\right]\cdot\left[1-\left(\frac{2z}{w}\right)^{m}\right] \qquad (4.2\text{-}15),$$

where the maximum velocity is correlated to the superficial liquid phase velocity as follows:

$$U_{\max} = U_{LS}\left(\frac{m+1}{m}\right)\cdot\left(\frac{n+1}{n}\right) \qquad (4.2\text{-}16).$$

For channels of moderate aspect ratios ($h/w \geq 1/3$) the values of n and m may be estimated by:

$$m = 1.7 + 0.5\left(\frac{h}{w}\right)^{-1.4} \text{ and } \qquad n = 2 + 0.3\left(\frac{h}{w} - \frac{1}{3}\right) \qquad (4.2\text{-}17).$$

In equation 4.2-15, y and z are the coordinates within the horizontal and vertical plane of the cross-section relative to the channel centre axis. A principle sketch of this is shown in figure 4.18a. In our set-up (see section 4.1) the depth of focus of the objective is 200 µm, which means that the velocity field recorded here is averaged across a layer of 200 µm in thickness. For our single-phase experiments we positioned the lower limit of the focal plane of the microscope objective just below the middle of the depth of the microchannel. In order to estimate the corresponding theoretical velocity profile, it was calculated as the average of the velocity profiles at the z-coordinate of the upper and lower limits of the focal depth, z_1 and z_2, respectively. This approach assumes the linearity of the velocity profile over the interval of the focal depth; this is a reasonable hypothesis since the focal depth is not centred in the middle of the microchannel. Accordingly, the average theoretical axial velocity profile is obtained as follows:

$$\overline{U}_{ax}(y,z) = \frac{U(y,z_1)+U(y,z_2)}{2} \qquad (4.2\text{-}18).$$

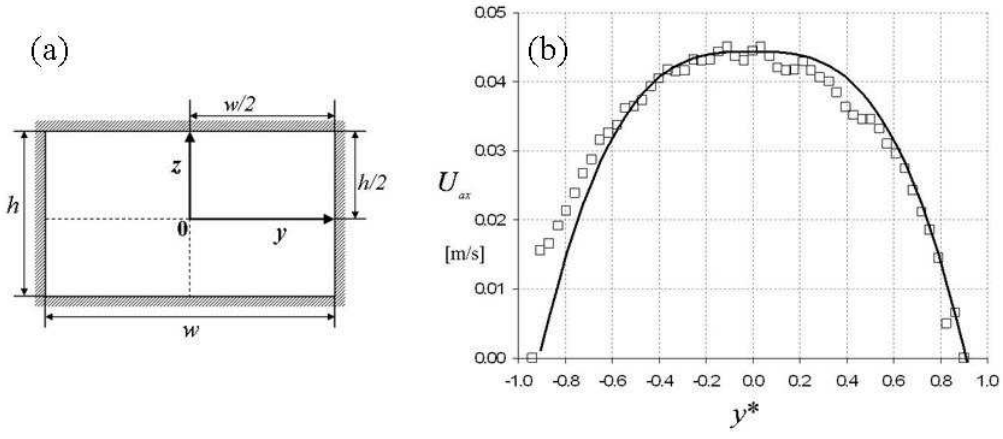

Figure 4.18: Calculation and comparison of the theoretical axial velocity profile with experimental results in single phase liquid flow through a microchannel of rectangular cross-section (a: channel cross-section and coordinates related to equation 4.2-15; b: Theoretical and experimental velocity profiles averaged over a depth of 200 µm, experiments conducted using ethanol at a superficial liquid velocity of U_{LS} = 0.031 m/s and a superficial liquid phase Reynolds-number of $Re_{LS} \approx 16$, theoretical profile computed by means of equations 3.2-15 – 3.2-18, y^* is the distance from the channel centre axis normalized by the channel half width, here $w/2 \approx 555$ µm).

In figure 4.18b, it can be seen that our experimental results agree well with the average theoretical velocity profile. This validates our experimental protocol, which was then applied to measurements of the liquid phase velocities in gas-liquid flow.

The liquid phase velocities in Taylor flow were measured in the liquid slug. 40 image pairs containing an entire liquid slug were selected and the corresponding instantaneous velocity fields were used to calculate the average velocity field. The relative velocities were obtained by subtracting the bubble velocity form the axial component of the liquid phase velocities. This enabled us to plot the relative liquid velocity field, as shown in figure 4.19.

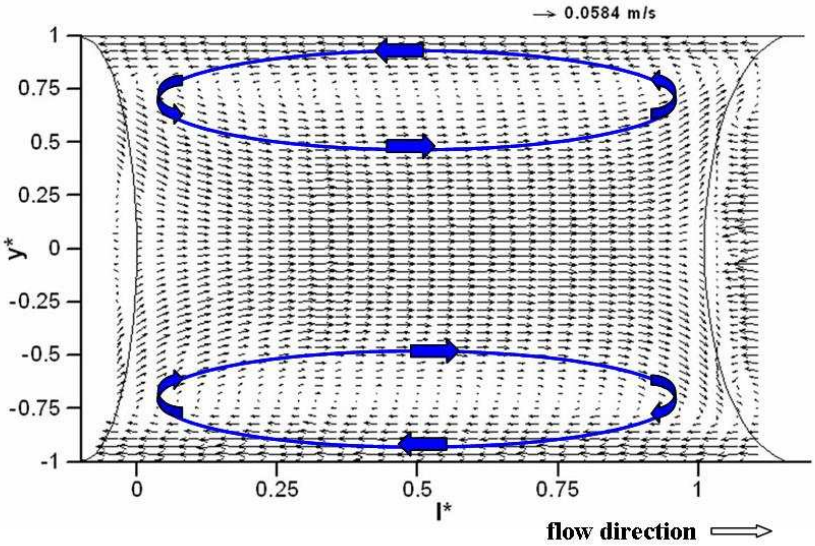

Figure 4.19: Relative velocity field within a liquid slug in gas-liquid Taylor flow through a microchannel of rectangular cross-section. (y^* is the distance from the channel centre axis normalized by the channel half width, here $w/2 \approx 555$ µm; l^* is the distance between the bubble caps normalized by the length of the slug, here $l_S \approx 1.75$ mm; flow conditions: ethanol served as liquid phase, superficial two-phase velocity $U_{TP} = 0.059$ m/s, liquid hold-up $\varepsilon_L = 0.53$, two-phase Capillary number $Ca_{TP} \approx 2.7 \cdot 10^{-3}$, two-phase Reynolds-number $Re_{L,TP} \approx 31$, dimensionless bubble velocity $\psi = 1$).

With respect to the present operating conditions, the two-dimensional velocity field in figure 4.19 is representative for the case of a dimensionless bubble velocity of $\psi = 1$ and the size of the vectors is proportional to the velocity. The velocity field is bounded by the gas-liquid interface of the bubble caps, sketched at $l^* < 0$ and $l^* > 1$. It should be pointed out that gas-liquid interface is depicted by a thin line here however, in reality the interface has some finite thickness due to curvature effects throughout the 200 µm focal depth. Within the liquid slug ($0 \leq l^* \leq 1$) the velocities approach zero between the microchannel centerline and the walls, corresponding to the centre of the vortex. In between the vortex centers, we find the inner recirculation region where the velocity vectors are in the same direction as the two-phase flow until reaching the bubble cap. At this, the flow is conducted into the outer recirculation region, indicated by the reverse flow between vortex centre and channel wall. These characteristics of the liquid phase velocity field are in general agreement with the descriptions undertaken in chapter 3, section 3.3. In order to quantitatively compare our experimental results to those presented in chapter 3 (section 3.3) for the case of a circular channel at the same dimensionless bubble velocity, we initially decided to determine the position of the vortex center. For this purpose we extracted the relative velocity profile. This is shown in figure 4.20 for $l^* = 0.5$. Here, we identified the positions of zero velocity as $y^* = -0.70$ and $y^* = 0.73$. We may thus assume an average value of the dimensionless vortex position of $w_0/w \approx 0.715$. This value is very close to that previously derived in chapter 3 (section 3.3) for a circular channel ($r_0/R \approx 0.707$, see equation 4.3-4 and figure 4.7). Furthermore, we checked if the reverse flow in the outer region is entirely part of the recirculation system. In this context we extracted the average velocity of each region of the recirculation zone. For the inner region ($-0.7 < y^* < 0.73$) we obtained a value of 0.0365 m/s. We respect to the outer region

(- 1 ≤ y^* < - 0.7 and 0.73 < y^* ≤ 1) a value of 0.0361 m/s could be attributed. Providing that the volumetric flow rates and the cross-sectional area of both regions are equal (see chapter 3, section 3.3, figure 3.6), this suggests that for a channel of rectangular cross-section at ψ =1, the entire liquid volume of the liquid slug is carried within the recirculation flow and with that the width of the recirculation zone is equal to the channel width (w_{rc}/w = 1).

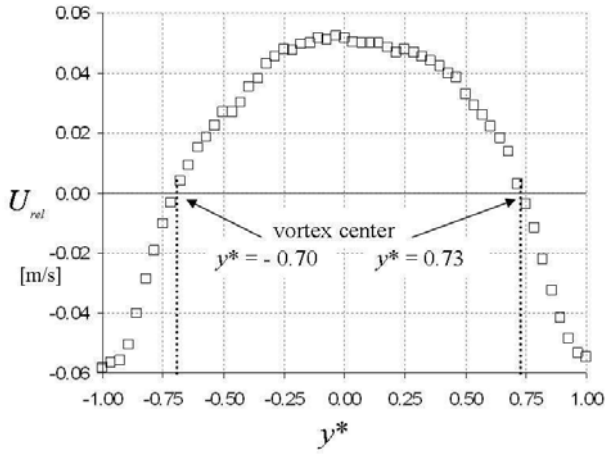

Figure 4.20: Relative velocity profile within a liquid slug (l^* = 0.5) in gas-liquid Taylor flow through a microchannel of rectangular cross-section. (y^* is the distance from the channel centre axis normalized by the channel half width, here $w/2 \approx 555$ µm; flow conditions: ethanol served as liquid phase, superficial two-phase velocity U_{TP} = 0.059 m/s, liquid hold-up ε_L = 0.53, two-phase Capillary number $Ca_{TP} \approx 2.7 \cdot 10^{-3}$, two-phase Reynolds-number $Re_{L,TP} \approx 31$, dimensionless bubble velocity ψ = 1).

According to the results derived above, the relationship between the dimensionless width of the recirculation zone and the position of the vortex centre may be written in a similar way as for a channel of circular cross-section (equation 3.3-3):

$$\frac{w_{rc}}{w} = \sqrt{2}\,\frac{w_0}{w} \qquad (4.2\text{-}19).$$

Expression 4.2-19 assumes that the recirculation flow follows the symmetry of the channel cross-section. This means that in depth-wise direction the extension of the recirculation zone may be given by $h_{rc} = w_{rc}/2$ and the position of the vortex expressed as $h_0 = w_0/2$. On the basis of these considerations we may now extract the average velocity of recirculation U_{rc} in our system. To do this, we have integrated the dimensionless relative velocity profile shown in figure 4.20 over the cross-sectional area of the recirculation flow in microchannel, which gives a value of U_{rc} = 0.023 m/s. In order to evaluate the validity of this result we decided to compare it to the average recirculation velocity that would be yielded for the same operating conditions in a channel of circular cross-section. For this purpose, we consider the corresponding expression derived in chapter 3 (section 3.3). According to this U_{rc} is given as follows:

$$U_{rc} = U_{TP}\left(1 - \frac{1}{2}\psi\right) \qquad (4.2\text{-}20).$$

Setting, U_{TP} = 0.059 m/s and ψ =1 we obtain an average velocity of recirculation of $U_{rc} \approx 0.029$ m/s. This value is very close to our result obtained experimentally in the microchannel of rectangular cross-section with an aspect ratio w/h = 2 and it suggests that for the order of magnitude of velocities studied here, expression 4.2-20 may serve as a good approximation for the recirculation velocity in the liquid slug. Considering this, the recirculation time within the liquid slug can also be deduced in the same manner as for the microchannel of circular cross-section (see equation 3.3-9):

$$t_{rc} = \frac{V_{rc}}{Q_{rc}} = \frac{w_{rc} h_{rc} l_S}{w_0 h_0 U_{rc}} = \frac{2l_S}{U_{rc}} \approx \frac{2l_S}{U_{TP}\left(1 - \frac{1}{2}\psi\right)} \qquad (4.2\text{-}21)$$

This is identical to the recirculation time given for cylindrical microchannels. With the recirculation velocity of 0.023 m/s and a slug length of 1.75 mm as measured in this study, the recirculation time is 0.15 s; this can be compared with 0.12 s, obtained using the approximation of the recirculation velocity in equation 4.2-20. The recirculation time is an important parameter with respect to gas-liquid mass transfer, since it serves as an indication for the interfacial contact time at the bubble caps and the mixing within the slug.

4.3 Conclusions

The experimental study of hydrodynamic parameters generally confirmed the theoretical analysis and criteria previously presented in chapter 3 (section 3.5). This mainly concerns the discussion carried-out with respect to the dependency of bubble lengths on fluid properties, Capillary number and liquid hold-up, as well as phenomena like film dewetting and bubble velocity fluctuations.

We presented modified scaling laws and proofed their ability to predict bubble and slug lengths as a function of parameters like leakage flow and gas-inlet channel dimensions.

The characteristics of the liquid phase velocity field within the slugs identified here, revealed many similarities with that previously discussed for channels of circular cross-section (see chapter 3, section 3.3). This suggests that the considerations carried out concerning the evolution of the velocity field and related parameters in circular channels may serve as a good approximation for channels of rectangular cross-section with moderate aspect ratios.

Furthermore it turned out that for water the formation of Taylor is strongly influenced by the longitudinal channel geometry as demonstrated by the comparison of the meandering channel configurations. A possible source of this circumstance is definitely due to the design of the inlet section. In this context one may generally conclude that in the case of water or liquids of comparable surface tension the use of a pseudo-T-junction for the generation of Taylor flow is inappropriate.

Using water as liquid phase, a stable and regular Taylor flow was only obtained in the meandering microchannel with sharp bends. Here especially the inverted contacting mode, offered the largest range of stable flow conditions. For this reason, we will use them as operating conditions for the investigation of gas-liquid mass transfer.

5 Characterization of Gas-Liquid Mass-Transfer in Taylor flow through microchannels

An important topic in the design and development of gas-liquid microreactors is the reliable estimation of the gas-liquid mass transfer, or more precisely of the mass transfer coefficient. Since most of the gas-liquid reaction systems that are considered for operation in microchannels involve gases of poor solubility, we are, in the first instance, principally interested in the volumetric liquid-side mass transfer coefficient $k_L a$. With respect to Taylor flow, the preceding chapter showed that the $k_L a$-value can be modeled based on the hydrodynamic parameters of the flow pattern. Since this model was exclusively developed for channels of circular or square cross-section the aim of this section is to make a first step in the direction of developing a mass transfer model for microchannels of rectangular cross-sectional shape. The way we have chosen to achieve this, requires the measurement of the volumetric liquid-side mass transfer coefficients and a simultaneous recording of the hydrodynamics of the flow. The hydrodynamic parameters obtained are then used to set-up a modified model of the volumetric liquid side mass-transfer coefficient and the $k_L a$-value predicted on this basis will be compared with the experimental ones. In order to facilitate the reading of this chapter a condensed introduction into the fundamentals of gas-liquid mass-transfer is initially given. This is followed by a description of the method and the experimental set-up employed for the $k_L a$-measurements. The results are then discussed and are used to establish and evaluate a theoretical approximation of $k_L a$-values. The experimental work presented in this section was carried out during a scientific stay at the Faculty of Chemical and Process Engineering at the Warsaw University of Technology (WUT), Poland.

5.1 Fundamentals of gas-liquid mass transfer

In general a gas-liquid reaction can only take place if the gas is absorbed by the liquid and diffuses from the interface to the liquid reactant. This process is principally illustrated in figure 5.1.

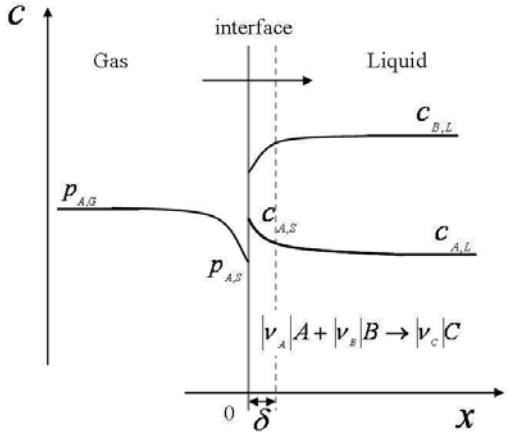

Figure 5.1: Schematic illustration of the mass-transfer process between a gas and a liquid phase with chemical reaction. (*A* gaseous component or dissolved gas; *B* liquid reactant; *C* reaction product; *v* stoichiometric coefficient; $p_{A,G}$ partial pressure of *A* in the bulk of the gas phase; $p_{A,S}$ partial pressure of *A* at the interface; $c_{A,S}$ concentration of *A* at the interface; $c_{A,L}$ concentration of *A* in the bulk of the liquid phase; $c_{B,L}$ concentration of *B* in the liquid phase; δ thickness of the stagnant layer next to the interface. This parameter originates from the film model, which is explained later in section 5.1.1.

According to figure 5.1 one may write the mass balance in the interface plane as follows (Emig and Klemm, 2005):

$$\frac{\partial c_A}{\partial t} = D_A \frac{\partial^2 c_A}{\partial x^2} + \nu_A r \qquad (5.1\text{-}1),$$

where c_A is the concentration of dissolved gas in the liquid phase, r labels the reaction rate and ν_A the stoichiometric coefficient of the solute in the reaction. D_A is the diffusivity of dissolved gas in the liquid phase. In the absence of reaction, equation 5.1-1 becomes Fick's second law of diffusion. The mass balance given in 5.1-1 may be solved by setting certain boundary conditions. These conditions

are dependent on the different models applied, which are shortly described in the following. The solutions result in the definition of parameters, such as the mass transfer coefficient, the Hatta-number and the enhancement factor which will also be described.

5.1.1 Mass transfer models

There are three principal models used for describing mass transfer. The most commonly used is the film model proposed by Lewis and Whitman (1924). In this model it is assumed that there is a stagnant layer of fluid at both sides of the gas-liquid interface where mass transfer takes place purely by molecular diffusion. In this context one also refers to gas-side and liquid-side mass transfer resistances. Away from these stagnant layers in the bulk, the phases are perfectly mixed. In order to better visualize this theory, it will be explained using the notation in figure 5.1. Here, we will initially consider the liquid-side. The influence of the gas-side resistance will be the topic of section 5.1.3. For the case of gas-absorption without chemical reaction one may write the concentration equation as:

$$\frac{\partial c_A}{\partial t} = D_A \frac{\partial^2 c_A}{\partial x^2} \qquad (5.1\text{-}2).$$

Since the boundary layer at the interface is assumed as stagnant the concentration field does not change with time ($\partial c_A/\partial t = 0$, stationary diffusion) and 5.1-2 may be rewritten as:

$$D_A \frac{\partial^2 c_A}{\partial x^2} = 0 \qquad (5.1\text{-}3).$$

The integration of this equation yields a linear function with constants C_1 and C_2:

$$c_A(x) = C_1 x + C_2 \qquad (5.1\text{-}4).$$

The boundary conditions may be imposed using figure 5.1, and assuming a layer of thickness δ at the liquid-side to the interface. Thus one may state that:

$$\text{at} \quad x = 0 \qquad c_A = c_{A,S} \qquad (5.1\text{-}5),$$

$$\text{and at} \quad x = \delta \qquad c_A = c_{A,L} \qquad (5.1\text{-}6).$$

Insertion of these conditions into 5.1-4 enables the determination of the constants C_1 and C_2 and by multiplication by the diffusivity one obtains a linear concentration profile, whose first derivation writes as follows (Emig and Klemm, 2005):

$$D_A \frac{\partial c_A}{\partial x} + D_A \frac{\left(c_{A,S} - c_{A,L}\right)}{\delta} = 0 \qquad (5.1\text{-}7).$$

Replacing the first term in 5.1-7 by Fick's first law of diffusion results in:

$$F = \dot{N}_A = \frac{D_A}{\delta}\left(c_{A,S} - c_{A,L}\right) \qquad \text{in [mol/m}^2\text{ s]} \qquad (5.1\text{-}8),$$

where F is the molar flux according to Fick's first law of diffusion and N_A the absorption rate per unit surface area usually used in connection with gas-liquid mass transfer. The first term on the right hand side of 5.1-8 is denoted as liquid-side mass transfer coefficient k_L.

$$k_L = \frac{D_A}{\delta} \qquad \text{in [m/s]} \qquad (5.1\text{-}9).$$

The validity of the film model has been a matter of controversy (Danckwerts, 1970). On the one hand it may constitute a good approach in the case of quiescent fluids; but on the other hand it has been argued that in systems with strong convection next to the interface, the stagnant layer may be ruptured. In addition to this the existence of two stagnant layers at both sides of the interface is generally doubted. This has given rise to the development of alternative models. Two important examples in this area are the models proposed by Higbie (1935) and Danckwerts (1951). Both models are often referred to as the penetration or surface renewal theory. In these models it is assumed that the layer next to the interface is ruptured so that a fluid element from the bulk of the respective phase may reach the interface. These fluid elements remain in contact with the other phase for a certain time during which

mass-transfer takes place by diffusion, until convection transports them back in the bulk. In connection to this time, Higbie (1935) assumed a constant residence time, which is also referred to as the exposure time and proposed to correlate the mass transfer coefficient as follows:

$$k_L = 2\sqrt{\frac{D_A}{\pi\tau}} \qquad (5.1\text{-}10).$$

Danckwerts (1951) refined Higbie's theory by assuming a residence time distribution instead of constant exposure time. From numerous experimental studies it has been shown that the difference between predictions based on these models are less than uncertainties (Danckwerts, 1970). This may justify the common use of the film model, which will be applied in the following to quantitatively depict the process, where mass-transfer and chemical reaction take place simultaneously.

5.1.2 Definition of the Hatta-number and the Enhancement factor

As mentioned above we will use the film model (i.e. $\partial c_A/\partial t = 0$) for describing the absorption process, where dissolved gas A undergoes a chemical reaction with a liquid reactant B. For the purpose of simplicity we assume a reaction of peudo-1st order with respect to the solute. Accordingly, one may rewrite the mass balance given in 5.1-1 as follows:

$$D_A \frac{\partial^2 c_A}{\partial x^2} + \nu_A k_1 c_A = 0 \qquad (5.1\text{-}11).$$

This expression constitutes a homogeneous, linear second order differential equation. According to the procedure for solving this type of equation analytically, the general solution writes as:

$$c_A(x) = C_3 e^{(\lambda 3)x} + C_4 e^{(\lambda 4)x} \qquad (5.1\text{-}12).$$

where C_3 and C_4 are constants, and the exponents are given by:

$$\lambda_3 = \sqrt{\frac{\nu_A k_1}{D_A}} \quad \text{and} \quad \lambda_4 = -\sqrt{\frac{\nu_A k_1}{D_A}} \quad \text{for } \nu_A = -|\nu_A| \qquad (5.1\text{-}13).$$

Multiplying these exponents with the thickness of the stagnant film layer and rearrangement results in a dimensionless parameter denoted as the Hatta number.

$$Ha = \frac{\delta}{D_A}\sqrt{D_A \nu_A k_1} = \sqrt{\frac{D_A \nu_A k_1}{k_L^2}} \qquad (5.1\text{-}14).$$

The Hatta number is the ratio between the rate of mass transfer and the reaction rate. For a reaction of general order it is defined as:

$$Ha = \sqrt{\frac{\frac{2}{m+1} D_A k_{m,n} c_{A,S}^m c_{B,L}^n}{k_L^2}} \qquad (5.1\text{-}15),$$

where *m* and *n* are the reaction orders with respect to the reactant A and B, respectively. With 5.1-14 one may rewrite the general solution 5.1-12 as:

$$c_A(x) = C_3 e^{\frac{Ha}{\delta}x} + C_4 e^{-\frac{Ha}{\delta}x} \qquad (5.1\text{-}16).$$

The boundary conditions given in 5.1-5 and 5.1-6 enable the determination of the constants C_3 and C_4 and one obtains the concentration profile, whose first derivation results in (Emig and Klemm, 2005):

$$D_A \frac{\partial c_A}{\partial x} + D_A \frac{Ha}{\delta} \frac{\left(c_{A,S}\cosh(Ha) - c_{A,L}\right)}{\sinh(Ha)} = 0 \qquad (5.1\text{-}17).$$

Insertion of Fick's first law of diffusion and rearrangement yields the absorption rate per unit surface area as:

$$\dot{N}_A = k_L c_{A,S} \frac{Ha}{\tanh(Ha)} \left(1 - \frac{c_{A,L}}{c_{A,S} \cosh(Ha)} \right) \qquad (5.1\text{-}18).$$

This may generally be expressed as:

$$\dot{N}_A = k_L c_{A,S} E \qquad \text{in [mol/m}^2\text{ s]} \qquad (5.1\text{-}19),$$

where E, the enhancement factor is the ratio of the absorption rate with chemical reaction to that of pure physical diffusion. It thus expresses how the gas-liquid mass transfer is enhanced by the consumption of the solute in the chemical reaction. The interaction between the enhancement factor and the Hatta number is important with respect to the choice of method for the characterization of gas-liquid mass transfer. This will be shown by means of some examples within section 5.2. At this stage, it should be pointed out that the interfacial area has not appeared as a parameter in the considerations carried out above. Since in this chapter, we are interested in the product of the mass transfer coefficient and the specific interfacial area, it is useful to conclude here with some basic definitions. If the absorption rate given above is multiplied by the gas-liquid interfacial area A_S, the molar flow rate between the gas and the liquid phase is obtained.

$$\dot{n}_A = \dot{N}_A A_S = k_L A_S c_{A,S} E \qquad \text{in [mol/s]} \qquad (5.1\text{-}20).$$

Division of the molar flow rate by the reaction volume then yields the rate of absorption per unit volume of the system:

$$\frac{\dot{n}_A}{V_R} = \dot{N}_A \frac{A_S}{V_R} = k_L a c_{A,S} E \qquad \text{in [mol/m}^3\text{ s]} \qquad (5.1\text{-}21),$$

where a is the specific interfacial area in [m^2/m^3]. Previously in chapter 2 (see section 2.3), the absorption rate per unit volume has been called the effective reaction rate, in the case of strong mass transfer limited reactions.

As already mentioned in section 5.1.1 the film model suggests the existence of a stagnant layer at both sides of the interface. For this reason it is also referred to as the two-film model. At this, the issue of the gas-side resistance needs to be accounted for when the soluble gas is mixed with an insoluble gas, since in this case the soluble gas must diffuse through the latter in order to reach the interface (Danckwerts, 1970). Gas mixtures are a typical feature in absorption processes and with it for characterizing gas-liquid mass transfer (see section 5.2). Hence, we will complete the present fundamental considerations by inclusion of the influence of the gas-side on the rate of absorption. In this manner one obtains an illustration of the overall mass transfer process.

5.1.3 Gas-side resistance

As previously mentioned, the initial situation considered in order to deal with this issue is the existence of a gas mixture, composed of a soluble and an insoluble gas. In the present context, one may also term the latter as carrier gas. Certainly the carrier gas is not truly insoluble, but we assume here that its solubility is negligible compared to that of the gas which is intended to be removed by the liquid. If one supposes a stagnant layer at the gas-side of the interface where the soluble gas is transported by stationary diffusion ($\partial p_A/\partial t = 0$), the partial pressure of the soluble gas at the interface $p_{A,S}$ is generally less than in the bulk of the gas mixture ($p_{A,G}$). This pressure profile is schematically drawn in figure 5.1. Accordingly, in the case the absorbed gas undergoes an arbitrary reaction in the liquid phase one may generally express the rate of absorption as:

$$\dot{N}_A = k_G \left(p_{A,G} - p_{A,S} \right) = k_L c_{A,S} E \qquad (5.1\text{-}22),$$

where k_G is the gas-side mass transfer coefficient in [mol/m^2 s bar]. If Henry's law is obeyed the concentration of dissolved gas at the interface $c_{A,S}$ is related to $p_{A,S}$ as follows:

$$c_{A,S} = Hp_{A,S} \qquad (5.1\text{-}23),$$

where H is Henry's law constant in [mol/m^3 bar]. Rearrangement of 5.1-22 with respect to the interface terms and insertion into 5.1-23 allows expressing the rate of absorption as:

$$\dot{N}_A = Hp_{A,G} \frac{1}{\left(\frac{1}{k_L E} + \frac{H}{k_G} \right)} \qquad (5.1\text{-}24).$$

Here the expression in brackets is the reciprocal of the overall mass transfer coefficient referred to the liquid-side (unit: m/s). When it is multiplied by Henry's law constant one talks of the overall mass transfer coefficient referred to the gas-side (unit: mol/m^2 s bar). From equation 5.1-24 it can be seen that the gas-side resistance is integrated by the term H/k_G and thus its extent depends on the solubility of the gas. In general one may state that the gas-side resistance decreases with decreasing solubility of the gas. This issue will be discussed in the following using Henry's law constants of various gases typically occurring in absorption processes (see table 5.1).

Gas	H_2	O_2	CO_2	SO_2	NH_3
H [kmol/m^3·bar]	$\approx 7.7 \cdot 10^{-4}$	$\approx 1.3 \cdot 10^{-3}$	$\approx 3.4 \cdot 10^{-2}$	1.2 – 1.5	55.3 – 60.2

Table 5.1: Examples of various gases typically occurring in absorption processes and their Henry's law constants in water at 25 °C (298.15 K; values according to Sander, 1999).

Within the examples listed in table 5.1, hydrogen, oxygen and CO_2 are generally classified as sparingly soluble gases, while SO_3 and NH_3 are generally considered as highly soluble gases. From experiments in absorption columns (Pohorecki and Moniuk, 1988a; Hoffman et al., 2007) one may state typical orders of magnitude of liquid-side mass transfer coefficients as $k_L \approx O(10^{-4})$ m/s and those of the gas-side mass transfer coefficients as $k_G \approx O(10^{-3})$ kmol/m^2·s·bar. Considering CO_2 as an example with a Henry's law constant in the order of 10^{-2} kmol/m^3·bar one obtains $k_G/H \approx O(10^{-1})$ m/s. This value is three orders of magnitude greater than that of k_L mentioned above. This means that the mass transfer process is entirely limited by the liquid-side. Hence, the example shown here is representative for the case of negligible gas-side resistance, which may generally be expressed as:

$$\frac{k_G}{H} >> k_L E \qquad (5.1\text{-}25).$$

In this case one may assume that the partial pressure at the interface virtually corresponds to that in the bulk of the gas phase ($p_{A,S} = p_{A,G}$) and the rate of absorption is given by:

$$\dot{N}_A = Hp_{A,G} k_L E \qquad (5.1\text{-}26).$$

On the other hand, if we consider the physical absorption (E = 1) of SO_2 and NH_3 ($H \geq O(10^0)$ kmol/m^3·bar), one attains values of k_G/H that approach or even equal the abovementioned order of magnitude of k_L. Under these circumstances the gas-side resistance needs to be taken into account and the rate of absorption is represented according to equation 5.1-24. If a highly soluble gas additionally undergoes a reaction with a liquid reactant the absorption process may become entirely dependent on the gas-side mass transfer. An example for this will be presented in section 5.2. The fundamental overview gained in section 5.1 will be used in the following to discuss the methods for characterizing gas-liquid mass transfer.

5.2 Methods for characterizing gas-liquid mass transfer

A general classification of methods for characterizing gas-liquid mass transfer can be initially undertaken by considering the nature of the gas which may be employed. In accordance to the discussion undertaken in section 5.1.3 the use of sparingly soluble gases should enable to exclusively characterize the liquid-side mass transfer. On the other hand the absorption of highly soluble gases should give information about the overall mass-transfer coefficient. A detailed overview on the characterization methods for gas-liquid mass transfer can be found in Hoffman et al. (2007). The aim of the present section is rather to give a general and short introduction of gas-liquid systems that are suitable for measuring mass transfer parameters. In general, one is interested in characterizing either the liquid-side mass transfer or the gas-side mass-transfer.

An example for the latter case concerns the absorption of a highly soluble gas followed by its instantaneous reaction with a liquid reactant. At this each gas molecule that reaches the interface is immediately consumed by the reaction (see profiles in figure 5.2a). Consequently, the partial pressure of the gaseous component as well as its interface concentration drop to zero. In this case the absorption process is entirely dependent on the gas-side mass transfer. Setting $p_{A,S} = 0$ and $c_{A,S} = 0$ in equation 5.1-24 one may express the rate of absorption per unit volume of the system as:

$$\dot{N}_A a = k_G a p_{A,G} \qquad (5.2\text{-}1).$$

Examples of these systems are NH_3/H_2SO_4 and SO_2/NaOH and as can be seen from equation 5.2-1 this method is suitable for measuring the volumetric gas-side mass transfer coefficient $k_G a$.

However, in the context of the present chapter we are principally interested in characterizing the liquid-side mass transfer. Hence, in the following we will focus on methods employing gases of low solubility like oxygen or CO_2, since the resistance of the gas-side transfer can be neglected in this case. Under these circumstances the rate of absorption per unit volume of the system may be written as:

$$\dot{N}_A a = k_L a c_{A,S} E \qquad (5.2\text{-}2).$$

In this context, a first group of the methods concerns gas-liquid systems without chemical reaction or with a slow pseudo-1st order reaction in the liquid phase ($Ha < 0.3$). Considering equations 5.1-18 and 5.1-19 it can be seen that if $Ha \ll 1$ the enhancement factor tends towards $E = 1$. From 5.2-2 it reveals that this method is appropriate to measure the $k_L a$-value. Examples of these systems are the physical absorption of CO_2 or O_2 in water or the absorption of CO_2 into aqueous bicarbonate/carbonate buffer solutions.

A second group of gas-liquid systems involves those where the solute undergoes a fast chemical reaction of pseudo-1st order ($3 < Ha < E_i/2$). The term labeled as E_i is the enhancement factor corresponding to an instantaneous reaction. Its meaning will be explained in the end of this section. Under the abovementioned circumstances the dissolved gas all reacts in the stagnant film layer and none diffuses in the unreacted state into the bulk of the liquid. In this case the thickness of the stagnant film layer and with it the value of k_L are irrelevant. From equations 5.1-18 and 5.1-19 it turns out that if $Ha \gg 1$ and $c_{A,L} = 0$ one may assume that:

$$E = Ha \qquad (5.2\text{-}3).$$

According to 5.2-3 and 5.1-14 it follows:

$$\dot{N}_A a = k_L a c_{A,S} \sqrt{\frac{D_A \nu_A k_1}{k_L^2}} = a c_{A,S} \sqrt{D_A \nu_A k_1} \qquad (5.2\text{-}4).$$

Thus this method is suitable to measure the specific interfacial area. An example of a gas-liquid system that is appropriate for this type of measurement is the absorption of CO_2 in aqueous solutions of hydroxides (e.g. NaOH).

A third method is called the Danckwerts method (Danckwerts, 1970). It is based on the absorption of CO_2 in a bicarbonate/carbonate buffer solution already mentioned above. In addition, the consumption

of CO_2 by a slow reaction in the liquid phase may be catalyzed by anions such as hypochloride, or arsenite anions (Roberts and Danckwerts, 1962; Danckwerts, 1970; Pohorecki, 1976). This results in a system of intermediate reaction speed ($0.3 < Ha < 3$), where the enhancement factor may be expressed as:

$$E = \sqrt{1 + Ha^2} \qquad (5.2\text{-}5).$$

Assuming that the reaction is of pseudo 1st-order equation, 5.2-2 becomes:

$$\dot{N}_A a = k_L a c_{A,S} \sqrt{1 + \frac{D_A \nu_A k_1}{k_L^2}} = k_L a c_{A,S} + a c_{A,s} \sqrt{D_A \nu_A k_1} \qquad (5.2\text{-}6).$$

This method usually consists in a modification of the pseudo 1st-order reaction rate constant k_1 by variation of the catalyst concentration. If one rearranges 5.2-6 as:

$$\left(\frac{\dot{N}_A a}{c_{A,S}} \right)^2 = (k_L a)^2 + a^2 D_A \nu_A k_1 \qquad (5.2\text{-}7)$$

a plot of the left-hand side of 5.2-6 versus k_1 allows the $k_L a$-value and the interfacial area to be determined from the y-intercept and the slope, respectively. This method thus offers the possibility to obtain the mass-transfer coefficient k_L and the specific interfacial area a separately. However, it is also the most difficult method to implement experimentally since the catalyst is added and its amount is varied at very low concentrations. The exact measurement and handling of these concentration ranges are the main challenges related to this method.

As already annotated above the pre-condition for the use of chemical methods in characterizing gas-liquid mass transfer is that the respective reactions behave as pseudo-1st order with respect to the dissolved gas ($r = k_1 c_A$). That means that, the liquid reactant diffuses towards the interface fast enough to prevent the reaction causing any significant depletion there, so that the concentration of the liquid reactant equals everywhere virtually its bulk concentration $c_{B,L}$. This is an important requirement, because if this condition is not fulfilled the absorption process is limited by the transport of the liquid reactant from the bulk towards the interface. Hence, it is impossible to obtain reliable values for mass-transfer coefficients and/or specific interfacial areas. The criterion for a pseudo-1st order behavior of the reaction system may generally be written as follows:

$$\sqrt{\frac{D_A k_1}{k_L^2}} < \frac{1}{2} \left(1 + \frac{c_{B,L}}{\nu_B c_{A,S}} \frac{D_B}{D_A} \right) \qquad \text{with} \qquad k_1 = k_2 c_{B,L} \qquad (5.2\text{-}7),$$

where the pseudo-1st order rate constant k_1 of the reaction between one mole A ($\nu_A = 1$) and ν_B moles of B is determined by the second order rate constant k_2 and the bulk concentration of the liquid reactant $c_{B,L}$. D_B and D_A are the diffusivities of the respective components in the liquid phase. The left hand side of criterion 5.2-7 is the Hatta number. It is a measure of the amount of dissolved gas which reacts in the stagnant interface layer, compared to that which reaches the bulk liquid in the unreacted state. Accordingly, in case of a slow reaction we have $Ha << 1$. On the other hand, in case of a fast reaction $Ha >> 1$ since a considerable amount of dissolved gas already reacts within the interface layer. The expression within the brackets on the right hand side of criterion 5.2-7 is the enhancement factor for an instantaneous reaction E_i. This term may be regarded as a mass flux ratio of the liquid reactant B diffusing towards the interface to the transport of the solute A from the interface into the stagnant interface layer. In the present context this ratio should typically be much greater than unity. Thus criterion 5.2-7 generally states that the consumption of the liquid reactant B within the film should be much lower than the rate at which it can diffuse to the interface. In order to summarize this section representative schematic sketches of pressure and concentration profiles corresponding to the methods presented above are shown in figure 5.2.

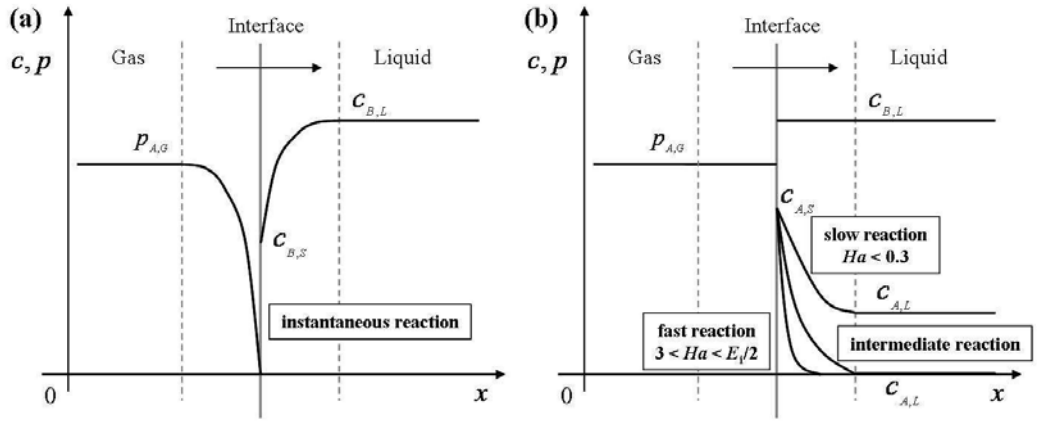

Figure 5.2: Schematic sketches of pressure and concentration profiles related to different methods for characterizing gas-liquid mass-transfer. Broken lines indicate the limits of the stagnant layers located at both sides of the interface according to the film model. (a) absorption of a highly soluble gas followed by its instantaneous reaction with a liquid reactant at the interface; (b) absorption of a sparingly soluble gas followed by chemical reaction of different pseudo-1st order reaction rates (*A* gaseous component or dissolved gas; *B* liquid reactant; $p_{A,G}$ partial pressure of *A* in the bulk of the gas phase; $c_{A,S}$ concentration of *A* at the interface; $c_{A,L}$ concentration of *A* in the bulk of the liquid phase; $c_{B,S}$ concentration of *B* at the interface; $c_{B,L}$ concentration of *B* in the bulk of liquid phase).

5.3 Experimental measurements of the volumetric liquid side mass transfer coefficient ($k_L a$)

The gas-liquid system chosen in order to obtain $k_L a$-values in this work is the absorption of CO_2 in an aqueous buffer solution of K_2CO_3/$KHCO_3$. During this process a number of reversible reactions take place, which are given as follows:

$$R_1: \quad CO_{2(L)} + H_2O \leftrightarrow H^+ + HCO_3^- \qquad (5.3\text{-}1),$$

$$R_2: \quad HCO_3^- \leftrightarrow H^+ + CO_3^{2-} \qquad (5.3\text{-}2),$$

$$R_3: \quad H^+ + OH^- \leftrightarrow H_2O \qquad (5.3\text{-}3),$$

$$R_4: \quad CO_{2(L)} + OH^- \leftrightarrow HCO_3^- \qquad (5.3\text{-}4),$$

and the overall reaction can be written as:

$$CO_{2(L)} + CO_3^{2-} + H_2O \leftrightarrow 2HCO_3^- \qquad (5.3\text{-}5),$$

with an apparent pseudo1st-order reaction rate constant $k_{1,app}$ of about 0.86 s^{-1} (at 293 K; Roberts and Danckwerts, 1962). If the reaction system mentioned above is in equilibrium, there is always a concentration of free CO_2 in the buffer solution, which is determined by (Danckwerts, 1970):

$$[CO_2]_e = c_e = \frac{K_2}{K_1}\frac{[HCO_3^-]^2}{[CO_3^{2-}]} \qquad (5.3\text{-}6),$$

where K_1 and K_2 are the equilibrium constants of reactions R_1 and R_2, respectively. This concentration is an important parameter that needs to be estimated in order to compute the $k_L a$-values, as will be shown later. The equilibrium constants are a function of the ionic strength of the solution and are correlated as (Kucharski, 1978):

$$\log\frac{K_1}{K_1^\infty} = \frac{1.017\sqrt{I}}{1+\sqrt{I}} - 0.103\,\mathrm{I} \qquad (5.3\text{-}7) \text{ and}$$

$$\log\frac{K_2}{K_2^\infty} = \frac{2.02\sqrt{I}}{1+1.66\sqrt{I}} - 0.055\,\mathrm{I} \qquad (5.3\text{-}8),$$

where the equilibrium constants at infinite dilution are dependent on the temperature of the solution and may be estimated as (Kucharski, 1978):

$$\log K_1^{\infty} = 14.843 - \frac{3404.7}{T} - 0.03279\,T \qquad (5.3\text{-}9)$$ and

$$\log K_2^{\infty} = 6.498 - \frac{2902.4}{T} - 0.0238\,T \qquad (5.3\text{-}10).$$

The ionic strength of the buffer solution may be written as:

$$I_{buffer} = I_{K_2CO_3} + I_{KHCO_3} \quad \text{with} \quad I = 0.5\sum c_i z_i^2 \qquad (5.3\text{-}11),$$

where c_i and z_i are the concentration and the valency of the respective ion-species. In our study the concentrations of K_2CO_3 and $KHCO_3$ were 0.3 mol/l, respectively. Experiments were conducted at a temperature of about 22 °C (295 K). The corresponding values of the ionic strengths, the equilibrium constants and the resulting equilibrium concentration of CO_2 are given in table 5.2.

$I_{K_2CO_3}$	I_{KHCO_3}	K_1^{∞}	K_1	K_2^{∞}	K_2	c_e
[mol/l]	[mol/l]	[mol/l]	[mol/l]	[mol/l]	[mol/l]	[mol/m^3]
0.9	0.3	$4.3\cdot10^{-7}$	$1.12\cdot10^{-6}$	$4.3\cdot10^{-11}$	$2.28\cdot10^{-10}$	$6.13\cdot10^{-2}$

Table 5.2: Values of the ionic strengths *I*, the equilibrium constants (*K*) and the equilibrium concentration of CO_2 for its absorption in an aqueous buffer solution containing 0.3 mol/l K_2CO_3 and 0.3 mol/l $KHCO_3$ at 295 K (values are computed from equations 5.3-6 – 5.3-11).

Another important parameter required for the calculation of the k_La-values is the concentration of CO_2 at the interface, c_S. Assuming equilibrium at the interface and no mass transfer resistance at the gas-side, c_S may be expressed by means of the pressure of the gas phase *p*, the mole fraction of CO_2 in the gas stream x_{CO2} and the Henry constant H_{CO2} of CO_2 in the aqueous electrolyte solution:

$$c_S = H \cdot x_{CO_2} p \qquad (5.3\text{-}12).$$

The Henry constant for CO_2 in the aqueous electrolyte solution can be estimated from the following correlations (Pohorecki and Moniuk, 1988a, 1988b; Barrett, 1966):

$$\log\frac{H_{CO_2}}{H_w} = -\sum I_i h_i = \left(I_{K_2CO_3} + I_{KHCO_3}\right)h \quad \text{with} \quad h = h_{K^+} + h_{CO_3^{2-}} + h_{CO_2(G)} \qquad (5.3\text{-}13),$$

where *h* contains the contributions of cations, anions and the gas and H_w is the Henry constant for CO_2 in pure water given as:

$$\log H_w = 9.1229 - 5.9044\cdot10^{-2}T + 7.8857\cdot10^{-5}T^2 \qquad (5.3\text{-}14).$$

The values of the contributions, H_w and the resulting Henry constant for the present experimental conditions are summarized in table 5.3.

h_{K^+}	$h_{CO_3^{2-}}$	$h_{CO_2(G)}$	H_W	H_{CO_2}
	[l/mol]		[mol/l·bar]	
0.074	0.021	-0.019	$3.69\cdot10^{-2}$	$\approx 3\cdot10^{-2}$

Table 5.3: Values of the contributions *h* of ions and the gas, the Henry constant H_w of CO_2 for pure water and the Henry constant of CO_2 for an aqueous buffer solution containing 0.3 mol/l K_2CO_3 and 0.3 mol/l $KHCO_3$ at 295 K (values are computed from equations 5.3-13 and 5.3-14).

The experimental set-up is shown in figure 5.3a. A mixture of nitrogen and CO_2 (c_{in}) was contacted with the buffer solution in the meandering microchannel with sharp corner bends. The molar flow rate of each gas is given as:

$$\dot{n}_i = Q_i \frac{\rho_i}{M_i} \qquad (5.3\text{-}14),$$

where Q_i is corresponding volumetric flow rate, ρ_i the density and M_i the molar weight. The inlet concentration of CO_2 (c_{in}) is then obtained as follows:

$$c_{in} = \frac{\dot{n}_{CO_2,in}}{Q_G} \qquad \text{with} \qquad Q_G = Q_{CO_2} + Q_{N_2} \qquad (5.3\text{-}15).$$

The mole fraction for CO_2 in this gas-mixture writes as:

$$x_{CO_2} = \frac{\dot{n}_{CO_2}}{\dot{n}_{CO_2} + \dot{n}_{N_2}} \qquad (5.3\text{-}16).$$

The pressure drop Δp_{in} of the gas phase was measured by a differential pressure indicator. The total pressure of the gas at the inlet is then given as:

$$p_{in} = p_{atm} + \Delta p_{in} \qquad (5.3\text{-}17),$$

where p_{atm} is the atmospheric pressure displayed by the same indicator. The flow conditions used to carry-out the experiments were limited to four gas-liquid flow rate combinations at which a stable and regular Taylor flow was obtained (see table 5.4).

Experiment number	Q_G [10^{-8} m^3/s]	Q_L [10^{-8} m^3/s]	Q_{N_2} [10^{-8} m^3/s]	$\dot{n}_{N_2}$ [10^{-6} mol/s]	Q_{CO_2} [10^{-8} m^3/s]	$\dot{n}_{CO_2,in}$ [10^{-6} mol/s]
1	7.6	1.15	4.5	2.01	3.1	1.39
2	7.6	4.44	4.5	2.01	3.1	1.39
3	10.1	2.3	6.0	2.68	4.1	1.84
4	10.1	4.44	6.0	2.68	4.1	1.84

Table 5.4: Operating conditions for CO_2-N_2 gas mixture as well as for the aqueous K_2CO_3/$KHCO_3$ buffer solution (Q volumetric flow rate; $\dot{n}$ molar flow rate; subscripts: G CO_2-N_2 gas mixture; L aqueous buffer solution; N_2 nitrogen; CO_2 carbon dioxide; *in* gas inlet).

The physico-chemical properties of the gases, as well as other constant parameters of the gas inflow are summarized in table 5.5.

ρ_{N_2} [kg/m^3]	M_{N_2} [kg/mol]	ρ_{CO_2} [kg/m^3]	M_{CO_2} [kg/mol]	$x_{CO_2,in}$	c_{in} [mol/m^3]
1.25	0.028	1.98	0.044	0.41	≈ 18

Table 5.5: Properties of gases used in absorption experiments with an aqueous K_2CO_3/$KHCO_3$ buffer solution (ρ density at 293 K; M molar weight; x mole fraction in gas mixture, c concentration of carbon dioxide in the gas mixture; subscripts: N_2 nitrogen; CO_2 carbon dioxide; *in* gas inlet).

At the outlet of the microchannel, the two phase flow was discharged to a phase separator as shown in figure 5.3b. It should be pointed out that this part of the experimental set-up constituted a particular challenge. Typically in this type of separator, the two phase flow enters via the side junction and then is separated in the vertical tube. In figure 5.3b however, it can be seen that the gas-phase leaves the

separator by the side-junction. This is because the microfluidic connector fixed at the microchannel outlet was too large to be connected to the side junction. Thus, the microchannel outlet was connected to the upper opening of the separator. The latter, however, was much larger than the diameter of the microfluidic connector and thus needed to be partially closed. This was realized by gluing the front part of a syringe in it, serving as a kind of closing cap. A hole was then drilled in this cap, whose diameter was only slightly larger than that of the microfluidic connector. After insertion of the microfluidic connector, the conjunction to the separator was sealed by polysiloxane-paste. This sealing was permanently controlled during the entire measurement campaign.

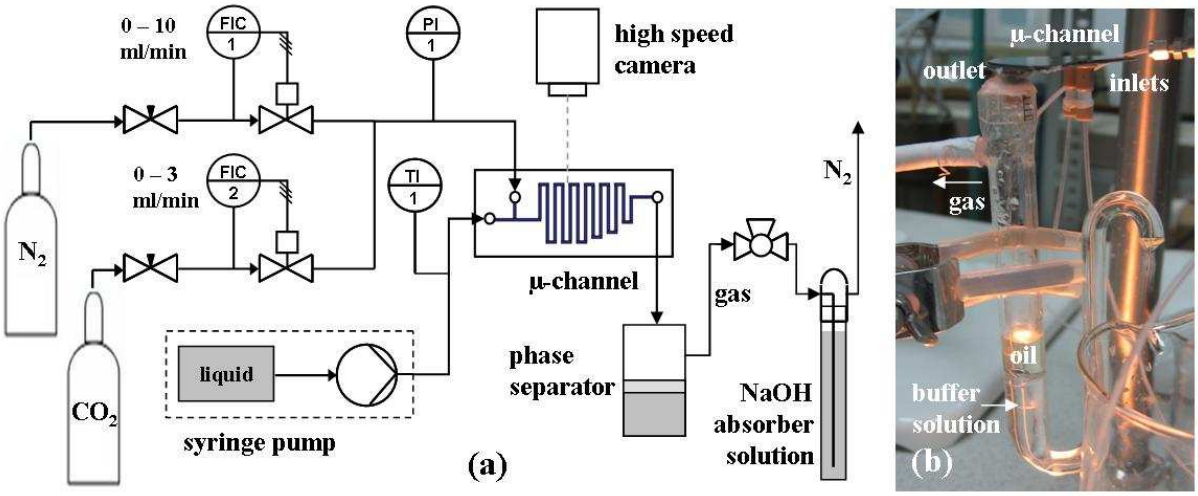

Figure 5.3: Illustration of the experimental set-up used for measuring $k_L a$-values by the absorption of CO_2 in aqueous buffer solution containing 0.3 mol/l K_2CO_3 and 0.3 mol/l $KHCO_3$ at 295 K (a: flow sheet; b: photo of the microchannel plate connected to the phase separator; FIC flow indication and control; PI pressure indicator, TI temperature indicator; further characteristics of the feeding equipment and the camera are specified in table 4.1, section 4.1.1).

During the experiments the two-phase flow in the microchannel was recorded using a high speed camera. A representative example image of this is shown in figure 5.4. From the separator, the gas-mixture was fed to an absorber bottle filled with a 1M NaOH solution. The N_2/CO_2 mixture was dispersed into tiny bubbles in the solution thereby ensuring the absorption of all the CO_2 (c_{out}) in the gas phase at the outlet of the microchannel. This was done for a defined measurement time $t_{measure}$, which was used for the computation of outflow concentration. The number of moles of CO_2 in the outlet flow was determined by titrating liquid samples from the absorption bottle. The method employed here is the Warder method, which consists in a two-point titration with HCl using phenolphthalein and methyl orange as indicators for the first and second end-points, respectively. Together with the measuring time, this enabled the molar flow rate and with it the outlet concentration of CO_2 to be computed.

$$c_{out} = \frac{\dot{n}_{CO_2,out}}{Q_G} \qquad \text{with} \qquad \dot{n}_{CO_2,out} = \frac{n_{CO_2,out}}{t_{measure}} \qquad (5.3\text{-}18).$$

The concentration change of CO_2 in the gas phase between the inlet concentration c_{in} and the outlet concentration c_{out} is used in the following to determine the experimental volumetric liquid side mass transfer coefficient $k_L a$.

Figure 5.4: Example image of Taylor flow in a microchannel with w = 1000 µm, h = 500 during measurements of mass transfer (gas-phase: CO_2-N_2 mixture; liquid phase: K_2CO_3/$KHCO_3$ buffer solution; superficial gas velocity U_{GS} = 0.202 m/s; superficial liquid velocity U_{LS} = 0.089 m/s).

The absorption process was modelled in a manner analogous to the heat transfer process in a heat exchanger (Hewitt et al., 1994). According to this one may write the amount of CO_2 transferred to the liquid phase over the length of the microchannel as:

$$\dot{n}_A = Q_G\left(c_{in} - c_{out}\right) \qquad (5.3\text{-}19),$$

and the volumetric liquid side mass transfer coefficient as:

$$k_L a = \frac{\dot{n}_A}{V_{mc} \cdot \Delta c_m} \qquad (5.3\text{-}20),$$

where V_{mc} is the volume of the microchannel and Δc_m the logarithmic mean concentration difference. The latter is similar to the logarithmic mean temperature difference used in heat transfer and is thus represented as follows:

$$\Delta c_m = \frac{\Delta c_{\max} - \Delta c_{\min}}{\ln \dfrac{\Delta c_{\max}}{\Delta c_{\min}}} \qquad (5.3\text{-}21).$$

Combination of 5.3-19 – 21 results in:

$$k_L a = \frac{Q_G}{V_{mc}} \frac{c_{in} - c_{out}}{\Delta c_{\max} - \Delta c_{\min}} \ln \frac{\Delta c_{\max}}{\Delta c_{\min}} \qquad (5.3\text{-}22).$$

With respect to the modeling of the concentration differences $\Delta c_{\max}$ and $\Delta c_{\min}$ one may distinguish two cases. Firstly, we may consider the case where the reaction in the bulk of the liquid is much faster than the rate of mass transfer. If the exposure or contact time between the gas and the liquid phases is large enough such that CO_2 is transferred to the liquid phase, the dissolved CO_2 then immediately reacts with the buffer solution. This means that during the absorption process there is always a concentration of free CO_2 in the liquid phase that is in equilibrium with the buffer solution c_e (see table 5.2). For this case, the maximum concentration difference is that between the interface concentration at the inlet $c_{S,in}$ and equilibrium concentration in the liquid phase c_e, whilst the minimum concentration difference is that between the interface concentration at the outlet $c_{S,out}$ and c_e. Consequently expression 5.3-22 can be rewritten as:

$$k_L a = \frac{Q_G}{V_{mc}} \frac{c_{in} - c_{out}}{c_{S,in} - c_{S,out}} \ln \frac{c_{S,in} - c_e}{c_{S,out} - c_e} \qquad \text{for} \qquad k_L a < \varepsilon_L k_{1,app} \qquad (5.3\text{-}23).$$

The second case concerns systems which are limited by the reaction rate. In such a case, the transfer rate is much faster than the reaction rate in the bulk, and the dissolved CO_2 remains practically unreacted. The mass transfer process thus can be considered as a pure physical absorption process. In this case a zero concentration of CO_2 in the bulk of the inlet buffer solution can be assumed and the $k_L a$-value can be expressed as:

$$k_L a = \frac{Q_G}{V_{mc}} \frac{c_{in} - c_{out}}{c_{S,in} - \left(c_{S,out} - c_{L,out}\right)} \ln \frac{c_{S,in}}{c_{S,out} - c_{L,out}} \qquad \text{for} \qquad k_L a > \varepsilon_L k_{1,app} \qquad (5.3\text{-}24),$$

where $c_{L,out}$ is the concentration of transferred CO_2 in the bulk liquid phase at the outlet. It can be estimated from the CO_2 mass balance given by:

$$\dot{n}_{CO_2,L,out} - \dot{n}_{CO_2,L,in} = \dot{n}_{CO_2,in} - \dot{n}_{CO_2,out} \qquad \text{where} \quad \dot{n}_{CO_2,L,in} = 0 \qquad (5.3\text{-}25),$$

which can be rewritten as:

$$c_{L,out} = \frac{Q_G}{Q_L}\left(c_{in} - c_{out}\right) \qquad (5.3\text{-}26).$$

The interface concentrations $c_{S,in}$ and $c_{S,out}$ are computed by means of equation 5.3-12 using p_{in} and p_{atm} as pressure values, respectively.

Before going to the results it is necessary to check if under the present operating conditions the reaction of CO_2 in the carbonate/bicarbonate buffer solution can be considered as pseudo-1st order. The corresponding criterion is given by Danckwerts and Sharma (1966) as:

$$c_S\left(\frac{1}{\left[CO_3^{2-}\right]} + \frac{2}{\left[HCO_3^{-}\right]}\right)\left(\sqrt{1+Ha} - 1\right) << 1 \qquad \text{with } Ha = \sqrt{\frac{D_{CO_2} k_{1,app}}{k_L^2}} \qquad (5.3\text{-}27).$$

In order to estimate the Hatta number, the diffusivity of CO_2 in the buffer solution D_{CO2} is needed. It is related to the diffusivity in pure water D_w as given by (Barrett, 1966; Danckwerts, 1970; Pohorecki and Moniuk, 1988a):

$$\left(D_w \mu_w\right)_T = \left(D_{CO_2} \mu_L\right)_T \quad \text{with} \quad \log D_w = -8.164 + \frac{712.5}{T} - \frac{2.591 \cdot 10^5}{T^2} \qquad (5.3\text{-}28),$$

where T is the temperature (295 K in present study), and μ_w and μ_L are the dynamic viscosities of pure water and of the buffer solution, respectively. The latter can be estimated from (Pohorecki and Moniuk 1988a):

$$\log \mu_L = \frac{878.159}{T} - 3.0254 + 0.11029\left(c_{B0} + 2c_{D0}\right) + 0.08947\left(\frac{c_{D0}}{0.5c_{B0} + c_{D0}}\right) \qquad (5.3\text{-}29).$$

In relation to this study, c_{B0} and c_{D0} in equation 5.3-29 are the concentrations of K_2CO_3 and $KHCO_3$, respectively, which are both 0.3 mol/l. From equations 5.3-28 and 5.3-29 the diffusivity of CO_2 in the buffer solution is obtained as $D_{CO2} = 1.4 \cdot 10^{-9}$ m^2/s. Since the value of the liquid side mass transfer coefficient is unknown we assume that $k_L \approx O(10^{-4})$ m/s (see section 5.1.3). Furthermore, we use $k_{1,app} = 0.86$ s^{-1} (at 293 K; Roberts and Danckwerts, 1962). Even if the present experiments are conducted at 295 K, we assume that this circumstance does not affect the order of magnitude of the rate constant. Using these values one obtains $Ha \approx 0.12$. This is in accordance with the general classification of this characterization method ($Ha < 0.3$). Computation of the left hand side of criterion 5.3-27 additionally requires the estimation of the concentration of CO_2 at the interface c_S. In this context we use the interface concentration at the entry of the microchannel ($c_S = c_{S,in}$). From equation 5.3-12, using the Henry's law constant given in table 5.3 and a CO_2 mole fraction of 0.41 (see table 5.5) as well as the inlet pressures listed in table 5.6 one obtains $c_S \approx 0.013$ mol/l. Putting all together, 5.3-27 now writes as: 0.008 << 1. The condition for a pseudo-1st order behavior of the reaction system is thus satisfied.

5.4 Results and theoretical approximation of the k_La -value

5.4.1 Determination of the experimental volumetric liquid side mass transfer coefficient k_La

The gas-liquid system used in the mass transfer experiments is the absorption of CO_2 into an aqueous buffer solution of K_2CO_3/$KHCO_3$. This reaction system is considered as one whereby the rate of mass transfer is much faster than the rate of reaction, which initially suggests that equation 5.3-24 can be used to compute the k_La. However, due to the large flow rate ratios Q_G/Q_L used (see table 5.4), as well as differences between inlet and outlet concentrations of CO_2 in the gas phase c_{in} and c_{out} (tables 5.5 and 5.6), the computation of the k_La-values by means of equations 5.3-24 and 5.3-26 was not possible. Consequently, the volumetric liquid side mass transfer coefficients were calculated via equation 5.3-23, which typically considers systems whereby the rate of reaction is faster than the rate of mass transfer. Table 5.6 shows the measured outlet concentrations of CO_2 in the gas phase c_{out} and the inlet pressures of the gas mixture, together with additional parameters required for the estimation of the k_La-values.

Experiment number	p_{in} [bar]	$c_{S,in}$ [mol/m^3]	c_{out} [mol/m^3]	$x_{CO_2,out}$	$c_{S,out}$ [mol/m^3]	k_La [s^{-1}]
1	1.026	12.57	12.22	0.32	9.54	0.28
2	1.063	13.03	8.25	0.24	7.17	0.52
3	1.038	12.66	11.99	0.31	9.39	0.39
4	1.068	13.02	9.72	0.27	8.09	0.56

Table 5.6: Measured and calculated values required for the computation of the k_La-value from the absorption of CO_2 from a CO_2-N_2 gas mixture in an aqueous K_2CO_3/$KHCO_3$ buffer solution (p_{in} gas phase pressure at the inlet; $c_{S,in}$ interface concentration of CO_2 at the inlet calculated from equation 5.3-12 using p_{in}, a molar fraction of 0.41 and the Henry's law constant given in table 5.3; c_{out} measured concentration of CO_2 in the outlet gas stream, $x_{CO2,out}$ molar fraction of CO_2 in the outlet gas stream calculated by means of expression 5.3-16 and 5.3-18; $c_{S,out}$ interface concentration of CO_2 in the outlet gas stream calculated from equation 5.3-12 using p_{atm} = 1.008 bar, the molar fraction $x_{CO2,out}$ and the Henry's law constant given in table 5.3; the k_La-value was computed by means of 5.3-23 using the equilibrium concentration of free CO_2 given in table 5.2, the gas flow rates Q_G listed in table 5.4 and a microchannel volume of $1.5 \cdot 10^{-7}$ m^3).

In order to check of validity of our data and the use of equation (5.3-23) for the calculation of the mass transfer coefficient, the gas-phase concentration of CO_2 at an infinite channel length was firstly estimated. This should be smaller than the values of c_{out} measured in the microchannel. By assuming that at infinite channel lengths the only amount of CO_2 in equilibrium with the gas-phase is given by the equilibrium concentration of free CO_2 in the liquid phase, we can write:

$$c_e = H \cdot x_{CO_2,\infty} p_{atm} \qquad \text{with} \qquad x_{CO_2,\infty} = \frac{\dot{n}_{CO_2,\infty}}{\dot{n}_{CO_2,\infty} + \dot{n}_{N_2}} \tag{5.4-1}$$

Rearrangement of 5.4-1 with respect to the molar flow rate of CO_2 at infinite channel lengths and assuming that at this point Q_G is approximately equal to the inlet flow rate of nitrogen one obtains:

$$c_{out,\infty} = \frac{c_e}{\left(Hp_{atm} - c_e\right)} \frac{\dot{n}_{N_2}}{Q_{N_2}} \tag{5.4-2}$$

Insertion of the parameters listed in tables 5.2 – 5.4 results in a concentration $c_{out,\infty}$ of about 0.09 mol/m^3. Comparison with the values of c_{out} shown in table 5.6, it can be seen that the mass transfer is not complete at the outlet of the microchannel and the data can therefore be considered as acceptable.

Secondly, the estimation of $k_L a$ based on expression 5.3-23 suggests that the reaction in the bulk of the buffer solution is faster than the rate of mass-transfer. This means that the operating conditions used in this study should fulfill the following criterion:

$$k_L a < \varepsilon_L k_{1,app} \qquad (5.4\text{-}3),$$

where $k_{1,app}$ is the apparent pseudo 1st-order reaction rate constant of about 0.86 s^{-1} and ε_L is the liquid hold-up, which for Taylor flow can be estimated as (see also chapter 3, section 3.5.1):

$$\varepsilon_L = (1 - \varepsilon_G) \quad \text{with} \quad \varepsilon_G = \frac{U_{GS}}{U_B} \qquad (5.4\text{-}4).$$

Table 5.7 compares the rate of reaction and the rate of mass transfer as given in 5.4-3, as well as the hydrodynamic parameters required for the computation of the reaction rate criterion. The contact time between the gas and the liquid in the film region, which is roughly estimated by dividing the bubble length by the bubble velocity, is also given.

Experiment number	U_{GS} [m/s]	U_B [m/s]	l_B [10^{-3} m]	t_{film} [10^{-3} s]	ε_L	$\varepsilon_L k_{1,app}$ [s^{-1}]	$k_L a$ [s^{-1}]
1	0.152	0.277	11.3	≈ 41	0.45	0.39	0.28
2	0.152	0.395	3.47	≈ 8.8	0.62	0.53	0.52
3	0.202	0.405	7.13	≈ 18	0.50	0.43	0.39
4	0.202	0.460	3.92	≈ 8.5	0.65	0.48	0.56

Table 5.7: Operating conditions, corresponding hydrodynamic parameters and measured $k_L a$-values for the absorption of CO_2 from a CO_2-N_2 gas mixture in an aqueous K_2CO_3/$KHCO_3$ buffer solution (U_{GS} superficial gas velocity; U_B bubble velocity; l_B bubble length; $t_{film} = l_B/U_B$ film contact time; ε_L liquid hold-up computed from expression 5.4-4, $k_{1,app}$ apparent pseudo-1st order rate constant for the reactions of CO_2 with the bulk buffer solution).

From table 5.7, it can be seen that the criterion 5.4-3 is generally fulfilled, except in the case of experiment number 4 where one obtains the $k_L a > \varepsilon_L k_{1,app}$. However, our experimental $k_L a$ values are in principle similar to these obtained by two former studies, using the same method (Yue et al., 2007; Sobieszuk et al., 2008). In addition, when the $k_L a$ is plotted against the inverse square root of the film contact time, as shown in figure 5.5, it can be seen that there is a direct linear correlation. This shows the reliability of our results and we may thus trust in the computation of the $k_L a$-values according to expression 5.3-23.

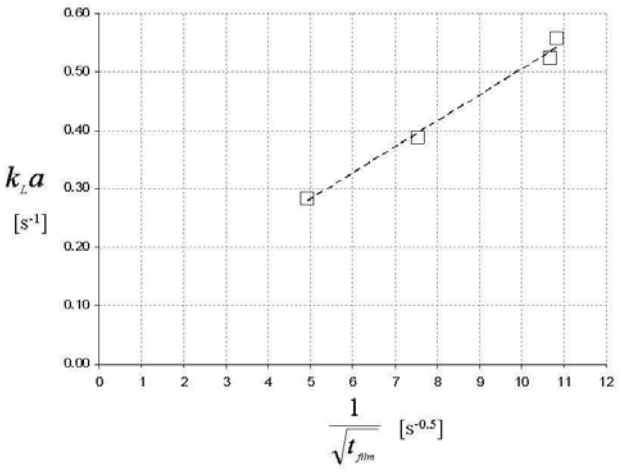

Figure 5.5: Graph of measured volumetric liquid-side mass tranfer coefficients ($k_L a$-values) versus the inverse square root of the corresponding film contact times t_{film}.

In the context of discussing the reliability of our results one may finally consider possible influences due to the experimental performance. The standard deviations of the k_La-values are in a range between 1 % and 3 %, which shows a good reproducibility of the experimental protocol. As possible error sources on may initially consider the preparation of the absorber solution, the exact implementation of the measuring time and the concentration measurements by titration. The latter was carried out by an automatic titration device with a systematic error 0.1 % regarding the dosing accuracy. The absorber solution was freshly prepared for each day of the measurement campaign and one may attribute a relative error of less than 1 %. At the end of the measuring time the complete cut-off of the gas-feed took about 2 s, so that some tiny bubbles still passed the absorber. However, compared to a measuring time of 45 min the amount of CO_2 additionally absorbed until the complete closing of the valve may be considered as negligible. Another point, which may have a greater influence on the accuracy of our results are outlet effects. That means that at after the exit of the microchannel mass transfer may still occur until the gas-phase leaves the separator. The determination of this feature usually requires performing the same experimental runs with a mirco-structured device of same dimensions, but without a main channel. That means that inlet and outlet sections are directly connected to each other (see Yue et al., 2007 for example). Since this was not possible in the frame of the present study one may generally state that the error attached to our results is less than 10 % and we may consider that the values obtained here constitute a slight overestimation of the real k_La values.

5.4.2 Prediction of the volumetric liquid side mass transfer coefficient k_La

In the following the operating conditions and the corresponding hydrodynamic parameters of the gas-liquid flow that have been measured are used to make an theoretical approximation of the prediction of the volumetric liquid side mass transfer coefficient in microchannels of rectangular cross-section. The parameters needed in this context were determined form the recordings of the flow and are summarized in table 5.8. The bubble velocity, the bubble length and the liquid slug length were measured at two positions in the microchannel: after the formation of Taylor flow and close to the outlet of the microchannel. The data given in table 5.8 constitute the averages of the data obtained at the different measurement points.

Experiment number	U_{TP} [m/s]	U_B [m/s]	Ca	l_B [10^{-3} m]	l_S [10^{-3} m]	k_La [s^{-1}]
1	0.175	0.277	$4.8\cdot10^{-3}$	11.3	1.44	0.28
2	0.241	0.395	$6.9\cdot10^{-3}$	3.47	1.59	0.52
3	0.248	0.405	$7.1\cdot10^{-3}$	7.13	1.32	0.39
4	0.291	0.460	$8\cdot10^{-3}$	3.92	1.5	0.56

Table 5.8: Operating conditions, corresponding hydrodynamic parameters and measured k_La-values for the absorption of CO_2 from a CO_2-N_2 gas mixture in an aqueous K_2CO_3/$KHCO_3$ buffer solution (U_{TP} superficial two phase velocity; U_B bubble velocity; Ca Capillary number; l_B bubble length; l_S slug length).

According to the analysis of the work done by van Baten and Krishna (2004) (see chapter 3, section 3.4), their mass transfer model can be generally written as:

$$k_{L,cap}a_{cap} + k_{L,film}a_{film} = 2\sqrt{\frac{D}{\pi t_{cap}}}\frac{A_{S,cap}}{V_{UC}} + 2\sqrt{\frac{D}{\pi t_{film}}}\frac{A_{S,BB}}{V_{UC}} \qquad (5.4\text{-}5),$$

where $A_{S,cap}$ is the surface area of the bubble caps, $A_{S,BB}$ the area of the lateral shell of the bubble body and V_{UC} the volume of the unit-cell, given by:

$$V_{UC} = (l_B + l_S)A_{Ch} \qquad (5.4\text{-}6)$$

Hence, the specific interfacial area of each region is determined by dividing the respective area with the volume of the unit-cell. In order to estimate the contact times and the interfacial area of the bubble, it is necessary to know the bubble shape. This topic was discussed in chapter 4 (section 4.2.1, figure 4.15). Considering the values of dimensionless bubble velocities obtained here, we suggested that the cross-sectional bubble profile may be approximated by an elliptical shape (see figure 5.6).

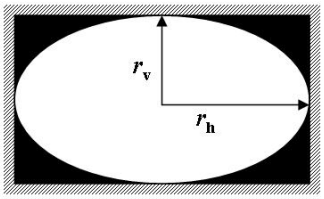

Figure 5.6: Principle sketch of an elliptical bubble profile in channels of rectangular cross-section.

For determining the interfacial area it is necessary estimate the possible dimensions of the bubble and to obtain these we need estimate the cross-sectional area of the bubble, which can be given as:

$$A_B = \pi \cdot r_v \cdot r_h \qquad (5.4\text{-}7).$$

In the microchannel geometry used here, the aspect ratio (*w/h*) is equal to 2 and we therefore consider that:

$$r_h = 2r_v \qquad (5.4\text{-}8).$$

Using the measured hydrodynamic parameters, the cross-sectional area of the bubble can be determined by applying a continuity relationship for the Taylor flow regime (chapter 3) which may be written as:

$$A_B = A_{Ch}\frac{U_{TP}}{U_B} \qquad (5.4\text{-}9),$$

where for the present microchannel dimensions the cross-sectional area of the channel A_{Ch} is about $5.25 \cdot 10^{-7}$ m^2. The dimensions of the bubble derived by means of equations 5.4-7 – 5.4-9 and the measured bubble velocities are summarized in Table 5.9.

Experiment number	U_{TP} [m/s]	U_B [m/s]	A_B [m^2]	r_v [10^{-4} m]	r_h [10^{-4} m]
1	0.175	0.277	$3.16 \cdot 10^{-7}$	2.24	4.48
2	0.241	0.395	$3.05 \cdot 10^{-7}$	2.20	4.41
3	0.248	0.405	$3.06 \cdot 10^{-7}$	2.21	4.41
4	0.291	0.460	$3.16 \cdot 10^{-7}$	2.24	4.48

Table 5.9: Comparison of superficial two-phase velocities U_{TP}, measured bubble velocities U_B and bubble dimensions derived by means of equation (5.4-7)-(5.4-9) for series of experiments specified in Table 5.8 (A_B is the cross-sectional area of the bubble; r_v and r_h, are the bubble radii in the vertical and horizontal plane, respectively).

With the assumption that the addition of both bubble caps results in a spheroid (rotationally symmetrical ellipsoid), the surface area of the bubble caps can now be computed from:

$$A_{S,caps} = \frac{2\pi \cdot r_v^2 r_h}{\sqrt{r_h^2 - r_v^2}}\left[\frac{r_h}{r_v^2}\sqrt{r_h^2 - r_v^2} + \arcsin\left(\frac{\sqrt{r_h^2 - r_v^2}}{r_h}\right)\right] \qquad (5.4\text{-}10).$$

The lateral shell of the bubble body is approximated from the bubble perimeter P_B

$$P_B \approx 2\pi\sqrt{\frac{r_h^2 + r_v^2}{2}} \qquad (5.4\text{-}11),$$

multiplied by the length of the bubble body:

$$A_{S,BB} = P_B\left(l_B - 2r_v\right) \qquad (5.4\text{-}12).$$

The contact time at the bubble caps is obtained by dividing the bubble perimeter by the average recirculation velocity within the liquid slug. At this we use the expression of the recirculation velocity derived in chapter 3 (section 3.3) for a circular channel since it was shown to give a good approximation for channels of rectangular cross-section (see chapter 4, section 4.2.2). It takes into account the evolution of the liquid phase velocity field as a function of the bubble velocity and the superficial two phase velocity.

$$t_{cap} = \frac{P_B}{2\left(U_{TP} - 0.5U_B\right)} \qquad (5.4\text{-}13).$$

In a similar way, the contact time in the film region can be modeled using the length of the bubble body and the bubble velocity.

$$t_{film} = \frac{\left(l_B - 2r_v\right)}{U_B} \qquad (5.4\text{-}14).$$

Finally in order to estimate k_L, the diffusivity of CO_2 in the buffer solution is needed. This value was previously computed by means of expressions 5.3-28 and 5.3-29. Accordingly, we set $D = 1.4 \cdot 10^{-9}$ m^2/s. Furthermore, by means of equations 5.4-5, 5.4-13 – 5.4-14, the mass-transfer coefficients for the bubble caps $k_{L,cap}$ and the film region $k_{L,film}$ can now be rewritten as:

$$k_{L,cap} = 2\sqrt{\frac{2D\left(U_{TP} - 0.5U_B\right)}{\pi P_B}} \qquad (5.4\text{-}15)$$

and

$$k_{L,film} = 2\sqrt{\frac{DU_B}{\pi\left(l_B - 2r_v\right)}} \qquad (5.4\text{-}16).$$

According to equation 5.4-5 and 5.4-6, the specific interfacial areas of the bubble caps a_{cap} and the film region a_{film} are given as:

$$a_{cap} = \frac{A_{S,caps}}{\left(l_s + l_B\right)A_{Ch}} \qquad (5.4\text{-}17)$$

and

$$a_{film} = \frac{P_B\left(l_B - 2r_v\right)}{\left(l_s + l_B\right)A_{Ch}} \qquad (5.4\text{-}18).$$

Combining equations 5.4-15 – 5.4-18 gives the following relation for k_La:

$$k_L a = 2\sqrt{\frac{2D\left(U_{TP} - 0.5U_B\right)}{\pi P_B}}\frac{A_{S,caps}}{\left(l_s + l_B\right)A_{Ch}} + 2\sqrt{\frac{DU_B}{\pi\left(l_B - 2r_v\right)}}\frac{P_B\left(l_B - 2r_v\right)}{\left(l_s + l_B\right)A_{Ch}} \qquad (5.4\text{-}19).$$

Table 5.10 presents the values obtained using equations 5.4-10, 5.4-11 and 5.4-15 – 5.4.18 with the data given in Tables 5.8 and 5.9.

Experiment number	P_B [10^{-3} m]	a_{cap} [m^2/m^3]	a_{film} [m^2/m^3]	$k_{L,cap}$ [10^{-4} m/s]	$k_{L,film}$ [10^{-4} m/s]	$(k_La)_{cap}$ [s^{-1}]	$(k_La)_{film}$ [s^{-1}]
1	2.23	257	3797	2.43	2.14	0.06	0.81
2	2.19	628	2619	2.68	4.85	0.17	1.27
3	2.19	377	3471	2.73	3.31	0.10	1.15
4	2.23	607	2851	3.13	4.89	0.19	1.40

Table 5.10: Composition of interfacial areas and mass-transfer coefficients estimated by means of equations 5.4-10, 5.4-11 and 5.4-15 – 5.4-18 using the values given in Tables 5.8 and 5.9 (P_B is the bubble perimeter).

Predicted and measured k_La-values are compared in figure 5.7. As can be seen here, the theoretical approach generally overestimates the experimental results by one order of magnitude. This

discrepancy may principally be attributed to an overestimation of the mass-transfer coefficients $k_{L,cap}$ and $k_{L,film}$. In order to explain that one needs to reconsider the original definition of k_L or more specifically the meaning of the time t as it was given by the surface renewable theory (see section 5.1.1). According to Higbie (1935) it is defined as a residence time of a liquid element at the interface. This means that the contact times as defined above do not constitute an appropriate way for approaching these residence times.

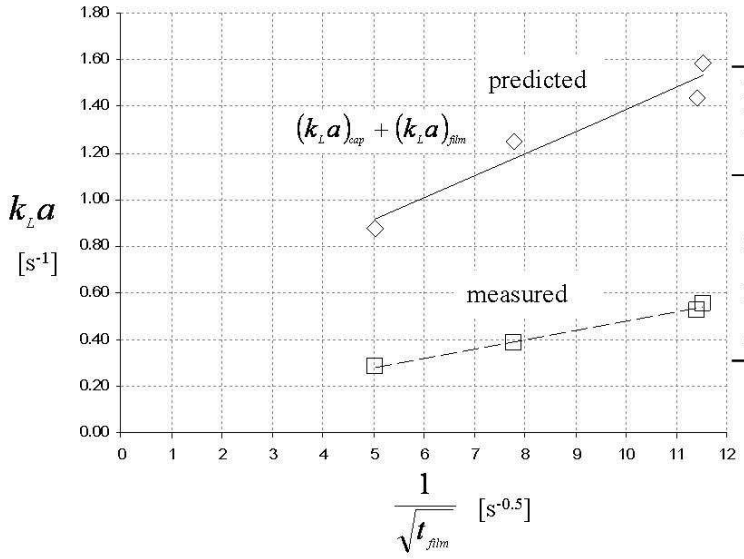

Exp. No.	measured (k_La) [s^{-1}]	predicted (k_La) [s^{-1}]	t_{film} [10^{-3} s]
1	0.28	0.87	≈ 39
2	0.52	1.44	≈ 7.7
3	0.39	1.25	≈ 17
4	0.56	1.4	≈ 7.5

Figure 5.7: Comparison of predicted and measured volumetric liquid-side mass tranfer coefficients ($k_L a$-values) versus the inverse square root of the corresponding film contact times t_{film} ($k_L a$-values are predicted according to expression 5.4-5 using the values listed in table 5.10; film contact times are computed by means of equation 5.4-14 using the values listed in tables 5.8 and 5.9).

However, from figures 5.5 and 5.7 it can clearly be seen that there is a direct correlation between the measured $k_L a$-values and the film contact time. It would thus be of interest to re-modify the mass transfer model given in 5.4-5 so that, still on the basis of hydrodynamic information, an approximation of the experimental values can be attained. To do this, we reconsider the concept of the liquid elements as mentioned above. These liquid elements are volumes. In this context one may initially state that the contact time t_{film} and the corresponding mass transfer coefficient $k_{L,film}$ can be attributed to the liquid elements located within the film region. On the other hand the contact time t_{cap} and the corresponding mass transfer coefficient $k_{L,cap}$ can be attributed to the liquid elements located within the region around the bubble caps and the liquid slug. However, the liquid elements of each region are only a fraction of the entire liquid volume within the unit cell. Hence, we suggest that the corresponding mass transfer coefficients only contribute with these respective fractions to the total value of the $k_L a$. In order to express these fractions we divide the liquid volume within the unit cell into two regions, the liquid volume within the film V_F and the remaining liquid which is composed of the volume around the bubble caps $V_{L,cap}$ and the liquid slug V_S. Basically one may define the liquid fraction ε_L as the volume of the liquid phase within the unit cell divided by the total volume of the unit cell V_{UC}. Accordingly, one may write:

$$\varepsilon_L = \frac{V_F}{V_{UC}} + \frac{V_{L,cap} + V_S}{V_{UC}} \qquad (5.4\text{-}20).$$

The first term on the right hand side of equation 5.4-20 is the fraction of the liquid film volume within the unit cell $\varepsilon_{L,F}$. It may be expressed as:

$$\varepsilon_{L,F} = \frac{A_F l_B}{A_{Ch}\left(l_B + l_S\right)} = \varepsilon_F \frac{l_B}{\left(l_B + l_S\right)} \qquad \text{with} \qquad \varepsilon_F = \left(1 - \frac{U_{TP}}{U_B}\right) \tag{5.4-21}$$

Following the explanations given above we state that $k_{L,film}$ contributes with a fraction of $\varepsilon_{L,F}$ to the total value of the volumetric liquid-side mass transfer coefficient whereby $k_{L,cap}$ may be attributed to a fraction of ε_L - $\varepsilon_{L,F}$. Hence, one may write the re-modified mass transfer model as:

$$k_L a = \left(\varepsilon_L - \varepsilon_{L,F}\right) k_{L,cap} a_{cap} + \varepsilon_{L,F} k_{L,film} a_{film} \quad \text{with} \quad \varepsilon_L = \left(1 - \frac{U_{GS}}{U_B}\right) \tag{5.4-22}$$

Here, ε_L is expressed according to equation 5.4-4. Table 5.11 presents the values of the respective liquid fractions and mass transfer contributions obtained using equation 5.4-21 and the data given in Tables 5.7, 5.8 and 5.10. These values are used in the following for the prediction of the volumetric liquid-side mass transfer coefficients, which are compared to the measured $k_L a$-values in figure 5.8.

Experiment number	$\varepsilon_{L,F}$	ε_L - $\varepsilon_{L,F}$	$k_{L,cap}(\varepsilon_L - \varepsilon_{L,F})$ [10^{-4} m/s]	$k_{L,film}\,\varepsilon_{L,F}$ [10^{-4} m/s]	$(k_L a)_{cap}(\varepsilon_L - \varepsilon_{L,F})$ [s^{-1}]	$(k_L a)_{film}\,\varepsilon_{L,F}$ [s^{-1}]
1	0.33	0.12	0.30	0.70	0.01	0.26
2	0.27	0.35	0.93	1.30	0.06	0.34
3	0.33	0.17	0.48	1.08	0.02	0.37
4	0.27	0.30	0.93	1.30	0.06	0.37

Table 5.11: Composition of liquid fractions and mass-transfer contributions estimated according to the re-modified mass transfer model given by expression 5.4-22. ($\varepsilon_{L,F}$ is the fraction of the liquid film within the unit-cell estimated by means of equation 5.4-21 using the values given in Table 5.8; ε_L liquid fraction, values are taken from table 5.7; values for k_L and $k_L a$ are taken from table 5.10).

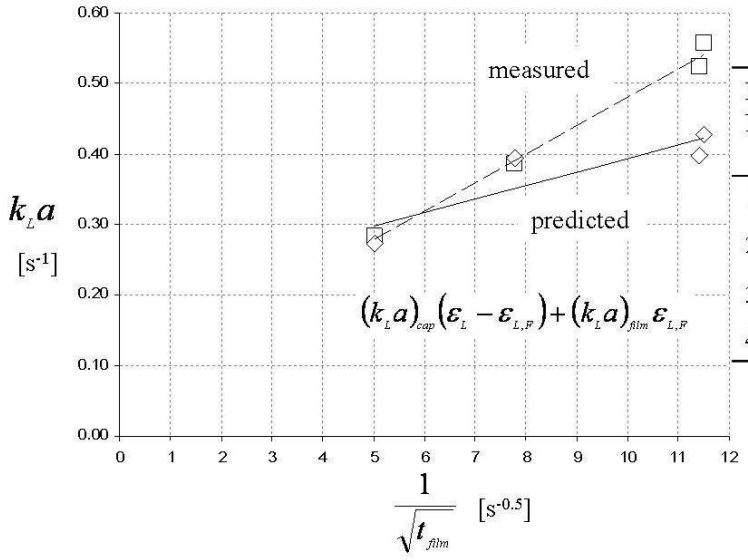

Exp. No.	measured ($k_L a$) [s^{-1}]	predicted ($k_L a$) [s^{-1}]	t_{film} [10^{-3} s]
1	0.28	0.27	≈ 39
2	0.52	0.40	≈ 7.7
3	0.39	0.39	≈ 17
4	0.56	0.43	≈ 7.5

Figure 5.8: Comparison of predicted and measured volumetric liquid-side mass tranfer coefficients ($k_L a$-values) versus the inverse square root of the corresponding film contact times t_{film} ($k_L a$-values are predicted according to expression 5.4-22 using the values listed in table 5.11; film contact times are computed by means of equation 5.4-14 using the values listed in tables 5.8 and 5.9).

Form figure 5.8 it can be seen that our re-modified model well predicts the measured $k_L a$-values in the case of film contact times in the order of 10^{-2} s (experiments number 1 and 3, long bubble data). On the other hand the experimental values obtained at film contact times of $t_{film} \approx O(10)^{-3}$ s (short bubble data) are generally underestimated by this approach. However, in general the predicted values show the same tendency as the experimental results, an increase of $k_L a$ with decreasing film contact time. In

addition, the circumstance that our re-modified mass transfer model well fits the long bubble data but fails in the case of the short bubble data may be attributed to two further hydrodynamic features, related to the mass transfer from the bubble caps. Basically one may assume that the contribution of this region should become more important with decreasing bubble lengths. The first feature to discuss in this context concerns the velocity fields within the liquid slug. In straight micro channels, gas-liquid Taylor flow gives rise to recirculating flow patterns within the liquid slug composed of an axi-symmetrical circulation loop. In curved micro channels, such as meandering channels, the recirculation loop in the liquid slug is distorted and is no longer symmetrical. This in turn results in improved mixing within the liquid slug compared with the Taylor flow in straight channel geometries. It is believed that the improved mixing within the slug in curved geometries increases the refreshment rate of the gas-liquid interface and with that the mass transfer at the bubble caps. The second factor that may explain the under-prediction of k_La in the case of the short bubble data may be due to the simplistic manner in which the cross-sectional bubble profile is estimated. It is the determining feature for the estimation of the specific interfacial area. Indeed, detailed information on the cross sectional shape of the bubbles is extremely difficult to obtain. Nevertheless, it was shown in figures 5.4 (see section 5.3) and 4.13 (see section 4.2.1) that the bubble shape is modified as it passes through the channel bend; the bubble is stretched and distorted. Especially in the case of short bubbles, these hydrodynamic effects should have important and positive effects on the gas-liquid mass transfer due to the increased interfacial area.

5.5 Conclusions

In this chapter we have employed an experimental protocol for measuring the volumetric liquid-side mass transfer coefficient of gas-liquid flow in micro channels and we have used it to measure the gas-liquid mass transfer of Taylor flow in a meandering microchannel. In addition, a model for mass transfer in circular micro channels taken from the literature has been modified to take into account the effects of the geometry of rectangular micro channels as well as the local hydrodynamic behavior within the liquid slugs. This model additionally includes the attempt to approach the residence times of liquid elements at the interface by so-called contact times. The volumetric liquid-side mass transfer coefficient obtained by the modified model has then been compared to experimental data. It has been found that the modified model overestimates the measured mass transfer coefficient. The discrepancies are mainly due to the circumstance that the contact times defined here underestimate the residence times of liquid elements at the interface. A re-modified approach which relates the mass transfer contributions of cap and film regions to specific fractions of the liquid phase was shown to well predict the experimentally measured values in the case of long bubbles and film contact times in the order of 10^{-2} s. On the other hand, k_La-values obtained for short bubbles and contact times in the order of 10^{-3} s were underestimated by the re-modified model. We attribute this to distortions of the velocity field and the bubble shape (see figures 5.4 and 4.13) induced by the bends of the meandering channel. The results of our re-modified model also showed that, especially in the case of short bubbles, precise information on the cross-sectional bubble profile and with it on the specific interfacial areas are of great importance for the prediction of k_La.

6 General Conclusions and Outlook

In order to improve the design of gas-liquid microreactors we have carried out a detailed literature survey and theoretical analysis on hydrodynamics and mass transfer in microchannels. The overall conclusions are as follows:

- In general, gas-liquid hydrodynamics are typically characterized by two-phase flow regimes. In microchannels and capillaries, these may generally be termed as bubbly, slug/Taylor, churn and annular flow. From an introductory literature review of gas-liquid flow regimes in small tubes and capillaries, we have suggested a criterion for gravity independent flow. According to this surface tension dominates gravitational acceleration if the channel hydraulic diameter is smaller or approximately equal to half the Laplace-lengths, which corresponds to Bond numbers of $Bo \leq 0.3$.

- The literature also provided a universal flow pattern map approach based on superficial phase Weber numbers (We_{LS} and We_{GS}), highlighting the impact of the competition between surface tension and inertia on flow pattern transitions. We adopted these universal flow transition criteria to discuss the state of the art of gas-liquid flow in microchannels. We have found several examples in the literature where the transition from slug/Taylor flow to annular flow could be correctly predicted by this Weber number based approach. However in general, the stability, as well as the occurrence of a certain flow characteristics are strongly dependent on the way the fluids are contacted. Furthermore, in the case of direct injection of the gas phase into higher viscosity liquids, we demonstrated that these Weber-number based criteria do not correctly predict the flow transitions

- In order to complete the universal flow transition approach, it appears that the quantitative description of flow pattern transitions should be extended to account for the influence of liquid phase viscosity. This could be done by including the ratio of the Capillary number and the Reynolds number Ca/Re. Also, for microchannels of rectangular cross-section, the aspect ratio should additionally be taken into consideration.

- From a comparison of flow patterns with respect to their mass transfer capacity, as well as the flexibility offered with respect to operating conditions, the Taylor flow pattern appears to be the most promising flow characteristic for performing fast, highly exothermic and mass transfer limited reactions. This flow pattern is characterized by elongated bubbles surrounded by a liquid film and separated from each other by liquid slugs. In addition to the fact that this flow regime is accessible within a large range of gas and liquid flow rates, and has a relatively high specific interfacial area, Taylor flow features a recirculation motion within the liquid slugs, which is generally assumed to increase molecular transport between the gas-liquid interface and the bulk of the liquid phase.

- Concerning Taylor flow and the transport of elongated bubbles through microchannels, we have identified the Capillary number and the dimensionless bubble velocity ψ as the basic characteristic flow parameters. The Capillary number, which indicates the competition between viscous forces and surface tension, is directly correlated to the deposition of the liquid film at the front of the bubble and determines the pressure within the bubble, as well

as the fraction of the channel cross-section occupied by the liquid film. The latter is the determining factor for the dimensionless bubble velocity, which is generally greater than unity ($\psi \geq 1$).

- The possibilities to estimate the gas-liquid two-phase pressure drop in Taylor flow has been discussed. From a literature review of this topic, it appears that prediction by means of conventional approaches like the homogeneous model or the separated flow model is not sufficient. Moreover, a number of studies suggest that it would be more appropriate to account for the hydrodynamic characteristics of the flow regime. Following this, the pressure drop in Taylor flow may be modeled as the sum of frictional pressure drop across the liquid slugs and the pressure within the bubbles. Hence in contrast to the conventional models, the two phase pressure drop becomes a function of the principle hydrodynamic parameters which, in addition to those mentioned above, may include bubble and slug lengths. In this context we also discussed the impact of further phenomena like the dewetting of the liquid film, which may induce a strong increase of pressure drop compared to Taylor flow with fully lubricated bubbles.

- Since one of the promising features of Taylor flow is the recirculation of the liquid phase within the liquid slugs we have been interested in a detailed depiction of the characteristics of the liquid phase velocity field. Considering a channel of circular cross-section as an example, we presented the theoretical basis of this flow character and analyzed the evolution of the relative liquid phase velocity field with respect to parameters like the fraction of recirculation flow, recirculation velocity and recirculation time. In this way we could show that the recirculation flow within the liquid slug strongly decreases with increasing dimensionless bubble velocity and that its existence is restricted to a specific range of dimensionless bubble velocities ($1 \leq \psi < 2$). For $\psi \geq 2$ the relative velocity field within the liquid slug is refereed to as complete by-pass flow. We thus, quantitatively depicted the parameters which are important concerning mixing within the liquid slug and a possible enhancement of mass transfer.

- Following up this context we were interested in the interaction of hydrodynamics and gas-liquid mass transfer. With respect to this topic, the literature provided a validated model which allows the estimation of the volumetric liquid side mass transfer coefficient ($k_L a$-value) as a function of hydrodynamic parameters for channels of circular cross-section. This approach distinguished two contributions to the overall $k_L a$-value: one from the bubble caps to the liquid slug and the other from the bubble body to the liquid film. Here, the specific interfacial area is directly computed by means of the shape and length of the bubble, as well as liquid slug lengths, determining the volume of a unit cell. The mass-transfer coefficient k_L may be modeled as inversely proportional to the gas-liquid contact time. For the film region, this is given by dividing the bubble lengths by the bubble velocity. With respect to the cap contact time, we propose that the model may be improved by implication of the recirculation velocity. Hence, at this point of our study we demonstrate that the local hydrodynamic characteristics, as well as gas-liquid mass transfer are governed by the bubble velocity, bubble lengths and slug lengths.

- In the following step we have dealt with the prediction of these key hydrodynamic parameters.
    - With respect to bubble velocities, the principle points are the evolution of the liquid film thickness and the cross-sectional profile of the bubble for Capillary numbers of several orders of magnitude. This has been presented in detail for channels of circular, square and rectangular cross-sections.
    - We also addressed the phenomenon of film dewetting. Besides a strong increase of pressure drop, the occurrence of this phenomenon affects the film region, containing the largest specific interfacial area within the unit cell, and thus constitutes a remarkable loss for gas-liquid mass-transfer. The literature enabled us to extract a criterion for its prediction. According to this, the drying out of the liquid film is likely to appear under conditions of partial wettability at low Capillary numbers ($Ca \leq O(10^{-3})$) and high film contact times ($t_{film} \geq 10^{-3}$).
    - From a literature survey concerning the formation of bubbles and slugs it has been shown that bubble and slug lengths are inversely proportional to the liquid hold-up and the gas hold-up, respectively. However, this scaling represents a lower limit since it does not account for the influence of fluid properties.
    - With respect to the mechanism of bubble formation, we discussed the role of the forces involved in this process. These are surface tension and viscous forces. The latter squeezes the bubble neck at the inlet and is finally responsible for the bubble pinch-off, while surface tension creates a pressure gradient which drives the liquid around the bubble neck, also called leakage flow. The process of bubble formation is thus governed by the competition of surface tension and viscous forces, which is represented by the superficial two-phase Capillary number Ca_{TP}.
    - The prediction of bubble lengths based on several literature correlations for Ca_{TP} of several orders of magnitudes has been compared. The observed tendencies enabled us to evaluate the influence of liquid phase properties on bubble lengths, which may be applied also to the slug lengths. This means that at low Capillary numbers ($Ca \leq O(10^{-3})$), the influence of surface tension leads to bubbles and slugs substantially larger than indicated by the lower limits. With increasing Capillary number at fixed hold-ups, the relative influence of surface tension decreases, and that of viscous forces increases. This leads to a decrease of bubble and slug lengths until the lower limit is reached. At this, the extent of the leakage flow and hence the deviation from the lower limit also depends on the space provided for the liquid phase to flow around the bubble tip and is therefore also a function of the shape of the channel cross-section. Following up the discussion concerning the influence of such design parameters, another literature model allows description of the dependency of bubble lengths on the dimensions of the gas-inlet channel, in the case of a pseudo-T-shaped inlet section. In this context, we complemented our theoretical considerations with the derivation of an expression for the prediction of liquid slug lengths.

This literature survey and the related theoretical analysis lead to the identification of several gaps of knowledge which have been the basis for experimental study. Following this, microchannels of rectangular cross-section where gas and liquid phases were contacted in a pseudo-T-junction were employed. The dimensions of the gas inlet channel were smaller than that of the main channel.

Our experimental study was divided into two parts. The first part was concerned with the investigation of hydrodynamic parameters, whilst the second dealt with the inter-linkage of hydrodynamics and mass transfer.

- Concerning the study of hydrodynamics we were initially interested in the prediction of bubble and slug lengths taking into account both, fluid properties and design parameters. For this purpose we set-up a modified model and conducted our experiments under conditions of increased influence of surface tension forces using air and ethanol as fluids (Ca = $O(10^{-3})$). A good agreement was found between the modified literature model and our experimental results.

- Using water as the liquid phase enabled partially wetting conditions to be created. This lead to the drying-out of the liquid film and the criterion previously extracted within the theoretical section was confirmed.

- In a further task we visualized the liquid phase velocity field within the liquid slugs at Ca = $O(10^{-3})$ using microParticle Image Velocimetry. From the resulting relative liquid phase velocity field we extracted characteristic hydrodynamic parameters, such as vortex centre position and recirculation velocity. At this our results obtained in the rectangular channel revealed many similarities with those theoretically depicted for channels of circular cross-sections. This suggests that the considerations made with respect to circular channels may serve as a good approximation for rectangular microchannels concerning the evolution of the velocity field and related parameters, like the recirculation velocity, recirculation flow fraction and recirculation time.

In the second part we focused on the prediction of gas-liquid mass transfer in Taylor flow. Measurements of the volumetric liquid side mass transfer coefficient ($k_L a$-value) were conducted and the related two-phase flow was recorded. The measured bubble velocities, bubble lengths and slug lengths, as well as the findings previously obtained from the characterization of the velocity field were used to set-up a modified model for the prediction of $k_L a$-values in channels of rectangular cross-section. A particular feature of this model is that the residence times, needed to estimate k_L, are re-placed by so-called contact times which are modeled on the basis of hydrodynamic parameters characteristic for the Taylor flow regime. The $k_L a$-values computed in this manner were then compared to the measured ones. Our model overestimates the experimental values by a factor of about 3. In this context, we believe that the contact times defined here generally underestimate the residence times of liquid elements at the interface. However, since the real residence time of liquid elements at the interface is a parameter which is experimentally difficult to obtain, we decided to maintain these contact times and proposed a re-modification of our model by assuming that the mass transfer coefficients of film and cap regions contribute with specific fractions of the liquid phase to the total value of $k_L a$. This re-modified approach indeed well fitted the experimental $k_L a$-values obtained for long film contact times ($t_{film} \approx O(10)^{-2}$ s) but resulted in an underestimation in the case of short film contact times ($t_{film} \approx O(10)^{-3}$ s). We attribute this to two factors. The channel used in this study was arranged in a meandering manner. When the flow passes through the bends the velocity field within the slug as well as the bubble shape is noticeably distorted. We believe that these phenomena have a significant influence on mass-transfer from bubble caps. In addition to this, the measured hydrodynamic parameters did not allow the determination of the real nature of the cross-sectional bubble profile and whereby this point was based on a supposition. However, the knowledge of the

cross-sectional bubble profile is an important prerequisite for a reliable estimation of the specific interfacial area. Consequently in order to obtain a satisfying correlation between hydrodynamics and mass transfer in Taylor flow through rectangular microchannels a detailed investigation of the evolution of the cross-sectional bubble profile and the liquid film thickness for Capillary numbers of several orders of magnitudes should be an item for further studies. In this context, the influence of the channel aspect ratio and the shape of the inlet section (X-, Y, T-junction) on the formation of bubbles and slugs should be considered. Exact information about the liquid film thickness is additionally an important point for the estimation of the saturation/exhaustion time. Furthermore, the evolution of the bubble profile and the film thickness are determining parameters for the prediction of the evolution of the film fraction, from what bubble velocities can be predicted. Finally, it appears that the residence time of liquid elements at the interface is a topic which needs to be explored furthermore.

A possible way to achieve this is to carry-out 3-dimenional numerical simulations of Taylor flow, since it allows a more detailed insight into the local hydrodynamics of the flow. In this manner the modified model for the prediction of $k_L a$-values given in the present study may be refined and compared to the results obtained form simulations of gas-liquid mass transfer, which may be undertaken in a further step. The simulations would also allow the determination of the evolution of the bubble pressure, which is an important parameter for modelling gas-liquid two-phase pressure drop in Taylor flow.

A second area which is particularly important with respect to the design of the channel cross-section is the estimation of the heat transfer in Taylor flow. This topic may be treated in a similar manner to mass transfer and a model may be set-up by considering the film region and the liquid slug separately.

References

A

Ajaev, V., Homsy, G.M., 2006. Modeling shapes and dynamics of confined bubbles. Annual Review of Fluid Mechanics 38, 277-307.

Akbar, M.K., Plummer, D.A., Ghiaasiaan, S.M., 2003. On gas-liquid two-phase flow regimes in microchannels. International Journal of Multiphase Flow 29, 855-865.

Aussillous, P., Quéré, D., 2000. Quick deposition of a fluid on the wall of a tube. Physics of Fluids 12 (10), 2367-2371.

B

Barajas, A.M., Panton, R.L., 1993. The effects of contact angle on two-phase flow in capillary tubes. International Journal of Multiphase Flow 19 (2), 337-346.

Barrett, P.V.L., 1966. Ph.D. Thesis. University of Cambridge.

Blackmore, B., Li, D., Gao, J., 2001. Detachment of bubles in slit microchannels by shearing flow. Journal of Colloid and Interface Science 241, 514-520.

Bercic, G., Pintar, A., 1997. The role of gas bubbles and liquid slug lengths on mass transport in Taylor flow through capillaries. Chemical Engineering Science 52, 3709-3719.

Bretherton, F.P., 1961. The motion of long bubbles in tubes. Journal of Fluid Mechanics 10, 166-188.

Buckingham, E., 1914. On physically similar systems: illustrations of the use of dimensional equations. Physical Review Letters 4, 345-376.

C

Chang, H.-C., 2005. Bubble/drop transport in microchannles. In: Gad-el-Hack, M. MEMS Handbook, Second Edition. Taylor and Francis, Introduction and Fundamentals, chapter 13.

Chambers, R.D., Fox, M.A., Holling, D., Nakano, T., Okazoe, T., Sandford, G., 2005. Versatile gas/liquid microreactors for industry. Chemical Engineering Technology 28 (3), 344-352.

Chaudhari, R.V., Mills, P.L., 2004. Multiphase catalysis and reaction engineering for emerging pharmaceutical processes. Chemical Engineering Science 59, 5337-5344.

Chen, W.L., Twu, M.C., Pan, C., 2002. Gas-liquid two-phase flow in microchannels. International Journal of Multiphase Flow 28, 1235-1247.

Chisholm, D., 1967. A theoretical basis for the Lockhart-Martinelli correlation for two-phase flow. International Journal of Heat and Mass Transfer 10, 1767-1778.

Chung, P.M.-Y., Kawaji, M., 2004. The effect of channel diameter on adiabatic two-phase flow characteristics in microchannels. International Journal of Multiphase Flow 30, 735-761.

Coulson, J.M., Richardson, J.F., Backhurst, J.R., Harker, J.H., 1990. Chemical Engineering. Pergamon Press.

Cubaud, T., Ho, C.-M., 2004. Transport of bubbles in square microchannels. Physics of Fluids 16 (12), 4575-4585.

Cubaud, T., Tatineni, M., Zhong, X., Ho, C.-M., 2005. Bubble dispenser in microfluidic devices. Physical Review E 72 (3), 037302.

D

Danckwerts, P.V., 1951. Significance of liquid-film coefficients in gas absorption. Industrial and Engineering Chemistry 43 (6), 1460-1467.

Danckwerts, P.V., Sharma, M.M., 1966. Absorption of carbon dioxide into solutions of alkalis and amines. Journal of Chemical Engineering Reviews Series No. 2, The Chemical Engineer, CE 244-280.

Danckwerts, P.V., 1970. Gas-liquid reactions. McGraw-Hill, New York.

de Gennes, P.-G., Brochard-Wyart, F., Quéré, D., 2002. Gouttes, bulles, perles et ondes. Éditions Belin, Paris.

de Mas, N., Günther, A., Schmidt, M.A., Jensen, K.F., 2003. Microfabricated multiphase reactors for the selective direct fluorination of aromatics. Industrial and Engineering Chemistry Research 42, 689-710.

E

Ehrfeld, W., Hessel, V., Löwe, H., 2000. Microreactors . Wiley-VCH, Weinheim.

Emig, G., Klemm, E., 2005. Technische Chemie. Springer, Berlin Heidelberg.

F

Fairbrother, F., Stubbs, A.E., 1935. Studies in electro-endosmosis. Part VI. The bubble-tube method of measurement. Journal of the Chemical Society 1, 527-529.

Fries, D.M., Trachsel, F., von Rohr, P.R., 2006. Druckeinfluss auf Gas/Flüssig-Zweiphasenströmung im Mikroreaktor. Chemie Ingenieur Technik, 78 (9), 1210.

Fries, D.M., Waelchli, S., von Rohr, P.R., 2008. Gas-liquid two-phase flow in meandering microchannels. Chemical Engineering Journal 135 (Supplement 1), S37-S40.

Fuerstman, M.J., Lai, A., Thurlow, M.E., Shevkoplyas, S.S., Stone, H.A., Whitesides, G.M., 2007. The pressure drop along rectangular microchannels containing bubbles. Lab on a Chip 7, 1479-1489.

G

Garstecki, P., Fuerstman, J.M., Stone, H.A., Whitesides, G.M., 2006. Formation of droplets and bubbles in a microfluidic T-junction – scaling and mechanism of break-up. Lab on a Chip 6, 437-446.

Günther, A., Khan, S.A., Thalmann, M., Trachsel, F., Jensen, K.F., 2004. Transport and reaction in Microscale segmented gas-liquid flow. Lab on a Chip 4, 278-286.

Günther, A., Jhunjhuwala, M., Thalmann, M., Schmidt, M.A., Jensen, K.F., 2005. Micromixing of Miscible liquids in segmented gas-liquid flow. Langmuir 21, 1547-1555.

Günther, A., Jensen, K.F., 2006. Multiphase microfluidics: from flow characteristics to chemical and materials synthesis. Lab on a Chip 6, 1487-1503.

H

Haverkamp, V., 2002. Charakterisierung einer Mikroblasensäule zur Durchführung stofftransportlimitierter und/oder hoch-exothermer Gas/Flüssig-Reaktionen. Ph.D. Thesis. University of Erlangen, Erlangen, Germany.

Haverkamp, V., Hessel, V., Löwe, H., Menges, G., Warnier, M.J.F., Rebrov, E.V., de Croon, M.H.J.M., Schouten, J.C., Liauw, M.A., 2006. Hydrodynamics and mixer-induced bubble formation in micro bubble columns with single and multiple-channels. Chemical Engineering Technology 29 (9), 1015-1026.

Hazel, A.L., Heil, M., 2002. The steady propagation of a semi-infinite bubble into tubes of elliptical and rectangular cross-section. Journal of Fluid Mechanics 470, 91-114.

Hessel, V., Ehrfeld, W., Herweck, T., Haverkamp, V., Löwe, H., Schiewe, J., Wille, C., Kern, T., Lutz, N., 2000. Gas/liquid microreactors: hydrodynamics and mass transfer. IMRET 4: Proceedings of the 4th International Conference on Microreaction Technology, 174.

Hessel, V., Angeli, P., Gavriilidis, A., Löwe, H., 2005. Gas-liquid and gas-liquid-solid microstructured reactors: contacting principles and applications. Industrial and Engineering Chemistry Research 44, 9750-9769.

Hewitt, G.F., Shires, G.L., Bott, T.R., 1994. Process heat transfer. CRC Press, London.

Higbie, R., 1935. The rate of absorption of a pure gas into a still liquid during short periodics of exposure. Transactions of the American Institute of Chemical Engineers 31, 365-388.

Hoffmann, A., Mackowiak, J.F., Gorak, A., Haas, M., Löning, J.M., Runowski, T., Hallenberger, K., 2007. Standardization of mass transfer measurements – A basis for the description of absorption processes. Chemical Engineering Research and Design 85 (A1), 40-49.

J

Jähnisch, K., Hessel, V., Löwe, H., Baerns, M., 2004. Chemistry in microstructured reactors. Angewandte Chemie International Edition 43, 406-446.

Jiang, F., Drese, K.S., Hardt, S., Küpper, M., Schönfeld, F., 2004. Helical flows and chaotic mixing in curved micro channels. A.I.Ch.E. Journal 50 (9), 2297-2305.

K

Kawahara, A., Chung, P.M.-Y., Kawaji, M., 2002. Investigation of two-phase flow pattern, void fraction and pressure drop in a microchannel. International Journal of Multiphase Flow 28, 1411-1435.

Kirschneck, D., Tekautz, G., 2007. Integration of a microreactor in an existing production plant. Chemical Engineering Technology 30, 305-308.

Klemm, E., Döring, H., Geißelmann, A., Schirrmeister, S., 2007. Mikrostruckturreaktoren für die heterogene Katalyse. Chemie Ingenieur Technik 79 (6), 697-706.

Kolb, W.B., Cerro, R.L., 1991. Coating the inside of a capillary of square cross-section. Chemical Engineering Science 46 (9), 2181-2195.

Kolb, W.B., Cerro, R.L., 1993. Film flow in the space between a circular bubble and a square tube. Journal of Colloid and Interface Science 46 (9), 2181-2195.

Kreutzer, M.T., Kapteijn, F., Moulijn, J.A., Heiszwolf, J.J., 2005a. Multiphase monolith reactors: Chemical reaction engineering of segmented flow in microchannels. Chemical Engineering Science 60, 5895-5916.

Kreutzer, M.T., Kapteijn, F., Moulijn, J.A., Kleijn, C.R., Heiszwolf, J.J., 2005b. Inertial and Interfacial Effects on Pressure Drop of Taylor Flow in Capillaries. A.I.Ch.E. Journal 51 (9), 2428-2440.

Kucharski, E., 1978. Ph.D. Thesis. Warsaw Technical University, Warsaw.

L

Laborie, S., Cabassud, C., Durand-Bourlier, L., Laine, J.M., 1999. Characterisation of gas-liquid two-phase flow inside capillaries. Chemical Engineering Science 54, 5723-5735.

Leclerc, A., Alame, M., Schweich, D., Pouteau, P., Delattre, C., de Bellefon, C., 2008. Gas-liquid selective oxidations with oxygen under explosive conditions in a micro-structured reactor. Lab on a Chip 8, 814- 817.

Lee, H.J., Lee, S.Y., 2001. Pressure drop correlations for two-phase flow within horizontal rectangular channels with small heights. International Journal of Multiphase Flow 27, 783-796.

Lewis, W., Whitman, W., 1924. Principles of gas absorption. Industrial and Engineering Chemistry 16, 1215-1219.

Lockhart, R.W., Martinelli, R.C., 1949. Proposed correlation of data for isothermal two-phase two-component flow in pipes. Chemical Engineering Progress 45, 39-48.

Liu, H., Vandu, C.O., Krishna, R., 2005. Hydrodynamics of Taylor Flow in Vertical Capillaries: Flow Regimes, Bubble Rise Velocity, Liquid Slug Length, and Pressure Drop. Industrial and Engineering Chemistry Research 44, 4884-4897.

Liu, D., Wang, S., 2008. Flow pattern and pressure drop of upward two-phase flow in vertical capillaries. Industrial and Engineering Chemistry Research 47 (1), 243-255.

M

Mills, P.L., Chaudhari, R.V., 1997. Multiphase catalytic reactor engineering and design for pharmaceuticals and fine chemicals. Catalysis Today 37, 367-404.

Mills, P.L., Chaudhari, R.V., 1999. Reaction engineering of emerging oxidation processes. Catalysis Today 48, 17-29.

Mishima, K., Hibiki, T., Nishihara, H., 1993. Some characteristics of gas-liquid flow in narrow rectangular ducts. International Journal of Multiphase Flow 19, 115-124.

Mishima, K., Hibiki, T., 1996. Some characteristics of air-water two-phase flow in small diameter vertical tubes. International Journal of Multiphase Flow 22 (4), 703-712.

P

Pohorecki, R., 1976. Mass transfer with chemical reaction during gas absorption on a sieve plate. Chemical Engineering Science 31, 637-644.

Pohorecki, R., Moniuk, W., 1988a. Plate efficiency in the process of absorption with chemical reaction – experiments and example calculations. The Chemical Engineering Journal 39, 37-46.

Pohorecki, R., Moniuk, W., 1988b. Kinetics of reaction between carbon dioxide and hydroxyl ions in aqueous electrolyte solutions. Chemical Engineering Science 43 (7), 1677-1684.

Pohorecki, R., 2007. Effectiveness of interfacial area for mass transfer in two-phase flow in microreactors. Chemical Engineering Science 62, 6495-6498.

Pohorecki, R., Kula, K., 2008. A simple mechanism of bubble and slug formation in Taylor flow in microchannels. Chemical Engineering Research and Design 86, 997-1001.

Q

Qian, D., Lawal, A., 2006. Numerical study on gas and liquid slugs for Taylor flow in a T-junction microchannel. Chemical Engineering Science 61, 7609-7625.

R

Ratulowski, J., Chang, H.-C., 1989. Transport of gas bubbles in capillaries. Physics of Fluids A 1 (10), 1642-1655.

Redon, C., Brochard-Wyart, F., Rondelez, F., 1991. Dynamics of dewetting. Physical Review Letters 66 (6), 715-718.

Roberts, D., Danckwerts, P.V., 1962. Kinetics of CO_2 absorption in alkaline solutions – I. Transient absorption rates and catalysis by arsenite. Chemical Engineering Science 17, 961-969.

S

Salman, W., Gavriilidis, A, Angeli, P., 2004. A model for predicting axial mixing during gas-liquid Taylor flow in microchannels at low Bodenstein numbers. Chemical Engineering Journal 101, 391-396.

Sander, R., 1999. Compilation of Henry's Law Constants for Inorganic and Organic Species of Potential Importance in Environmental Chemistry (Version 3). http://www.henrys-law.org

Serizawa, A., Feng, Z., Kawara, Z., 2002. Two-phase flow in microchannels. Experimental Thermal and Fluid Science 26, 703-714.

Simmons, M.J., Wong, D.C.Y., Travers, P.J., Rothwell, J.S., 2003. Bubble behavior in three-phase capillary microreactors. International Journal of Chemical Reactor Engineering 1, A30.

Sobieszuk, P., Pohorecki, R., Kula, K., Moniuk, W., Ilnicki, F., Cyganski, P., Gawinski, P., 2007. Measurements of bubble and slug frequency and length in gas-liquid flow in a microreactor channel. European Congress of Chemical Engineering – 6 Book of Abstracts 1, 859-860.

Sobieszuk, P., Cyganski, P., Pohorecki, R., 2008. Volumetric liquid side mass transfer coefficient in a gas-liquid microreactor. Chemical and Process Engineering 29, 651-661.

Stoessel, F., 2008. Thermal Safety of Chemical Processes: Risk Assessment and Process Design. Wiley-VCH, Weinheim.

Suo, M., Griffith, P., 1964. Two-phase flow in capillary tubes. Journal of Basic Engineering 86, 576-582.

T

Taha, T., Cui, Z.F., 2004. Hydrodynamics of slug flow inside capillaries. Chemical Engineering Science 59, 1181-1190.

Taylor, G.I., 1961. Deposition of a viscous fluid on the wall of a tube. Journal of Fluid Mechanics 10, 161-165.

Thulasidas, T.C., Abraham, M.A., Cerro, R.L., 1995. Bubble-train flow in capillaries of circular and square cross-section. Chemical Engineering Science 50 (2), 183-199.

Thulasidas, T.C., Abraham, M.A., Cerro, R.L., 1997. Flow patterns in liquid slugs during bubble-train flow inside capillaries. Chemical Engineering Science 52 (17), 2947-2962.

Triplett, K.A., Ghiaasiaan, S.M., Abdel-Khalik, S.I., Sadowski, D.L., 1999a. Gas-liquid two-phase flow in microchannels, Part I: two-phase flow patterns. International Journal of Multiphase Flow 25, 377-394.

Triplett, K.A., Ghiaasiaan, S.M., Abdel-Khalik, S.I., LeMouel, A., McCord, B.N., 1999b. Gas-liquid two-phase flow in microchannels, Part II: void fraction and pressure drop. International Journal of Multiphase Flow 25, 395-410.

V

van Baten, J.M., Krishna, R., 2004. CFD simulations of mass transfer from Taylor bubbles rising in circular capillaries. Chemical Engineering Science 59, 2535-2545.

van Steijn, V., Kreutzer, M.T., Kleijn, C.R., 2007. microPIV study of the formation of segmented flow in microfluidic T-junctions. Chemical Engineering Science 62, 7505-7514.

van Steijn, V., Kreutzer, M.T., Kleijn, C.R., 2008. Velocity fluctuations of segmented flow in microchannels. Chemical Engineering Journal 135 (Supplement 1), S159-S165.

Vandu, C.O., Liu, H., Krishna, R., 2005. Mass transfer from Taylor bubbles rising in single capillaries. Chemical Engineering Science 60, 6430-6437.

von Böckh, P., 2004. Fluidmechanik. Springer, Berlin Heidelberg.

W

Waelchli, S., von Rohr, P.R., 2006. Two-phase flow characteristics in gas-liquid microreactors. International Journal of Multiphase Flow 32, 791-806.

Wallis, G. B., 1969. One-dimensional two-phase flow. McGraw-Hill, New York.

Warnier, M.J.F., Rebrov, E.V., de Croon, M.H.J.M., Hessel, V., Schouten, J.C., 2008. Gas hold-up and liquid film thickness in Taylor flow in rectangular microchannels. Chemical Engineering Journal 135 (Supplement 1), S153-S158.

Wong, H., Morris, S., Radke, C.J., 1992. Three-dimensional menisci in polygonal capillaries. Journal of Colloid and Interface Science 148 (2), 317-336.

Wong, H., Radke, C.J., Morris, S., 1995a. The motion of long bubbles in polygonal capillaries. Part 1. Thin films. Journal of Fluid Mechanics 292, 71-94.

Wong, H., Radke, C.J., Morris, S., 1995b. The motion of long bubbles in polygonal capillaries. Part 2. Drag, fluid pressure and fluid flow. Journal of Fluid Mechanics 292, 95-110.

Y

Yang, C.-Y., Shieh, C.-C., 2001. Flow patterns of air-water and two-phase R-134a in small circular tubes. International Journal of Multiphase Flow 27, 1163-1177.

Yarin, L.P., Mosyak, A., Hetsroni, G., 2008. Fluid flow, heat transfer and boiling in micro-channels. Springer,Berlin Heidelberg.

Yue, J., Chen, G., Yuan, Q., 2004. Pressure drops of single and two-phase flows through T-type microchannel mixers. Chemical Engineering Journal 102, 11-24.

Yue, J., Chen, G., Yuan, Q., Luo, L., Gonthier, Y., 2007. Hydrodynamics and mass transfer characteristics in gas-liquid flow through a rectangular microchannel. Chemical Engineering Science 62, 2096-2108.

Z

Zlokarnik, M., 1983. Modellübertragung in der Verfahrenstechnik. Chemie Ingenieur Technik 55, 363-372.

Appendix A1

Buckingham π-theorem for two-phase flows

In order to have a general idea about the main dimensionless parameters, it is sufficient to treat the two-phase flow like a fluid flow with a free surface. As already mentioned, it is assumed that the system contains six influencing variables (ρ, μ, γ, d_h, U, g). These parameters are used in the following to set up the MLT-matrix as shown below. According to Zlokarnik (1983), the MLT-matrix may be divided into a core-matrix and a rest-matrix. In order to decide which variables should be included in the latter it is necessary to predefine the variables that should occur later in only one of the dimensionless parameters. Here the velocity U, the dynamic viscosity μ and the gravitational acceleration g, were chosen. The subdivided MLT-matrix may be written as follows:

	ρ	d_h	γ	U	μ	g
M (mass) [kg]	1	0	1	0	1	0
L (length) [m]	-3	1	0	1	-1	1
T (time) [s]	0	0	-2	-1	-1	-2
	core-matrix			rest-matrix		

Table A.1: Dimension matrix of influencing variables according to Buckingham (1914) and Zlokarnik (1983).

There are six dimensional parameters in a matrix with a rank of three. Hence, there are three dimensionless π-factors. In order to find them, one needs to transform the core matrix into a unit matrix by Gaussian elimination. This means that the elements of the core matrix have to be transformed into unity on the main diagonal and into zero elsewhere.

- transformation of the M-row:

$$\begin{array}{c} T \\ M \\ L \end{array}\left(\begin{array}{ccc} 0 & 0 & -2 \\ 1 & 0 & 1 \\ -3 & 1 & 0 \end{array}\right)\Bigg\| \begin{array}{l} \cdot\frac{1}{2} \\ \hookleftarrow + \\ \end{array} \rightarrow \begin{array}{c} T \\ M+\frac{1}{2}T \\ L \end{array}\left(\begin{array}{ccc} 0 & 0 & -2 \\ 1 & 0 & 0 \\ -3 & 1 & 0 \end{array}\right) \qquad \text{(A.1-1)}$$

- transformation of the L-row:

$$\begin{array}{c} M \\ L \\ T \end{array}\left(\begin{array}{ccc} 1 & 0 & 1 \\ -3 & 1 & 0 \\ 0 & 0 & -2 \end{array}\right)\Bigg\| \begin{array}{l} \cdot 3 \\ \hookleftarrow + \\ \end{array} \rightarrow \begin{array}{c} M \\ L+3M \\ T \end{array}\left(\begin{array}{ccc} 1 & 0 & 1 \\ 0 & 1 & 3 \\ 0 & 0 & -2 \end{array}\right) \qquad \text{(A.1-2)}$$

$$\begin{array}{c} M \\ T \\ L+3M \end{array}\left(\begin{array}{ccc} 1 & 0 & 1 \\ 0 & 0 & -2 \\ 0 & 1 & 3 \end{array}\right)\Bigg\| \begin{array}{l} \cdot\frac{3}{2} \\ \hookleftarrow + \\ \end{array} \rightarrow \begin{array}{c} M \\ T \\ (L+3M)+\frac{3}{2}T \end{array}\left(\begin{array}{ccc} 1 & 0 & 1 \\ 0 & 0 & -2 \\ 0 & 1 & 0 \end{array}\right) \qquad \text{(A.1-3)}$$

- transformation of the T-row:

$$\begin{array}{c} M \\ L \\ T \end{array}\left(\begin{array}{ccc} 1 & 0 & 1 \\ -3 & 1 & 0 \\ 0 & 0 & -2 \end{array}\right)\Bigg\| \begin{array}{l} \\ \\ \cdot -\frac{1}{2} \end{array} \rightarrow \begin{array}{c} M \\ L \\ -\frac{1}{2}T \end{array}\left(\begin{array}{ccc} 1 & 0 & 1 \\ -3 & 1 & 0 \\ 0 & 0 & 1 \end{array}\right) \qquad \text{(A.1-4)}$$

Adoption of the same transformations to the rest-matrix yields:

	ρ	d_h	γ	U	μ	g
M + $\frac{1}{2}$ T	1	0	0	- $\frac{1}{2}$	$\frac{1}{2}$	-1
(L + 3M) + $\frac{3}{2}$ T	0	1	0	- $\frac{1}{2}$	$\frac{1}{2}$	-2
- $\frac{1}{2}$ T	0	0	1	$\frac{1}{2}$	$\frac{1}{2}$	1
	unit-matrix			rest-matrix		

Table A.2: Transformed dimension matrix of influencing variables.

From the transformed dimension matrix the following dimensionless π-factors can be derived:

$$\Pi_1 = \frac{U}{\rho^{-\frac{1}{2}} \cdot d_h^{-\frac{1}{2}} \cdot \gamma^{\frac{1}{2}}} = \frac{\rho^{\frac{1}{2}} \cdot U \cdot d_h^{\frac{1}{2}}}{\gamma^{\frac{1}{2}}} \qquad \text{(A.1-5)},$$

$$\Pi_2 = \frac{\mu}{\rho^{\frac{1}{2}} \cdot d_h^{\frac{1}{2}} \cdot \gamma^{\frac{1}{2}}} \qquad \text{(A.1-6)},$$

$$\Pi_3 = \frac{g}{\rho^{-1} \cdot d_h^{-2} \cdot \gamma} = \frac{\rho \cdot g \cdot d_h^2}{\gamma} = Bo \qquad \text{(A.1-7)}.$$

With a further transformation of the π-factors one obtains:

$$\Pi_1^2 = \frac{\rho \cdot U^2 \cdot d_h}{\gamma} = We \qquad \text{(A.1-8)}, \qquad \Pi_2^2 = \frac{\mu^2}{\rho \cdot d_h \cdot \gamma} = \frac{Ca}{\mathrm{Re}} \qquad \text{(A.1-9)},$$

$$\Pi_1 \cdot \Pi_2 = \frac{\mu \cdot U}{\gamma} = Ca \qquad \text{(A.1-10)}, \qquad \Pi_1 \cdot \Pi_2^{-1} = \frac{\rho \cdot U \cdot d_h}{\mu} = \mathrm{Re} \qquad \text{(A.1-11)}.$$

Appendix A2

Layout for microchannels and covering pyrex plate with holes for inlets and outlets

For the fabrication of the microchannel plate a silicon wafer and pyrex-glass wafers with a diameter of 4 inch (≈ 100 mm) are used. Microchannels are etched into silicon by DRIE (Deep Reactive Ion Etching). This process is not applied within a zone of 5 mm measured from the wafer edges. That means that all channels including inlets and outlets are located within an inner circle of 90 mm in diameter. The way the different channel configurations were arranged on the silicon-wafer is schematically shown in figure A.1. This layout represents a stack composed of the top pyrex-wafer, containing the holes for inlet and outlet connections, and a silicon wafer with microchannels. The dimensions indicate the positions of inlet and outlet holes, which are manufactured by ultrasonic drilling.

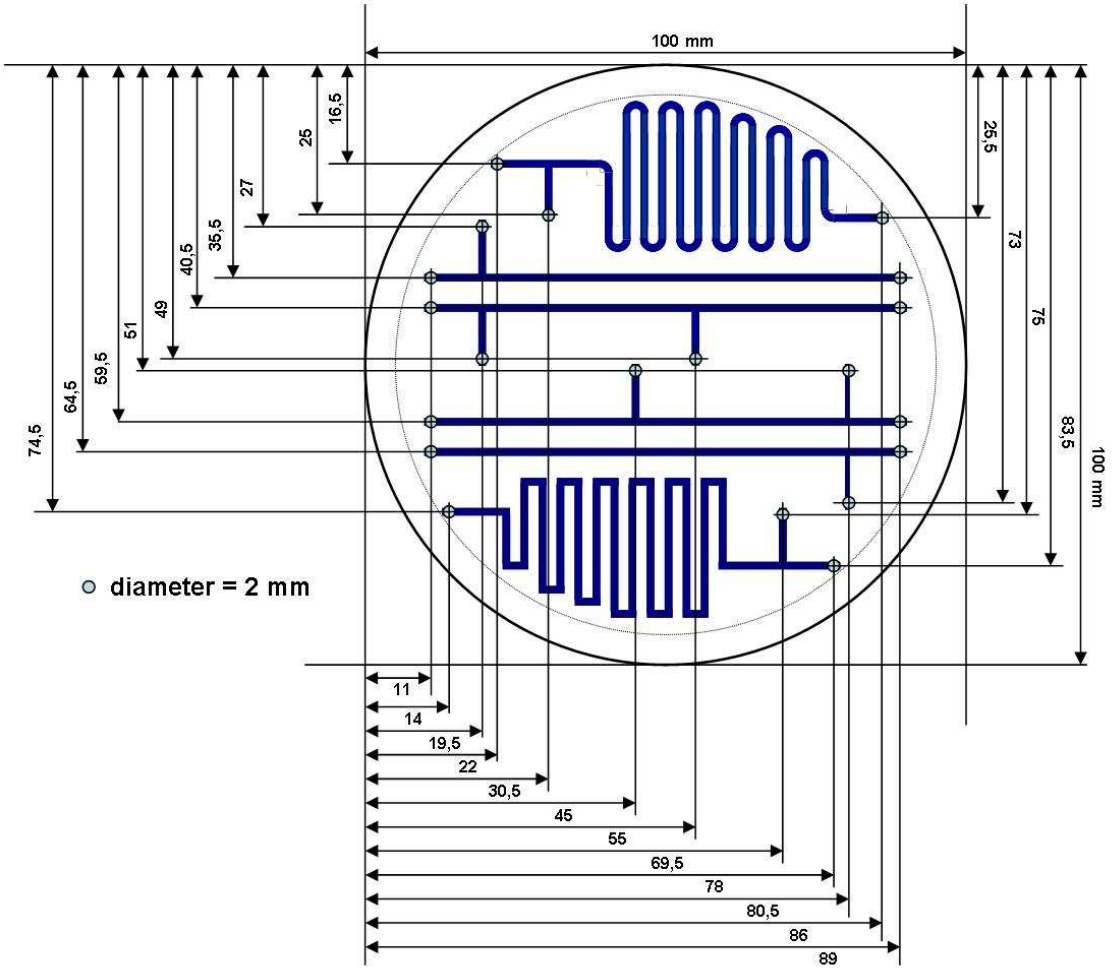

Figure A.1: Layout for microchannels and top pyrex wafer. The dimensions (given in mm) indicate the centre-positions of holes with 2 mm in diameter needed to establish the connections with channel inlets and outlets.

In order to maximize the length of the meandering channel with smoothed bends the maximum remaining space on the wafer is exploited. Approaching the outlet section this results in a descending longitudinal channel shape. The layout of the meandering channel with sharp corner bends is adjusted in analogical manner, so that both meandering channel configurations are of almost the same lengths. Further details concerning the individual dimensions of the meandering channels are given in figure A.2.

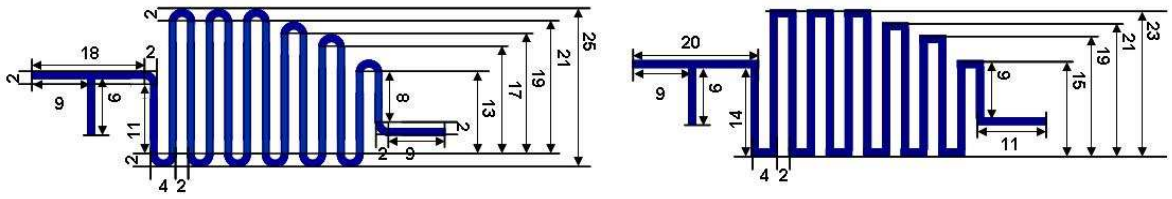

Figure A.2: Individual dimensions (given in mm) of the meandering microchannel with smoothed bends (left-hand) and the meandering microchannel with sharp corner bends (right-hand).

Further specifications with respect to the dimensions and the arrangement of microchannels on the silicon wafer are shown in figure A.3. At this all measures are given in µm units and are indicated relative to two planes, whose intersection is located in the centre of the wafer. This is done in order to transfer the layout into an AutoCAD file (Computer Aided Design), which is required to start the first step of the microchannel fabrication process.

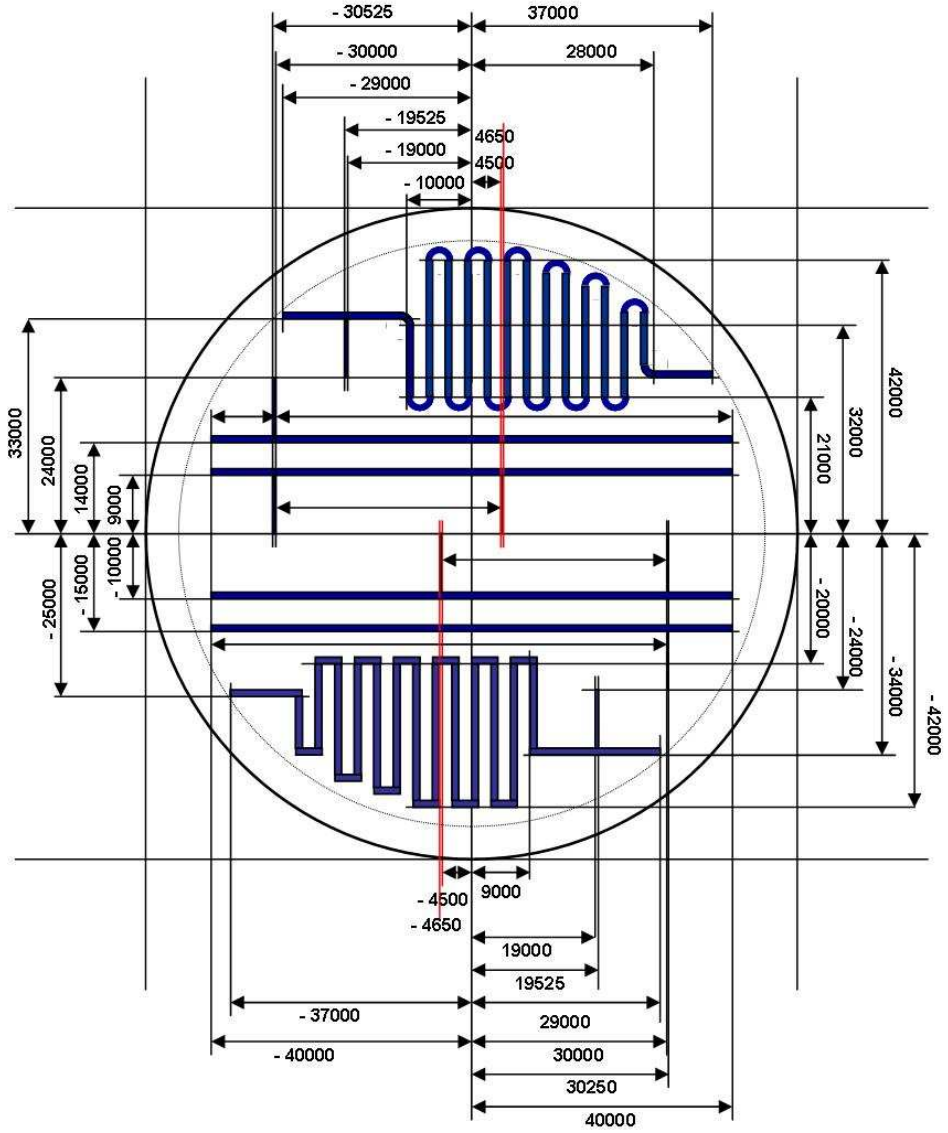

Figure A.3: Layout for microchannels on a silicon wafer. The dimensions (given in µm) indicate control positions needed to transfer the layout into and AutoCAD file.

Nomenclature

symbol	unit	definition	further specifications
a	$m^2 \cdot m^{-3}$	specific interfacial area	applies exclusively to sections 2.3, 3.4 & chapter 5; defined by (= A_S/V_R)
a	-	constant	used in eq. 3.2-6, table 3.1, eq. 3.2-15, eq. 3.2-16 & table 3.3
a_1, a_2	-	constants	used in eq. 3.2-7 & table 3.2
A	-	gaseous component or dissolved gas	applies exclusively to sections 5.1 & 5.2
A	-	constant	used in eq. 3.5-35 & table 3.9
A_1	m^2	cross-sectional area of the inner recirculation region	
A_2	m^2	cross-sectional area of the outer recirculation region	
A_B	m^2	area of the cannel cross-section occupied by the bubble	
A_{Ch}	m^2	channel cross-sectional area	
A_F	m^2	area of the cannel cross-section occupied by the liquid film	
A_S	m^2	gas-liquid interfacial area	
b	-	constant	used in eq. 3.2-16 & table 3.3
B	-	liquid component or liquid reactant	applies exclusively to sections 5.1 & 5.2
Bo	-	Bond number	defined by eq. 2.2-1 (p.6)
B,C,D,E	-	exponents	used in eq. 3.5-35 & table 3.9; apply exclusively to section 3.5.2
c_{B0}	$mol \cdot m^{-3}$	concentration of K_2CO_3 in the buffer solution	applies exclusively to eq. 5.3-29
c_{D0}	$mol \cdot m^{-3}$	concentration of $KHCO_3$ in the buffer solution	applies exclusively to eq. 5.3-29
c_e	$mol \cdot m^{-3}$	concentration of free CO_2 in the buffer solution	
c_i	$mol \cdot m^{-3}$	concentration of the component i	applies exclusively to sections 5.1 & 5.2
c_i	$mol \cdot m^{-3}$	concentration of the ion-species i	applies exclusively to eq. 5.3-11
$c_{i,L}$	$mol \cdot m^{-3}$	concentration of the component i in the bulk of the liquid phase	applies exclusively to sections 5.1 & 5.2
$c_{i,S}$	$mol \cdot m^{-3}$	concentration of the component i at the interface	applies exclusively to sections 5.1 & 5.2
c_{in}	$mol \cdot m^{-3}$	gas phase concentration of CO_2 at the inlet	
c_L	$mol \cdot m^{-3}$	concentration of CO_2 in the liquid phase	refers to the amount of CO_2 transferred from the gas phase to the liquid phase
c_{out}	$mol \cdot m^{-3}$	gas phase concentration of CO_2 at the outlet	
c_S	$mol \cdot m^{-3}$	concentration of CO_2 at the interface	
Δc_m	$mol \cdot m^{-3}$	logarithmic mean concentration difference	
Δc_{max}	$mol \cdot m^{-3}$	maximum concentration difference	
Δc_{min}	$mol \cdot m^{-3}$	minimum concentration difference	

C	-	reaction product	applies exclusively to figure 5.1, section 5.1
C_1, C_2		constants of integration	used in eq. 5.1-4
C_3, C_4		constants of integration	used in eq. 5.1-12 & eq. 5.1-16
Ca	-	Capillary number	defined by eq. 3.1-17 (p.32)
Ca_{LS}	-	superficial liquid phase Capillary number	given by eq. 2.1-4 (p.6) using μ_L and U_{LS}
Ca_{TP}	-	two-phase Capillary number	defined by eq. 3.2-14 (p.36)
d	m	diameter of the largest inscribed sphere within the channel cross-section	circular x-section: d = channel diameter square & rectangular x-section: d = channel height (h)
d	m	channel diameter	used in section 3.4
d_h	m	hydraulic diameter	
d_{dp}	m	bubble diameter in the diagonal plane	
d_{sp}	m	bubble diameter in the side plane	
D	$m^2 \cdot s^{-1}$	Diffusivity a component or solute in the liquid phase	used in sections 3.4 & 5.4.2; in section 5.4.2 (=D_{CO2})
D_i	$m^2 \cdot s^{-1}$	diffusivity of the component i in the liquid phase	
D_{CO2}	$m^2 \cdot s^{-1}$	diffusivity of CO_2 in the buffer solution	
D_w	$m^2 \cdot s^{-1}$	diffusivity of CO_2 in pure water	
E	-	enhancement factor	applies exclusively to chapter 5
E_i	-	enhancement factor for an instantaneous reaction	
f	-	friction factor	
F	$mol \cdot m^{-2} \cdot s^{-1}$	molar flux	applies exclusively to section 5.1
F_P	N	pressure force	
F_γ	N	surface tension force	
g	$m \cdot s^{-2}$	gravitational acceleration	
h	m	channel height	
h_0	m	position of the centre of the recirculation vortex within the vertical plane of the channel cross-section relative to the channel centre axis	
h_i	$m^3 \cdot mol^{-1}$	contribution of the component i	as used in eq. 5.3-13 & table 5.3
h_{rc}	m	height of the recirculation zone	
h_z	m	position of the image plane	
$h_{z,m}$	m	position of the image plane adjusted by the microscope	
H	$mol \cdot m^{-3} \cdot bar^{-1}$	Henry's law constant	as used in section 5.1.3
H_i	$mol \cdot m^{-3} \cdot bar^{-1}$	Henry's law constant of the component i	
H_{CO2}	$mol \cdot m^{-3} \cdot bar^{-1}$	Henry's law constant of CO_2 in the buffer solution	
H_w	$mol \cdot m^{-3} \cdot bar^{-1}$	Henry's law constant of CO_2 in pure water	
Ha	-	Hatta number	defined by eq. 5.1-15 (p.95)
I_i	$mol \cdot m^{-3}$	ionic strength of the component i	
IA	m^2	interrogation area	
k	-	flow coefficient	applies to frictional pressure drop in laminar flow (p.35, section 3.2)
k	s^{-1}	reaction rate constant	as used in eq. 5.1-15

k_1	s^{-1}	pseudo-1st order reaction rate constant	
$k_{1,app}$	s^{-1}	apparent pseudo1st-order reaction rate constant	
k_2	s^{-1}	second order reaction rate constant	
k_G	$m \cdot s^{-1}$	gas-side mass transfer coefficient	
$k_G a$	s^{-1}	volumetric gas-side mass transfer coefficient	
k_L	$m \cdot s^{-1}$	liquid-side mass transfer coefficient	
$k_L a$	s^{-1}	volumetric liquid side mass transfer coefficient	
K_1, K_2	$mol \cdot m^{-3}$	equilibrium constants	refer to eq. 5.3-1 & eq. 5.3-2
K_1^{∞}, K_2^{∞}	$mol \cdot m^{-3}$	equilibrium constants at infinite dilution	
l	m	channel length	
l^*	-	distance between the bubble caps normalized by the length of the slug	used in figure 4.19 & section 4.2.2
l_B	m	bubble length	
$l_{B,ini}$	m	initial bubble length	refers to the initial step of bubble formation (see section 4.2.1 & figure 4.3)
l_{BB}	m	length of the bubble body	see also subscripts
l_m	m	length of the dynamic meniscus	
l_S	m	slug length	
M_i	$kg \cdot mol^{-1}$	molar weight of the component i	used in section 5.3
m, n	-	constants & exponents	used in eq. 4.2-15 & eq. 4.2-16; defined by eq. 4.2-17 (p.89)
m, n	-	reaction orders	used in eq. 5.1-15
n	-	exponent	used in eq. 3.2-15
n	-	refractive index of the liquid phase	applies exclusively to section 4.1.2
n_1, n_2	-	exponents	used in eq. 3.2-7 & table 3.2
n_B	-	number of bubbles within the channel	defined by (= $l/(l_B + l_S)$)
n_S	-	number of slugs within the channel	defined by (= $l/(l_B + l_S)$)
n_i	mol	molar amount of the component i	exclusively used in eq. 5.3-18
$\dot{n}_i$	$mol \cdot s^{-1}$	molar flow rate of the component i (refers to the mass transfer between gas and liquid phase)	defined by (= $\dot{N}_i A_s$), applies exclusively to eq. 5.1-20, eq. 5.1-21, eq. 5.3-19 & eq. 5.3-20
$\dot{n}_i$	$mol \cdot s^{-1}$	molar flow rate of the component i in the gas phase	defined by (= $Q_i \rho_i / M_i$)
$\dot{n}_{i,L}$	$mol \cdot s^{-1}$	molar flow rate of the component i in the liquid phase	
$\dot{N}_i$	$mol \cdot m^{-2} \cdot s^{-1}$	absorption rate of the component i per unit surface area	corresponds to molar flux
p	Pa or bar	total pressure of the gas phase	used in chapter 5
p_{atm}	Pa or bar	atmospheric pressure	
p_F	Pa or bar	pressure within the liquid film	applies exclusively to section 3.1
p_i	Pa or bar	partial pressure of the component i	
$p_{i,G}$	Pa or bar	partial pressure of the component i in the bulk of the gas phase	applies to sections 5.1 & 5.2
$p_{i,S}$	Pa or bar	partial pressure of the component i at the interface	applies to sections 5.1 & 5.2
p_{in}	Pa or bar	total pressure of the gas phase at the inlet	applies exclusively to sections 5.3 & 5.4
p_{in}, p_B	Pa or bar	pressure inside of a bubble	applies exclusively to section 3.1

p_{out}	Pa or bar	pressure of the liquid around a bubble	applies exclusively to section 3.1
P_B	m	bubble perimeter	applies exclusively to section 5.4.2
Δp	Pa or bar	Laplace pressure	defined by eq. 3.1-1 (p.29)
Δp_a	Pa or bar	acceleration pressure drop	
Δp_B	Pa or bar	bubble pressure drop	
Δp_f	Pa or bar	two phase frictional pressure drop	
Δp_{fs}	Pa or bar	frictional pressure drop of the liquid slug	
Δp_{in}	Pa or bar	gas phase pressure drop at the inlet	applies exclusively to section 5.3
Δp_s	Pa or bar	static pressure drop	
Δp_{tot}	Pa or bar	total pressure drop in two-phase flow	
Q_1	$m^3 \cdot s^{-1}$	volumetric liquid flow rate through the inner recirculation region	used in section 3.3
Q_2	$m^3 \cdot s^{-1}$	volumetric liquid flow rate through the outer recirculation region	used in section 3.3
Q_B	$m^3 \cdot s^{-1}$	volumetric gas flow rate referred to the bubble	
Q_F	$m^3 \cdot s^{-1}$	volumetric liquid film flow rate	
Q_G	$m^3 \cdot s^{-1}$	volumetric gas flow rate	
$Q_{G,in}$	$m^3 \cdot s^{-1}$	volumetric gas flow rate entering the control volume	
$Q_{G,out}$	$m^3 \cdot s^{-1}$	volumetric gas flow rate leaving the control volume	
Q_i	$m^3 \cdot s^{-1}$	volumetric gas flow rate of the component i	applies exclusively to sections 5.3 & 5.4
Q_L	$m^3 \cdot s^{-1}$	volumetric liquid flow rate	
$Q_{L,in}$	$m^3 \cdot s^{-1}$	volumetric liquid flow rate entering the control volume	
$Q_{L,out}$	$m^3 \cdot s^{-1}$	volumetric liquid flow rate leaving the control volume	
Q_{rc}	$m^3 \cdot s^{-1}$	volumetric recirculation flow rate	
r	m	radius of the largest inscribed sphere within the channel cross-section	for further explanations see specifications made for d
r	m	bubble radius or radius of a hemispherical bubble cap	applies exclusively to section 3.1
r	m	radial position relative to the channel centre axis	applies exclusively to section 3.3
r	$mol \cdot m^{-3} \cdot s^{-1}$	reaction rate	applies exclusively to sections 5.1 & 5.2
r_0	m	radial position of the centre of the recirculation vortex relative to the channel centre axis	
r_{ax}	m	axial curvature of the bubble cap	
r_{BB}	m	radius of the bubble body	
r_c	m	mean radius of the interfacial curvature in the corners of the channel	
r_{eff}	$mol \cdot m^{-3} \cdot s^{-1}$	effective volumetric reaction rate	
r_h	m	bubble radius in the horizontal plane	
r_{neck}	m	radius of the bubble neck	see also subscripts
r_{rad}	m	radial curvature of the bubble cap	
r_{rc}	m	radius of the entire recirculation zone	
r_v	m	bubble radius in the vertical plane	
R	m	channel radius	applies exclusively to sections 3.3 & 4.2.2

Re	-	Reynolds number	defined by eq. 2.1-5 (p.6)
Re_{LS}	-	superficial liquid phase Reynolds number	given by eq. 2.1-5 (p.6) using ρ_L and U_{LS}
$Re_{L,TP}$	-	liquid phase Reynolds number in Taylor flow	defined by eq. 3.2-5 (p.35)
t	s	time	
t^*	-	dimensionless time of an image within an image sequence	time value corresponding to an image normalized by the time of the entire image sequence
t_{cap}	s	gas-liquid contact time at the bubble caps	
t_{film}	s	gas-liquid contact time in the film region	in section 5.4.1 & figure 5.5, defined by ($=l_B/U_B$); in section 5.4.2, defined by eq. 5.4-14 (p.110)
$t_{measure}$	s	measurement time	
t_{rc}	s	recirculation time	
T	K	temperature	
δt	s	time interval between two images of an image pair	applies exclusively to section 4.1.2
U	$m \cdot s^{-1}$	velocity	
U_{ax}	$m \cdot s^{-1}$	axial liquid phase velocity	
U_B	$m \cdot s^{-1}$	bubble velocity	
U_{dew}	$m \cdot s^{-1}$	dewetting velocity	see also subscripts
U_F	$m \cdot s^{-1}$	liquid film velocity	
U_{GS}	$m \cdot s^{-1}$	superficial gas phase velocity	defined by ($= Q_G/A_{Ch}$)
U_{LS}	$m \cdot s^{-1}$	superficial liquid phase velocity	defined by ($= Q_L/A_{Ch}$)
U_{max}	$m \cdot s^{-1}$	maximum velocity within a liquid phase	
U_{rc}	$m \cdot s^{-1}$	recirculation velocity	
U_{rel}	$m \cdot s^{-1}$	relative liquid phase velocity	defined by ($= U_{ax} - U_B$)
U_S	$m \cdot s^{-1}$	average velocity of the liquid slug	defined by ($= U_{TP}$)
U_{TP}	$m \cdot s^{-1}$	superficial two-phase velocity	defined by ($= U_{GS} + U_{LS}$)
V_F	m^3	liquid film volume	
V_G	m^3	gas volume	
V_L	m^3	liquid volume	
V_{mc}	m^3	volume of the microchannel	
V_{rc}	m^3	volume of the recirculation zone	
V_R	m^3	reaction volume or volume of the system where the absorption process takes place	
V_S	m^3	volume of the liquid slug	
V_{UC}	m^3	volume of the unit-cell	defined by ($= A_{Ch} \cdot (l_B + l_S)$)
w	m	channel width	refers usually to the main channel
w_0	m	position of the centre of the recirculation vortex within the horizontal plane of the channel cross-section relative to the channel centre axis	
w_{in}	m	width of the inlet channel	
w_{neck}	m	width of the bubble neck	see also subscripts
w_{rc}	m	width of the recirculation zone	
We	-	Weber number	defined by eq. 2.1-1 (p.6)
We_{GB}	-	bubble Weber number	as used in section 2.2.1; defined by eq. 2.2-3 (p.11)

We_{LB}	-	bubble Weber number	as used in section 3.5.1; given by eq. 2.2-3 (p.11) using ρ_L instead of ρ_G
We_{GS}	-	superficial gas phase Weber-number	defined by eq. 2.2-5 (p.11)
We_{LS}	-	superficial liquid phase Weber-number	defined by eq. 2.2-4 (p.11)
x	m	distance from the gas-liquid interface	refers to the liquid side; applies exclusively to sections 5.1 & 5.2
x_i	-	mole fraction of the component i in the gas phase	used in sections 5.3 & 5.4
Δx	m	particle traveling distance between two laser pulses	applies exclusively to section 4.1.2
y	m	coordinate within the horizontal plane of the channel cross-section relative to the channel centre axis	used in section 4.2.2; defined by figure 4.18a (p.89)
y^*	-	distance from the channel centre axis normalized by the channel half width	defined by (= $2y/w$)
z	m	coordinate within the vertical plane of the channel cross-section relative to the channel centre axis	used in section 4.2.2; defined by figure 4.18a (p.89)
z_1, z_2	m	z-coordinate of the upper and lower limits of the focal depth	used in eq. 4.2-18, section 4.2.2
z_i		valency of the ion-species i	applies exclusively to eq. 5.3-11

Greek symbols

α	-	constant	used in eq. 3.5-54; defined by (= w_{in}/w)
α_1,α_2	-	constants	used in eq. 3.5-56, eq. 3.5-57, eq. 4.2-1, eq. 4.2-4 - eq. 4.2-6; in section 4.2.1: defined by eq. 4.2-2 & eq. 4.2-3 (p.77)
α_c	-	inverse value of r_c scaled by the radius of the largest inscribed sphere	defined by eq. 3.5-8 (p.50) & eq. 3.5-9 (p.51)
γ	$N{\cdot}m^{-1}$	surface tension	
δ	m	liquid film thickness	used in chapter 3
δ	m	thickness of the stagnant layer at the liquid-side of the interface	applies exclusively to chapter 5
ε_F	-	fraction of the channel cross-sectional area occupied by the liquid film (liquid film fraction)	defined by (= A_F/A_{Ch}); see sections 3.1 & 3.5.1, also referred to as film hold-up
ε_G	-	gas hold-up	generally defined by eq. 3.5-2 & eq. 3.5-4 (p.47); in sections 3.5.2 & chapter 4 defined by (= U_{GS}/U_{TP})
ε_L	-	liquid hold-up or liquid fraction	generally defined by eq. 3.5-3, eq. 3.5-2 & eq. 3.5-4 (p.47); in sections 3.5.2 & chapter 4 defined by (= U_{LS}/U_{TP})
$\varepsilon_{L,F}$	-	fraction of the liquid volume within the unit cell which is occupied by the liquid film	defined by eq. 5.4-21 (p.112)
ε_{rc}	-	recirculation fraction	defined by eq. 3.3-5a-b (p.41)
ς	-	constant	used in eq. 3.5-24; defined by eq. 3.5-25

θ	°	contact angle	
ι	-	constant	used in eq. 3.5-25
λ_3, λ_4		variables	used in eq. 5.1-12; defined by eq. 5.1-13 (p.95)
λ_C	m	Laplace-length constant or capillary constant	defined by eq. 2.2-2 (p.7)
μ	Pa·s	dynamic viscosity	
μ_L	Pa·s	liquid viscosity	
μ_w	Pa·s	viscosity of pure water	
ν_i	-	stoichiometric coefficient of the component i	used in chapter 5
ρ	$kg \cdot m^{-3}$	density	
ρ_G	$kg \cdot m^{-3}$	density of the gas phase	
ρ_i	$kg \cdot m^{-3}$	density of the component i	used in section 5.3
ρ_L	$kg \cdot m^{-3}$	density of the liquid phase	
$\tau_{blockage}$	s	blockage time	see also subscripts
$\tau_{pinch\text{-}off}$	s	pinch-off time	see also subscripts
τ_{rc}	-	dimensionless recirculation time	defined by eq. 3.3-13 (p.42)
ψ	-	dimensionless bubble velocity	defined by (= U_B/U_{TP}); see also section 3.1
ω	°	angle	used in eq. 3.5-12

Subscripts

A	gaseous component or dissolved gas (applies to sections 5.1, 5.2 & 5.3)
B	liquid component or liquid reactant (applies exclusively to sections 5.1 & 5.2)
BB	refers to the bubble body, i.e. that part of an elongated bubble which is located between the bubble caps
blockage	refers to the initial step of bubble formation, i.e. the time when the interface reaches the channel wall opposite to the gas inlet and the bubble approximately fills the channel cross-section
C	reaction product (applies exclusively to figure 5.1, sections 5.1)
cap	refers to the cap of an elongated bubble
corners	refer to the areas of the channel cross-section which remain for the liquid phase to flow around the bubble after the forming bubble reached the channel wall opposite to the gas inlet (see also blockage)
crit	refers to the critical value of a parameter used here to mark the moment of the occurrence of dry patches within the film region
dew	refers to the dewetting of the liquid film, i.e. the growths of dry patches within the film region
front	refers to the front cap of an elongated bubble
growth	refers to the growth of a forming bubble in downstream direction
in	refers to a parameter at the inlet (applies to sections 5.3 & 5.4)
leakage	refers to leakage flow occurring during the process of bubble formation, i.e. the flow of the liquid phase which is driven around the bubble growing downstream
neck	refers to the part of a forming bubble which connects the bubble nose to the gas inlet channel
nose	refers to the front cap of a forming bubble
out	refers to a parameter at the outlet (applies to sections 5.3 & 5.4)
pinch-off	refers to the time when the interface at the bubble neck is completely squeezed and the bubble detaches from the gas inlet
rear	refers to the rear cap of an elongated bubble
∞	refers to the value of a parameter at infinite time